



Technische Universität München

Fakultät für Physik

Physics of Energy Conversion and Storage

**LASER-Assisted Determination of the Potential of
Maximum Entropy. Applications in Electrocatalysis**

Xing Ding

Vollständiger Abdruck der von der Fakultät für Physik der Technischen Universität München zur Erlangung des akademischen Grades eines

Doktors der Naturwissenschaften

genehmigten Dissertation.

Vorsitzender: Prof. Dr. David A. Egger

Prüfer der Dissertation: 1. Prof. Dr. Aliaksandr S. Bandarenka
2. Prof. Dr. Peter Müller-Buschbaum

Die Dissertation wurde am 26.07.2021 bei der Technischen Universität München eingereicht und durch die Fakultät für Physik am 14.09.2021 angenommen.

This thesis is based on the following published (in preparation) manuscripts and conference contributions:

Manuscripts:

1. X. Ding, B. Garlyyev, S.A. Watzele, T.K. Sarpey, A.S. Bandarenka. Spotlight on the effect of electrolyte composition on the potential of maximum entropy. Supporting electrolytes are not always inert // *Chemistry—A European Journal* 27 (2021) 10016-10020.
2. A. Auer(1), X. Ding(1), A.S. Bandarenka, J. Kunze-Liebhäuser. The potential of zero charge and the electrochemical interface structure of Cu(111) in alkaline solutions // *J. Phys. Chem. C* 125 (2021) 5020-5028
3. S. Xue, R.W. Haid, R.M. Kluge, X. Ding, B. Garlyyev, J. Fichtner, S. Watzele, S. Hou, A.S. Bandarenka. Enhancing the hydrogen evolution reaction activity of platinum electrodes in alkaline media using Ni-Fe clusters // *Angewandte Chemie International Edition* 59 (2020) 10934-10938
4. B. Garlyyev, Y. Liang, S. Xue, S. Watzele, J. Fichtner, W.J. Li, X. Ding, A.S. Bandarenka. Theoretical and experimental identification of active electrocatalytic surface sites // *Current Opinion in Electrochemistry* 14 (2019) 206-213
5. X. Ding,(1) D. Scieszka,(1) S. Watzele, S. Xue, B. Garlyyev, R.H. Haid, A.S. Bandarenka. Why electrolytes control the catalytic activity (submitted)
6. S. Hou, X. Ding, R.M. Kluge, T.K. Sarpey, R.W. Haid, B. Garlyyev, J. Warnan, W.

Li,* R.A. Fischer,* A.S. Bandarenka*. Elucidating cation effects on electrocatalytic oxygen evolution reaction activities of surface-mounted metal-organic framework derivatives (submitted)

Conference contributions:

1. 11th Energy Colloquium of the Munich School of Engineering 2021, Munich, 28th – 29th July 2021. (Attendance)
2. ECS Student Chapter: 3rd Symposium, Garching, 24th September 2019. (Attendance)
3. e-conversion Conference, Venice, Italy, 9th – 13th September 2019, *Laser-Induced Current Transient technique: Tool for Investigating the Electrified Solid/Liquid Interfaces. (Poster)*
4. 9th Energy Colloquium of the Munich School of Engineering, Garching, 1st August, 2019. (Attendance)
5. 8th Energy Colloquium of the Munich School of Engineering, Garching, 19th July 2018. (Attendance)

Abstract

The optimization of various electrochemical systems requires a detailed understanding of the properties of the electrified interface. The net orientation of solvent (e.g., water molecules) at the electrode/electrolyte interface, one of the essential interfacial properties, can tremendously influence the electrochemical processes such as the electrode activity and the charge and mass transfer at the interface. The potential of maximum entropy (PME), a significant parameter to associate with the electrode processes, can be used to reflect the net orientation of water molecules at the interface. The PME can be identified by the laser-induced current transient (LICT) technique. This *in-situ* technique has been considered a powerful tool for the investigation of various electrochemical systems.

For a specific electrocatalytic reaction, the performance of this reaction can be affected by the nature of the electrode, such as the electrode composition and its structure. In the case of aqueous electrolytes, however, electrocatalytic processes can additionally be influenced by the electrolyte composition. Particularly interesting is the influence of electrolytes containing alkali metal cations since alkali metal cations are widely employed in laboratories and industries. Besides, the concentration of H^+ and OH^- ions (denoted as pH) also exhibits an obvious influence on the electrode processes. Although many scientific articles underlined the effect of electrolyte composition on various electrochemical processes, there is still a deficit in systematic and quantitative research. Therefore, it is imperative to understand why and how tuning the electrolyte compositions controls the electrocatalytic activity quantitatively.

This work aims to correlate the influence of the electrolyte nature on the interfacial water structure and electrochemical processes via the determination of the PME by the LICT. Noble metal electrodes, i.e., polycrystalline platinum and gold, were used for

studying electrocatalysis at different pH values in the presence of HClO_4 and $(\text{AM})_2\text{SO}_4$ ($\text{AM} = \text{Li}^+, \text{Na}^+, \text{K}^+, \text{and } \text{Cs}^+$) solutions. It has been demonstrated that the electrolyte can, in fact, affect the activity of the electrodes towards the hydrogen evolution or oxygen reduction reactions. The identified PME shows a clear trend between the nature of the electrolyte with the electrocatalytic reactions. Moreover, the LICT was applied to investigate the atomic structure of the Cu(111) electrode surface. Merging the LICT technique with *in-situ* electrochemical scanning tunneling microscopy, the results revealed that the Cu(111) surface slowly starts to restructure at the PME at pH 13 and pH 11 of NaClO_4 solutions. Interestingly, the PME of Cu(111) shows a pH dependence on the standard hydrogen electrode scale in alkaline media. Furthermore, the cation effect on the oxygen evolution reaction (OER) activity of the surface-mounted metal-organic framework (SURMOF) derivatives was studied with the LICT technique in alkaline media. It was found that the interface water structure of SURMOF correlates with the OER performance.

Based on the observed results, it is believed that the LICT can help to improve the fundamental understanding of electrolyte effects on various electrochemical systems. This is a prerequisite for rational electrolyte engineering in electrocatalysis.

Acknowledgment

This thesis would not have been accomplished without the help and support of many people. Therefore, I would like to thank...

... **Prof. Dr. Aliaksandr Bandarenka** for giving me the opportunity to perform my PhD thesis in his group. His guidance helped me in all the time of research and writing of this thesis. I could not have imagined having a better supervisor for my PhD study.

... **Prof. Dr. Julia Kunze-Liebhäuser** and **Andrea Auer** for collaborations related to the investigation of the Cu(111)/liquid interface structure and dynamics.

... **Dr. Weijin Li** and **Shujin Hou** for collaborations related to the cation effect on the metal-organic framework derivatives.

... **Dr. Daniel Scieszka** for the research guidance of my project. He taught me how to operate the laser-induced current transient technique. I appreciated his good advice and profound discussions.

... **Dr. Batyr Garlyyev**, **Dr. Sebastian Watzele**, and **Dr. Song Xue** for the constant supports in many projects and great guidance for writing papers.

... **Theophilus Kobina Sarpey**, **Richard Haid**, **Dr. Batyr Garlyyev**, **Dr. Sebastian Watzele**, **Dr. Elena Gubanova**, **Regina Kluge**, and **Shujin Hou** for their constructive feedback on the topic of my thesis and their supports in scientific work.

... all the former and current members of the ECS: **Dr. Yunchang Liang**, **Dr. Jeongsik Yun**, **Enggar Pramanto Wibowo**, **Jongho Kim**, **Xiaohan Sun**, **Dr. Johannes Fichtner**, **Philipp Marzak**, **Xaver Lamprecht**, **Leon Katzenmeier**, **Leif Carstensen**, **Thorsten Schmidt**, **Dr. Rohit Ranganathan Gaddam**, **Kun-Ting Song**, **Xiaoxin Ma**, and **Peter Schneider** for having a nice lab environment during my studies.

... **Siegfried Schreier** for his professional technical assistance. I am very thankful to

Siegfried for designing and taking care of the setups.

... **China Scholarship Council** for the 48 month PhD study financial support.

... **my family** for their endless support, encouragement, and understanding. Especially, many thanks to **my sister**. Without her good care for our parents in the past years, I couldn't focus on my doctorate since I was far away from home.

Finally, my special thanks go to my partner, **Zhiying**, for all love and support. Without her advice, patience, and emotional support, I would not have been able to finish this project.

Content

Abstract.....	5
Acknowledgment.....	7
1. Introduction.....	13
1.1 Energy Conversion and Storage: Current Situation and Outlook	13
1.2 The Role of the Electrolyte Composition in Electrocatalysis	15
1.2.1 Effect of Cations	16
1.2.2 Effect of Anions	18
1.2.3 Effect of pH.....	18
1.3 Aim of the Thesis	20
2. Theoretical Part.....	21
2.1 The Sabatier Principle.....	21
2.2 Active Sites	23
2.3 Fundamental Electrochemical Equations.....	23
2.3.1 Nernst Equation	23
2.3.2 Butler-Volmer Equation	27
2.3.3 Tafel Equation	30
2.4 Important Electrocatalytic Reactions.....	31
2.4.1 Water Splitting	31
2.4.1.1 Hydrogen Evolution Reaction	32
2.4.1.2 Oxygen Evolution Reaction	34
2.4.2 Fuel Cells	37
2.4.2.1 Hydrogen Oxidation Reaction.....	38

2.4.2.2 Oxygen Reduction Reaction.....	39
2.5 The Electrochemical Interface	41
2.5.1 Development of the Double Layer.....	41
2.5.2 Interfacial Water Layer	43
2.5.3 Potential of Zero Charge and Potential of Maximum Entropy	46
2.5.4 Determination of the Potential of Zero Charge and the Potential of Maximum Entropy	49
2.5.4.1 Electrocapillary Methods.....	49
2.5.4.2 Capacitance Methods.....	51
2.5.4.3 CO Charge Displacement	52
2.5.4.4 N ₂ O Reduction	54
2.5.4.5 Laser-Induced Current Transient Technique.....	56
2.6 Other Techniques Applied in this Work	63
2.6.1 Cyclic Voltammetry	63
2.6.2 Chronoamperometry	64
3. Experimental Part.....	65
3.1 Electrochemical Cells	65
3.2 Setup for the Laser Measurements.....	67
3.3 Preparation Before the Electrochemical Measurements	68
3.3.1 Preparation of Electrolytes.....	68
3.3.2 Preparation of Electrodes	69
3.4 Electrochemical Measurements	72
3.4.1 LICT Measurements	72
3.4.1.1 LICT Measurements for the AT-cut Polycrystalline Au Quartz Crystal Wafer Electrodes	72

3.4.1.2 LICT Measurements for the AT-cut Polycrystalline Pt Quartz Crystal Wafer Electrodes	74
3.4.1.3 LICT Measurements for Cu(111) Crystals	76
3.4.1.4 LICT Measurements for SURMOFs	76
3.4.2 Activity Measurements	76
4. Results and Discussion.....	77
4.1 Interface Structure and Electrode Activity.....	77
4.1.1 pH Effect	78
4.1.1.1 pH Effect for Pt _{pc} and Au _{pc} Electrodes in HClO ₄ Solutions	78
4.1.1.2 Oxygen Effect for Pt _{pc} and Au _{pc} Electrodes in HClO ₄ Solutions.....	88
4.1.2 Cation Effect	94
4.1.2.1 pH Effect in the Presence of Alkali Metal Cations.....	94
4.1.2.2 Influence of Cations on the Electrode Activity.....	106
4.1.3 Anion Effect	113
4.2 The Investigation of the Electrochemical Interface Properties at Cu(111) in Alkaline Solutions.....	116
4.3 The Cation Effect on Metal-Organic Framework Derivatives.....	122
5. Conclusions and Outlook	127
Appendix.....	131
A. pH Effect in the Presence of Alkali Metal Cations for Pt Electrode.....	131
B. Anion Effect for Pt Electrode	134
C. The Electrochemical Interface Structure of Cu(111) in Alkaline Solutions.....	136
D. Abbreviations and Symbols	139

E. Publications	145
References	161

1. Introduction

1.1 Energy Conversion and Storage: Current Situation and Outlook

Renewable energy sources, such as wind, solar energy, and hydro energy, are widely developed to meet the continuous growth of total energy consumption of human society and to solve the environmental problems caused by traditional fossil fuels.¹⁻³ Because of the variability and intermittency of these renewable energy sources, large-scale energy conversion and storage systems are required for efficient and sustainable energy applications.⁴⁻⁶ Hydrogen has been considered the most significant energy carrier due to its theoretical high energy conversion efficiency, convenient storage and transport, and high energy density.⁷⁻⁹ A large number of industries have already focused on the development of hydrogen production and application pathways and technologies after the Paris conference in 2015.¹⁰ For instance, hydrogen energy has emerged as one of the most promising energy options. It has successfully decreased air pollutions in China and Japan since 2017.⁷ Germany proposes to significantly cut CO₂ emission (around 179 MtCO₂eq) by transitioning road transport partially from fossil to hydrogen energy.¹¹ Well, 28% of the total CO₂ emissions are caused by transportation, according to energy agencies reports.¹² Fuel cells, being electrochemical cells for the conversion of chemical energy into electricity, are considered in this respect an ideal player in the transportation sector owing to their high efficiency and low environmental impacts.¹³⁻¹⁵ Recently, fuel cells are applied extensively in submarines, ships, trains, and vehicles.¹⁶ Thus, comparing the future renewable alternatives with the conventional use of fossil resources, one can expect fewer environmental issues, such as global warming, acid rain, and climate change (**Figure 1.1**).^{3,17,18} Therefore, the hydrogen-based energy storage systems provide a potential route to address various environmental problems

caused by classic fossil resources.

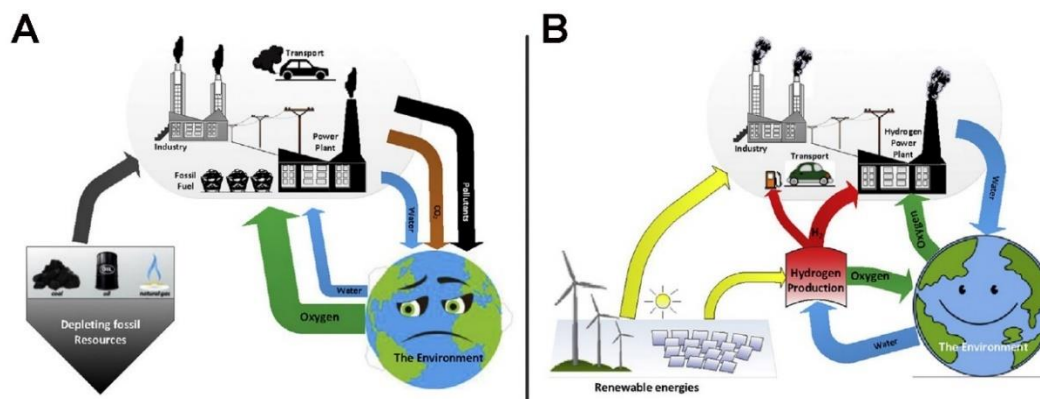


Figure 1.1. A hypothetical comparison between the energy systems based on (A) traditional fossil fuels and (B) hydrogen energy. Reproduced with permission from reference 18.

Hydrogen, as a secondary energy carrier, can be produced from various energy sources such as water and natural gas. Nowadays, about 71% of hydrogen is produced by steam reforming of natural gas.¹⁹ However, this production method can cause massive CO₂ emissions (around 10 times the amount of the hydrogen mass).²⁰ Electrolytic water splitting, as a mature energy conversion method, is one of the most promising ways to develop an environmental-friendly and low-cost technology for large-scale hydrogen production.²¹⁻²⁴ In such a system, water can be electrolyzed by electricity in the so-called water electrolyzers to generate hydrogen and oxygen. The oxygen can be vented to the atmosphere, while the hydrogen is stored as a fuel and can be further oxidized in a fuel cell to regenerate water to release energy. However, the efficiency of the current state-of-the-art electrolyzers is insufficient. The production of hydrogen *via* water electrolysis continues to be a relatively expensive process. The global hydrogen production obtained by water electrolysis is far less than 1%, according to data reported in 2018.¹⁹ Thus, optimization of the electrolysis system is necessary.

1.2 The Role of the Electrolyte Composition in Electrocatalysis

Theoretically, a voltage of 1.23 V is required to split water electrochemically under standard conditions.²⁵ However, to overcome the activation barrier of the reaction, a high overpotential is always needed. This goes for fuel cells as well, especially for the slow four-electron transfer kinetics of the reactions taking place at the cathode (oxygen reduction reaction).²⁶ The most efficient catalysts are always requested for both the anode and cathode sides to decrease the complicity and cost of the system. To increase the number of active sites at the electrode surface and improve the electrocatalytic performance, one can introduce certain facets or defects to change electrode surface structure²⁷⁻²⁹ or create alloys to change electrode surface composition³⁰⁻³². Countless studies have already focused on the optimization of the electrode to enhance the electrocatalytic activity.³³⁻⁴¹ For instance, the hydrogen evolution reaction (HER) performance on Pt(111) modified with Ni and Fe electrocatalyst (NiFe@Pt(111)) was investigated in our previous work, as shown in **Figure 1.2A** and **B**. The HER activity of Pt modified with Ni-Fe clusters can be significantly increased in alkaline media. The overpotential at 10 mA cm⁻² was approximately 128 mV.⁴²

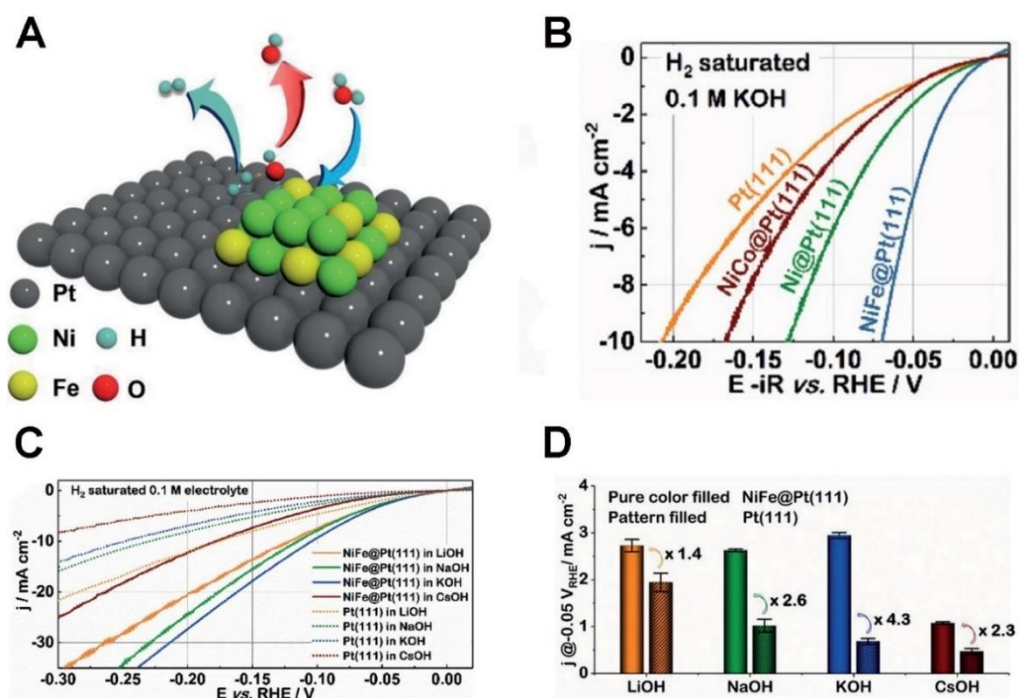


Figure 1.2. (A) Proposed mechanism of HER on NiFe@Pt(111) electrode in alkaline media. (B) Polarization curves of Pt(111) and modified Pt(111) electrodes observed in 0.1 M H₂-saturated KOH solution. (C) and (D) HER activities of Pt(111) and NiFe@Pt(111) recorded in 0.1 M H₂-saturated LiOH, NaOH, KOH, and CsOH, respectively. Reproduced with permission from reference 42.

Although most studies focus on the modification of the electrode materials, the interest in the electrolyte composition effect is gradually increasing.⁴³⁻⁴⁷ The improved understanding of the electrochemical systems and better experimental methodologies contribute to more investigation of the electrolyte composition influence.⁴⁸⁻⁵² Especially, the activity of certain electrocatalysts can be drastically influenced by the electrolyte composition, such as the Pt(111) and NiFe@Pt(111) electrodes in different alkali metal cation-containing electrolytes, as presented in **Figure 1.2C** and **D**.

1.2.1 Effect of Cations

The most prominent example for the cation effect is the alkali metal cation-containing

electrolyte due to their wide applications in both the laboratory and industry.⁵³⁻⁵⁵ For instance, Strmcnik *et al.* found that the non-covalent interactions between hydrated alkali metal cations and adsorbed OH species correlate to the oxygen reduction reaction (ORR) activities on Pt(111).⁵⁶ The ORR on Pt(111) decreases in the sequence $\text{Cs}^+ > \text{K}^+ > \text{Na}^+ > \text{Li}^+$, which is inversely proportional to the hydration energies of the corresponding cations, as shown in **Figure 1.3A**. The same trend was observed in a similar study on Pt/C catalyst (**Figure 1.3B**), where only K^+ , Na^+ , and Li^+ were involved.⁵⁷

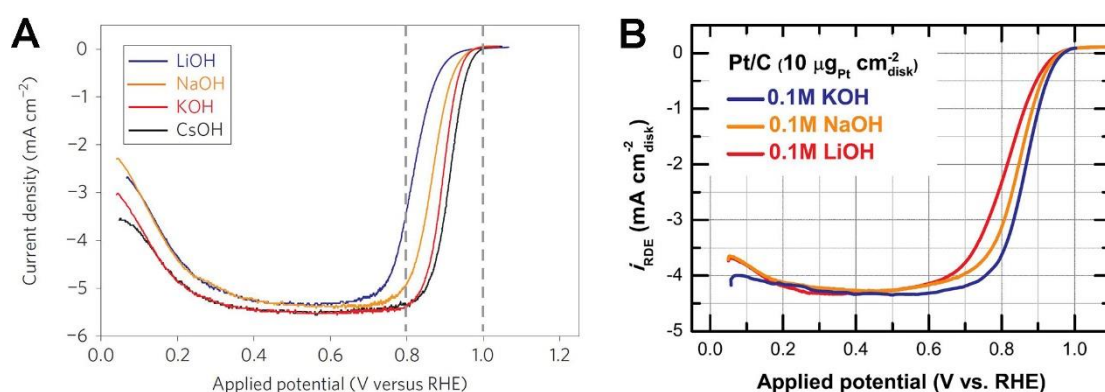


Figure 1.3. Polarization curves for the ORR of (A) Pt(111) and (B) Pt/C in various alkali metal cation-containing electrolytes. The ORR results for Pt(111) are taken from reference 56, while outcomes for Pt/C are taken from reference 57.

The influence of alkali metal cations on the HER was observed for Pt(111) in acidic electrolytes, as shown in **Figure 1.4**.⁵⁸ However, it has no linear relationship with the hydration energies of these cations due to the specifically adsorbing (bi)sulfate anions, which can block the active sites.

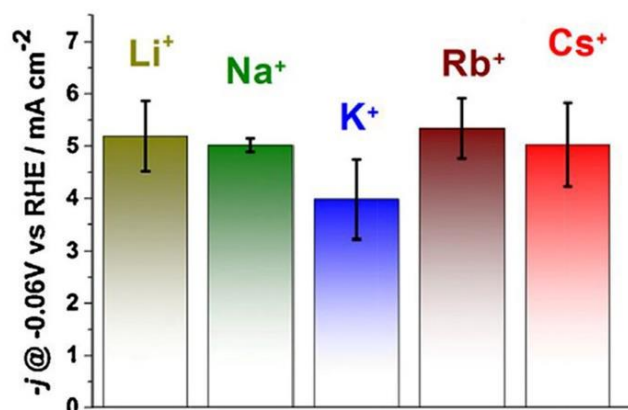


Figure 1.4. HER activities of Pt(111) electrodes in H₂-saturated 0.05 M H₂SO₄ containing 0.05 M (AM)₂SO₄ (AM = Li⁺, Na⁺, K⁺, Rb⁺, Cs⁺). Reproduced with permission from reference 58.

1.2.2 Effect of Anions

The specific adsorption of anions is poisonous to the catalytic centers, which can be considered the main reason for the anion effects.⁵⁹⁻⁶² For instance, Lamy-Pitara *et al.* presented that the strongly adsorbed anions (HSO₄⁻, Cl⁻) can cause a decrease in the electrocatalytic oxidation of hydrogen of Pt.⁶³ Zhu *et al.* found that CO₃²⁻ and SO₄²⁻ had significant effects on Pt/C and lowered the ORR activity even at a very low concentration in alkaline solution.⁶⁴ Shin *et al.* demonstrated the effect of anions (Cl⁻, Br⁻, I⁻, ClO₄⁻, BF₄⁻, PF₆⁻) on the ORR activity of palladium nanoparticles in acidic media. They believed the influence of anions resulted from the interactions between the anions and the electrolytes affecting the local proton concentration around the catalyst surfaces, namely the local pH.⁶⁵

1.2.3 Effect of pH

The role of the electrolyte pH is of crucial importance for electrocatalytic reactions,

such as the HER and ORR, due to the huge activity difference for various electrodes in alkaline and acidic media.⁶⁶⁻⁶⁹ However, the interpretation of the pH effect is a bit difficult.^{70,71} For instance, the metal- H_{ad} bond energy is regarded as a sole descriptor for the HER mechanism by many researchers.^{72,73} But this does not sufficiently explain the lower HER activity in alkaline solutions. The nature of the proton source and the presence of the surface adsorption must be considered.⁷⁴ Strmcnik *et al.* summarized the pH effect on the HER activity of Au(111) in various pHs of 0.1 M NaClO₄ solutions, as shown in **Figure 1.5**.⁷⁴ Interestingly, increasing the electrolyte pH from 1 to 4 changes the typical HER polarization profile, which indicates that the HER is apparently controlled by the mass transport of reactive hydronium species in this case. However, the polarization curves become pH-independent above pH 5. Under this condition, the HER is mainly governed by the pH-independent transformation of H₂O to evolve H₂.

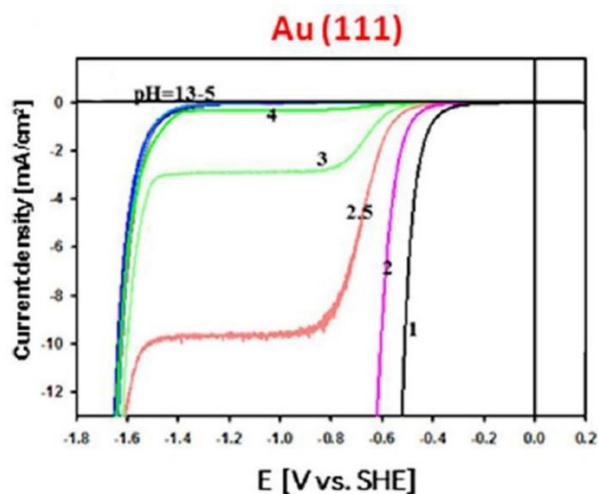


Figure 1.5. pH-dependent polarization curves for the HER of Au(111) in 0.1 M NaClO₄ at rotation rates of 1600 rpm and sweep rate of 50mV/s. Reproduced with permission from reference 74.

It should be mentioned that the cation and anion effect needs to be considered when investigating the pH effect, especially when involving specifically adsorbed anions.⁷⁵

This makes it extremely difficult to decouple the pH effects and the contributions emanating from cations and anions.

1.3 Aim of the Thesis

The vital role of the electrolyte composition in electrocatalytic systems has been discussed in **Section 1.2**. However, it is difficult for electrochemists to interpret how and why electrolytes control the electrocatalytic processes experimentally. In this thesis, determination of the potential of maximum entropy (PME) was performed with the laser-induced current transient (LICT) technique, which is one of the most effective methods to study the electrolyte significance:

1. The pH effect on the electrocatalytic activity was investigated for polycrystalline Pt and Au electrodes. The HER and ORR were used as model energy-relevant processes. The effect of dissolved oxygen on the interfacial water structure for both Pt and Au electrodes was considered. The corresponding PME measurements were carried out in HClO₄ solutions at different pHs.
2. The cation effect on the HER and ORR activities was investigated for polycrystalline Pt electrodes. Alkali metal cations were selected for the cation effect study due to their wide application in industry and laboratory. Beyond that, the pH effect in the presence of alkali metal cations was investigated for Pt and Au. The oxygen-saturated electrolytes were considered as well.
3. The anion (NO₃⁻, ClO₄⁻, Cl⁻, Ac⁻, and SO₄²⁻) effect on the HER and ORR activities was studied for polycrystalline Pt.
4. The investigation of the electrochemical interface structure of Cu(111) was carried out in alkaline solutions, and the pH effect on the interfacial structure for Cu(111) was investigated in 0.1 M NaClO₄ solutions.
5. The cation effect on metal-organic framework derivatives was studied.

2. Theoretical Part

2.1 The Sabatier Principle

The Sabatier principle, described by Paul Sabatier at the beginning of the 20th century, is one of the heterogeneous catalysis fundamentals.⁷⁶ It states that the binding energy between the catalyst surface sites and the reaction intermediates should be neither too weak nor too strong. If the interaction is too weak, the catalyst fails to activate the reactants. Conversely, the intermediates or products block the catalyst surface if the interaction is too strong. Consequently, the binding energy between the surface sites and the reaction intermediates should be “just right” to provide efficient catalysis.⁷⁷ However, the original Sabatier principle is only qualitative.

The quantification of the Sabatier principle can be achieved by the construction of the so-called volcano plots, which Balandin first reported.⁷⁸ This is because the Sabatier principle can be related to the linear free energy relationships, such as the Brønsted relation, which represents a bridge between thermodynamics and kinetics.⁷⁹ They are based on the observation that differences in activation energy arise from dissimilar reaction enthalpies. Therefore, in a volcano plot, the reaction activity (for example, in the case of electrocatalysis, the current density, half-wave potential, or overpotential) is plotted *versus* a descriptor (such as the heat of formation of a bulk compound or the heat of adsorption of one of the reactants), which is correlated with the stability of the intermediates.

For instance, **Figure 2.1** presents a volcano plot for the hydrogen evolution reaction (HER) on various metallic surfaces.⁸⁰ The strength of the Me–H bond is used as the descriptor. The HER exchange current densities are applied to represent the reaction activity. The catalysts on the left side exhibit weaker Me–H bonds, and their activity is restricted by the adsorption of H atoms on the free catalytic site of the

electrode. The catalysts on the right side exhibit stronger Me–H bonds, and their activity is limited by creating an H–H bond and subsequent desorption of produced H₂. Thus, the ideal catalyst for the HER activity should be located at the top of the volcano plot, that is, the highest exchange current densities, where the strength of the Me–H bond is just right.

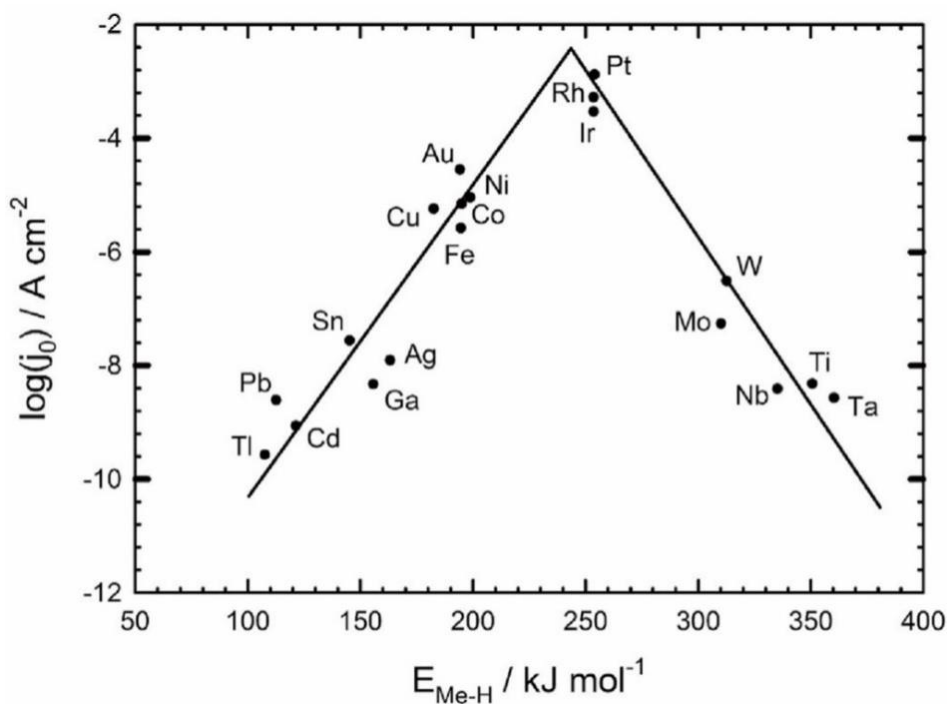


Figure 2.1. Volcano plot for the HER. Exchange current densities, $\log(i_0)$, on monometallic surfaces are plotted as a function of the Me–H bond strength. Reproduced with permission from reference 80.

The volcano plot, which combines the Sabatier principle with the scaling relations, has been successfully utilized to predict and explain the catalytic properties quantitatively.⁸¹⁻⁸⁵ In addition, with the development of the density functional theory (DFT) methodology, more advanced descriptors of material properties (for instance, the OH adsorbates formation potential) were developed, and thus, the predictive power in catalyst design was improved.^{84,86-88}

2.2 Active Sites

The concept of active sites, which is fundamental to electrocatalytic reactions, states that several sites or regions on the catalyst surface mainly determine its overall performance.⁸⁹⁻⁹¹ As mentioned in the last section, the Sabatier principle elucidates that the interaction between the catalyst surface and reaction intermediates should be optimal for the best activity performance. However, this interaction can differ between dissimilar sites on the surface, and it is not homogeneous at the atomic level.⁹² Thus, introducing the hypothesis of active sites is of significance for the fundamental understanding of electrocatalysis and the development of superior catalysts.

Langmuir first claimed the existence of active sites to explain the catalytic activity of catalyst surfaces in 1922.⁹³ According to his postulate, the catalyst surface comprises a finite number of sites that govern the overall activity. Taylor further elaborated this idea in 1925 and proposed that not all atoms on the surface of catalyst would be active for a particular reaction but only the so-called active sites.⁹⁴ These reactions, which are predominated by the interaction between specific surface motifs and the reaction intermediates, are known as structure-sensitive reactions.⁹⁵ The identification of the active sites at the solid/liquid interfaces is required to better understand the mechanism and improve catalyst design. As an example of an experimental tool, electrochemical scanning tunneling microscopy was successfully employed in the determination of the active sites by analyzing the noise level of the signal (n-EC-STM).⁹⁶⁻⁹⁸

2.3 Fundamental Electrochemical Equations

2.3.1 Nernst Equation

In electrochemistry, a certain reaction will only take place at an electrode in an electrolyzer if the applied potential reaches a certain value. Therefore, to study

electrochemical systems, the electrode potential needs to be defined. However, the absolute potentials cannot be measured.⁹⁹

The chemical potential of component i , μ_i , is defined as

$$\mu_i = \mu_i^0 + RT \ln a_i \quad (2.1)$$

where R is the universal gas constant, T is the temperature, a_i is the activity of component i , and μ_i^0 is the corresponding standard chemical potential of component i (when $a=1$).

However, **Equation 2.1** does not consider the electric contribution to the reaction processes. According to the modifications by Butler and Guggenheim^{100,101}, **Equation 2.1** becomes

$$\tilde{\mu}_i = \mu_i^0 + RT \ln a_i + z_i F \varphi \quad (2.2)$$

where z_i is the charge of component i , F is the Faraday constant, φ is the electrostatic potential, $\tilde{\mu}_i$ is the electrochemical potential.

Under equilibrium conditions (*i.e.*, no net current flow), the free energy change, ΔG_r , must be zero. Therefore, the fundamental equation for a chemical reaction in equilibrium can be written as

$$\Delta G_r = \sum_i v_i \tilde{\mu}_i = 0 \quad (2.3)$$

where v_i is the stoichiometric number of component i .

For a general redox reaction, this chemical reaction under equilibrium conditions can be expressed as



where S_{Red} and S_{Ox} term the reduced and oxidized components in the redox reaction,

respectively. n is the stoichiometric number of electrons involved in the reaction. In this case, the corresponding chemical equation in the form of the electrochemical potentials can be written as

$$\tilde{\mu}_{Red} = \tilde{\mu}_{Ox} + n\tilde{\mu}_{e^-} \quad (2.5)$$

where $\tilde{\mu}_{Red}$, $\tilde{\mu}_{Ox}$ and $\tilde{\mu}_{e^-}$ are the electrochemical potentials of the reduced components, the oxidized components, and the electrons, respectively.

The combination of **Equations 2.2, 2.3, and 2.5** yields

$$\mu_{Red}^0 + RT \ln a_{Red} + nF\varphi_M = \mu_{Ox}^0 + RT \ln a_{Ox} + nF\varphi_S + n\mu_{e^-}^0 \quad (2.6)$$

where φ_M and φ_S are the potentials of the electrode and the electrolyte, respectively. From this equation, the Galvani potential difference between the electrode and the solution, $\Delta\varphi$, can be obtained as

$$\begin{aligned} \Delta\varphi = \varphi_M - \varphi_S &= \frac{\mu_{Ox}^0 + n\mu_{e^-}^0 - \mu_{Red}^0}{nF} + \frac{RT}{nF} \ln \frac{a_{Ox}}{a_{Red}} \\ &= \Delta\varphi^0 + \frac{RT}{nF} \ln \frac{a_{Ox}}{a_{Red}} \end{aligned} \quad (2.7)$$

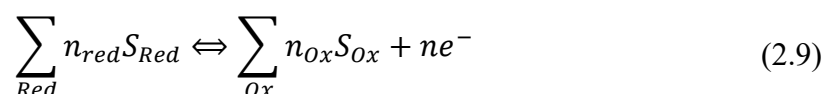
$\Delta\varphi^0$ is called the standard Galvani potential difference, which is defined as the difference in the Galvani potentials of the electrolyte and the electrode when a_{Ox} and a_{Red} are equal.

However, the Galvani potential difference cannot be experimentally measured. This is because the Galvani potential difference is always influenced if an additional measuring probe is introduced to the system. Instead, introducing a second electrode with a constant Galvani potential difference ($\Delta\varphi' = const.$) into the system, the potential of the working electrode (WE) can be measured by referencing it to the second electrode ($E = \Delta\varphi - \Delta\varphi'$). This second electrode is called the reference electrode (RE). The potential difference between the WE and RE, E , is termed the electrode potential. The standard

electrode potential can be written as $E_0 = \Delta\phi_0 - \Delta\phi'$ in the case of standard conditions. Combining with **Equation 2.7**, the working electrode potential can be expressed as

$$E = E_0 + \frac{RT}{nF} \ln \frac{a_{Ox}}{a_{Red}} \quad (2.8)$$

This equation is the so-called Nernst equation. Considering an electrochemical process, which involves several redox reactions,



Equation 2.6 becomes

$$\begin{aligned} & \sum_{Red} n_{Red} (\mu_{Red}^0 + RT \ln a_{Red}^{n_{Red}}) + nF\phi_M \\ & = \sum_{Ox} n_{Ox} (\mu_{Ox}^0 + RT \ln a_{Ox}^{n_{Ox}}) + nF\phi_S + n\mu_{e^-}^0 \end{aligned} \quad (2.10)$$

Thus, the generalized Nernst equation can be expressed as

$$E = E^0 + \frac{RT}{nF} \ln \frac{\prod_{Ox} a_{Ox}^{n_{Ox}}}{\prod_{Red} a_{Red}^{n_{Red}}} \quad (2.11)$$

where $\prod_t a_t^{n_t} = a_{S_1}^{n_1} \cdot a_{S_2}^{n_2} \cdot \dots \cdot a_{S_i}^{n_i}$.

In electrochemistry, the Nernst equation correlates the potential of an electrochemical reaction to the standard electrode potential, the temperature, and the activities of the chemical species, which undergo reduction and oxidation processes. The Nernst equation specifies the dependence of the electrochemical system on changes in the concentration of the electroactive species or on alterations of the working electrode potential. Because the standard electrode potential, E_0 , is defined in equilibrium, the

Nernst equation holds only for equilibrium conditions according to **Equation 2.11**.

Various REs exhibit stable potentials for aqueous and non-aqueous systems. One of the primary reference electrodes is the standard hydrogen electrode (SHE). However, its definition is based on an idealized solution of molarity 1 mol kg⁻¹ at a standard pressure of 1 bar. In addition, the H⁺ ions were assumed not to interact with other ions. Instead, the reversible hydrogen electrode (RHE), which is a practical hydrogen electrode, is widely used for experimental measurements. At 25°C, the relationship between RHE and SHE can be expressed as

$$E_{RHE} = E_{SHE} + 0.0591 \cdot pH \quad (2.12)$$

Thus, the RHE depends on the pH of the solution. Besides, there are many common REs, which can be applied depending on the investigated systems, such as the saturated calomel electrode (SCE), the mercury–mercurous sulfate electrode (MMS), and the silver-silver chloride electrode (SSC). In this research, both MMS and SSC electrodes were selected as the REs. However, in most cases, the potentials are recalculated to RHE.

2.3.2 Butler-Volmer Equation

As mentioned above, the Nernst equation describes the electrochemical system under equilibrium conditions. In addition, this chapter covers the non-equilibrium situation. The net electric current of a reaction depends on the magnitude of the applied potential. This tendency is mathematically described by the Butler–Volmer equation (named after John Alfred Valentine Butler and Max Volmer), and gives the most fundamental relationship in electrochemical kinetics.

The current density, j , of an electrochemical reaction can be defined as

$$j = nFv \quad (2.13)$$

where n is the number of electrons involved in the reaction, F is the Faraday constant, and v is the reaction rate.

The reaction rate depends on several parameters, such as the nature of the electrode, the electrolyte composition, and the electrode potential. For a redox reaction (**Equation 2.4**), the forward (anodic or oxidation), v_a , and backward (cathodic or reduction), v_c , reaction rates are given by

$$v_a = k_a \cdot C_{Red} \quad (2.14)$$

$$v_c = k_c \cdot C_{Ox} \quad (2.15)$$

where k_a and k_c are the anodic and cathodic reaction rate constants, C_{Ox} and C_{Red} are the concentrations of the reactants.

Assuming the reaction rate constants depend on the temperature, k_a and k_c can be written as

$$k_a = k_a^0 \exp\left(-\frac{\Delta G_a}{RT}\right) \quad (2.16)$$

$$k_c = k_c^0 \exp\left(-\frac{\Delta G_c}{RT}\right) \quad (2.17)$$

where k_a^0 and k_c^0 are the anodic and cathodic reaction rate constants at the equilibrium, and ΔG_a and ΔG_c are the standard Gibbs free energies of activation for the anodic and cathodic reaction, respectively.

According to the Nernst equation, the ratio of the reactant and product concentration at the equilibrium state is given by

$$\ln \frac{C_{Ox}}{C_{Red}} = F \left(\frac{E_{eq} - E^0}{RT} \right) \quad (2.18)$$

where E_{eq} and E^0 are the equilibrium and standard half-cell potentials, respectively.

Then combining with the **Equations 2.16, 2.17 and 2.18**, one can obtain

$$\Delta G_c - \Delta G_a = nF(E_{eq} - E^0) \quad (2.19)$$

where n is the number of exchanged electrons.

Since the free energies of the reduced and oxidized components are dependent on the electrode potential, ΔG_a and ΔG_c can be written as

$$\Delta G_c = \Delta G_0 + \alpha_c nF(E_{eq} - E^0) \quad (2.20)$$

$$\Delta G_a = \Delta G_0 - \alpha_a nF(E_{eq} - E^0) \quad (2.21)$$

where ΔG_0 is the free energy of the activation when $E_{eq} = E^0$, α_c , and α_a are the cathodic and anodic transfer coefficients, respectively, and $\alpha_c + \alpha_a = 1$.

Under non-equilibrium conditions, the difference between the actual half-cell potential and the equilibrium potential is called the overpotential, η .

$$\eta = E - E_{eq} \quad (2.22)$$

When net current flows through the electrochemical cell, the cathodic and anodic activation free energy change should be $\alpha_c nF\eta$ and $-\alpha_a nF\eta$ depending on the electrode potential. Thus **Equations 2.16 and 2.17** become

$$k_a = k_a^0 \exp\left(\frac{\alpha_a nF\eta}{RT}\right) \quad (2.23)$$

$$k_c = k_c^0 \exp\left(-\frac{\alpha_c nF\eta}{RT}\right) \quad (2.24)$$

In the case of the reaction given in **Equation 2.4**, since the difference between the anodic and cathodic reaction rate is proportional to the net current (**Equation 2.13**), the current density, j , is given by

$$j = j_a - j_c = nF(k_a C_{Red} - k_c C_{Ox}) \quad (2.25)$$

where j_c and j_a are the current densities caused by the cathodic and anodic reactions, respectively. Combining with **Equations 2.23** and **2.24**, the relationship between the current density and the overpotential can be expressed as

$$j = nF[k_a^0 C_{Red} \exp\left(\frac{\alpha_a nF\eta}{RT}\right) - k_c^0 C_{Ox} \exp\left(-\frac{\alpha_c nF\eta}{RT}\right)] \quad (2.26)$$

or

$$j = j_0 \left[\exp\left(\frac{\alpha_a nF\eta}{RT}\right) - \exp\left(-\frac{\alpha_c nF\eta}{RT}\right) \right] \quad (2.27)$$

where j_0 is called the exchange current density. This is called the Butler-Volmer equation, which is one of the most fundamental relations in electrochemical kinetics. It describes the connection between the electrode potential and the current density. This is important in investigating the mechanisms of the electrode process kinetics.

2.3.3 Tafel Equation

This chapter is dedicated to the two extreme cases of the Butler-Volmer equation, i.e., for low and high overpotentials, respectively. Considering at first, low overpotentials η : the approximation of **Equation 2.27** yields

$$j = j_0 \left(\frac{nF\eta}{RT} \right) \quad (2.28)$$

In this case, the overpotential depends linearly on the current density.

On the other hand, if the overpotential is sufficiently high, $\left| \frac{F\eta}{RT} \right| \gg 1$, one of the exponential terms in **Equation 2.27** will be negligible. For instance, when the overpotential is negative, one obtains

$$\eta = -\frac{RT}{\alpha_c nF} \ln j_0 + \frac{RT}{\alpha_c nF} \ln |j| \quad (2.29)$$

Alternatively, **Equation 2.29** can be written in the general form

$$\eta = a + b \ln|j| \quad (2.30)$$

Equation 2.30 is known as the Tafel equation. The constant, a , is equal to the overpotential required for a current density of 1 A/cm². According to the value of a , the difficulty of the electron transfer steps in different electrochemical systems can be compared. The constant, b , is called the Tafel slope. Both constants depend on the nature of the electrode, the electrode surface state, the electrolyte composition, and the temperature. This logarithmic current-potential relation, named after the Swiss chemist Julius Tafel, can be used to investigate the electrode kinetics, e.g., to evaluate the rate-determining steps.

2.4 Important Electrocatalytic Reactions

The energy conversion and storage of the hydrogen economy mainly involve two important processes: water splitting (water to hydrogen) and reactions that occur in the fuel cell (hydrogen applied as a fuel). In this chapter, reactions taking place at the anode and the cathode for water splitting and the fuel cell are discussed.

2.4.1 Water Splitting

Water splitting is the process in which water decomposes into hydrogen and oxygen, which are driven by the electric current. Water splitting includes hydrogen evolution reaction, HER, on the cathode, and oxygen evolution reaction, OER, on the anode (see **Figure 2.2**). Since water splitting was first claimed in 1789¹⁰², it has been investigated and applied widely.¹⁰³⁻¹¹⁰ Hydro, solar, and wind energies can be energy sources for electricity generation, which can be further applied to split water to produce hydrogen, as shown in **Figure 2.2**. The generated hydrogen can be stored as fuel and can be used in many applications ranging from fuel cells to ammonia synthesis.

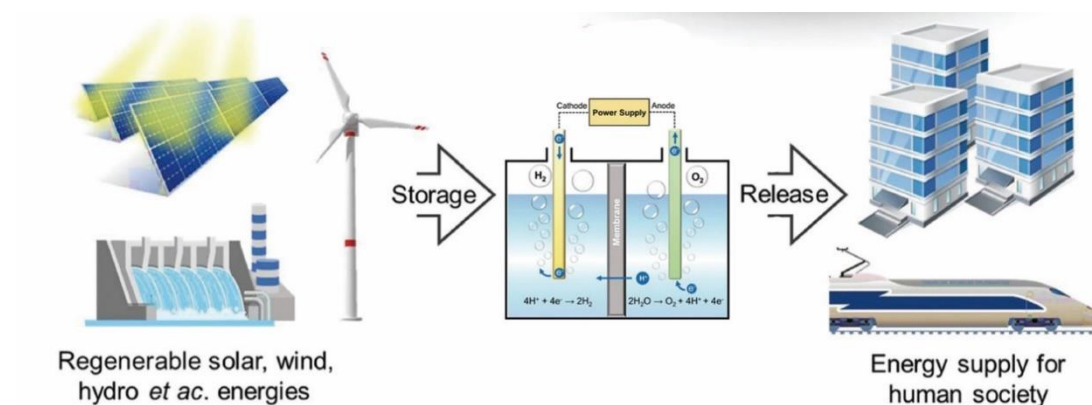
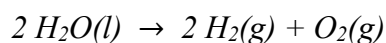


Figure 2.2. A scheme of water electrolysis. The electricity is obtained from hydro, solar, and wind energies to provide the energy for water splitting. The HER occurs at the cathode, while the OER takes place at the anode. Reproduced with permission from reference 110.

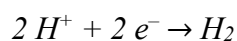
The overall reaction of water electrolysis is



The overall cell reaction of electrochemical water electrolysis is the sum of two half-cell reactions, HER and OER.

2.4.1.1 Hydrogen Evolution Reaction

Depending on the electrolyte pH, the pathways of the HER can be different. In acidic solutions, the HER proceeds as follows:



The mechanism of the HER involves the transfer of two electrons. The HER includes the following steps:¹¹¹





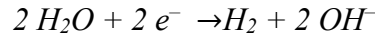
Heyrovsky step



Tafel step

where * represents an adsorption site on the surface. After combining a proton and an electron on the catalyst surface, which leads to an adsorbed hydrogen atom (Volmer step), the adsorbed hydrogen can further either combine with a proton and an electron (Heyrovsky step) or combine with another adsorbed hydrogen atom to produce hydrogen molecule (Tafel step).

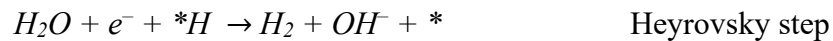
In alkaline solutions, the HER is described by the following equation:



The HER proceeds through different Volmer and Heyrovsky reactions because of the high pH:



Volmer step



Heyrovsky step



Tafel step

In contrast to acidic electrolytes, in alkaline solutions, one H₂O molecule combines with an electron on the catalyst surface during the Volmer step. Then, the adsorbed hydrogen atom couples with a water molecule and an electron to generate hydrogen (Heyrovsky step). The Tafel step is the same as in acidic solutions.

The mechanism of the HER follows Volmer-Heyrovsky or Volmer-Tafel reactions. The pathways of the HER depend on the overpotentials and the nature of catalysts. In some cases, both types of electron transfer can be simultaneously present.¹¹² The HER mechanism can be deduced from the Tafel plot, which is derived from the polarization curve. The Tafel slope presents an intrinsic nature of the catalyst and can be used to

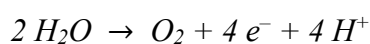
explain the mechanisms of the HER.^{113,114} If the rate-limiting step of the HER is the Volmer one, the Tafel slope will be around 120 mV dec⁻¹. Conversely, if the HER rate is determined by the Heyrovsky step or Tafel step, smaller Tafel slopes of 40 and 30 mV dec⁻¹ were observed.¹¹⁵ However, it should be mentioned that the Tafel slope can be interfered with by many other factors such as electrode potential, adsorption processes, and mass transfer.¹⁰³ Thus, the rate-determining step of the HER could be changed by those factors.

Platinum and platinum group metals are thought of as the best-known pure metal catalysts for the HER. This is because the hydrogen binding energy on the platinum surface is close to the optimum, according to the Sabatier principle.¹¹⁶ Recently, with the consideration of low-cost and high-efficiency materials, especially in alkaline electrolytes, non-noble metal-based materials such as nickel and nickel-based alloy have been found to have high activity and long-term stability.^{42,117}

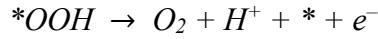
2.4.1.2 Oxygen Evolution Reaction

Theoretically, the thermodynamic equilibrium potential of the OER is 1.23 V *versus* RHE. However, high overpotentials are always required in a practical water splitting process. Because the OER involves a four-electron transfer and has several reaction intermediates (*OOH, *OH, *O), which makes the mechanism of the OER much more complex than that of the HER.¹¹⁸ Moreover, the OER is recognized as the bottleneck of the overall water splitting process due to its sluggish kinetics.

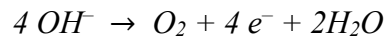
As in the HER case, the OER mechanism depends on the pH of the electrolyte. In acidic solutions, the reaction equation is as follows:



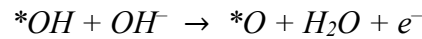
The possible reaction pathways of the OER in acidic media are considered as:



In contrast, the reaction in alkaline electrolytes is:



The reaction pathways in alkaline electrolytes are similar to the acidic case:



For both acidic and alkaline cases, after the second reaction pathway of the OER, the O_2 could be generated by combining two $*O$ intermediates directly:



However, the thermodynamic barrier of this reaction pathway is always higher than the reaction(s) forming $*OOH$ intermediate.¹⁰³

As mentioned above, the complex mechanism of the OER causes sluggish kinetics and low energy efficiency for the overall water electrolysis. Hence, several attempts have been dedicated to enhance the OER activity's performance by increasing the number of active sites on the electrocatalyst surfaces.¹¹⁹⁻¹²¹ This would eventually result in balancing the binding energies of the reaction intermediates (i.e., $*OOH$, $*OH$, $*O$)

according to the Sabatier principle.^{122,123} Recently, Liu *et al.* claimed that promoting the mass transfer is equally important as increasing the number of active sites.¹²⁴ Besides, the electrolyte composition has considerable influence on the OER activity as well. For instance, Michael *et al.* systematically investigated the effect of alkali metal cations on the OER activity for nickel oxyhydroxide catalyst.¹²⁵ They found that the performance of the OER improved in the presence of Cs⁺ while introducing Li⁺ lowered the OER activity (see **Figure 2.3**). Amanda *et al.* also found a similar trend of the alkali metal cation effect on the OER activity for a nickel oxyhydroxide catalyst.⁵⁴ Although various methods have been applied to enhance the performance of the OER, more studies are still required to understand the internal OER mechanism to address the sluggish kinetics and poor energy efficiency.

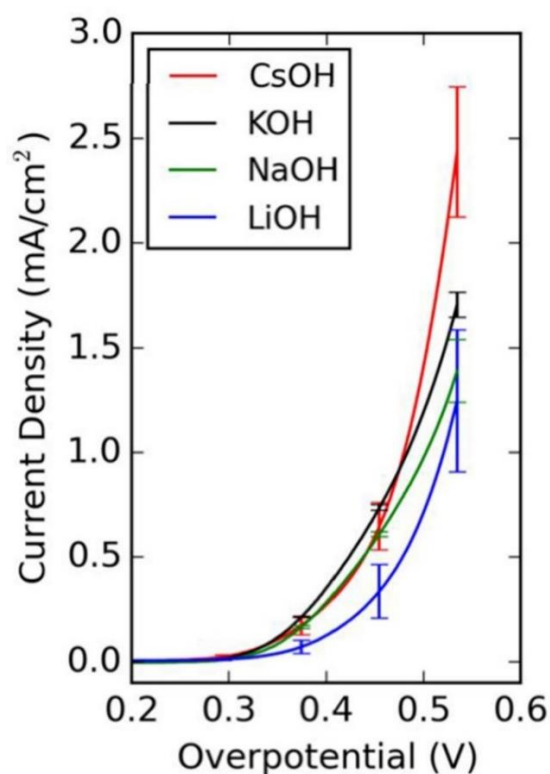


Figure 2.3. Linear sweep voltammetry of NiOOH in purified LiOH (blue), NaOH (green), KOH (black), and CsOH (red). Error bars represent one standard deviation from the mean current density at each respective potential. Scan rate: 1 mV s^{-1} . Reproduced with permission from reference 125.

2.4.2 Fuel Cells

A fuel cell is an electrochemical device through which chemical energy from fuel(s), such as hydrogen, is converted into electrical energy. Unlike batteries, it continues to produce electricity as long as fuel is supplied. Sir William Robert Grove first introduced the idea of the fuel cell in 1839.¹²⁶ Then the fuel cells were further developed until the first practical device was realized in the NASA space program in the 1960s.¹²⁷ Based on the type of electrolyte used, the fuel cell(s) can be categorized distinctively, such as the alkaline fuel cell (AFC), the solid oxide fuel cell (SOFC), phosphoric acid fuel cell (PAFC), and the polymer electrolyte membrane or proton exchange membrane fuel cell (PEMFC).^{128,129} Among them, PEMFCs are particularly interesting and have been widely reported in the literature.¹³⁰⁻¹³⁴ For example, using hydrogen as fuels, PEMFCs show excellent performance at low operating temperatures.¹³⁵

A fuel cell comprises three main components: an anode, a cathode, and an electrolyte, as illustrated in **Figure 2.4**. With hydrogen as the used fuel, the overall reaction happening in the fuel cell(s) is:



The hydrogen is oxidized at the anode (where the hydrogen oxidation reaction (HOR) occurs). The oxygen is reduced to water at the cathode (where the ORR takes place). During the redox reaction, the electric current flows through the external circuit.

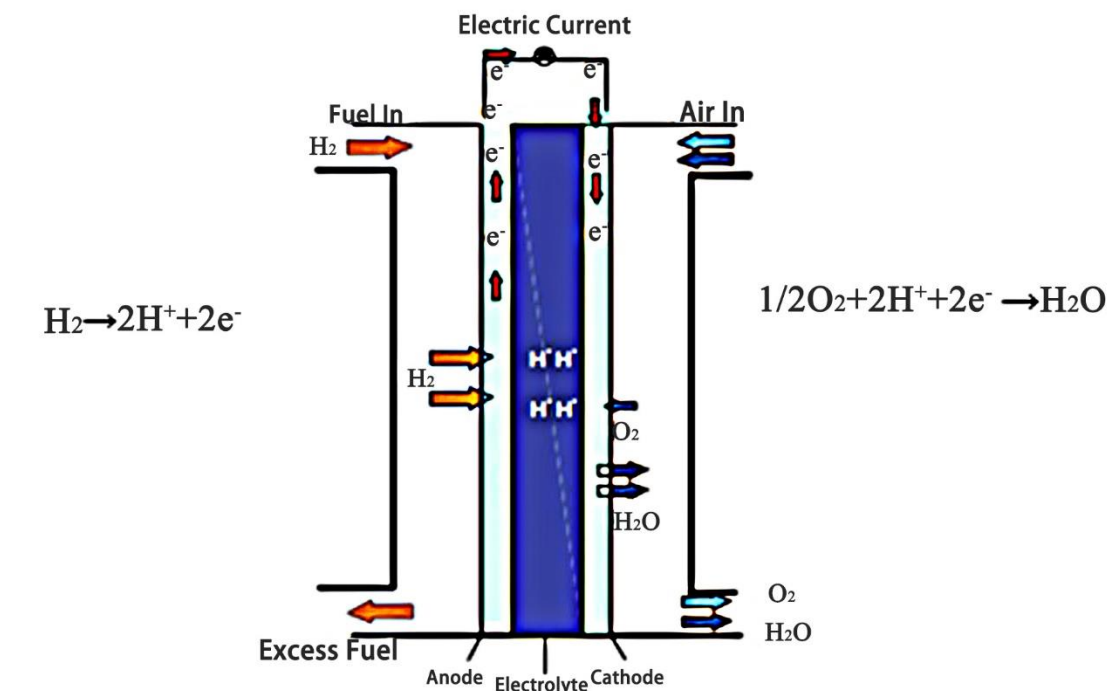


Figure 2.4. Schematic of a hydrogen fuel cell in an acidic media. Reproduced with permission from reference 129.

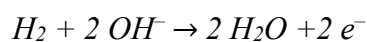
2.4.2.1 Hydrogen Oxidation Reaction

Depending on the pH of the used electrolyte, the mechanisms of the reactions of the HOR differ and are as follow:

In acidic media:



In alkaline media:



The HOR, which is the reverse of the HER, is significant for developing hydrogen-based energy sources. During the reaction, both HER and HOR involve only

one intermediate, namely adsorbed hydrogen. Besides, the HOR is supposed to follow the Volmer-Heyrovsky-Tafel mechanism as well. Therefore, in most cases, the performance of these two reactions should be comparable.

As is the case for HER, the rate of HOR in alkaline electrolytes is slower than in acid. Platinum and platinum group metals are also considered as the best-known pure metal catalysts for the HOR, despite various efforts towards the development of metal and metal-free catalysts.¹³⁶⁻¹³⁹

2.4.2.2 Oxygen Reduction Reaction

The ORR involves similar reaction intermediates (*OOH, *OH, *O) as the OER. However, the mechanism of the ORR is substantially different. In general, there are several pathways for O₂ electroreduction. Depending on the pH of electrolyte in the studies, the ORR which involves a multi-electron transfer process takes place as follow:

- i. In acidic media, the ORR can happen by two pathways: the reduction of O₂ to H₂O and H₂O₂ via four-electron and series of two-electron steps, respectively.



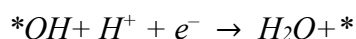
- ii. In alkaline media, O₂ can be reduced to OH⁻ and HO₂⁻ by four-electron and two-electron pathways, respectively.



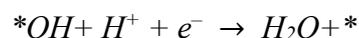
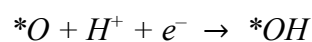
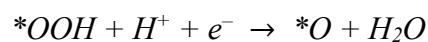
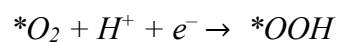
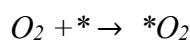
It should be mentioned that O_2 can also be reduced to superoxide (O_2^-) in non-aqueous aprotic electrolytes, in which one electron transfer takes place.¹⁴⁰

For the ORR on Pt, a major four-electron electron transfer process was suggested in both acidic and alkaline aqueous electrolytes.¹⁴¹ The reaction mechanism proceeds via either the associative or dissociative pathway.^{142,143} Taking Pt in acidic media as an example, these two mechanisms are as follow:

i. Dissociative mechanism:



ii. Associative mechanism:



The ORR is of utmost importance in electrochemical energy conversion technologies. Despite various devices such as PEMFCs showing their great potential to convert chemical energy into electrical energy, huge overpotential is still required to drive the ORR because of the sluggish reaction kinetics. Even on the best Pt-based catalysts, much higher Pt loading is demanded to reach a sufficiently good ORR performance.¹⁴⁰ Besides, the relatively poor long-term stability of ORR electrocatalysts is also a major

stumbling block. For instance, for the commercial Pt/C (Pt on carbon support), it was reported that the ORR activity significantly decreased after long-cycling times.¹⁴⁴ Therefore, developing low-cost, excellent performance, and long-term durability of the electrocatalysts are necessary.

In addition, the electrolyte components can also influence the catalyst's ORR performance. As presented in **Section 1.2.1**, the performance of the ORR varies depending on the different cations present in the solution. Besides, the anion adsorption can also affect the ORR processes.¹⁴⁵ Especially, the ORR activity can be substantially decreased by the strongly adsorbed anion in the electrolyte. Moreover, the ORR activity can be influenced by the pH of electrolytes too, but the influence of pH is not consistent in acidic and alkaline media.^{146,147}

2.5 The Electrochemical Interface

2.5.1 Development of the Double Layer

In general, an electrified interface is formed between the electrode and the electrolyte when contacting an electron conductor with an electrolyte. The charged electrode will attract counterions to its surface. The charge layers formed at the electrode/electrolyte interface are called the electric double layer (EDL). This simplified EDL structure was first proposed by Helmholtz in 1853, as illustrated in **Figure 2.5A** (a positively charged electrode as an example).^{148,149} In the Helmholtz model, the two formed charge layers were separated by a distance H . The Helmholtz model structure is like that of conventional dielectric capacitors with two planar parallel electrodes separated by a dielectric. However, the Helmholtz model does not consider the ions' thermal motions in the double layer.

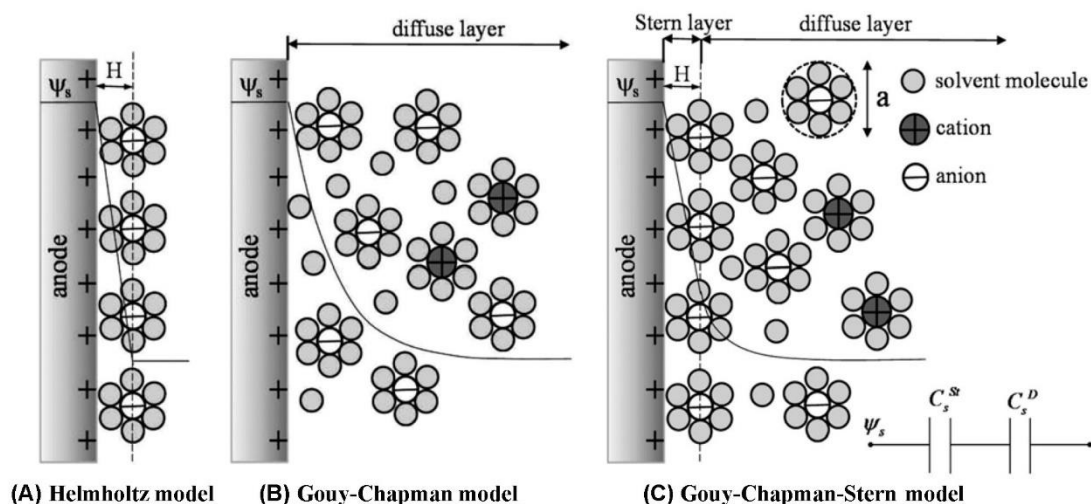


Figure 2.5. Schematic representation of the electric double layer at a positively charged anode: (A) Helmholtz model, (B) the Gouy-Chapman model, and (C) the Gouy-Chapman-Stern model. H is the distance of the double layer depicted in the Helmholtz model. Ψ_s is the potential across the electric double layer. Reproduced with permission from references 148 and 149.

Gouy¹⁵⁰ and Chapman¹⁵¹ further modified the Helmholtz model to incorporate the ions' thermal motions, and they introduced a diffuse model at the electrode/electrolyte interface. As illustrated in **Figure 2.5B**, the ions with opposite signs to that of the electrode surface are distributed in the so-called diffuse layer which is much larger than H . In the Gouy-Chapman model, the charge distribution of the ions in the diffuse layer is determined by the distance from the electrode surface, which follows the Maxwell-Boltzmann statistics. Therefore, the electric potential in this region decreases exponentially away from the electrode surface.¹⁵²

However, the Gouy-Chapman model ignores the existence of the Helmholtz layer. It was Stern¹⁵³ who suggested combining the Helmholtz model and the Gouy-Chapman model to describe the EDL as two different regions of charges: namely, the Helmholtz layer (or Stern layer) and the diffuse layer, as illustrated in **Figure 2.5C**. The Gouy-Chapman-Stern model was further modified by Grahame¹⁵⁴. The Helmholtz layer can

be separated into two planes, the inner Helmholtz plane (IHP) and the outer Helmholtz plane (OHP). The IHP passes through the centers of the so-called specifically adsorbed ions, while the OHP passes through the centers of the nearest solvated ions (non-specifically adsorbed ions). The Gouy-Chapman model applies the diffuse layer in the Gouy-Chapman-Stern model. Potentially, all the species (such as ions and solvent molecules) in the electrolyte can be adsorbed at the electrode surface by coulombic, van-der-Waals-forces, or chemisorption. Particularly, the anions can be specifically adsorbed at the interface even if the electrode surface is negatively charged, owing to its interaction with the electrode surface.

The EDL plays a fundamental role in many electrochemical systems such as electrolyzers, batteries, and capacitors.¹⁵⁵⁻¹⁵⁷ The EDL models reveal the relationship between the electrode surface and the electrolyte at the interface. Therefore, the concept of the EDL is significant for understanding the performance of various electrochemical processes. However, the question about the EDL structure in various systems remains unsolved, and more studies are required.

2.5.2 Interfacial Water Layer

One of the critical properties of the EDL is the net orientation of solvent molecules at the interface between the electrode and the electrolyte.¹⁵⁸ Particularly for aqueous electrolytes, the water structure at the electrode/electrolyte interface is of great importance, for instance, in the electrochemical energy conversion and storage and corrosion systems.¹⁵⁹⁻¹⁶¹ Despite the relatively weak interactions between the metal surfaces and the water molecules, the interfacial water layer is believed to control the electrochemical processes significantly.¹⁶² Therefore, characterizing the interfacial water layer's net orientation can help improve the understanding of the electrochemical processes taking place at the electrode/electrolyte interface.

Basically, the interfacial water structure is influenced by electrode potential, pH of the

electrolyte, and its composition.^{163,164} The net orientation of the interfacial water layer is mainly determined by the electrode's surface charge. Namely, the water molecules orient with hydrogen end towards the electrode surface when the electrode is negatively charged. In contrast, the oxygen of the water molecules tends to point towards the electrode surface if the electrode is positively charged, as shown in **Figure 2.6**.

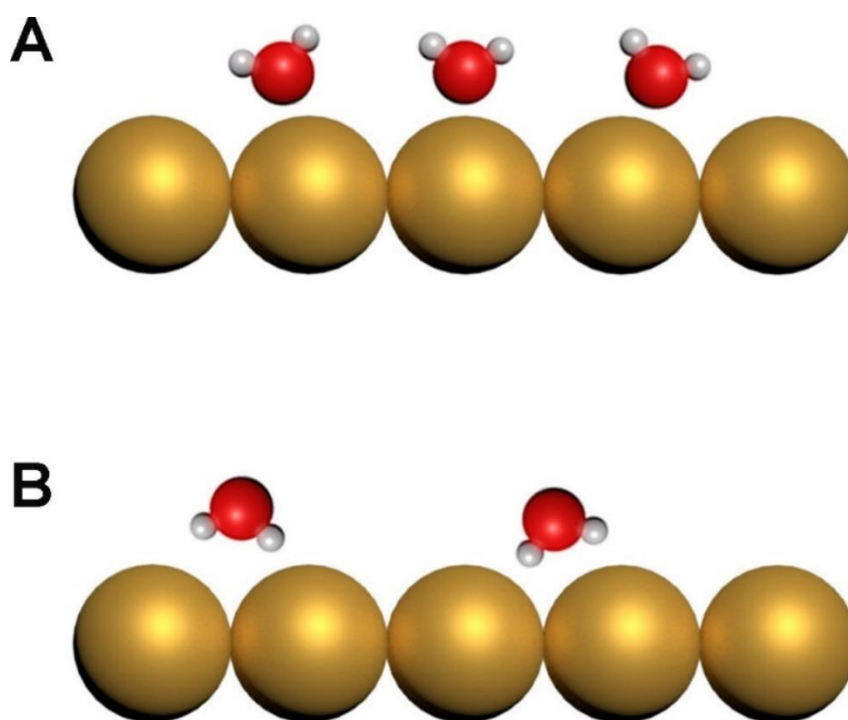


Figure 2.6. Orientation of water molecules at the electrode surface when the electrode is (A) positively charged and (B) negatively charged, respectively.

However, the interfacial water structure is much more complex and can be completely different depending on the nature of the electrodes.¹⁶² For example, Tong *et al.* claimed that the interfacial water molecules on the gold electrode tend to orient themselves with OH-groups pointing away from/towards the electrode surface owing to the interaction between water's permanent dipole and the surface field.¹⁶⁵ However, the density of the interfacial water can be increased when the electrode surface charge changes from negative to positive. Li *et al.* suggested that the structure of interfacial water molecules

on the gold electrode can be drastically changed at some points when the electrode is negatively charged.¹⁶⁶ They stated that the distribution and orientation of the interfacial water molecules could differ depending on the potential difference between the applied potential and the potential of zero charge (PZC) for the negatively charged electrode surface. When the potential difference is from -1.3 to \sim -1.9 V, all interfacial water maintains the ‘one-H-down’ configuration (see **Figure 2.7 A**). Nevertheless, all interfacial water tends to reorient to a ‘two-H-down’ configuration when moving the potential to more negative (**Figure 2.7 B**).

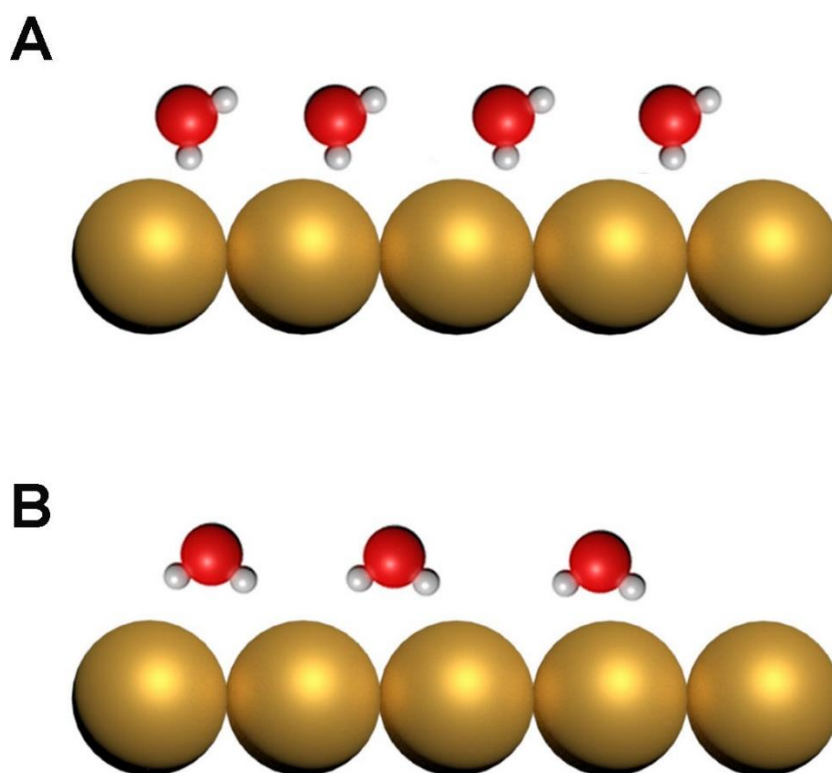


Figure 2.7. The orientation of interfacial water molecules depending on the electrode potential. (A) The ‘one-H-down’ configuration of interfacial water molecules when the potential difference between the applied potential and the potential of zero charge is from -1.3 to \sim -1.9 V. (B) The ‘two-H-down’ configuration of water molecules when the potential difference is more negative than -1.9 V.

The role of the interfacial water structure in various aqueous electrochemical processes has been characterized by, for instance, X-ray scattering (XRS), surface-enhanced infrared absorption spectroscopy (SEIRAS), and X-ray absorption spectroscopy (XAS).¹⁶⁷ Besides, several simulated calculation methods, such as ab initio molecular dynamics (AIMD), have been applied to study the interfacial water structure.¹⁶⁶ The understanding of the correlation between the orientation of the interfacial water and electrocatalytic reactions is still insufficient. The introduction of two key parameters, PZC and the potential of maximum entropy (PME), could address those issues.

2.5.3 Potential of Zero Charge and Potential of Maximum Entropy

The electrode surface charge depends on the applied potential. Thus, one can find a potential at which no excess charge exists on the electrode surface. This potential is defined as the PZC. The PZC, coined by Frumkin in 1928,¹⁶⁸ is one of the essential parameters for a detailed understanding of processes taking place at the EDL.

The charge of the metal surface (per unit area) can be written as

$$q^m = -F \sum_i \Gamma_i z_i \quad (2.31)$$

where Γ_i is the excess surface charge of the ionic species, i , in the interface, in moles per unit area of the interface; z_i is the charge with the sign of component i ; q^m is the charge of the metal side, which is equal but opposite in sign to the charge of the solution side in the EDL ($q^m = -q^s$).

At a constant temperature and pressure, one can obtain

$$d\sigma = -q^m dE + \sum_i \Gamma_i d\mu_i \quad (2.32)$$

where σ is the interfacial tension. The interfacial tension can be determined as a function of the electrode potential.

Hence, the excess charge density on the metal is given by

$$\left(\frac{\partial\sigma}{\partial E}\right)_{T,P,\mu_i} = -q^m \quad (2.33)$$

Thus, the potential at which the derivative $(\partial\sigma/\partial E)_{T,P,\mu_i}$ equals zero corresponds to the state where no excess charge is present on the metal electrode surface, namely, the location of the PZC.

It should be noted that the PZC is not a unique property of the metal but relies on the detailed composition of the whole system. Notably, the situation gets much more complicated for specific adsorption processes involving charge transfer at the interface between the electrode and electrolyte.¹⁶⁹ Therefore, it is necessary to distinguish between the two types of the PZC, the potential of zero free charge (PZFC) and the potential of zero total charge (PZTC). The PZFC is defined as the potential at which the true surface excess charge density becomes zero, while the PZTC is the potential where the sum of the free, electronic net charge density and the charge density transferred during reversible adsorption processes equal zero.¹⁷⁰ For an ideally polarizable electrode, the PZFC and the PZTC coincide since no charge transfer related to the adsorption process occurs.¹⁷¹ But these two parameters are not consistent for electrodes such as platinum group metals (Pt, Pd, Rh, Ir) when the adsorption process involves.¹⁷²⁻¹⁷⁵ The PZTC can be experimentally determined, for instance, from voltammetry.^{176,177} However, it is difficult to measure the PZFC in the same way since the traditional voltammetric and potentiostatic measurements cannot separate double layer charging current density from total current density.¹⁷⁸ Calculation of the PZFC from these electrochemical measurements always requires additional measurements and thermodynamic assumptions.¹⁶³ More information about the determination of the

PZC is discussed in **Section 2.5.4**.

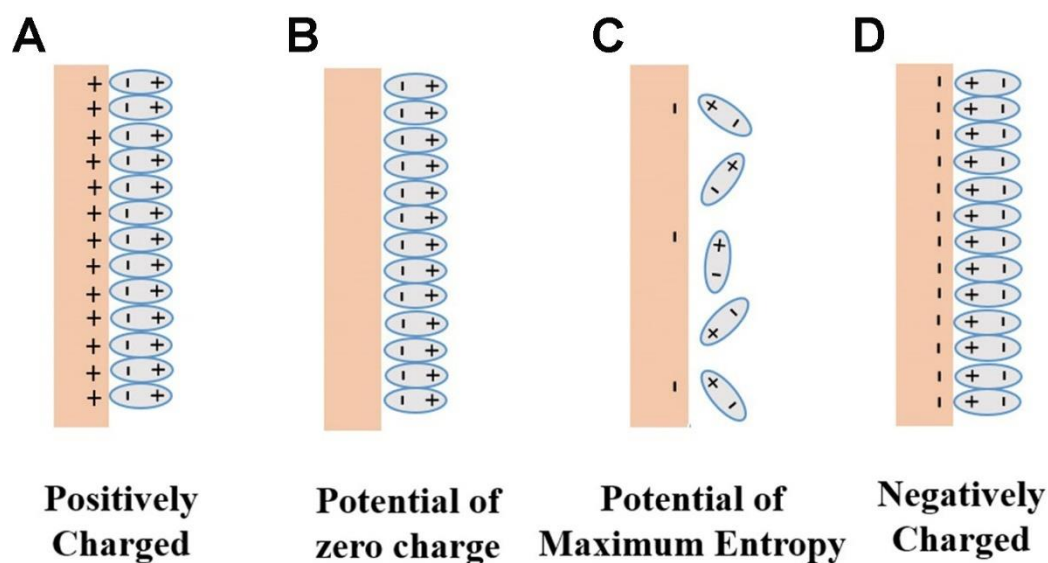


Figure 2.8. Schematic of the orientation of the interfacial water molecules at the electrode surface depending on the electrode surface charge in aqueous solutions. (A) When the electrode is positively charged, the interfacial water molecules tend to orient with oxygen end towards the electrode surface. (B) At the PZC, there is no excess charge on the electrode surface. But the oxygen still points towards the electrode surface due to the specific interaction between the oxygen atom with the (uncharged) metal surface. (C) At the PME, which is slightly negative than the PZC, the interfacial water layer has the highest disorder in the double layer. (D) When the electrode is negatively charged, the interfacial water molecules tend to orient with hydrogen end towards the electrode surface.

Another important parameter, the PME, is defined as the potential at which the entropy of the double layer formation reaches its maximum.¹⁷⁹ The PME is supposed to be related to the PZC. However, the PME is slightly negative than the PZC because of the specific interactions between the oxygen atom of the interfacial water molecules and the (uncharged) metal surface. In this case, a strong directional bond can be formed between the oxygen atom and the unoccupied d-orbitals of the transition metal surface.¹⁸⁰ Thus, a more negative potential is required to offset this specific interaction

to make the interfacial water have maximal disorder in the double layer, as shown in **Figure 2.8**. The knowledge of the PME is significant for assessing the stiffness of the interfacial water layer structure and, therefore, can be regarded as the predominant reason for energy barriers that hinder mass and charge transfer through the interface.¹¹⁷ At potentials remote from the PME, the water layer structure at the interface is quite rigid, which can prevent charge transfer. Inversely, at potentials close to the PME, the interfacial water has the maximal disorder and can reorient more easily.

2.5.4 Determination of the Potential of Zero Charge and the Potential of Maximum Entropy

Since the first quantitative data of the PZC for mercury electrodes were obtained, various methods have been applied to determine the values of the PZC.¹⁵⁴ However, the study of solid electrodes has been a challenge for past decades. The determination of the PZC with different techniques is never straightforward.¹⁸¹ Depending on the nature of electrode materials, different methods have been developed to identify the PZC. In this section, an overview of some common methods for the determination of the PZC is given. Note that in the following discussion, PZC stands for PZTC since the PZFC cannot be experimentally determined currently.

2.5.4.1 Electrocapillary Methods

One of the most widely applied methods to determine the PZC of liquid metals is the measurement of electrocapillary curves. This method is based on the investigation of the surface tension and its dependence on electrode potential. The potential where the electrocapillary curve reaches its maximum corresponds to the PZC of the investigated electrodes, as illustrated in **Figure 2.9**.

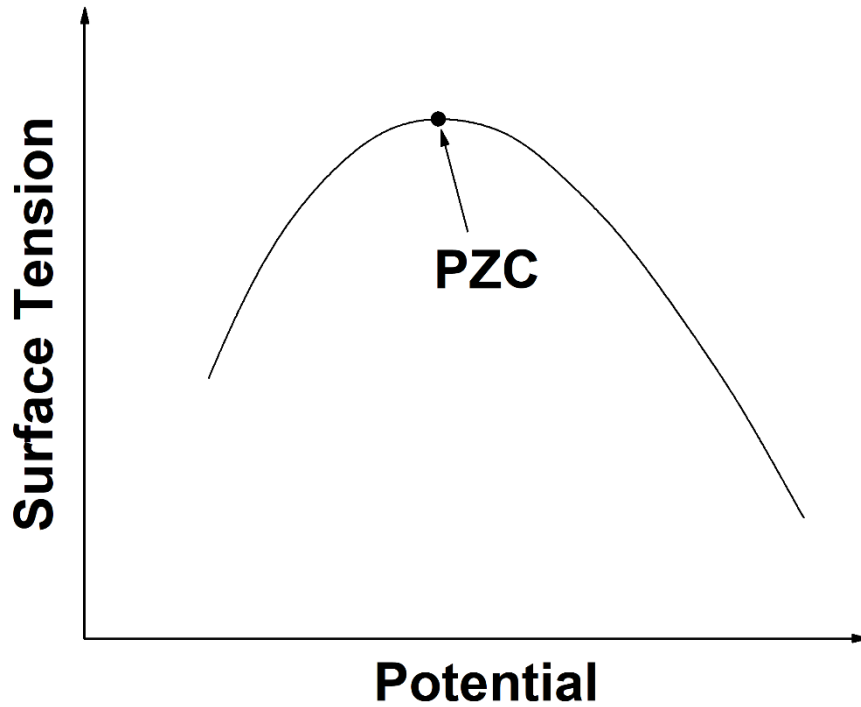


Figure 2.9. Scheme of the electrocapillary curve, i.e., the surface tension of electrode as a function of the applied potential. The PZC is typically the potential of maximum surface tension.

The electrocapillary curves of liquid metals can be recorded with a capillary electrometer, first proposed by Lippmann in 1875.¹⁸² The capillary electrometer can measure the pressure that is necessary to force the liquid metal down to a certain point of a conical capillary wetted by the electrolyte solution. Meanwhile, one must ensure that electrolyte solutions completely wet the capillary walls. The surface tension of liquid metal γ is a function of the EDL capacitance, which is suggested by the Young-Lippman equation as follow:

$$\gamma = \gamma_0 - \frac{1}{2} C V_{EDL}^2 \quad (2.34)$$

Here γ_0 is the surface tension between the electrolyte and the conductor at zero electric field, and C is the capacitance per unit area of the EDL. V_{EDL} is the voltage across the EDL. The surface tension is affected by electrical conditions at the interface

between the electrode and electrolyte. This phenomenon is known as electrocapillary.¹⁸³

The electrocapillary methods have been applied to determine the PZC of mercury, gallium, and their alloys.¹⁸⁴ Besides, this method can be used for certain metal-free electrodes. For instance, Shao *et al.* measured the PZC of carbon aerogel with the electrocapillary method.¹⁸⁵ However, the electrocapillary method is particularly limited for the determination of the PZC of liquid metals.

2.5.4.2 Capacitance Methods

The double layer capacitance (C_{dl}) is a key descriptor of the electrode/electrolyte interface. It can be used to infer the properties of the electrode/electrolyte interface.^{186,187} One of the properties is the PZC, which can be determined according to the Gouy-Chapman theory, as the electrode potential where the C_{dl} reaches its minimum. This method for the PZC determination was first suggested by Vorsina and Frumkin.¹⁸⁸ Based on the Gouy-Chapman-Stern model of the EDL, the reciprocal of the C_{dl} can be given as:

$$\frac{1}{C_{dl}} = \frac{1}{C_i} + \frac{1}{C_d} \quad (2.35)$$

where C_i and C_d are the capacitance of the inner double layer and the differential capacitance of the diffuse layer, respectively. In dilute electrolytes (ca. 10^{-3} M), C_i is constant, while C_d is a function of applied potential ($C_d = (\partial q / \partial E)_{T,P,\mu}$).¹⁸⁹ Therefore, the PZC should be located at the minimum of C_d , as shown in **Figure 2.10**. However, at high concentrations of electrolyte, C_i typically dominates C_{dl} . In this case, the capacitance methods can hardly be used for the PZC determination.¹⁹⁰

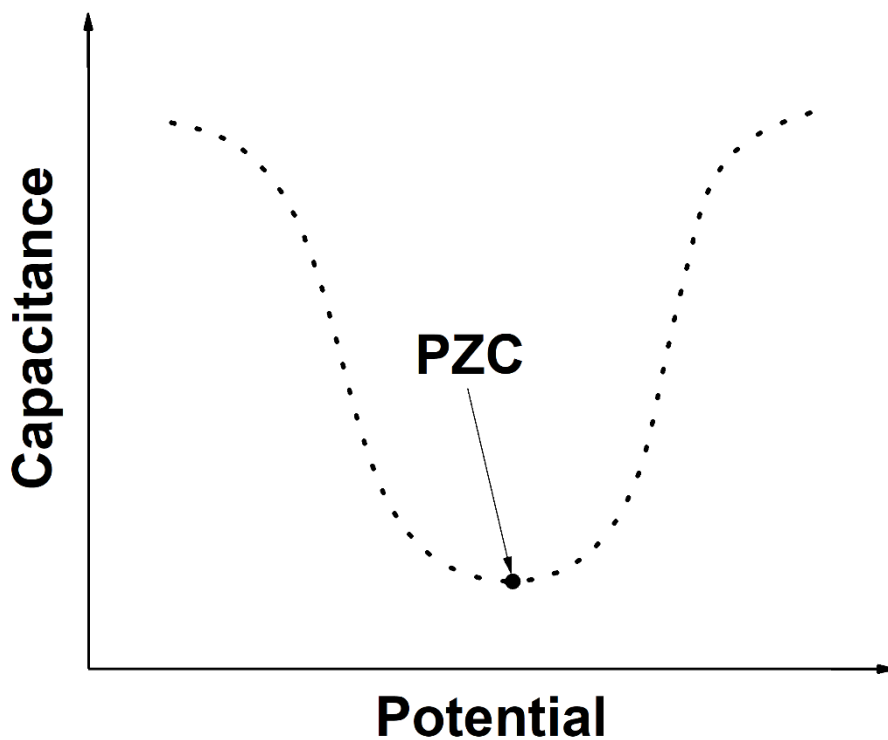


Figure 2.10. Scheme of the capacitance-potential curve. The PZC is located at the potential of the minimum of the differential double layer capacitance.

Although much information regarding the influence of various parameters on the PZC has been obtained with the capacitance methods, its application is limited to dilute solution and the absence of specific adsorption.¹⁸¹

2.5.4.3 CO Charge Displacement

The PZC of certain noble metal electrodes can be determined by the CO charge displacement method.¹⁹¹⁻¹⁹³ This technique is based on the fact that CO can be strongly adsorbed on some electrode surfaces.

Taking Pt as an example, during this measurement, the electrolyte is purged with CO, and the applied potential is kept constant, allowing adsorption of CO on the Pt surface. The measured current falls to zero when the CO adsorption is finished, and CO covers

a certain fraction of the electrode surface. Then, the excess CO in the solution will be removed by purging the electrolyte with argon while holding the potential. The surface blockage can be measured by recording the voltammogram. Finally, CO is eliminated by means of voltammetry from the electrode surface, and the electrode surface is further checked using the voltammetric profile. This final step is vital for the entire investigation. It allows checking whether the electrode surface has been neither modified nor contaminated during the CO adsorption process.

The CO adsorption occurs without alteration in the oxidation state of Pt. Thus, the charge measured during the CO adsorption process, q_{dis} , should be the same as the difference between the total electrode charges before (q_i) and after (q_f) CO adsorption:

$$q_{dis} = q_f - q_i \quad (2.36)$$

The initial charge before CO adsorption correlates to the total charge on the CO-free electrode at a certain investigated potential. The determination of its value requires knowledge of the charge after CO adsorption, q_f . Unfortunately, this value cannot be directly measured. But the value of q_f is negligibly small when compared with the total electrode charges before CO adsorption. Therefore, **Equation 2.36** can be approximated as:

$$q_{dis} \approx -q_i \quad (2.37)$$

With the approximation above, the CO charge displacement can be carried out as a direct measure of the total charge on the electrode at a specific potential of the measurement. Then, the measurement is repeated for the different potentials to obtain the relationship between the total charge q and the electrode potential E . As shown in **Figure 2.11**, the potential E where q_i equals zero corresponds to the PZC.^{177,194}

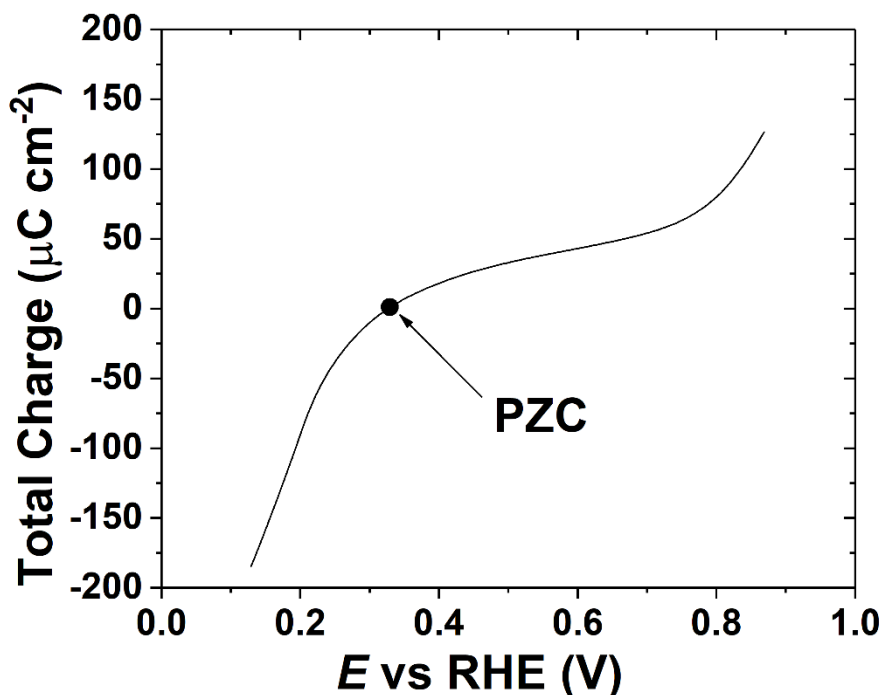


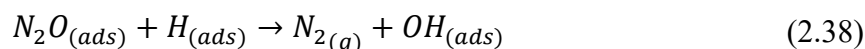
Figure 2.11. Scheme of total charge as a function of the electrode potential. The potential at which the total charge equals zero corresponds to the PZC.

The CO charge displacement method has been successfully applied to determine the location of the PZC for platinum electrodes.¹⁹⁵⁻¹⁹⁸ Especially, this method can be utilized to evaluate the dependence of the PZC on stepped single crystal surface¹⁹⁴ and electrolyte pH¹⁷⁷. However, the CO charge displacement cannot be applied at high anodic potentials (>0.5 V vs RHE) since it is limited by CO oxidation. Besides, another limitation of this method is the assessment of different local contributions to the PZC from terraces, steps, and kinks. Hence, the obtained value of the PZC is an average value of the whole surface where the total net charge equals zero. This total charge includes both positive and negative local contributions to the charge.

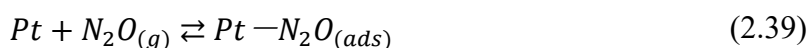
2.5.4.4 N₂O Reduction

The reduction of N₂O on single crystal platinum surfaces was first demonstrated by

Parsons and coworkers.¹⁹⁹ They claimed that this reaction was structure sensitive, and adsorbed hydrogen was considered as an essential catalytic intermediate in this reaction:



Six years later, Attard *et al.* reported that N₂O is sensitive to the local total charge, which can be regarded as a surface probe to determine the PZC.²⁰⁰ However, they disagreed with Parsons about the mechanism of the reduction of N₂O on the platinum electrodes. Attard *et al.* thought the mechanism of this reaction should be characterized by the pre-equilibrium step:²⁰¹



followed by



Thus, the rate of N₂O reduction would be faster when the amount of adsorbed N₂O is higher. Assuming that there is competitive adsorption between N₂O and other adsorbed species such as hydrogen, anions, and water on the electrode surface, the rate of N₂O reduction would be highest when a maximum in the number of free sites available for N₂O adsorption exists. Interestingly, Attard *et al.* found that the maximum current for N₂O reduction always took place at a potential close to or exactly at the PZC for Ir, Pd, Rh, and Pt electrodes.²⁰⁰ An example for Pt(111) in 0.1 M HClO₄ solution is presented in **Figure 2.12**. The maximal current peak of N₂O reduction is located at 0.34 V. The obtained results were consistent with the measurement performed by Frumkin and coworkers.²⁰²

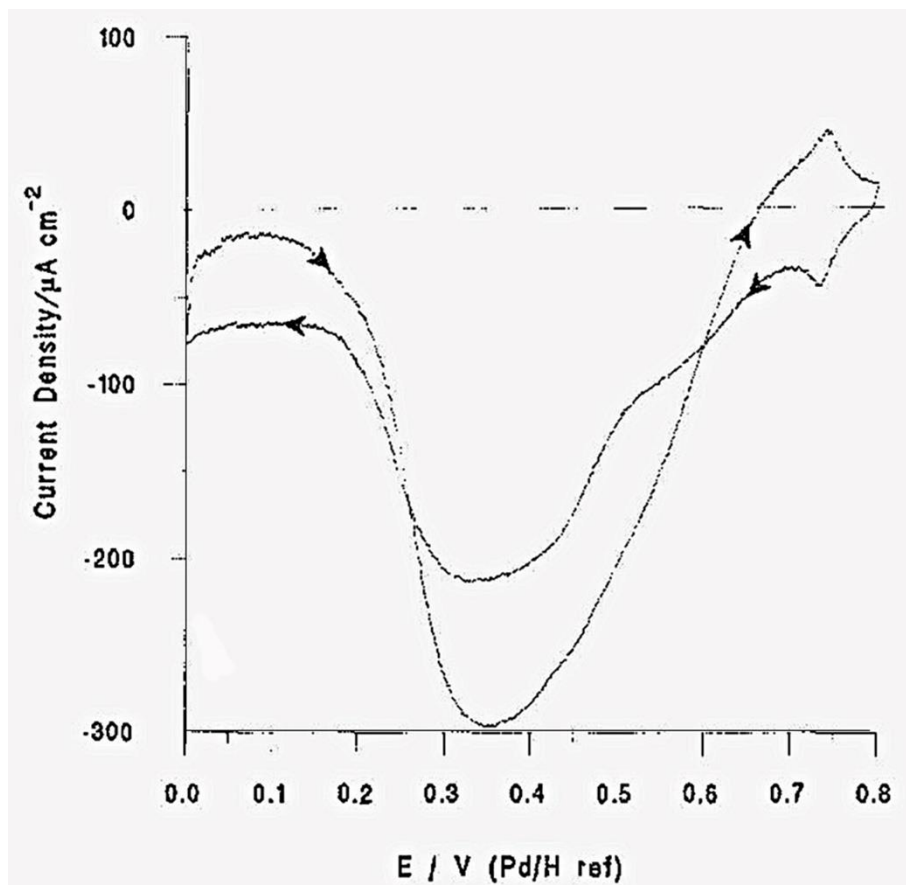


Figure 2.12. N_2O reduction on Pt(111) in 0.1 M $HClO_4$ for the determination of the PZC. Scan rate: 50 mV s^{-1} . Reproduced with permission from reference 200.

An essential advantage of the N_2O reduction method for the determination of the PZC is to investigate the systems which possess multiple local PZCs. Although adsorption of N_2O on, for instance, platinum is quite weak (around 20 kJ mol^{-1}). This method can only be applied for the interfacial structure, which is sensitive to the N_2O reduction reaction.¹⁹⁹

2.5.4.5 Laser-Induced Current Transient Technique

The importance of the role of solvent (e.g., water) at the electrode/electrolyte interface has been confirmed in many electrocatalytic systems.^{117,166,203-205} In **Section 2.5.2**, the

complexity of the interfacial water structure has been discussed. Moreover, a better understanding of the role of the interfacial water molecules is required for rational design and optimization of the electrocatalytic systems. The key challenge for investigating interfacial water is avoiding the interference of its response from the water in the bulk of the solution. In this regard, probing the interface between electrode and electrolyte with short, powerful laser pulses can be applied to address this issue.^{206,207} This technique was developed by Benderskii *et al.* for mercury electrodes in the 1980th.^{208,209} Later, Smalley *et al.* utilized this technique for the study on platinum electrodes in 1988.²¹⁰ Recently, this so-called temperature jump method has been widely applied for various electrochemical systems, such as the surface charge study of gold electrode^{181,211}, platinum electrode^{207,212,213}, and iridium electrode¹⁷⁹.

The illumination of a metallic electrode surface using a high-power laser source increases the temperature of the electrode/electrolyte interface. The short laser pulse (5–10 ns) can cause a rapid temperature change at the interface, but the double layer relaxes to its initial state almost immediately. Assuming that the only influence of the laser illumination is the heating of the electrode surface, then this method can be used to study the fast processes taking place at the electrode/electrolyte interface. If the rate of the temperature change is significantly faster than the relaxation time, then the kinetics of the process can be investigated separately. If the temperature change rate is slower than the relaxation time, thermodynamic information of the equilibrium can be obtained.²¹¹ It should be noted that a suitable selection of the laser illumination wavelength is significant in avoiding side effects, such as photoemission of electrons. Basically, the photoemission threshold for typical electrode metals is around 200–300 nm (work function around 4–5 eV).¹⁸¹ Besides, the intensity of the laser beam varies depending on the nature of the electrode and electrolyte. An appropriate laser beam intensity should allow a rapid increase in temperature without any destruction on the metallic electrode surface.

Assuming that the penetration depth of the light is negligible, the temperature change after a laser pulse can be described as:

$$\Delta T(t) = \frac{1}{\sqrt{\pi\kappa c d} + \sqrt{\pi\kappa_1 c_1 d_1}} \int_0^t q(t-t') \frac{1}{\sqrt{t'}} dt' \quad (2.42)$$

where κ , c , and d and κ_1 , c_1 , and d_1 are the thermal conductivity, thermal capacity, and density of the metal and the aqueous electrolyte, respectively. The function q represents the power density adsorbed at the metal surface. It depends on the temporal shape of the laser pulse:

$$q(t) = (1 - R)I(t) \quad (2.43)$$

where R is the reflectivity of the surface; $I(t)$ is the time-dependent energy flux per unit area.

In the case of a uniform laser pulse, the integration of **Equation 2.42** yields the following formulas:

$$\Delta T(t) = \frac{2(1 - R)I}{\sqrt{\pi\kappa c d} + \sqrt{\pi\kappa_1 c_1 d_1}} \sqrt{t} \quad (t \leq t_0) \quad \text{Heating} \quad (2.44)$$

$$\Delta T(t) = \frac{2(1 - R)I}{\sqrt{\pi\kappa c d} + \sqrt{\pi\kappa_1 c_1 d_1}} [\sqrt{t} - \sqrt{t - t_0}] \quad (t > t_0) \quad \text{Cooling} \quad (2.45)$$

For a long time, the term of $\sqrt{t - t_0}$ can be expanded, keeping only the lower terms in the series. With this approximation, the temperature change decreases with time as:

$$\Delta T(t) = \frac{1}{2} \Delta T_0 \sqrt{\frac{t_0}{t}} \quad (2.46)$$

In the case that the temperature change is small enough, a linear relationship between the temperature and the potential change can be obtained:

$$\Delta E = \left(\frac{\partial E}{\partial T}\right) \Delta T = \left(\frac{\partial E}{\partial T}\right)_q \frac{1}{2} \Delta T_0 \sqrt{\frac{t_0}{t}} \quad (2.47)$$

Thus, the temperature coefficient of the open circuit potential can be evaluated from the slope of the plot of ΔE vs $1/\sqrt{t}$. Besides, according to the electrocapillary equation, one can obtain:²¹⁴

$$\left(\frac{\partial E}{\partial T}\right)_q = -\left(\frac{\partial \Delta S}{\partial q}\right)_T \quad (2.48)$$

where ΔS represents the interfacial entropy of formation. Therefore, a plot of ΔS can be acquired by integrating the graph of the slopes of the ΔE vs $1/\sqrt{t}$ as a function of the double layer charge. It is obvious that $(\partial \Delta S / \partial q)_T$ will be zero when the curve ΔS vs q reaches its maximum. Then, according to **Equation 2.48**, at this point, the change of electrochemical potential resulting from the heating of laser illumination will also be zero. Hence, this methodology allows the identification of the PME of double layer formation.

However, the discussion above does not consider the influence of a thermodiffusion potential on the open circuit potential after laser illumination heating. The thermodiffusion potential can be estimated from the so-called Eastman entropy of transfer from the ions involved. It can be given as:

$$\frac{\Delta E_{Thermodiffusion}}{\Delta T} = -\frac{1}{F} \sum \frac{t_i}{z_i} \hat{S}_i \quad (2.49)$$

where t_i , z_i and \hat{S}_i are the transport number, the charge, and the Eastman entropy of the ion i , respectively. One can see from **Equation 2.49** that the thermodiffusion potential depends on the nature of the electrolyte. The applied electrode potential does not influence this potential contribution. Note that, considering the more significant response from the EDL, the thermodiffusion effect can often be neglected.^{207,215}

As discussed in **Sections 2.5.2** and **2.5.3**, the orientation of the water molecule at the electrode/electrolyte interface depends on the electrode potential. It is controlled by the interaction between the dipole moment of the solvent molecules and the electric field originating from the electrode surface charge (E_{charge}). The potential drop of the electrode mostly comes from the water molecules (E_{dipole}) due to their dipole moment. Therefore, the potential between the electrode and the electrolyte solution (E_{M-S}) is given by:²¹⁵

$$E_{M-S} = E_{charge} + E_{dipole} \quad (2.50)$$

Short laser illumination can cause a rapid temperature change at the electrode/electrolyte interface, which results in the change of E_{dipole} . According to **Equation 2.50**, the E_{M-S} can be changed by the alteration of E_{dipole} . Based on this phenomenon, the so-called laser-induced current transient (LICT) and laser-induced potential transient (LIPT) methods can be applied to check the electrode surface charge. With the LIPT, a change is induced at the open circuit potential, which indicates the orientation of the water dipoles depending on their sign. The LICT, which is applied in this work, is performed potentiostatically. During the measurement, the reorganization of the EDL caused by the laser illumination can be recorded as the current transient. If the electrode is positively charged, then positive current transients are observed; on the contrary, if the electrode is negatively charged, the laser pulse results in negative current transients. The PME is located at the potential where the sign of the current transient alters, as shown in **Figure 2.13**.

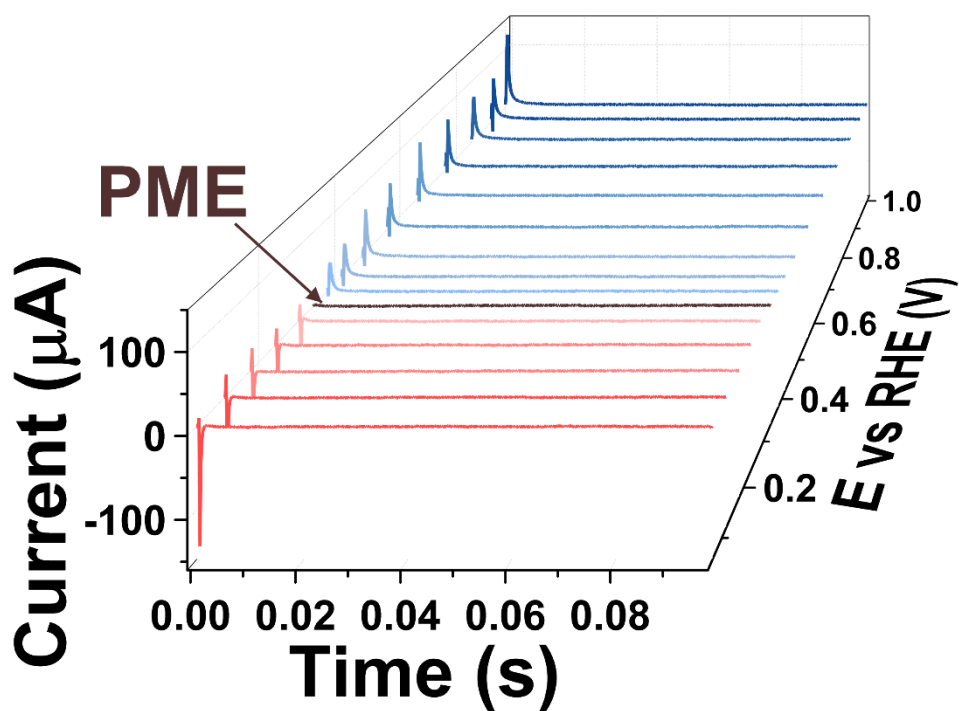


Figure 2.13. An example of typical current transients recorded during the laser measurement at different electrode potentials for polycrystalline gold in 0.5 M O₂-saturated Na₂SO₄ solution (pH 2). The sign of the current transient coincides with the sign of the electrode surface charge.

Alternatively, in order to see the PME location clearly, the extreme values of the current transients ($i_{X_{trm}}$) can be plotted as a function of the applied potential, as shown in **Figure 2.14**.

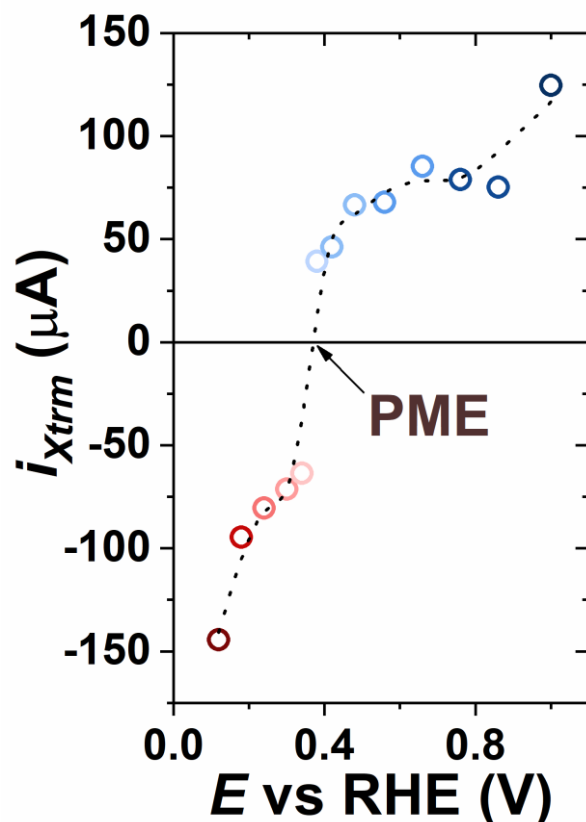


Figure 2.14. The extreme current values of the current transients (i_{Xtrm}) as a function of the working electrode potential utilized to find the PME. The data is taken from Figure 2.13. Note, only a part of current transients is presented here.

The PME is considered an important parameter related to the electrocatalytic activity.^{203,216,217} The PME provides information on the stiffness of the interfacial water layer. This can be used to assess the influence of the EDL structure on the electrochemical processes. For instance, recently, Koper *et al.* demonstrated that the water structure at the interface has a strong relationship with the HER activity rate of Pt(111)/Ni(OH)₂.¹¹⁷ Close to the PME, the interfacial water molecule is relatively free to reorient and easy to reorganize. The rate of reaction should be the fastest at the PME. Therefore, one can assume that the closer the PME is to the thermodynamic equilibrium potential of a certain reaction, the faster this reaction should be.

2.6 Other Techniques Applied in this Work

2.6.1 Cyclic Voltammetry

Cyclic voltammetry (CV) is one of the most common electroanalytical techniques employed to quantitatively analyze electrochemical processes.²¹⁸⁻²²⁰ During CV measurements, a periodic triangular potential is applied on the working electrode (**Figure 2.15A**), and the current-potential curves are recorded (**Figure 2.15B**). CV measurements reveal certain processes, such as the adsorption/desorption redox reactions. Moreover, it allows investigation of the stability of electrode materials and reaction products, quantitative analysis of electron transfer kinetics. The shape of CV mainly depends on the nature of the electrode but also on the nature of the electrolyte. Different compositions can result in an alteration of the shape of CV, e.g., certain electrochemical processes at the electrode/electrolyte interface result in specific features in the CV.²²¹

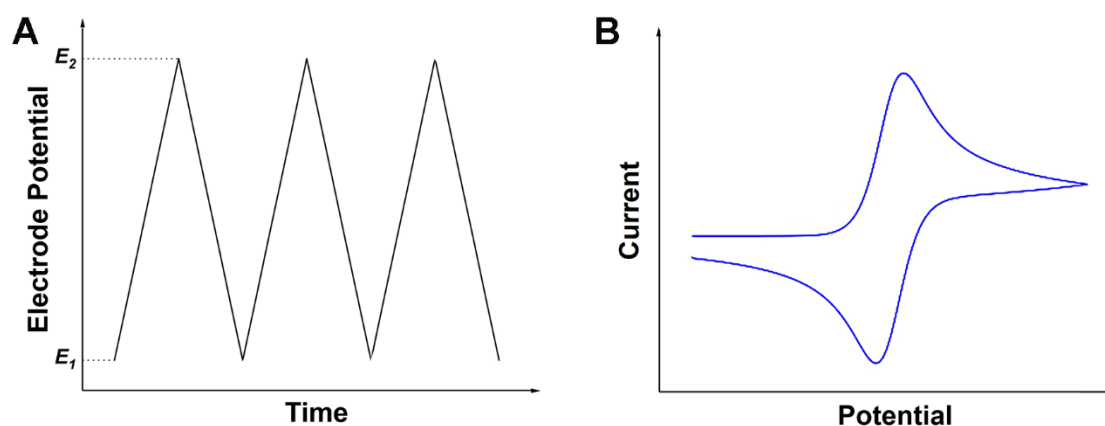


Figure 2.15. (A) The typical triangular potential profile applied during a CV. E_1 and E_2 are the initial and final potentials, respectively. (B) A schematic representation of a CV.

As shown in **Figure 2.15B**, a CV is typically presented by plotting the current *versus* the applied potential. The recorded current is often depicted as the current density for

easier comparison. CV can provide information about the properties and mechanisms of various electrochemical reactions and the kinetic parameters of these reactions. Besides, CV can also be used to determine the antioxidant capacity in food and even the skin.^{222,223}

2.6.2 Chronoamperometry

Chronoamperometry (CA) is a technique in which a constant potential is applied to the system, and the response of the current is recorded. The chronoamperometric response can be used to determine, e.g., the diffusion coefficient of electroactive species.^{224,225} Besides, one can also apply several potential-step CA to investigate the mechanism of reactions taking place at the electrode/electrolyte interface.^{226,227}

In this work, the CA technique was used during the laser measurements. The current transients were recorded at different potential steps.

3. Experimental Part

3.1 Electrochemical Cells

Two types of electrochemical cells were used in this thesis: one cell for voltammetry and laser measurements and one cell for activity experiments. Both cells used the three-electrode configuration. All glassware was cleaned with a piranha solution consisting of a 3:1 mixture of H₂SO₄ (96% Suprapur™, Merck, Germany) and H₂O₂ (30% Suprapur™, Merck, Germany) before the measurements. All compartments were then rinsed several times with near-boiling ultrapure water (Evoqua, Germany).

The cell for cyclic voltammetry (CV) and laser-induced current transient (LICT) measurements consisted of two parts: the preconditioning compartment (1) and the main compartment (2) (**Figure 3.1A**). The electrolyte solutions were preconditioned with purging gases (Ar 5.0 and O₂ 4.7, Air Liquid, were used in this thesis) in the compartment (1) before being introduced to the compartment (2). A flat, laser light transmittable glass window was designed on the main compartment (2) to allow the laser beam to reach the working electrode surface directly. During the experiments, the inside atmosphere can be controlled with a gas inlet and outlet on the main compartment (2). The temperature of the investigated electrolytes can also be adjusted by a water thermostat for this cell. AT-cut quartz crystal wafer electrochemical quartz crystal microbalance (EQCM) electrodes (polycrystalline Pt and Au with the surface area of 1.37 cm², Stanford Research Systems, USA) were used as working electrodes (WE) for the CV and LICT measurements. A crystal holder (Stanford Research Systems, USA) was used for the AT-cut quartz crystal wafer EQCM electrodes during the measurements. The 5 MHz QCM gold substrates, purchased from Biolin Scientific, Inc., were used as WE for the surface-mounted metal-organic frameworks (SURMOFs) synthesis and LICT measurements. A mercury-mercurous sulfate electrode (MMS) (SI Analytics, Germany) and a mercury-mercury oxide

electrode (1 M NaOH, Bio-Logic, France) served as the reference electrodes (RE) for the experiments of AT-cut quartz crystal wafer EQCM electrodes and SURMOFs, respectively. Both REs were connected to the electrolyte through a Luggin capillary. A Pt wire was used as the counter electrode (CE). All measurements were performed using a VSP-300 potentiostat (Bio-Logic, France).

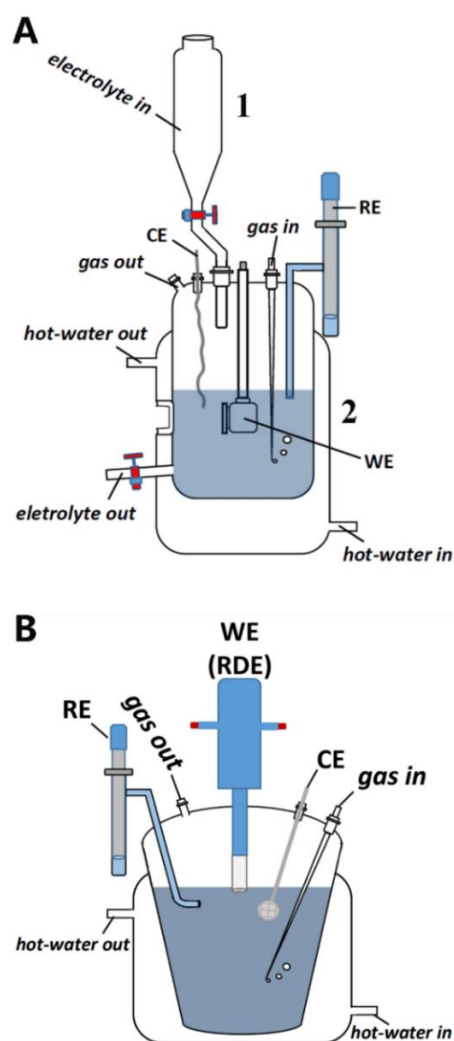


Figure 3.1. Schematics of the electrochemical cells used for (A) the CV and LICT measurements and (B) the activity experiments, respectively. Cell (A) can be divided into (1) the preconditioning compartment and (2) the main compartment. WE, RE, CE, and RDE labels correspond to the working electrode, reference electrode, counter electrode, and rotating disk electrode, respectively. Relative positions of the electrodes in the figure do not correspond to the real measurements, where RE is rather in between WE and CE.

The cell for the activity measurements with polycrystalline Pt electrode consisted of a single compartment (**Figure 3.1B**). The working electrode was connected using the rotating disk electrode (RDE) configuration to ensure better mass transport during the measurements.²²⁸ To obtain the meniscus for the WE in contact with the electrolyte, the movable shaft was used to adjust the position of the WE. A Pt mesh was used as the CE, while the MMS served as the RE through a Luggin capillary. Similar to the previous cell, the gas inlet and outlet were used to saturate the electrolyte with the gas (Ar for cleaning the WE; H₂ for the HER; and O₂ for the ORR measurements). The temperature of the electrolyte can also be controlled by a water thermostat.

3.2 Setup for the Laser Measurements

The laser measurements were conducted utilizing a Quanta-Ray INDI pulsed Nd:YAG laser (Spectra-Physics Lasers, USA) with a repetition rate of 10 Hz and 5–8 ns pulse width (**Figure 3.2**). The wavelength of the device applied in our experiments was 532 nm, which is believed to prevent the photoemission of electrons.²¹¹ The diameter of the laser beam was kept at 9 mm for all the laser measurements. Because the direct energy of the laser beam can reach 200 mJ, which is excessively high and can destroy the working electrode, a motorized beam splitter (VA-CB-532-CONEX, Newport Corp.) acted as an attenuator. This was used to control the energy of the laser pulses. The laser can be operated by either a table controller or a GCR controller software (Spectra-Physics Lasers, USA). The attenuator was manipulated by a Variable Attenuator software (model: CCVA-PR-CD, Spectra-Physics Lasers, USA) to adjust the energy of the laser beam. The current transients can be recorded from the response of the system after the laser illumination. The extreme values of the current transients can be plotted as a function of the applied potential to find the PME.

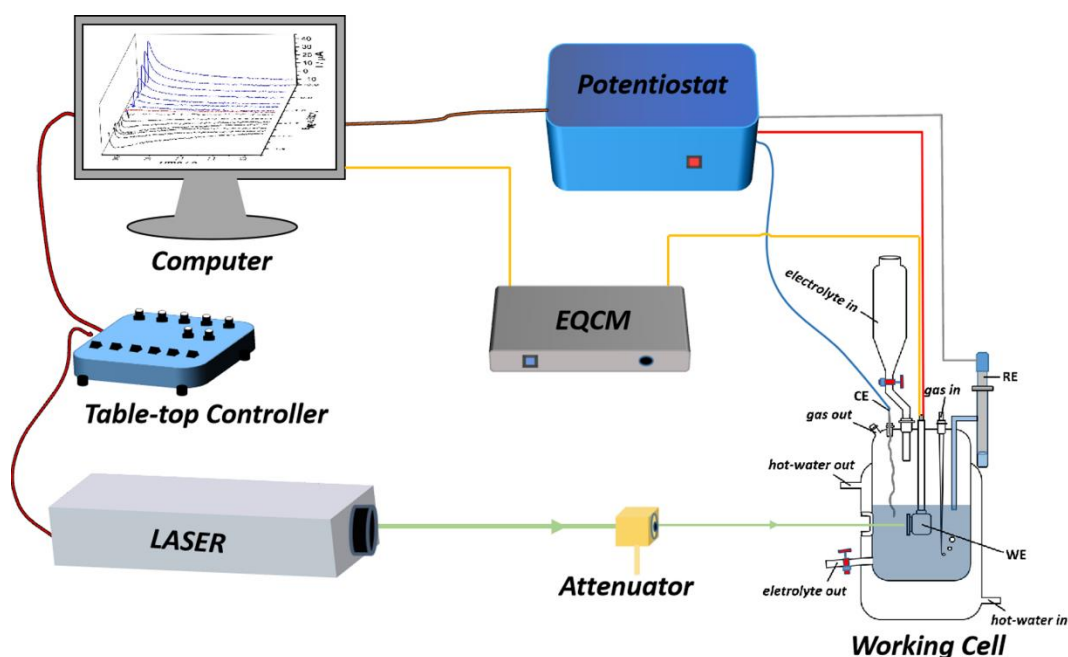


Figure 3.2. Schematic illustration of the laser-induced current transient technique setup. WE, RE, and CE labels correspond to the working electrode, reference electrode, and counter electrode, respectively. Relative positions of the electrodes in the figure do not correspond to the real measurements, where RE is rather in between WE and CE.

3.3 Preparation Before the Electrochemical Measurements

3.3.1 Preparation of Electrolytes

For electrolytes, different concentrations of HClO_4 and H_2SO_4 solutions used for the working electrodes cleaning and electrochemical experiments were prepared by diluting concentrated acid solutions with ultrapure water. The 0.5 M $(\text{AM})_2\text{SO}_4$ ($\text{AM} = \text{Li}^+, \text{Na}^+, \text{K}^+, \text{Cs}^+$) solutions were prepared by dissolving the corresponding salt powders (all 99.0%, Alfa Aesar) with ultrapure water. The pHs of 0.5 M $(\text{AM})_2\text{SO}_4$ solutions were adjusted with either H_2SO_4 or AMOH solutions (LiOH 99.995%, Alfa Aesar, NaOH 99.996%, Alfa Aesar, KOH 99.98%, Alfa Aesar, CsOH 99.9%, Sigma

Aldrich) using a PHH222 portable pH meter (Omega).

For the experiments done on Cu(111), different pHs of NaClO₄ (97%, Alfa Aesar) solutions were adjusted with NaOH solutions using the pH meter.

In the case of SURMOFs, 0.1 M AMOH solutions (LiOH 99.995%, Alfa Aesar, NaOH 99.99%, Alfa Aesar, KOH 99.98%, Alfa Aesar, and CsOH, 50 wt. % in H₂O, 99.9% trace, Sigma-Aldrich) were prepared by dissolving the corresponding salt powders or diluting the solution.

Before the measurements, the electrolytes were saturated with the necessary gases for at least 10 minutes. The electrolyte was also slowly purged with the same gas during the measurements.

3.3.2 Preparation of Electrodes

Before the experiments, the AT-cut polycrystalline Pt and Au quartz crystal wafer electrodes were electrochemically cleaned in Ar-saturated 0.1 M HClO₄ and 0.1 M H₂SO₄ solutions, respectively. The corresponding CV results were then collected in order to check the quality of the working electrode surface. In detail, the Pt electrode was cleaned in Ar-saturated 0.1 M HClO₄ within the potential range of 0.00–1.80 V *vs* RHE until the voltammograms were stable. The potential range was then narrowed to 0.05–1.00 V *vs* RHE, and the obtained CV (**Figure 3.3A**) was compared with those published in the literature to ensure similarities in the surface quality.^{229,230} In the case of Au, the cleaning procedures were performed in Ar-saturated 0.1 M H₂SO₄ within the potential range of 0.40–2.10 V *vs* RHE. The voltammograms (**Figure 3.3B**) within the potential range of 0.50–1.70 V *vs* RHE were then measured to further compare with those presented in the literature.^{231,232}

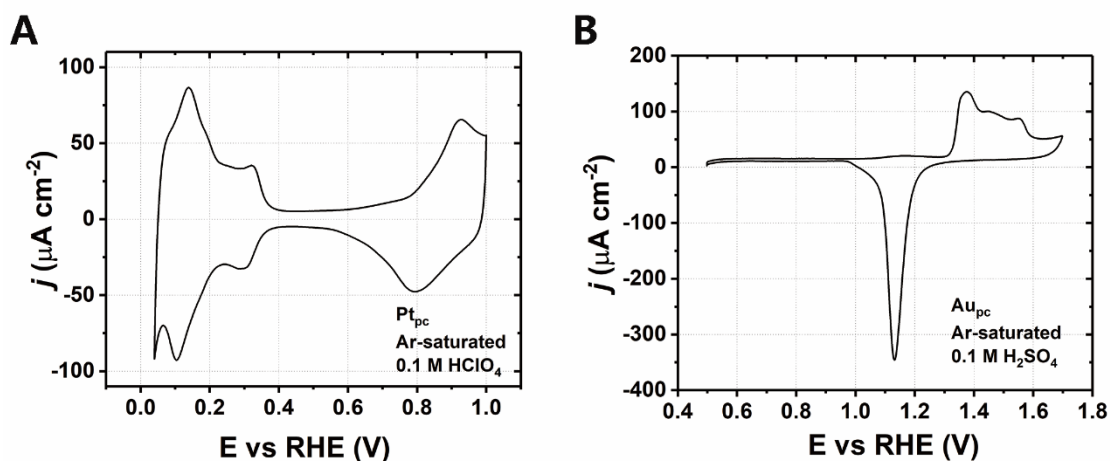


Figure 3.3. The stable cyclic voltammograms recorded after cleaning for (A) Pt_{pc} in $HClO_4$ and Au_{pc} in H_2SO_4 solutions. Scan rate: 50 mV s^{-1} .

As for the Pt electrode described above, the disk-shaped polycrystalline Pt electrode with a diameter of 5 mm was electrochemically cleaned in Ar-saturated 1 M $HClO_4$ within the potential range of $-0.10\text{--}1.80\text{ V vs RHE}$ until the recorded CV became stable. Afterwards, the scanned potential range was set to $0.04\text{--}1.02\text{ V vs RHE}$ to check the surface quality, as shown in **Figure 3.4A**.

The polycrystalline Au bead electrodes (homemade; surface area: 0.136 cm^2) were electrochemically cleaned by immersing them into the $0.1\text{ M H}_2\text{SO}_4$ electrolyte and cycling between $0.35\text{ V--}2.10\text{ V vs RHE}$ (scan rate: 50 mV s^{-1}). After getting stable CVs (see **Figure 3.4B**), they were compared with the voltammograms available in the literature.²³³

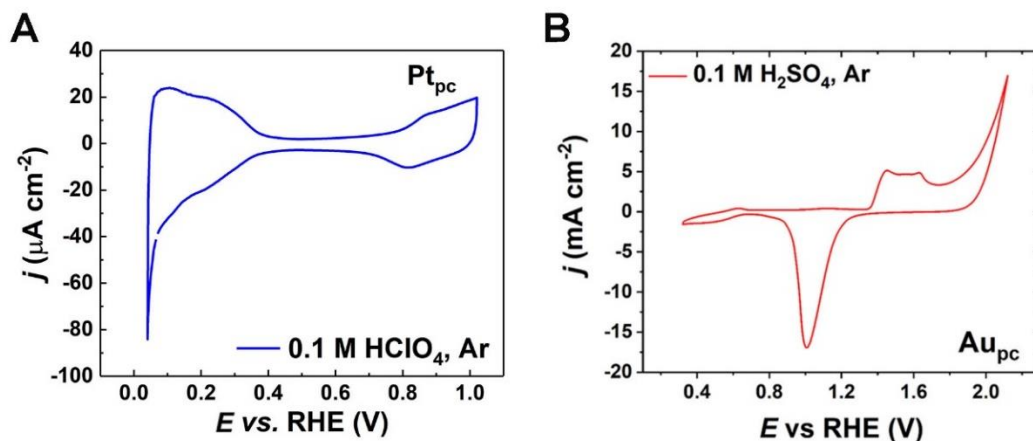


Figure 3.4. Cyclic voltammograms collected after cleaning for (A) the disk-shaped Pt_{pc} electrode in the 0.1 M $HClO_4$ and (B) the Au_{pc} bead electrode in the 0.1 M H_2SO_4 solutions. Scan rate: 50 mV s^{-1} .

Cu(111) crystals (Mateck, Jülich) were mechanically polished with diamond paste (ESCIL) down to $0.25 \mu\text{m}$. Then the crystals were electropolished in 60% H_3PO_4 (85% EMSURE, Merck) at 1.8 V *versus* a Cu counter electrode. Before each experiment, the crystals were annealed in a homemade horizontal tube furnace under H_2 flow. The crystals can be removed, maintaining the H_2 atmosphere, which allows a direct transfer to an Ar-filled (Messer, 5.0) glove box (Mbraun MB 200 MOD glovebox) to perform the experiments without traces of oxygen from the air.

The deposition of Ni|Fe-[TA]-SURMOFs can be obtained *via* a layer-by-layer (LBL) method in a homemade pump system. Before the deposition, the QCM gold substrates (Biolin Scientific, Inc.) were functionalized for 12 h in a mixed ethanol solution including $20 \mu\text{M}$ 16-mercaptohexadecanoic acid (MHDA, 90%, Sigma-Aldrich) and acetic acid (5 vol.%). Afterwards, the electrodes were rinsed with ethanol several times. A deprotonated organic linker solution (0.2 mM) can be prepared by stirring a mixture solution including 0.185 mmol terephthalic acid (TA, Sigma-Aldrich), 1.02 L ethanol (99.9%, Th. Geyer GmbH & Co. KG, Germany), 60 mL distilled water, and 0.8 mL trimethylamine (Et_3N , Acros) for 24 h. For the deposition of Ni|Fe-[TA]-SURMOFs,

the gold substrates were firstly immersed into the 0.25 mM NiCl₂·6H₂O (99.3%, Alfa Aesar) solution for 10 min. Then, the electrodes were washed with ethanol for 2 min to remove the unadsorbed species. Subsequently, the electrode was immersed into the prepared deprotonated organic linker solution for 10 min to generate the metal-organic bonds. Afterwards, the system was cleaned with ethanol for 2 min. Four immersion processes correspond to one LBL deposition cycle. The Ni-[TA] was gained after 45 cycles. For the top-layer Fe-[TA], 15 more cycles were performed in 0.25 mM FeCl₃ (98%, abcr GmbH & Co. KG, Germany) solution. Finally, the as-prepared heterostructured Ni|Fe-[TA]-SURMOFs electrode was rinsed carefully with absolute ethanol several times and dried at room temperature.

3.4 Electrochemical Measurements

3.4.1 LICT Measurements

3.4.1.1 LICT Measurements for the AT-cut Polycrystalline Au Quartz Crystal Wafer Electrodes

After the electrochemical cleaning, the polycrystalline Au electrodes were introduced into Ar-saturated or O₂-saturated HClO₄ solutions with different pH values (0, 0.5, 1.0, 1.5, and 2.0). The LICT technique was then applied in different systems to find the PMEs. The potential range investigated for the case of HClO₄ was 0.06–1.00 V vs RHE, and the scan direction was kept from positive to negative with 20 mV potential steps. The applied energy of the laser beam was fixed at 12 mJ (19 mJ cm⁻²).

Besides, the polycrystalline Au electrodes were characterized at different pHs (2, 4, 6, 8, and 10) in Ar-saturated and O₂-saturated 0.5 M Na₂SO₄ and K₂SO₄ solutions with the LICT. However, the laser beam energy was kept at 20 mJ (32 mJ cm⁻²) in this case. The potential ranges within which the LICT experiments were carried out slightly differ

depending on the system under study. All the potential ranges during the LICT measurements in all the systems, as well as the applied potential steps and the electrolytes, are listed in **Table 3.1**.

Table 3.1. Potential ranges and potential steps applied during the LICT measurements for polycrystalline Au.

pH	Electrolyte	Potential range (V _{RHE})	Potential step (mV)
2	0.5 M Na ₂ SO ₄ , Ar-sat.	0.10 – 1.00	20
2	0.5 M Na ₂ SO ₄ , O ₂ -sat.	0.12 – 1.00	20
4	0.5 M Na ₂ SO ₄ , Ar-sat.	0.10 – 1.02	20
4	0.5 M Na ₂ SO ₄ , O ₂ -sat.	0.10 – 1.02	20
6	0.5 M Na ₂ SO ₄ , Ar-sat.	0.11 – 1.01	20
6	0.5 M Na ₂ SO ₄ , O ₂ -sat.	0.11 – 1.01	20
8	0.5 M Na ₂ SO ₄ , Ar-sat.	0.23 – 1.03	20
8	0.5 M Na ₂ SO ₄ , O ₂ -sat.	0.23 – 1.03	20
10	0.5 M Na ₂ SO ₄ , Ar-sat.	0.25 – 1.11	20
10	0.5 M Na ₂ SO ₄ , O ₂ -sat.	0.29 – 1.11	20
2	0.5 M K ₂ SO ₄ , Ar-sat.	0.08 – 1.12	20
2	0.5 M K ₂ SO ₄ , O ₂ -sat.	0.10 – 1.00	20
4	0.5 M K ₂ SO ₄ , Ar-sat.	0.10 – 1.10	20
4	0.5 M K ₂ SO ₄ , O ₂ -sat.	0.10 – 1.10	20
6	0.5 M K ₂ SO ₄ , Ar-sat.	0.61 – 1.37	20

6	0.5 M K ₂ SO ₄ , O ₂ -sat.	0.61 – 1.51	20
8	0.5 M K ₂ SO ₄ , Ar-sat.	0.39 – 1.45	20
8	0.5 M K ₂ SO ₄ , O ₂ -sat.	0.43 – 1.45	20
10	0.5 M K ₂ SO ₄ , Ar-sat.	0.40 – 1.50	20
10	0.5 M K ₂ SO ₄ , O ₂ -sat.	0.42 – 1.54	20
8	0.5 M Na ₂ SO ₄ +K ₂ SO ₄ , Ar-sat.	0.39 – 1.45	20
8	0.5 M Na ₂ SO ₄ +K ₂ SO ₄ , O ₂ -sat.	0.43 – 1.45	20

3.4.1.2 LICIT Measurements for the AT-cut Polycrystalline Pt Quartz Crystal Wafer Electrodes

Similar to the case of Au electrode, the cleaned polycrystalline Pt electrodes were investigated at different pHs (0, 0.5, 1.0, 1.5, and 2.0) in Ar-saturated and O₂-saturated HClO₄ solutions and at different pHs (2, 4, 6, 8, and 10) in Ar-saturated and O₂-saturated 0.5 M Na₂SO₄ and K₂SO₄ solutions (see **Table 3.2**). The applied energy of the laser beam was 12 mJ for Pt in HClO₄ solutions but 20 mJ for Pt in the electrolytes containing alkali metal cations.

To study the cation effect on the PME and electrocatalytic activities (HER and ORR) of polycrystalline Pt electrode, the pH of 0.5 M (AM)₂SO₄ solutions (AM = Li⁺, Na⁺, K⁺, Cs⁺) was kept at pH 6 to reduce the influence of the H⁺ and OH⁻ ions on the system, without losing the ability to control their concentration. For this set of experiments, the potential range investigated was 0.06–1.00 V vs RHE. The energy of the laser pulse was fixed at 12 mJ, and the applied potential step was 20 mV.

Table 3.2. Potential ranges and potential steps applied during the LICIT measurements for polycrystalline Pt.

pH	Electrolyte	Potential range (V _{RHE})	Potential step (mV)
2	0.5 M Na ₂ SO ₄ , Ar-sat.	0.06 – 1.00	20
2	0.5 M Na ₂ SO ₄ , O ₂ -sat.	0.02 – 1.00	20
4	0.5 M Na ₂ SO ₄ , Ar-sat.	0.04 – 1.00	20
4	0.5 M Na ₂ SO ₄ , O ₂ -sat.	0.08 – 0.98	20
6	0.5 M Na ₂ SO ₄ , Ar-sat.	0.07 – 0.99	20
6	0.5 M Na ₂ SO ₄ , O ₂ -sat.	0.05 – 0.99	20
8	0.5 M Na ₂ SO ₄ , Ar-sat.	0.05 – 1.01	20
8	0.5 M Na ₂ SO ₄ , O ₂ -sat.	0.03 – 1.18	50
10	0.5 M Na ₂ SO ₄ , Ar-sat.	0.05 – 1.20	50
10	0.5 M Na ₂ SO ₄ , O ₂ -sat.	0.05 – 1.20	50
2	0.5 M K ₂ SO ₄ , Ar-sat.	0.08 – 1.03	50
2	0.5 M K ₂ SO ₄ , O ₂ -sat.	0.08 – 1.02	20
4	0.5 M K ₂ SO ₄ , Ar-sat.	0.04 – 1.00	20
4	0.5 M K ₂ SO ₄ , O ₂ -sat.	0.06 – 1.00	20
6	0.5 M K ₂ SO ₄ , Ar-sat.	0.04 – 1.00	20
6	0.5 M K ₂ SO ₄ , O ₂ -sat.	0.01 – 1.21	50
8	0.5 M K ₂ SO ₄ , Ar-sat.	0.03 – 1.18	50
8	0.5 M K ₂ SO ₄ , O ₂ -sat.	0.03 – 1.18	50

10	0.5 M K ₂ SO ₄ , Ar-sat.	0.05 – 1.20	50
10	0.5 M K ₂ SO ₄ , O ₂ -sat.	0.05 – 1.20	50

3.4.1.3 LICT Measurements for Cu(111) Crystals

For all the LICT measurements on Cu(111), a fixed laser irradiation energy (67 mJ cm^{-2}) was applied. The potential range was from -1.0 to -0.35 V_{SHE}, which is well below the oxidation onset of Cu(111).^{234,235} The LICT experiments were conducted potentiostatically with a potential step of 25 mV.

3.4.1.4 LICT Measurements for SURMOFs

In order to avoid damage of the electrode, a laser irradiation energy of 12.5 mJ cm^{-2} was applied for all the investigated SURMOF systems. The potential range was set between 0.81 and 1.21 V_{RHE}. The LICT experiments were conducted potentiostatically with a potential step of 20 mV.

3.4.2 Activity Measurements

The HER and ORR activities of the disk-shaped polycrystalline Pt electrode in H₂-saturated or O₂-saturated 0.5 M (AM)₂SO₄ solutions (AM = Li⁺, Na⁺, K⁺, Cs⁺) at pH 6 were measured using the CV. A rotation speed of 1600 rpm was applied for all the HER and ORR activity tests in this work. The applied potential regime (for the HER - 0.40– 0.10 V *vs* RHE and the ORR 0.10–1.00 V *vs* RHE) was identical for each system. The scan rate was kept at 50 mV s⁻¹.

The OER measurements for Ni|Fe-[TA]-SURMOFs were conducted within a potential range of 1.10–1.75 V_{RHE} for 5 cycles with a scan rate of 5 mV s⁻¹. It should be noted that the OER polarization curves were automatically iR-corrected.

4. Results and Discussion

4.1 Interface Structure and Electrode Activity

A fundamental understanding of the processes occurring at the electrode/electrolyte interface is required to develop high-performing electrocatalysts successfully.²³⁶⁻²⁴² Nowadays, the performance of a specific electrocatalytic reaction is generally believed to rely strongly on the composition and structure of the electrode surface.²⁴³⁻²⁴⁸ However, in the case of aqueous electrolytes, electrocatalytic processes can also be influenced by the electrolyte composition.^{47,63,249} To understand how the electrolyte composition controls the interface structure and activity, the degree of order of the electric double layer (EDL) can be considered a critical factor governing the electrocatalytic processes.¹¹⁷ It can be anticipated that the more ordered the interfacial water structure is, the more energy is required to rearrange the water dipoles at the interface after the electron transfer. Conversely, the process should be easily carried out at the potential of maximum entropy (PME), at which the interfacial water molecules have the maximal disorder, and reactant species can pass through the EDL relatively easily. It can thus be expected that the closer the PME is to the thermodynamic equilibrium potential of a certain reaction, the faster this reaction should be.

In the following sections, the results of experiments using polycrystalline Pt and Au electrodes in various electrolytes are discussed. First, the effect of the pH value in acidic solution was analyzed, and subsequently, the influence of alkali metal cations in the electrolyte was examined. The well-known hydrogen evolution and oxygen reduction reactions (HER and ORR), selected as model reactions, were investigated. The obtained results of the laser-induced current transient (LICT) measurements were associated with the HER and ORR activity data measured in the corresponding systems. The results suggest that the determination of the PME with the LICT method can be a valuable way to evaluate and investigate the influence of the electrolyte composition

on the electrocatalytic processes happening at the electrode/electrolyte interface.

4.1.1 pH Effect

4.1.1.1 pH Effect for Pt_{pc} and Au_{pc} Electrodes in HClO₄ Solutions

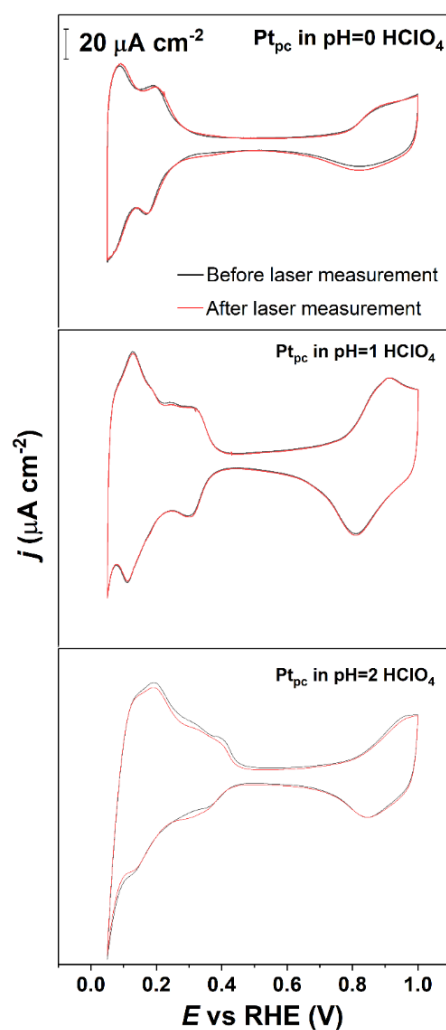


Figure 4.1. Typical cyclic voltammograms (CVs) of Pt_{pc} at different pH values (only data for pHs 0, 1, and 2 are shown) of the HClO₄ solutions. Scan rate: 50 mV s^{-1} . The shape of the CV after the laser illumination was practically unchanged, confirming that the surface quality is not affected by the LICM measurements.

Investigations are started using simple systems: Pt_{pc} in $HClO_4$ solutions of different pH values (0, 0.5, 1.0, 1.5, and 2.0). First, CV measurements were performed to check the surface quality (**Figure 4.1**). The CVs include three regions: the hydrogen adsorption/desorption ($H_{ads/des}$) region (approx. 0.05–0.45 V_{RHE}), the so-called double layer region (approx. 0.45–0.70 V_{RHE}), and the hydroxyl and oxygen adsorption/desorption ($OH/O_{ads/des}$) region (approx. 0.70–1.00 V_{RHE}). The CV shape was in good agreement with the results reported in the literature.^{250,251}

To investigate the pH effect on the EDL properties of Pt_{pc} , LICT measurements were conducted. In essence, the equilibrium at the interface is destroyed by a short heat burst of a laser pulse, followed by a fast return to the initial EDL-state. The response of the system is recorded as the current transient. The potential at which the current transient changes its sign corresponds to the PME. Sample current transients were acquired for Pt_{pc} in the $HClO_4$ solutions (**Figure 4.2**).

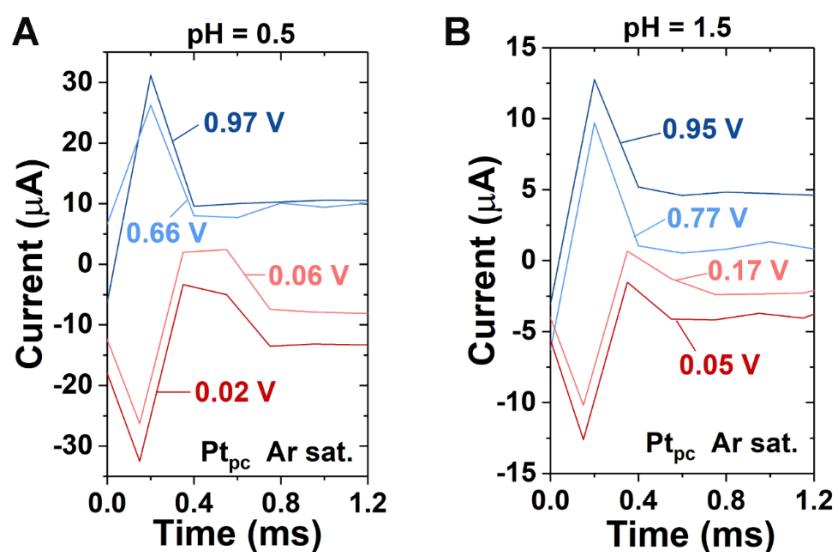


Figure 4.2. Sample LICTs recorded for Pt_{pc} in Ar-saturated $HClO_4$ solutions at (A) pH 0.5 and (B) pH 1.5. The PME can be found at a value between the two potentials where the current transient changes its sign.

Alternatively, the extreme values of the current transients ($i_{X_{trm}}$) can be plotted as a function of the applied potential to determine the PME location (Figure 4.3). A positive electrode surface charge should lead to a positive current transient and vice versa because the sign of the charge of the electrode surface coincides with the current transient^{205,252}.

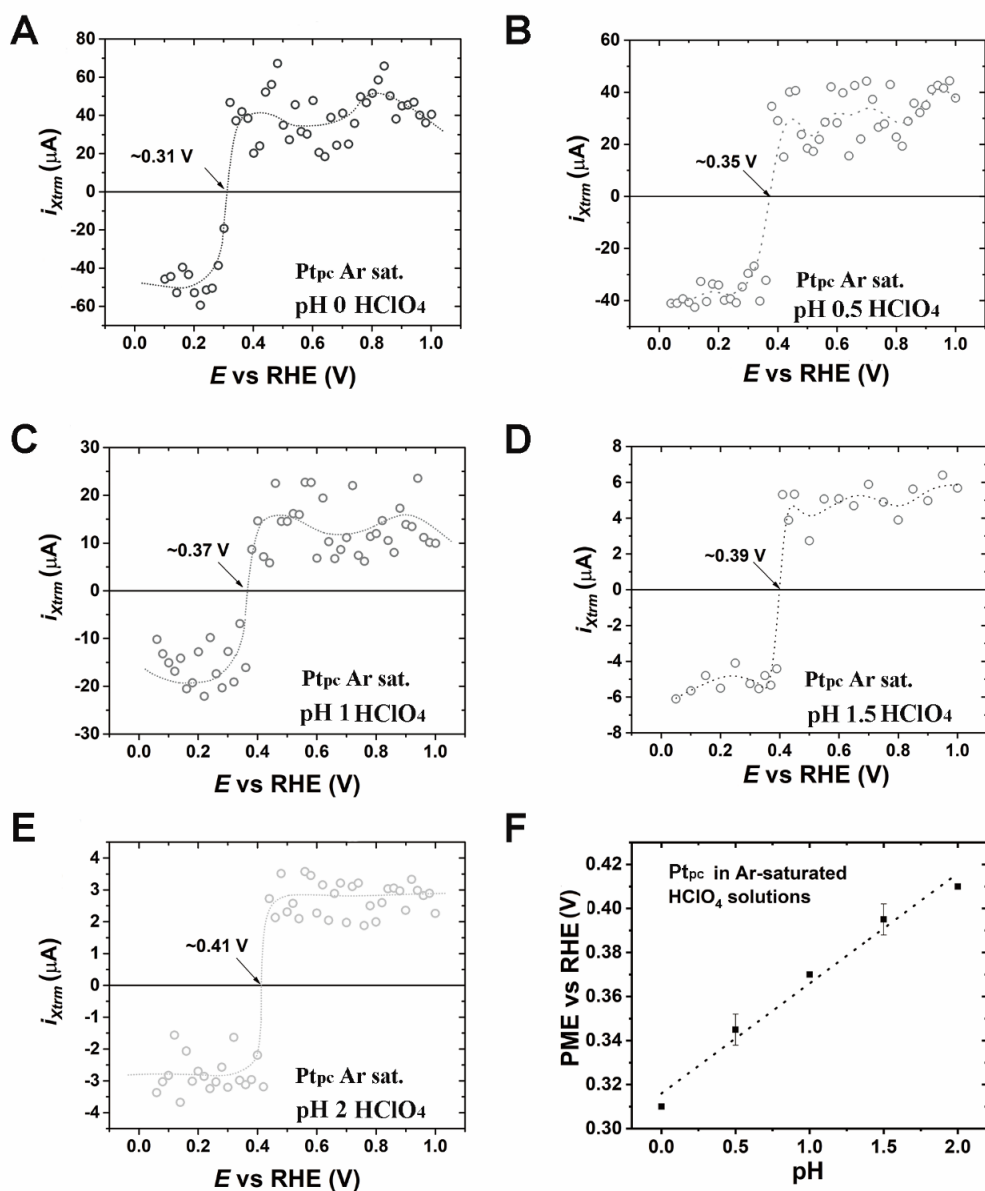


Figure 4.3. (A to E) The values of the current spikes maxima ($i_{X_{trm}}$) as a function of electrolyte pH for Pt_{pc} electrodes at different pH values (0, 0.5, 1.0, 1.5, and 2.0) of HClO₄ electrolytes. (F) The PME of the Pt_{pc} electrode shows a linear dependence on the pH value of the electrolyte.

Figure 4.3, A to E, shows the collected current transients for Pt_{pc} at different H⁺ concentrations of the HClO₄ solutions. The PME can be found at the potential at which the current transient changes its sign. The PME values of Pt_{pc} electrodes are thus ~0.31 V, ~0.35 V, ~0.37 V, ~0.39 V, and ~0.41 V vs RHE for the HClO₄ electrolytes at pHs 0, 0.5, 1.0, 1.5, and 2.0, respectively. The PME becomes more positive as the pH increases. Moreover, the PME shows a linear relationship with the pH values (see **Figure 4.3F**). A slope of ~52 mV per pH unit is observed. The results obtained coincide with the data exhibited in previous literature about the Pt electrode planes.²⁵³ It should be mentioned that the PME is supposed to be independent of the pH value of the electrolyte on the standard hydrogen electrode (SHE) scale when the PME is located within the potential region without the influence of adsorption.^{179,254,255} Therefore, the PME should shift by around 59 mV per pH unit on the reversible hydrogen electrode (RHE) scale. Our obtained outcomes are comparable with the expected results.

To check that the surface quality of the electrode is not affected by the laser irradiation, CVs were recorded after the LICT experiments. As **Figure 4.1** shows, the surface quality of the electrode before and after the LICT measurements is comparable.

As shown in **Figure 4.3F**, the PME of the Pt_{pc} electrodes shifts from the thermodynamic equilibrium potential for the HER (0.00 V vs RHE) but closer to the corresponding potential of the ORR (1.23 V vs RHE). As mentioned above, the reaction rate at the surface should be higher when the equilibrium potential for this reaction is closer to the PME of the system. It can thus be expected that Pt_{pc} electrodes in high H⁺ concentration (low pH) of HClO₄ solutions should perform better for the HER, while their activity towards the ORR should be higher in HClO₄ solutions of low H⁺ concentrations (high pH).

The expectation can be confirmed by the activity measurements performed at different pH values (0, 1.0, and 2.0) of H₂-saturated (for HER) or O₂-saturated (for ORR) HClO₄ solutions (**Figure 4.4A and B**). The activity of Pt_{pc} towards the HER decreases but

increases towards the ORR as a consequence of the pH increase. This is in good agreement with the expectations from the previous experiments and has similarly been reported by former studies on the pH effect on the activity for Pt_{pc} electrodes.^{256,257} It should be noted that microelectrodes (Pt_{pc} ME) were used for the activity measurements to increase the efficiency of the diffusion mass transport and the sensitivity of the activity measurements to potential changes.²⁵⁸

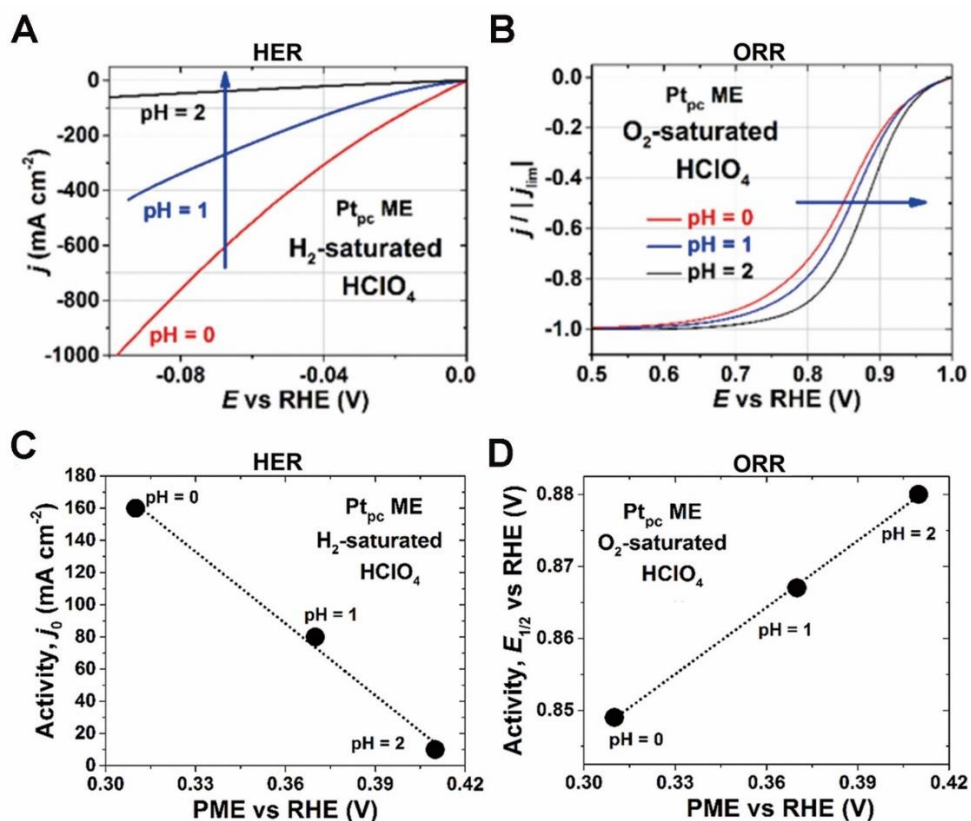


Figure 4.4. Typical (A) HER and (B) ORR polarization curves for the Pt_{pc} microelectrode (depicted as Pt_{pc} ME) recorded at different pH values (0, 1.0, and 2.0) of H₂-saturated or O₂-saturated HClO₄ solutions. For easier comparison, the currents obtained for the ORR measurements have been normalized to the limiting current density (j_{lim}). (C) The Pt_{pc} ME activities towards the HER expressed as the exchange current density, j_0 , and (D) the ORR activity expressed as the half-wave potential, $E_{1/2}$, in the HClO₄ solutions of various pH values as a function of the PME.

The effect of the electrolyte pH on electrode activity has been widely investigated.²⁵⁹⁻²⁶² For instance, Lamoureux *et al.* suggested that pH influences on the HER over Pt(111) could result from the change in proton donor using density functional theory (DFT) calculations.²⁶² Zheng *et al.* reported that the alteration of electrolyte pH could affect the hydrogen binding energy, leading to the change of the HER activity for various platinum-group metal catalysts.²⁶³ Thus, the hydrogen binding energy should be the dominant descriptor for the HER activity. However, the change in the properties of the EDL was not discussed for both hypotheses. Koper *et al.* have suggested that the pH dependence of the HER is due to the shift in the potential of zero free charge (PZFC, related to the PME), which results in a change in the interfacial structure and kinetics.¹¹⁷

The obtained results indicate that the PME has a significant influence on the electrode activity in our systems. Consequently, knowing the relations between the pH value, PME, and activity is essential to tune the catalytic performance. **Figure 4.4, C and D**, shows the correlations between the HER and ORR activities of the Pt_{pc} electrodes and the respective PME values. Both trends exhibit a linear relationship. Although some studies have already earlier described the pH influence on the electrocatalytic activity for various electrodes,^{70,71} introducing the PME as a key parameter to associate with activity is a novel approach, which can lead to a better understanding of the mechanism behind the effect of the electrolyte composition.

Similar experiments were done for Au_{pc} electrodes to investigate further the pH effect on the EDL properties at the electrode/electrolyte interface. The corresponding CV measurements are displayed in **Figure 4.5**. The typical anodic peaks between *approx.* 1.3–1.6 V_{RHE} and a sharp reduction peak at *approx.* 1.1 V_{RHE} are all visible. The observed CV features are consistent with those published in the literature.^{264,265} When comparing the peak areas of the oxidation and reduction processes on Au_{pc}, it seems they are promoted in the electrolyte containing a higher concentration of H⁺ ions. As in the case of Pt_{pc}, the shape of the CV did not change after the laser measurements.

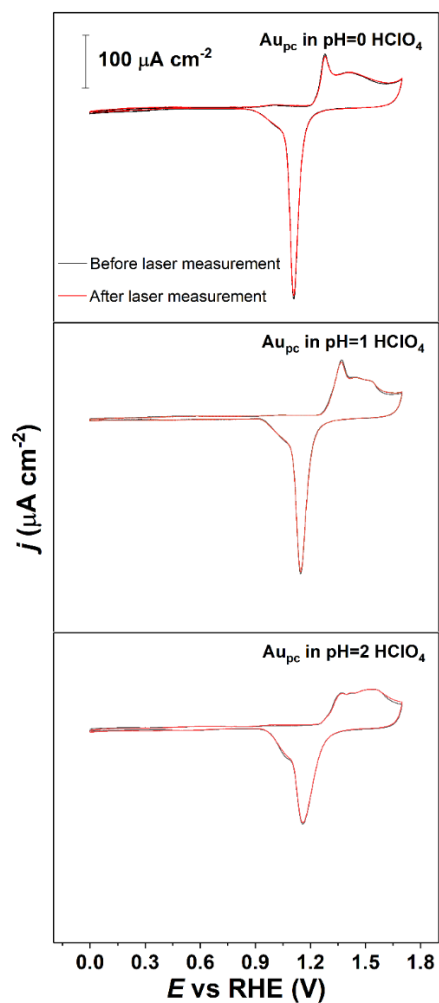


Figure 4.5. Typical cyclic voltammograms of Au_{pc} at different pH values (0, 1, and 2) of the $HClO_4$ solutions. Scan rate: 50 mV s^{-1} . Similar to the Pt_{pc} , the CVs before and after laser measurements are almost identical.

Sample current transients obtained for the Au_{pc} electrode are shown in **Figure 4.6**. The PME trends are analogous to the ones observed on the Pt electrode.

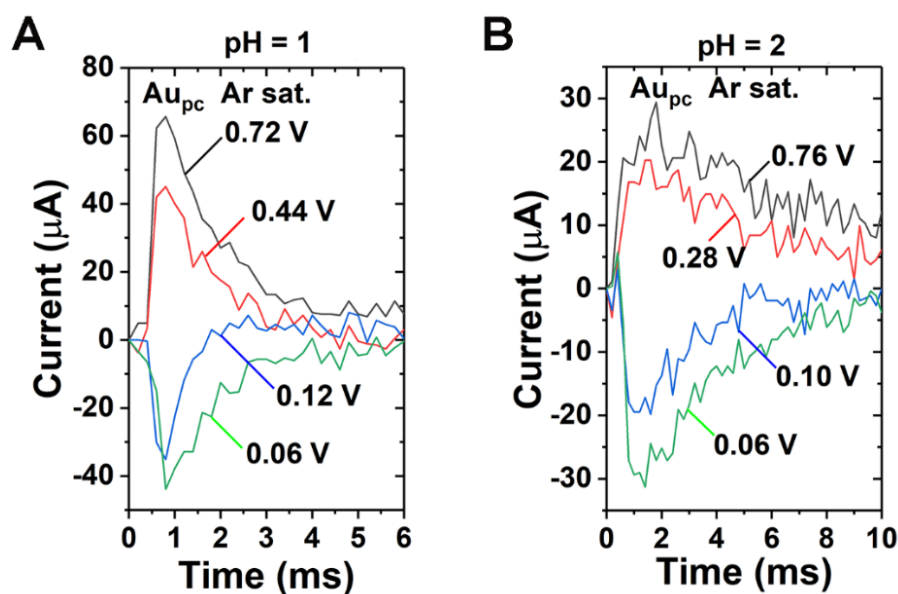


Figure 4.6. Sample LICTs recorded for Au_{pc} in Ar-saturated $HClO_4$ at (A) pH 1 and (B) pH 2. It should be mentioned that all initial current values of the obtained transient peaks have been normalized to zero for easier comparison. The PME can be found between the two potentials where the current transient changes its sign.

Specifically, as shown in **Figure 4.7, A to E**, the PME values of the Au_{pc} electrode are ~ 0.07 V, ~ 0.13 V, ~ 0.20 V, ~ 0.27 V, and ~ 0.32 V vs RHE at a pH of the $HClO_4$ electrolytes of 0, 0.5, 1.0, 1.5, and 2.0, respectively. The PME of the Au_{pc} electrode also shows a linear dependence on the pH value of the electrolyte (see **Figure 4.7F**). The collected results are comparable with the previous literature data.^{181,211,266} However, the PME does not shift by around 59 mV per pH unit on the RHE scale when the PME lies within the double layer potential region. This could be because the reconstruction of the gold surface influences the location of the PME.²¹¹

Like the Pt electrodes, the PME of Au_{pc} drifts away from the onset potential of the HER towards the potentials where the ORR takes place. An increase in pH makes the surface water layer at potentials close to the onset of the HER become stiffer. On the other hand, the order of the EDL decreases at the potentials close to the ORR onset. It can thus be

inferred that as the pH value rises, the activity of the Au electrode decreases towards the HER and increases towards the ORR.

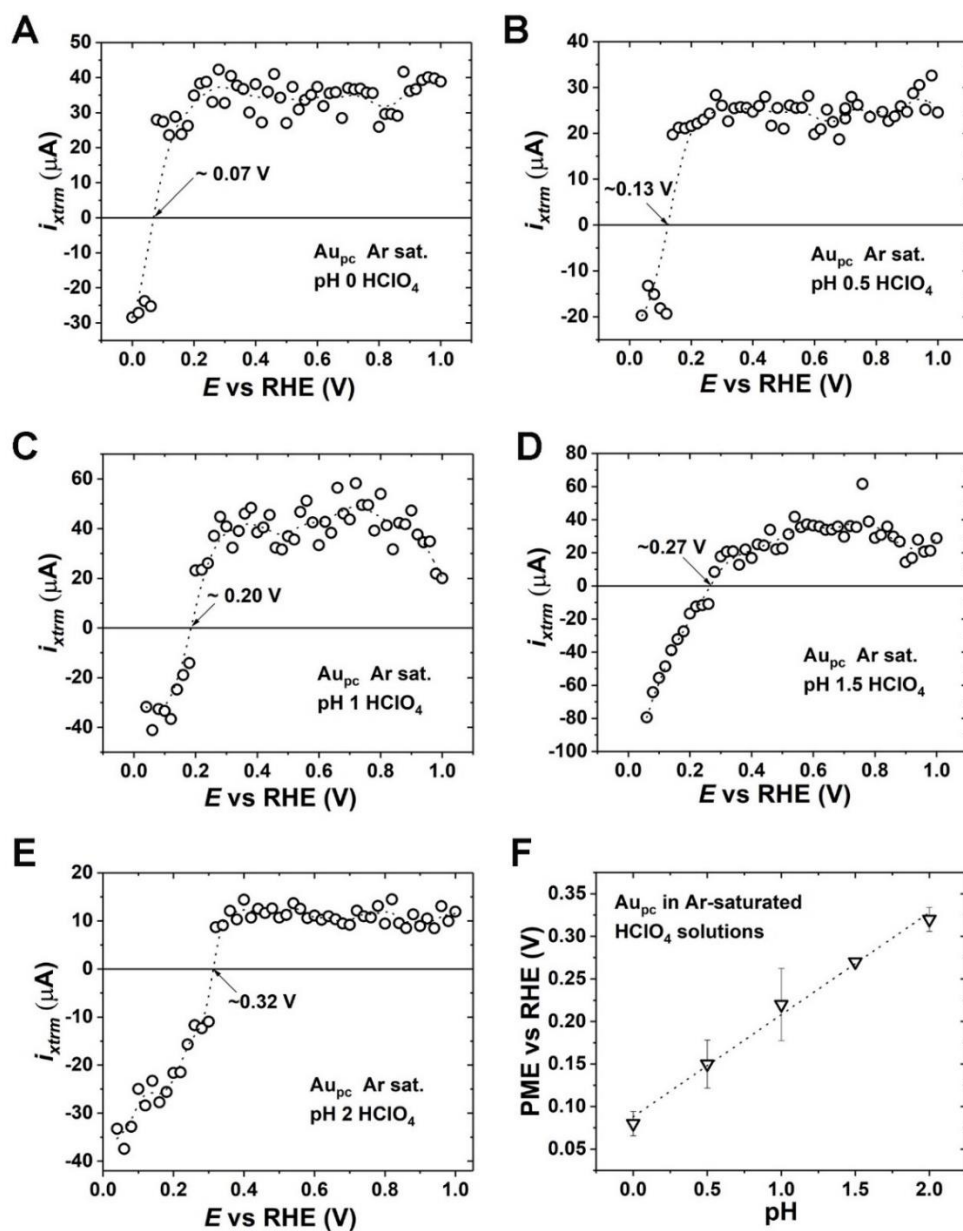


Figure 4.7. (A to E) Current extrema of the LICT results obtained for the Au_{pc} electrode at different pH values (0, 0.5, 1.0, 1.5, and 2.0) of Ar-saturated HClO₄ electrolytes. (F) The PME of Au_{pc} presented as a function of the electrolyte pH. Similar to Pt_{pc}, the PME of Au_{pc} shifts towards more positive values due to the pH rise.

In order to check these predictions, measurements of the Au_{pc} activity towards the HER and ORR were performed at several pH values (0, 1.0, and 2.0) of H_2 -saturated (HER) or O_2 -saturated (ORR) $HClO_4$ solutions (**Figure 4.8A and B**). As in the case of Pt_{pc} electrodes, the activity towards the HER increases at high H^+ concentrations of the electrolyte. In contrast, lower H^+ concentrations of the electrolyte lead to an enhancement of the activity towards the ORR. The HER activities (expressed as the exchange current density) of the Au_{pc} electrode show a linear relationship with the PME values (**Figure 4.8C**).

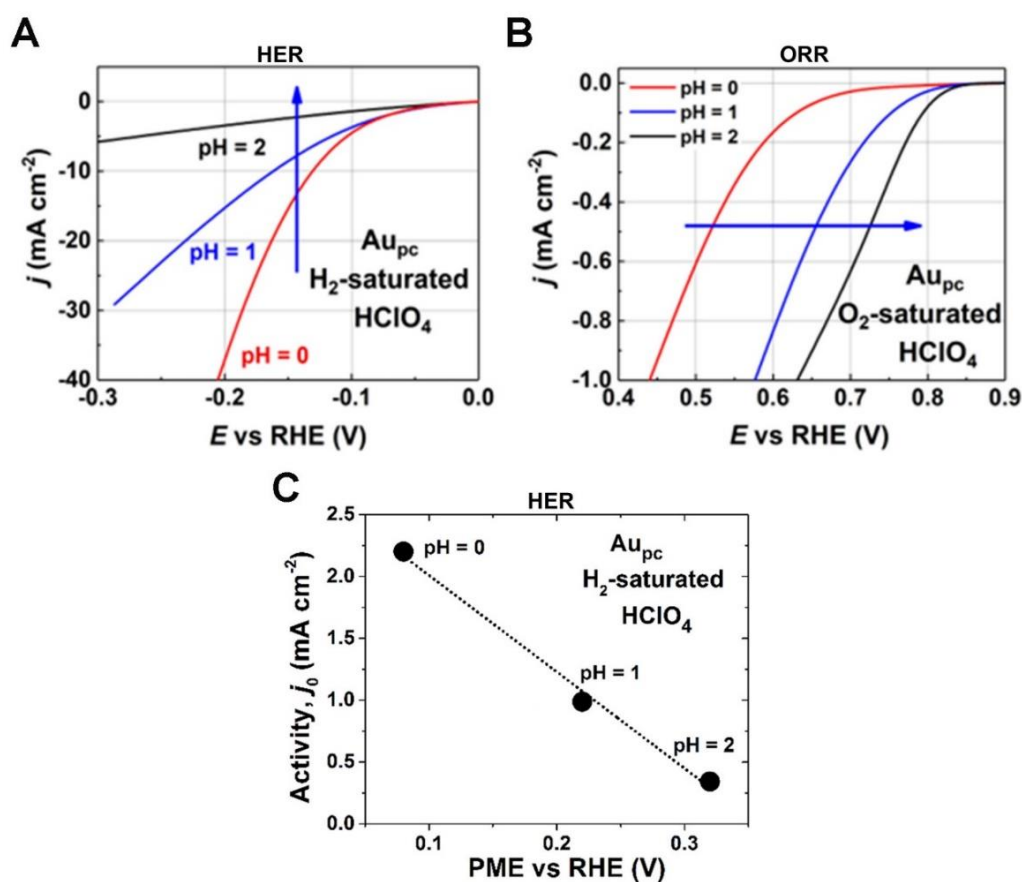


Figure 4.8. Typical (A) HER and (B) ORR polarization curves for Au_{pc} electrodes recorded at several pH values (0, 1.0, and 2.0) of H_2 -saturated or O_2 -saturated $HClO_4$ solutions. For a better visibility, only the region dominated by the four-electron ORR kinetics is shown in (B). (C) The HER activities of Au_{pc} , expressed as the exchange current density j_0 , as a function of the PME. Like in the case of Pt_{pc} , a linear trend is revealed between the PME and activity.

4.1.1.2 Oxygen Effect for Pt_{pc} and Au_{pc} Electrodes in HClO₄ Solutions

In the last section, we investigated how the pH affected the location of the PME for Pt_{pc} and Au_{pc} electrodes in Ar-saturated HClO₄ solutions at various pH values. This was related to the electrocatalytic activities (towards the HER and ORR) of the corresponding systems. In order to better understand the effect of the pH on the location of the PME, similar LICT measurements for Pt_{pc} and Au_{pc} electrodes in the O₂-saturated HClO₄ electrolytes of the various pH values were conducted.

The typical current transients for Pt_{pc} in O₂-saturated HClO₄ solutions were collected after the laser pulse (**Figure 4.9**). The acquired curves are superpositions of responses from different processes.

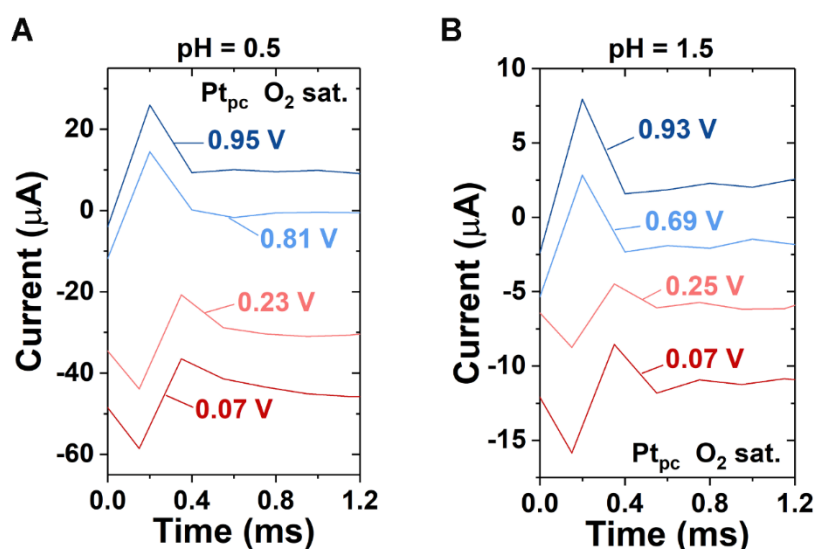


Figure 4.9. Sample LICTs recorded for Pt_{pc} in O₂-saturated HClO₄ solutions at (A) pH 0.5 and (B) pH 1.5.

The potentials at which the current transients change their sign for Pt_{pc} in the O₂-saturated HClO₄ solutions are ~0.35 V, ~0.40 V, ~0.45 V, ~0.53 V, and ~0.57 V vs RHE for pH values of 0, 0.5, 1, 1.5, and 2, respectively (**Figure 4.10, A to E**).

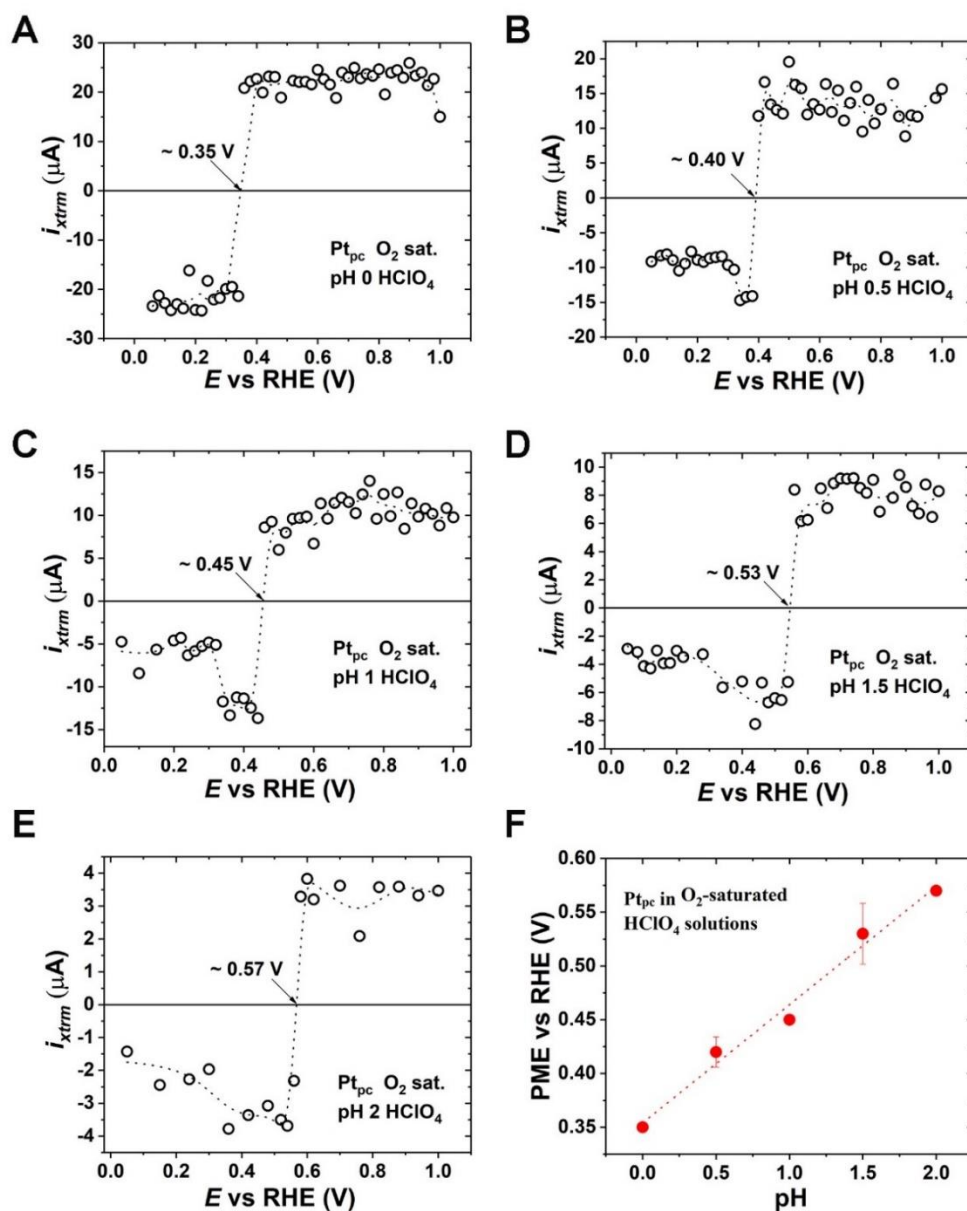


Figure 4.10. (A to E) Determination of the PME for Pt_{pc} at different pH values (0, 0.5, 1.0, 1.5, and 2.0) of O₂-saturated HClO₄ solutions. (F) The dependence of the PME values of Pt_{pc} depicted as a function of the pH. An increase in the pH results in an increase in the PME, similar to the Ar-saturated solutions.

As for Pt_{pc} in Ar-saturated HClO₄ solutions, the PME shifts towards more positive potentials as a result of a pH increase in the case of the O₂-saturated solutions.

Figures 4.10F and 4.11 indicate that the relationship between PME and pH value is rather linear.

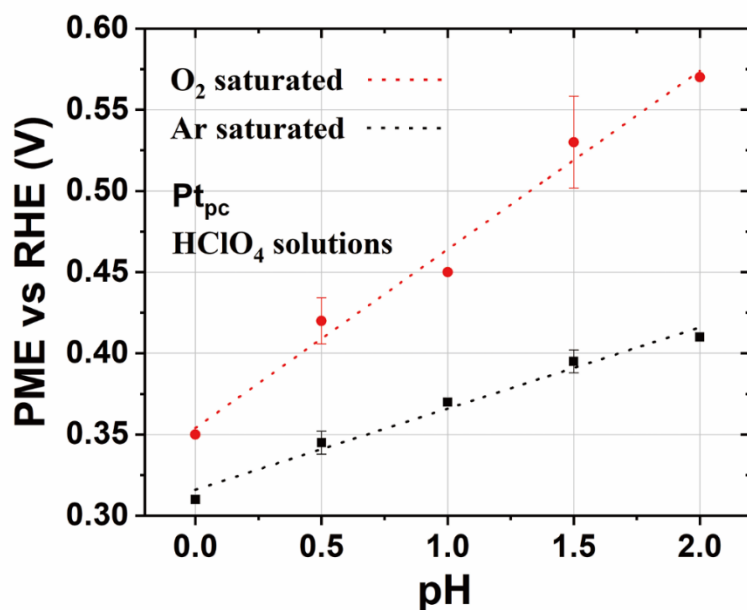


Figure 4.11. Comparison of the PME values collected for Pt_{pc} electrodes at the different pH values (0, 0.5, 1.0, 1.5, and 2.0) of both Ar-saturated (black), and O_2 -saturated (red) $HClO_4$ solutions.

However, the PME values measured in O_2 -saturated $HClO_4$ solutions are more positive than the values measured in Ar-saturated solutions for all the pH values investigated (**Figure 4.11**). For the case of O_2 -saturated solutions, it can be inferred that the protons can be consumed by reducing O_2 during the LICT measurements; this leads to a local change of pH at the interface between the electrode and electrolyte. The PME can thus be moved to a more positive potential for the same pH value when O_2 is involved.

A similar trend was observed for Au_{pc} electrodes for the different pH values of O_2 -saturated $HClO_4$ electrolytes. The sample current transients obtained for Au_{pc} are presented in **Figure 4.12**.

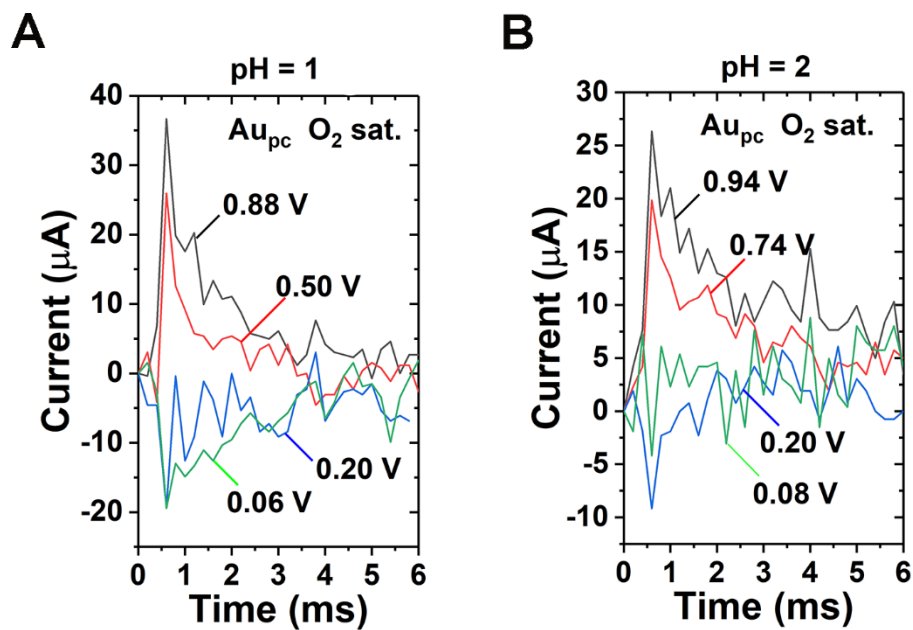


Figure 4.12. Sample LICTs recorded for Au_{pc} in O_2 -saturated $HClO_4$ solutions at (A) pH 1 and (B) pH 2. All initial current values of the obtained transient peaks have been normalized to zero for easier comparison.

The sign of the current transient flips at ~ 0.15 V, ~ 0.20 V, ~ 0.24 V, ~ 0.29 V, and ~ 0.35 V vs RHE for pH values of 0, 0.5, 1, 1.5, and 2, respectively (**Figure 4.13, A to E**). The PME values also increase linearly as a result of the increase in pH (**Figure 4.13 F**).

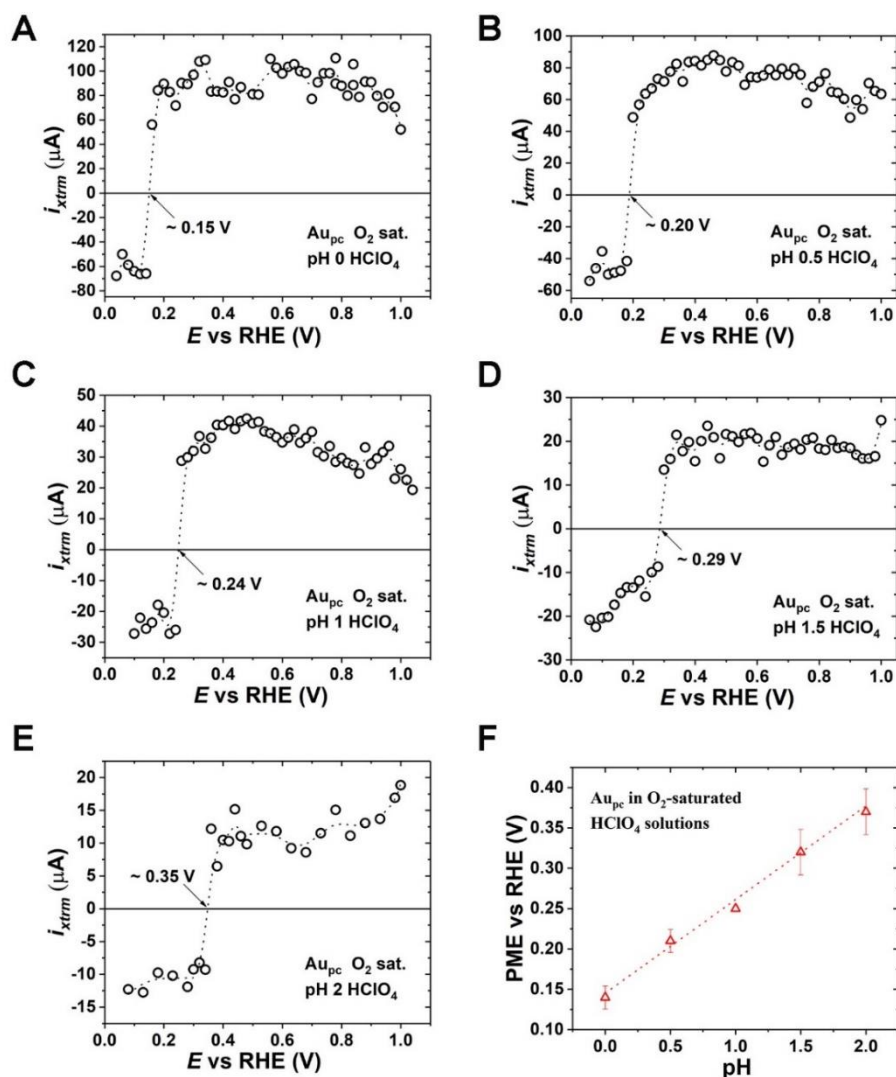


Figure 4.13. (A to E) Current extrema of the LICs obtained for Au_{pc} at different pH values (0, 0.5, 1.0, 1.5, and 2.0) for the O₂-saturated HClO₄ electrolytes. (F) The PME of Au_{pc} shifts towards more positive values as a consequence of the local pH rise at the electrode surface in the O₂-saturated HClO₄ solutions.

Although an analogous trend with Pt_{pc} was observed (i.e., the PME values for Au_{pc} measured in O₂-saturated HClO₄ solutions are more positive than the values measured in Ar-saturated solutions), O₂ can influence the location of the PME much more on Pt_{pc} than Au_{pc} when comparing **Figures 4.11** and **4.14**. Specifically, the PME values for Pt_{pc} and Au_{pc} in Ar-saturated and O₂-saturated HClO₄ solutions at pH 0 are very close to

each other (around 0.04 V difference). However, when changing the pH of the electrolyte to 2.0, the difference of the PME values for Pt_{pc} in the Ar-saturated and O₂-saturated HClO₄ solutions reaches 0.16 V. This difference could be due to the effect of oxygen on the state of the surface of platinum electrodes, which can influence the properties of the EDL.²⁶⁷⁻²⁶⁹

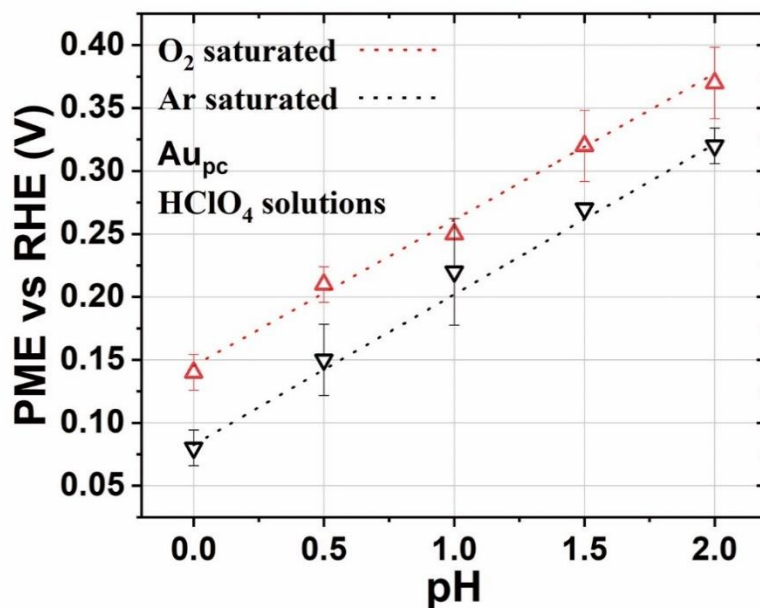


Figure 4.14. The values of the PME plotted versus pH values for Au_{pc} electrodes at the different pH values (0, 0.5, 1.0, 1.5, and 2.0) of (black) Ar-saturated and (red) O₂-saturated HClO₄ solutions.

In summary, in this section, Pt_{pc} and Au_{pc} electrodes were characterized using LICT at different pH values in Ar-saturated and O₂-saturated HClO₄ solutions. We demonstrate that the PME is dependent on the electrolyte pH value. For both electrodes, the PME increases linearly with the increase in pH. The HER and ORR activities for Pt_{pc} and Au_{pc} electrodes also show a strong relationship with the PME. Higher H⁺ concentrations of electrolytes lead to the enhancement of both electrode activities towards the HER, while lower H⁺ concentrations lead to the enhancement of activity towards the ORR. This confirms our expectation that the closer the PME is to the thermodynamic

equilibrium potential of a certain reaction, the faster this reaction should be. In addition, purging oxygen can shift the locations of the PME for both Pt_{pc} and Au_{pc} electrodes in HClO₄ solutions at different pH values. This could be a consequence of the local protons at the interface between electrode and electrolyte being consumed by reducing O₂ during the LICT measurements, thereby leading to a change of local pH. This ultimately changes the location of the PME. That means the EDL properties at the interface can be different for the same electrolyte composition with different dissolved gases. All results presented in this section indicate that the role of the electrolyte pH is essential in electrocatalytic systems.

4.1.2 Cation Effect

4.1.2.1 pH Effect in the Presence of Alkali Metal Cations

We demonstrated in the last section that the pH effect of the PME on the electrocatalytic activity was drastic. However, the pH influence can be quite different for various electrolyte compositions.²⁵⁶ Generally, electrocatalytic properties can be influenced by both H⁺ and other ions in the electrolyte.^{43,55,270} The effect of alkali metal cations has lately started to gain much attention.^{270,271} For instance, in a recent report, we demonstrated the influence of the alkali metal cations on the EDL capacitance of several single crystal electrodes.^{272,273} However, the effect of alkali metal cations on electrocatalytic processes is not fully understood yet. A series of LICT measurements for the Au_{pc} and Pt_{pc} electrodes were performed to investigate further the effect of pH and electrolyte ions on the interfacial processes. These were conducted at various pHs (2, 4, 6, 8, and 10) in Ar-saturated and O₂-saturated 0.5 M Na₂SO₄ and K₂SO₄ electrolytes. It is worth noting that since the hydration energies of the Na⁺ (406 kJ mol⁻¹) and K⁺ (322 kJ mol⁻¹) cations are much closer to that of the ClO₄⁻ (229 kJ mol⁻¹) anions, the SO₄²⁻ anions with higher hydration energy (1059 kJ mol⁻¹) were selected here to

avoid competition for the influence of other species in the electrolyte. Therefore, the changes in the interfacial properties would only correlate to the alterations in the H^+ concentration and the nature of the alkali metal cations in the investigated systems.

Firstly, CVs of Au_{pc} were recorded in Ar-saturated 0.5 M Na_2SO_4 and K_2SO_4 solutions at different pHs to check the surface quality of the electrode, as shown in **Figure 4.15**. At pH 2, CVs of Au_{pc} in both Na^+ - and K^+ -containing electrolytes are comparable with the results measured in 0.1 M H_2SO_4 solution (see **Figure 3.3B**). The usual three typical anodic peaks between *ca.* 1.3–1.6 V and a sharp reduction peak at *ca.* 1.1 V can be observed. When increasing the pH of electrolytes, both the oxidation and reduction processes on the Au_{pc} surface were influenced in both Na_2SO_4 and K_2SO_4 solutions. Particularly, when the electrolyte pH reaches 6, two broad reduction peaks are observed for Na^+ -containing electrolytes, and three reduction peaks in the presence of K^+ can be seen within the investigated potential range. This could be because the local protons at the interface have a low concentration in a nearly neutral pH electrolyte. Therefore, the generated and consumed protons during the oxidation and reduction processes on the Au_{pc} surface can easily change the local pH. For instance, during the O_2 reduction process, the protons at the interface can be immediately consumed in a nearly neutral pH electrolyte. This could lead to a lower reduction potential of Au oxide.^{164,274,275}

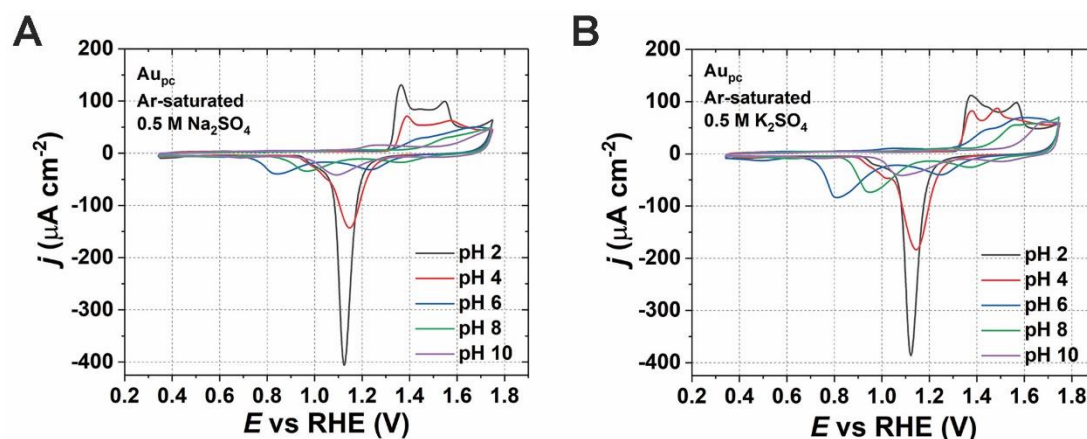


Figure 4.15. Typical cyclic voltammograms of Au_{pc} at various pHs (2, 4, 6, 8, and 10) in 0.5 M Ar-saturated Na_2SO_4 (A) and K_2SO_4 (B) solutions. Scan rate: $50 mV s^{-1}$.

The influence of alkali metal cations on the Au_{pc} electrode processes can be further observed at the same pH, such as at 6, as presented in **Figure 4.16**. One can see that K^+ cations promote the oxidation of Au, which is observed from the increased peak areas when compared to Na^+ .

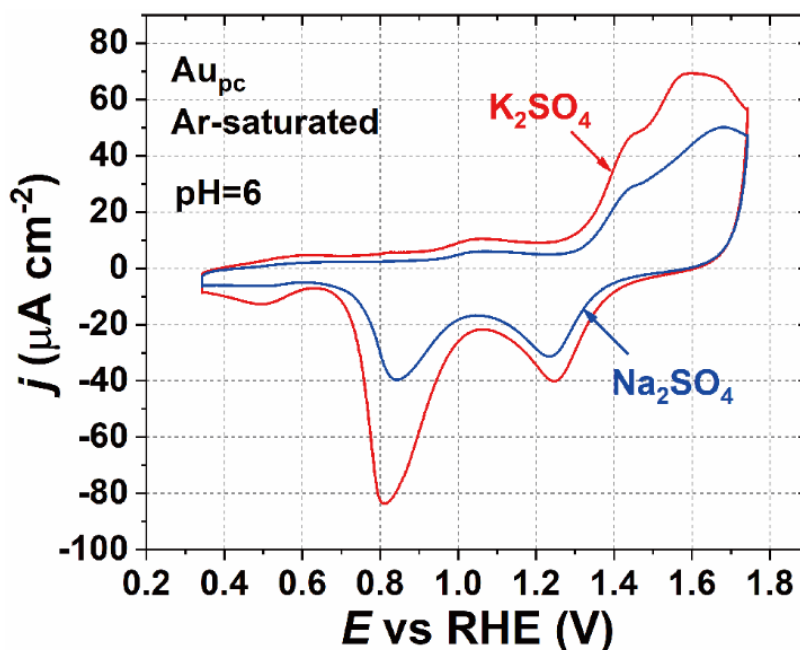


Figure 4.16. Cyclic voltammograms of Au_{pc} in 0.5 M Ar-saturated Na_2SO_4 (blue) and K_2SO_4 (red) electrolytes at pH 6. Scan rate: $50\ mV\ s^{-1}$.

In addition, CV measurements at different scan rates were conducted in 0.5 M K_2SO_4 solution. The results are shown in **Figure 4.17**. One can see that all the oxidation and reduction peaks increase with an increase in the scan rate quasi-linearly. Therefore, the observed oxidation and reduction processes are likely dominated by the adsorbed species at the electrode surface.

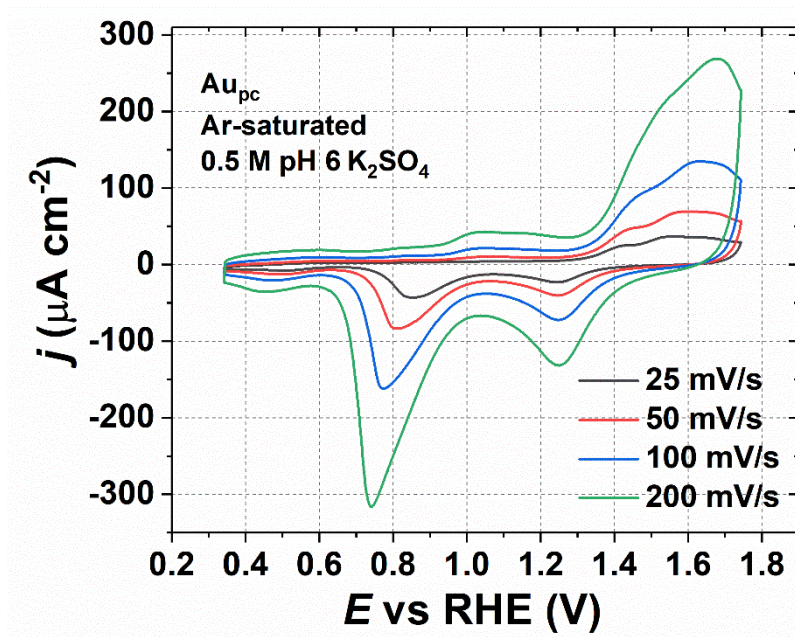


Figure 4.17. Cyclic voltammograms of Au_{pc} in 0.5 M Ar-saturated K_2SO_4 electrolytes at different scan rates.

To further study the influence of pH and cations, LICT measurements were conducted to identify the PME. The LICT experiments were performed in both Ar-saturated and O_2 -saturated solutions (**Figure 4.18, A and B**). The relaxation peaks were observed in both Ar-saturated and O_2 -saturated 0.5 M Na_2SO_4 solutions. To identify the location of the PME clearly, the extreme values of the current transients were plotted *versus* the working electrode potential (see **Figure 4.18C and D**). The PME values for Au_{pc} were assessed to be ~ 0.19 V and ~ 0.35 V vs RHE in the Ar-saturated and O_2 -saturated 0.5 M Na_2SO_4 solutions (pH 2), respectively.

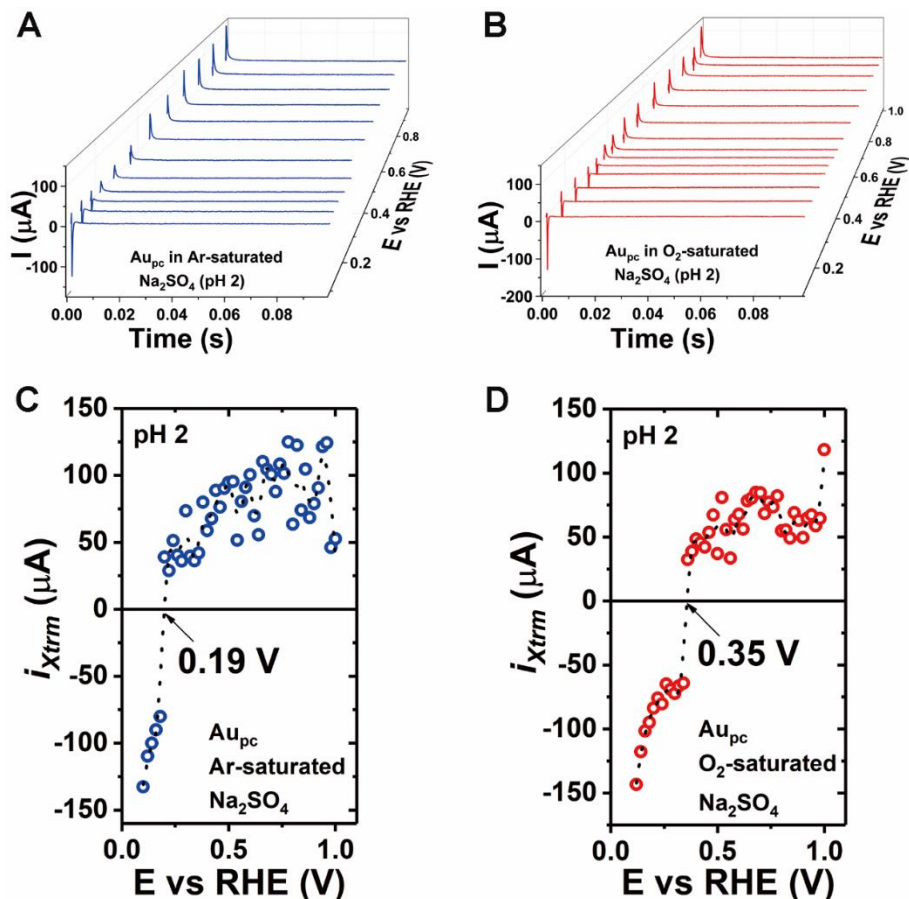


Figure 4.18. 3D plots of the LICT results obtained for Au_{pc} at pH 2 in (A) Ar-saturated and (B) O_2 -saturated 0.5 M Na_2SO_4 electrolytes, respectively. (C and D) The corresponding 2D LICT plots of the collected current extrema presented as a function of the working electrode potential.

Interestingly, the PME values become more positive if the pH increases in both cases of Ar-saturated and O_2 -saturated 0.5 M Na_2SO_4 solutions. **Figure 4.19, A to D**, shows that the collected PME values for Au_{pc} in the Ar-saturated 0.5 M Na_2SO_4 solutions are ~ 0.25 V, ~ 0.34 V, ~ 0.58 V, and ~ 0.88 V vs RHE for pHs 4, 6, 8, and 10, respectively. While in the case of O_2 -saturated 0.5 M Na_2SO_4 electrolytes (see **Figure 4.19E to H**), the PME values for Au_{pc} move towards ~ 0.39 V, ~ 0.46 V, ~ 0.66 V, and ~ 0.98 V vs RHE for pHs 4, 6, 8, and 10, respectively.

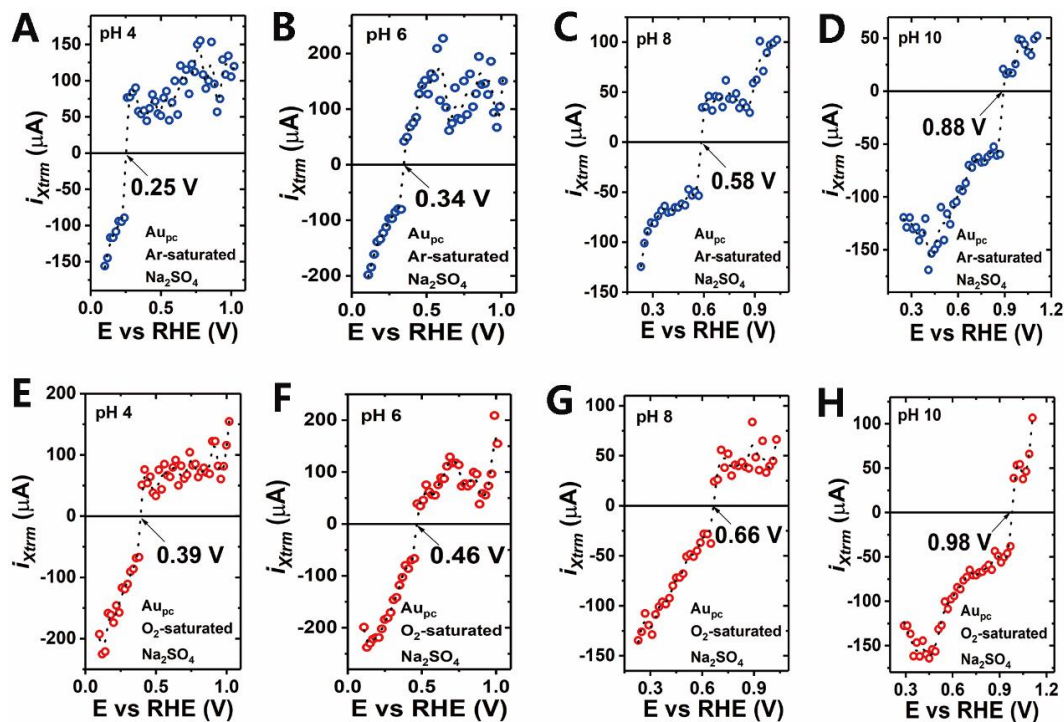


Figure 4.19. (A to D) Extreme current values of the laser-induced transients for Au_{pc} immersed into Ar-saturated 0.5 M Na_2SO_4 solutions of different pHs (4, 6, 8, and 10). (E to H) The similar extreme current values collected for Au_{pc} immersed into the O_2 -saturated 0.5 M Na_2SO_4 solutions.

It should be mentioned that the pH dependence of the PME here involves the influence of adsorption processes on the free charge distribution at the interface.^{179,254} The PME is supposed to be independent of the pH of electrolyte on the SHE scale when the PME is located within the potential range without adsorption influence.²⁵³ However, the PME is dependent on the electrolyte pH when the PME lies at the potentials where adsorption processes affect the free charge.²⁵⁴

As presented in **Figure 4.20**, the PME values shift towards more positive potentials due to the pH increase for Au_{pc} in both Ar-saturated and O_2 -saturated 0.5 M Na_2SO_4 solutions. But one can notice that the PME values measured in O_2 -saturated Na_2SO_4 solutions are more positive than the values measured in Ar-saturated cases for all the

investigated pH ranges. Similar to the Au_{pc} in $HClO_4$ solutions at different pHs (see Section 4.1.1.2), one can infer that this is because local protons at the electrode interface can be consumed by the reducing O_2 during the LICT experiments, which causes a change of the local pH and consequently shifts the location of the PME. This makes it possible to estimate the local pH at the interface by determining the PME. Interestingly, the PME can be drastically moved for Au_{pc} in both Ar-saturated, and O_2 -saturated 0.5 M Na_2SO_4 solutions, when changing the pH from 6 to higher values. And afterwards, the PME became more sensitive to the pH modification. However, the influence of O_2 on the PME of Au_{pc} became smaller with the pH increase when comparing the difference of the PME values in the Ar-saturated and O_2 -saturated 0.5 M Na_2SO_4 solutions at pH 2 (0.16 V) and pH 10 (0.10 V).

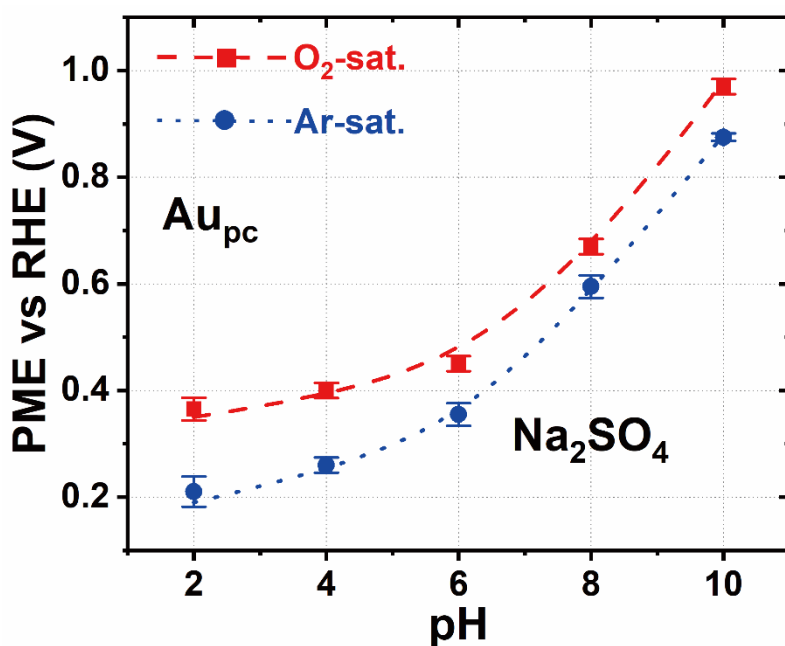


Figure 4.20. The values of the PME for Au_{pc} in Ar-saturated (blue) and O_2 -saturated (red) 0.5 M Na_2SO_4 solutions plotted as a function of the electrolyte pH.

Similar measurements for Au_{pc} electrodes at various pHs (2, 4, 6, 8, and 10) in Ar-saturated and O_2 -saturated 0.5 M K_2SO_4 solutions were conducted to investigate the

role of the alkali metal cation for the Au electrode. As shown in **Figure 4.21A to E**, the potentials at which the current transients change their sign for Au_{pc} in the Ar-saturated 0.5 M K₂SO₄ solutions are ~0.13 V, ~0.27 V, ~1.26 V, ~1.30 V, and ~1.43 V vs RHE for pHs 2, 4, 6, 8, and 10, respectively. While in the case of O₂-saturated 0.5 M K₂SO₄ electrolytes (see **Figure 4.21F to J**), the PME values for Au_{pc} are shifted towards ~0.27 V, ~0.37 V, ~1.40 V, ~1.38 V, and ~1.49 V vs RHE for pHs, 2, 4, 6, 8, and 10, respectively.

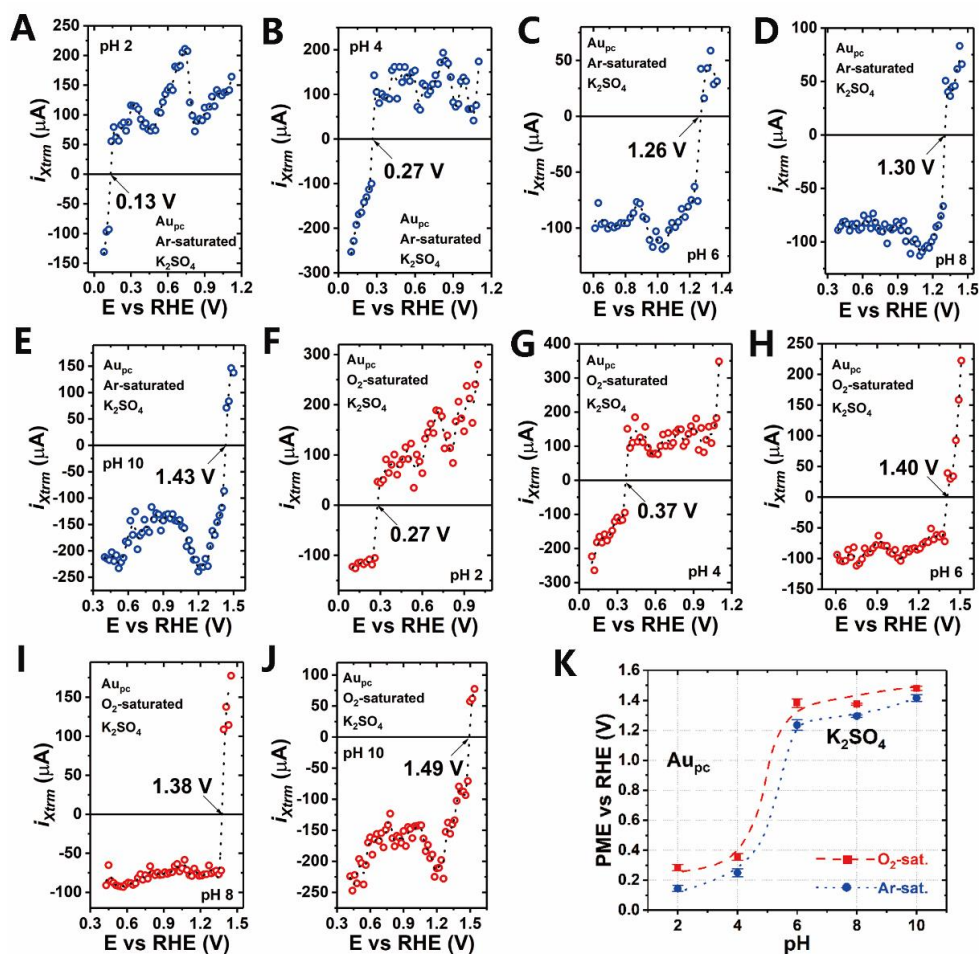


Figure 4.21. (A to E) Extreme values of laser-induced current transients obtained for Au_{pc} immersed into the Ar-saturated 0.5 M K₂SO₄ solutions of different pHs (2, 4, 6, 8, and 10). (F to J) The similar extreme current values collected for Au_{pc} immersed into the O₂-saturated 0.5 M K₂SO₄ solutions of the corresponding pH values. (K) The values of the PME plotted versus pH values for Au_{pc} in Ar-saturated (blue) and O₂-saturated (red) 0.5 M K₂SO₄ solutions.

As for Au_{pc} in the 0.5 M Na_2SO_4 solutions, pH increase and the involvement of oxygen can both move the PME values to more positive potentials. The only exception is the case for the Au_{pc} electrode in the O_2 -saturated 0.5 M K_2SO_4 electrolytes from pH 6 to 8. Note, the PME value was hugely shifted from pH 4 to 6 for Au_{pc} in both Ar-saturated and O_2 -saturated 0.5 M K_2SO_4 solutions, as presented in **Figure 4.21K**. This means that a slight change of pH within this pH region can alter the EDL structure significantly. One possible reason is that the presented specific adsorption, such as $*OH$ (* representing the adsorbed species) and sulfate adsorption, results in phase transition and interfacial water rearrangements in the double layer²⁷⁶ and finally moves the location of the PME. However, the outcome differed from the case of Au_{pc} in the Na_2SO_4 . The PME did not show higher sensitivity to the pH change for higher pH ($pH > 6$), even with a sudden PME change happening from pH 4 to pH 6. Besides, similar to the case of Au_{pc} in the 0.5 M Na_2SO_4 electrolytes, the influence of O_2 on the PME of Au_{pc} became smaller with the pH increase (except in the case of pH 6) when comparing the difference of the PME values for Au_{pc} in the Ar-saturated and O_2 -saturated 0.5 M K_2SO_4 solutions at pH 2 (0.14 V) and pH 10 (0.06 V).

Surprisingly, although the PME values for Au_{pc} in Ar-saturated 0.5 M K_2SO_4 solutions at pHs 6, 8, and 10 are more positive than the thermodynamic equilibrium potential of the ORR (1.23 V vs RHE), introducing oxygen further shifts the PME to more positive potentials. Thus, one can expect that the water structure at the interface between the electrode and electrolyte cannot only be influenced by dissolved O_2 but also by H^+ , OH^- , and SO_4^{2-} ions adsorbed on the electrode surface.

Additionally, the location of the PME shows higher sensitivity to the pH in the presence of K^+ than Na^+ on Au_{pc} , when comparing the effect of these two cations on Au_{pc} electrodes, as presented in **Figure 4.22**. Besides, when the pH of the electrolyte reaches 6 or higher, the difference of the PME value for the systems containing these two cations becomes large (around 0.92 V). In this regard, Na_2SO_4 and K_2SO_4 cannot be considered

as equal supporting electrolytes. The EDL properties in the presence of these two cations are significantly different at the same pH. Combining the CVs in **Figures 4.15** and **4.16**, it can be inferred that a strong phase transition takes place at the electrode surface in the case of a K_2SO_4 solution.

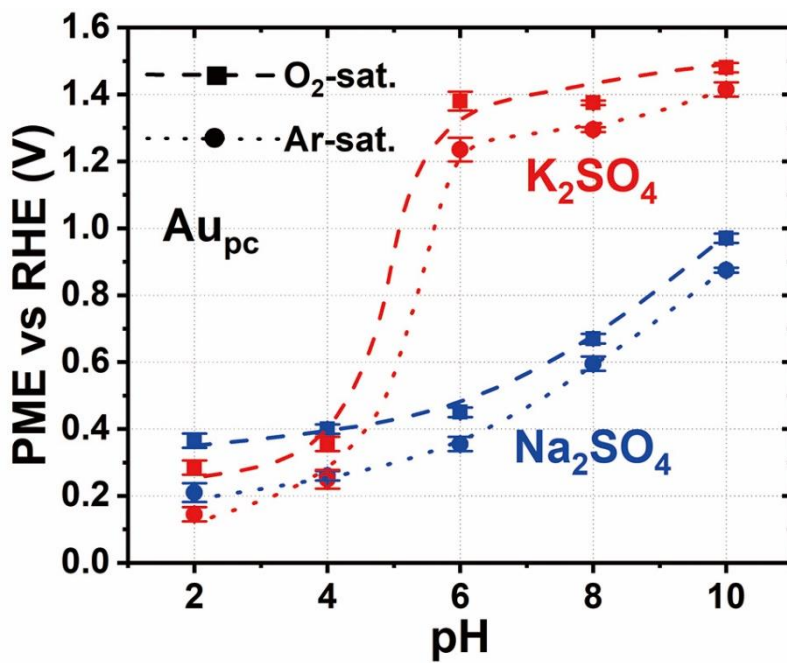


Figure 4.22. The values of the PME for Au_{pc} in Ar-saturated (dot) and O_2 -saturated (dash) 0.5 M Na_2SO_4 (blue) and K_2SO_4 (red) solutions depicted as a function of the electrolyte pH.

The laser experiments were conducted in a mixed solution (60 mL 0.5 M Na_2SO_4 and 60 mL 0.5 M K_2SO_4) at pH 8 to support the statement further, as shown in **Figure 4.23**. The PMEs are 0.96 V and 1.08 V vs RHE for Au_{pc} in the Ar-saturated and O_2 -saturated mixed solutions, respectively. The values of the PME for Au_{pc} in this mixed solution are located between the PMEs of Au_{pc} in Na_2SO_4 and K_2SO_4 solutions at the same pH value.

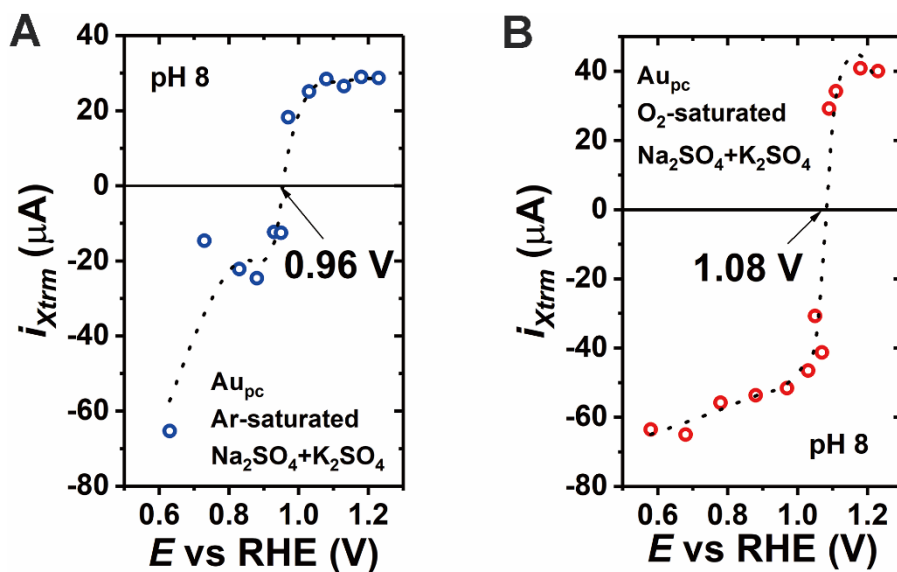


Figure 4.23. Determination of the PME of Au_{pc} in (A) Ar-saturated and (B) O_2 -saturated mixed solution of 60 mL 0.5 M Na_2SO_4 and 60 mL 0.5 M K_2SO_4 at pH 8.

To further understand the influence of the cations on the system behavior at various pHs, similar experiments for Pt_{pc} were performed in Ar-saturated and O_2 -saturated 0.5 M Na_2SO_4 and 0.5 M K_2SO_4 solutions at different pHs. As for Au_{pc} , one can observe a similar increase in the PME due to the pH rise in both Ar-saturated and O_2 -saturated 0.5 M Na_2SO_4 solutions (see **Figure A1** in **Appendix**). As shown in **Figure A1**, **A** to **D**, the estimated potential values at which the sign of the current transient changes are located at ~ 0.09 V, ~ 0.11 V, ~ 0.18 V, and ~ 0.82 V vs RHE for pHs 2, 4, 6, and 8, respectively. Note that the location of the PME can be drastically shifted when the pH value of 0.5 M Na_2SO_4 changes from 6 to 8. Quite surprisingly, all the observed current transients stayed negative within the investigated potential regimes for Pt_{pc} in Ar-saturated 0.5 M Na_2SO_4 solutions at pH 10 (see **Figure A1E**). Thus, the PME might be located at a more positive potential than the thermodynamic equilibrium potential of the OER. However, the applied potential range cannot be further extended to a more positive potential to avoid oxygen gas generation.

When argon gas is changed to oxygen to saturate the electrolytes, the PME values for

Pt_{pc} significantly move to more positive potentials. As depicted in **Figure A1F to H**, the sign of the current transients flips at ~ 0.67 V, ~ 0.79 V, and ~ 0.94 V *vs* RHE for pHs, 2, 4, and 6, respectively. But when increasing the pH of the electrolyte to 8 and 10, all the obtained current spikes stayed negative within the studied potential range (see **Figure A1I and J**). The PME might be located at the more positive potentials where the OER is supposed to happen.

The locations of the PME of Pt_{pc} were remarkably shifted to more positive potentials when the electrolyte pH changed from 6 to 8, as presented in **Figure A1K**. Especially in the case of Pt_{pc} in O₂-saturated 0.5 M Na₂SO₄ electrolytes, the PME moved beyond the examined potential regions when the pH of the electrolyte changed from 6 to 8.

Interestingly, Pt_{pc} immersed in the 0.5 M K₂SO₄ electrolytes do not portray the PME values within the entire examined potential regime for most of the investigated systems. As presented in **Figure A2**, for Pt_{pc} in Ar-saturated 0.5 M K₂SO₄ electrolytes at pH 2, the charge of the electrode surface stayed positive and did not change its sign with the potential change. The location of the PME might be more negative than the thermodynamic equilibrium potential of the HER (0.00 V *vs* RHE). However, the investigated potential cannot be extended to more negative potentials to avoid the generation of H₂. In the case of Pt_{pc} in Ar-saturated 0.5 M K₂SO₄ electrolytes, the PME values can only be found at pH 4 (0.09 V *vs* RHE) and pH 6 (0.22 V *vs* RHE), as shown in **Figure A2B and C**. When increasing the electrolyte pH to 8 and 10, the observed current transients for Pt_{pc} stayed negative within the whole investigated potential ranges (see **Figure A2D and E**).

Although the PME was not found for Pt_{pc} in Ar-saturated 0.5 M K₂SO₄ electrolytes at pH 2, while changing from Ar- to O₂-saturated solutions, the PME appeared at ~ 0.11 V *vs* RHE (see **Figure A2F**). For Pt_{pc} in O₂-saturated 0.5 M K₂SO₄ electrolytes at pH 4, the location of the PME was drastically shifted to ~ 0.89 V *vs* RHE compared to the Ar-saturated solutions, as depicted in **Figure A2G**. However, the charge of the electrode

surface stayed negative when Pt_{pc} was immersed into O_2 -saturated 0.5 M K_2SO_4 electrolytes at pHs, 6, 8, and 10, as shown in **Figure A2H to J**. Again, the PME for Pt_{pc} in these pHs of K_2SO_4 solutions might be located at more positive potentials where the OER takes place. As presented in **Figure A2K**, the location of the PME for Pt_{pc} showed a substantial sensitivity to O_2 and pH in the presence of K^+ .

When comparing the influence of Na^+ to K^+ cations on the electrode/electrolyte interface, one can notice that the interface order can be easily changed even with small adjustments in the concentration of the H^+ in the presence of the K^+ than Na^+ cations for both Ar- and O_2 - saturated cases, as shown in **Figure A3**. However, the situation for Pt is much more complicated than in the case of Au under the same conditions. Pt has a lower oxidation potential and a narrower double layer range. Besides this, the laser measurements were also conducted within the potential region of underpotential deposition, making it more difficult to correlate the PME with the EDL structure on the pristine Pt surface.

4.1.2.2 Influence of Cations on the Electrode Activity

To further investigate the influence of alkali metal cations on the electrode activity, the near-to-neutral pH (pH 6) electrolytes were selected. This ensures the avoidance of the strong influence from H^+ or OH^- ions on the PME and electrocatalytic performance.^{146,256,277,278} In this section, LICT and the HER and ORR activity measurements of Pt_{pc} electrode were performed in 0.5 M $(\text{AM})_2\text{SO}_4$ ($\text{AM} = \text{Li}^+, \text{Na}^+, \text{K}^+$ and Cs^+) electrolytes at pH 6.

Figure 4.24, A and B, shows that the measurements of Pt_{pc} activity towards the HER and ORR were conducted in 0.5 M $(\text{AM})_2\text{SO}_4$ ($\text{AM} = \text{Li}^+, \text{Na}^+, \text{K}^+$, and Cs^+) solutions saturated with either H_2 (for the HER) or O_2 (for the ORR) at pH 6. We observed notably improved activity towards the HER in the presence of the Li^+ while introducing Cs^+ ions enhanced the activity towards the ORR. The trends obtained for both the HER and

ORR coincide with previous scientific reports regarding the activity influence on Pt electrodes from alkali metal cations.^{56,279}

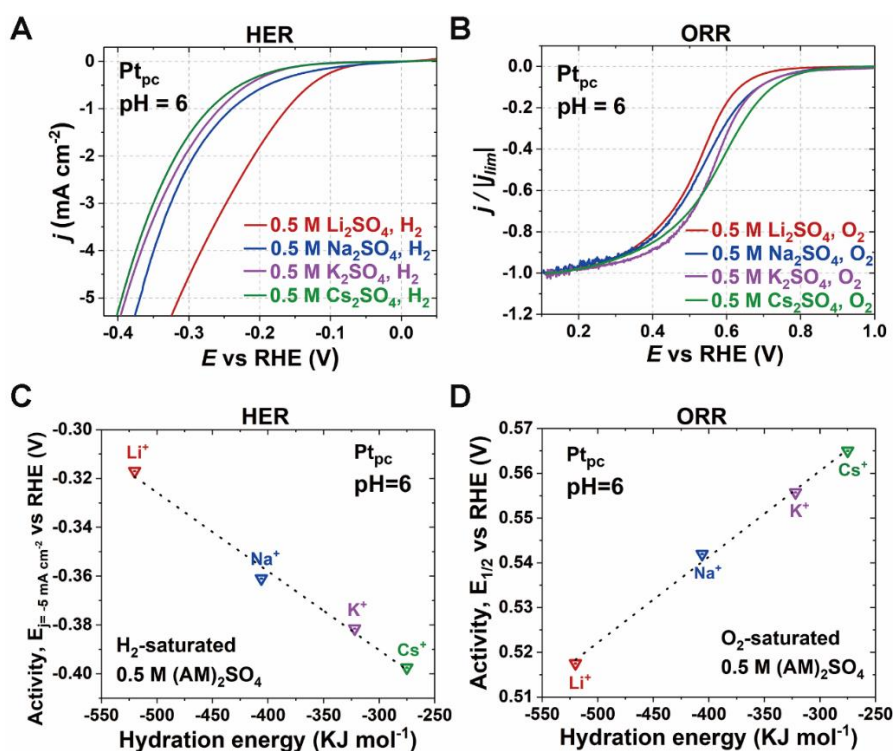


Figure 4.24. Polarization curves for (A) the HER and (B) the ORR on Pt_{pc} in H_2 - and O_2 -saturated 0.5 M $(AM)_2SO_4$ ($AM = Li^+, Na^+, K^+, \text{ and } Cs^+$) solutions, respectively. (C) The Pt_{pc} activities towards the hydrogen evolution expressed as the potential (vs RHE) required for a current density of -5 mA cm^{-2} and (D) the oxygen reduction activity expressed as the half-wave potentials versus the hydration energy of the related alkali metal cations. Both cases reveal a linear relationship with opposing trends.

To clarify the relationship between the activities and the nature of the alkali metal cations, the potentials (vs RHE) at a current density of -5 mA cm^{-2} for the HER and half-wave potentials ($E_{1/2}$) for the ORR were measured. Subsequently, we plotted the potentials at a current density of -5 mA cm^{-2} and half-wave potentials *versus* the alkali metal cation hydration energies (see **Figure 4.24C** and **D**). Remarkably, we find a clear linear trend in each case. In the case of the HER at Pt_{pc} , the potential at a current density

of -5 mA cm^{-2} rises with the PME moving away from the thermodynamic equilibrium potential of the HER. The half-wave potential ($E_{1/2}$) increases with the PME for the ORR activities. The presented results strongly suggest that there should be a particular dependence between the nature of the alkali metal cation and the activity of Pt_{pc} .

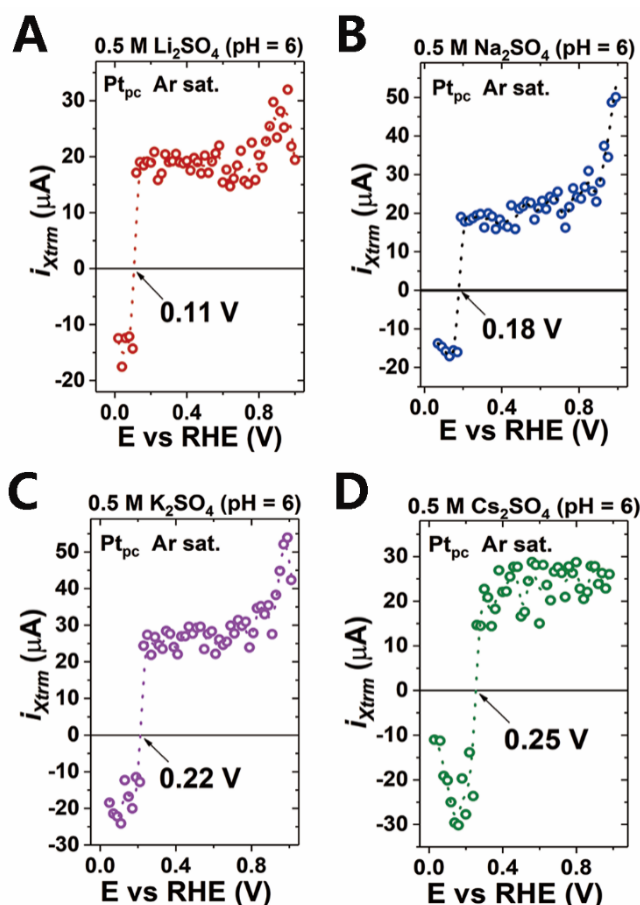


Figure 4.25. (A to D) The values of i_{Xtrm} plotted as a function of the applied potential (going from high to low potentials) in $0.5 \text{ M } (AM)_2\text{SO}_4$ ($AM = \text{Li}^+, \text{Na}^+, \text{K}^+, \text{and } \text{Cs}^+$) electrolytes (Ar-saturated) at pH 6. One can find the PME values at the point where the current transient changes its sign, i.e., $i_{Xtrm} = 0$.

As previously elaborated, we believe that the degree of order in the EDL influences the electrocatalytic activity. In other words, the stiffness of the water structure at the interface can be the main factor to decide how easily the EDL rearranges itself after the

electron transfer. The orientation of the interfacial water is strongly dependent on the interfacial electric field.²¹³ To elucidate more precisely how the electrolyte composition controls the electrocatalytic activity, we employed LICT measurements and determined the PME of the interfacial water layer. The corresponding current transients of each system are shown in **Figure 4.25**. The obtained PME values are ~ 0.11 V, ~ 0.18 V, ~ 0.22 V, and ~ 0.25 V *vs* RHE for the systems containing Li^+ , Na^+ , K^+ , and Cs^+ , respectively. It is evident that the PME values get shifted towards positive potentials with decreasing the hydration energy of the alkali metal cations.

Interestingly, plotting the obtained PME values against the hydration energy of the alkali metal cation reveals a linear relationship (**Figure 4.26A**). This confirms that the nature of the alkali metal cations can strongly influence the EDL and alter the potential drop within its structure. Similarly, the potential at a current density of -5 mA cm^{-2} and the half-wave potentials also exhibit a linear trend with the PME values (**Figure 4.26B and C**). The obtained results demonstrate that the HER and ORR activities of Pt have a strong relationship with the degree of order of the EDL. Thus, the PME can give a qualitative and quantitative explanation of the influence of the alkali metal cations on electrocatalytic reactions for Pt. Specifically, as the PME value was shifted from the vicinity of the thermodynamic equilibrium potential of the HER (0.00 V vs RHE) towards the corresponding potential value of the ORR (1.23 V vs RHE) along with the decreasing cation hydration energies, the degree of order of the EDL is supposed to become more rigid at the potentials close to the thermodynamic equilibrium potential of the HER but variably loose at that for the ORR. In other words, the charge or mass transfer barrier which must be overcome becomes higher for the HER but lower for the ORR. Thus, one can expect that the loss in the interfacial order for higher hydration energies at potentials close to the onset potential of the HER results in an increase of the HER activity. In contrast, lower hydration energies lead to a decreased interfacial order at the potentials remote from the potential of the HER, which in turn enhances the activity towards the ORR. The presented results strongly suggest that the

interactions between cation and water molecule affect the EDL structure at the interface and result in a different degree of order at the same potential. Consequently, the nature of cations can control the PME location and then tune the electrocatalytic activities.

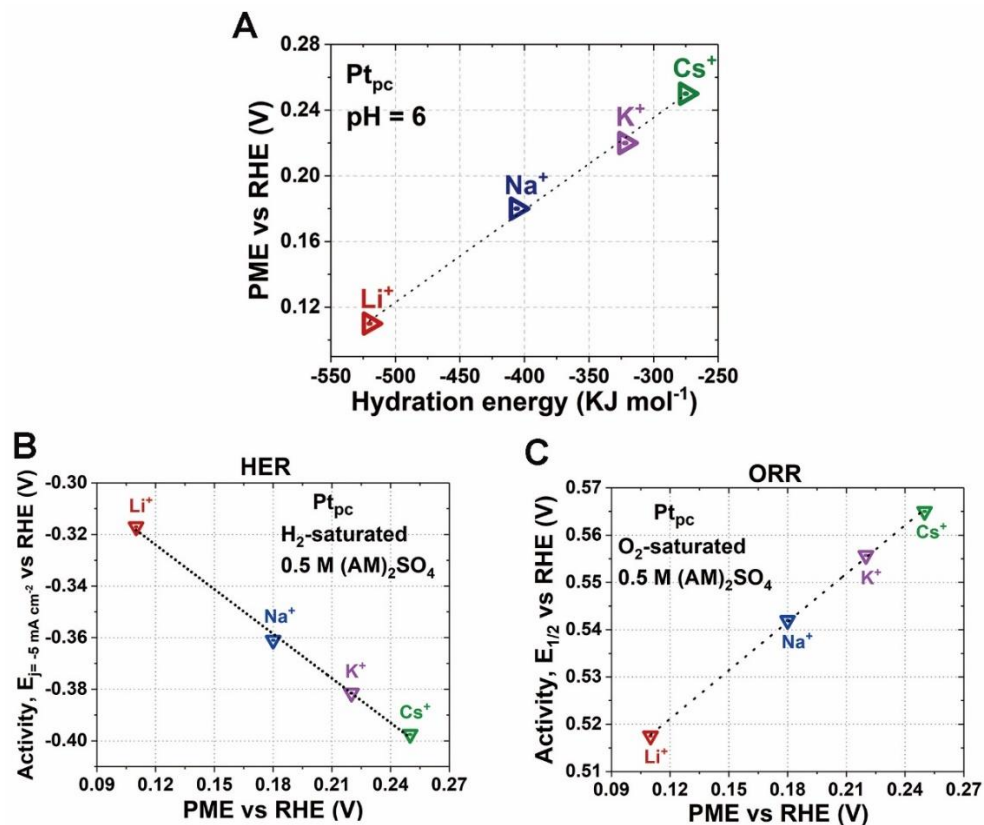


Figure 4.26. (A) The values of the PME plotted versus the hydration energies of the corresponding alkali metal cations. (B) The potential required for a current density of -5 mA cm^{-2} and (C) the half-wave potentials of Pt_{pc} versus the PME values in the case of the related alkali metal cations. In each case, we identify a linear relationship between the parameters. These results suggest that the HER gets enhanced by alkali metal cations with higher hydration energies, whereas for the ORR, we find the opposite trend.

Note, when comparing the ORR activity trends of Pt_{pc} in HClO₄ at different pHs (0, 1, and 2) and in 0.5 M (AM)₂SO₄ (AM = Li⁺, Na⁺, K⁺, Cs⁺) solutions at pH 6, both trends show a similar slope (see **Figure 4.24D** and **Figure 4.27**).

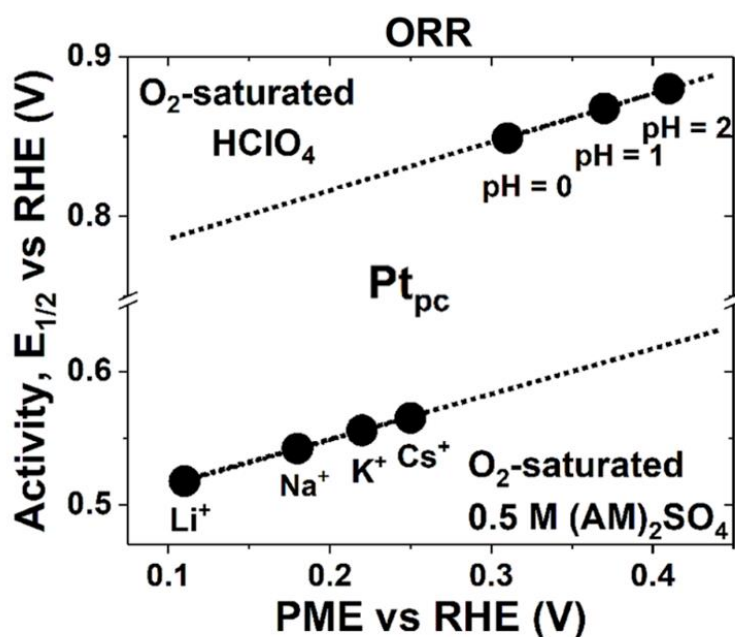


Figure 4.27. The $E_{1/2}$ vs PME dependencies obtained for Pt_{pc} , in $HClO_4$ solutions at different pHs (0, 1, and 2) and 0.5 M $(AM)_2SO_4$ ($AM = Li^+, Na^+, K^+, Cs^+$) at pH 6.

As presented in **Sections 4.1.1.1** and **4.1.2.2**, the investigated electrocatalytic activities (HER and ORR) for Pt_{pc} and Au_{pc} are highly related to the electrochemical interface order. One can predict the electrocatalytic activity with the PME change, which results from the influence of electrolyte species (concentration and their nature). As the observed relationship between the electrocatalytic activity and the PME shows a linear behavior in all investigated systems, the influence of the electrolyte can be described quantitatively. The degree of order of the interface between the electrode and electrolyte can be associated with the polarizability of the electrolyte, which can be quantified by the relative dielectric constant, ϵ_r .^{244,280} This physical parameter depends on the concentration of the ions as well as their nature. Within a certain concentration range ($C < 2$ M), this fundamental characteristic becomes a linear function of the nature and concentration of ions present in the solution²⁸⁰, as depicted by the following equation:

$$\epsilon_r = \epsilon_{pure\ H_2O} - \alpha(C_{ion}) \quad (4.1)$$

where $\varepsilon_{\text{pure } H_2O}$ is the dielectric constant of pure water ($\varepsilon_{\text{pure } H_2O} \sim 82$ at room temperature), α is the proportionality coefficient describing the relative ion contribution, and C_{ion} is the ion concentration. Remarkably, as shown in **Figures 4.3F** and **4.7F**, as well as in previous scientific reports^{179,253} performed within a narrow concentration range, a linear relationship is observed for the value of the PME. Thus, by analogy to **Equation 4.1**, the following expression is valid:

$$E_{\text{PME}} = E_{\text{PME}}^{\text{at } \varepsilon = \varepsilon_{\text{pure } H_2O}} \pm \beta C_{\text{ion}} \quad (4.2)$$

where E_{PME} is the mentioned PME value, while $E_{\text{PME}}^{\text{at } \varepsilon = \varepsilon_{\text{pure } H_2O}}$ stands for the corresponding value acquired for the system containing pure water, and the function β describes the relative contribution of the ion concentration.

As mentioned above, the observed relationship between the electrocatalytic activity and the PME value shows a linear trajectory in all our investigated systems. Therefore, by rearranging **Equation 4.1** in terms of C_{ion} , combining it with **Equation 4.2**, and taking the electrode activity in pure water, A_{H_2O} , as the reference, one can express the electrode activity, A , as follows:

$$A \propto A_{H_2O} \pm \check{\varphi} [\varepsilon_{\text{pure } H_2O} - \varepsilon_r^{\text{electrolyte}}] \quad (4.3)$$

where $\check{\varphi}$ is the proportionality coefficient dependent on the nature of the reaction.

In **Sections 4.1.1** and **4.1.2**, we systematically studied the influence of the electrolyte composition on the interfacial process. The presented results and analysis qualitatively and quantitatively explain a strong influence of the electrolyte composition on the performance of electrocatalytic systems. Associating the PME with the corresponding changes in the electrocatalytic reactions can “simply” reflect how the interface structure can control the related electrocatalytic processes. Therefore, the determination of the PME can be a powerful method to understand better the electrochemical processes happening at the electrode/electrolyte interface.

In summary, the obtained results indicate that the nature of alkali metal cations strongly influences the EDL properties. Increasing the electrolyte pH in the presence of Na^+ and K^+ can shift the PME to more positive potentials for Au and Pt electrodes. However, the PME shows a higher sensitivity to the pH in the presence of K^+ than Na^+ . Especially for Au_{pc} in 0.5 M Na_2SO_4 and K_2SO_4 solutions at pH 6, the difference of the PME for these two electrolytes is around 0.92 V, which means the EDL structure is vastly different for Au in the solution containing Na^+ and K^+ ions. In this case, Na_2SO_4 and K_2SO_4 cannot be regarded as electrolytes of the same strength under the same conditions. As for the case in HClO_4 solutions, oxygen can move the PME to more positive potentials in the presence of Na^+ and K^+ .

Interestingly, although the PME values for Au_{pc} in Ar-saturated 0.5 M K_2SO_4 solutions of pHs 6, 8, and 10 are more positive than the thermodynamic equilibrium potential of the ORR, introducing oxygen can still shift the PME to more positive potentials. When fixing the pH at 6, the PME obtained for Pt_{pc} in the electrolytes containing alkali metal cations shows a linear trend with the HER and ORR activities. Besides, the PME also exhibits a linear relationship with the hydration energies of the corresponding alkali metal cations. All presented results demonstrate that the nature of cation significantly influences the electrode processes. Therefore, determining the PME is considered a powerful approach to optimize electrochemical devices via the electrolyte composition.

4.1.3 Anion Effect

Inspired by the results on the pH and cation effect on the electrode processes, we further examined the influence of anions in this section. Five different anions (NO_3^- , ClO_4^- , Cl^- , Ac^- , and SO_4^{2-}) were chosen here. As presented in **Figure A4**, the HER activity measurements for Pt_{pc} in H_2 -saturated 0.5 M NaX ($X = \text{ClO}_4^-$, Cl^- , and SO_4^{2-}) solutions at pH 6 were performed. Note, NaAc and NaNO_3 were excluded for the HER activity measurement because of the reduction potential of Ac^- and NO_3^- located within the

explored potential regimes.^{281,282} One can find that Pt_{pc} exhibits different HER activities in various solutions in which Pt_{pc} possesses the highest activity in the presence of ClO₄⁻, followed by Cl⁻ and SO₄²⁻ in decreasing order of the HER activity. The potentials (*vs* RHE) at a current density of -5 mA cm⁻² for the HER are *ca.* -0.236 V, -0.365 V, and -0.37 V for the systems containing ClO₄⁻, Cl⁻, and SO₄²⁻, respectively.

Furthermore, the ORR activity measurements for Pt_{pc} in O₂-saturated 0.5 M NaX (X = NO₃⁻, ClO₄⁻, Cl⁻, Ac⁻, and SO₄²⁻) solutions at pH 6 were conducted, as shown in **Figure A4B**. Half-wave potentials ($E_{1/2}$) for the ORR were collected to compare the anion influence. Specifically, $E_{1/2}$ (*vs* RHE) for the ORR are ~0.708 V, ~0.697 V, ~0.58 V, ~0.549 V, and ~0.54 V for the systems containing NO₃⁻, Ac⁻, ClO₄⁻, Cl⁻, and SO₄²⁻ respectively. One can see that Pt_{pc} shows the highest activity towards the ORR in the presence of NO₃⁻, followed by Ac⁻, ClO₄⁻, Cl⁻, and SO₄²⁻ in decreasing order of the ORR activity.

Obviously, Pt_{pc} in both NaCl and Na₂SO₄ solutions exhibits lower HER and ORR activities since strongly adsorbed Cl⁻ and SO₄²⁻ can affect either the intermediates or the sites at the metallic electrode.²⁸³⁻²⁸⁷ For instance, for Pt in sulfuric acid, a (di)sulfate layer can be formed on the Pt surface, which can move the adsorption of reactants from the electrolyte to higher potentials.²⁸⁴ While for the investigation of the Pt in the electrolyte containing Cl⁻, the ORR properties influenced by adsorbed Cl⁻ can be explained as a superposition of the individual ORR properties of the Pt(111) / Cl_{ad} and Pt(100) / Cl_{ad} interface between solid and liquid with respect to both the kinetic limitations and the formation of H₂O₂.²⁸⁶ It is believed that ClO₄⁻ does not adsorb on the Pt electrode surface and does not interact with the reactants.¹⁷⁶ However, one-to-one interaction between perchlorate ions and adsorbed hydroxide was discovered, and this can reduce the ORR activity for the Pt electrode in the presence of ClO₄⁻.²⁸⁸ Although Pt shows the best activity towards the ORR in NaNO₃ solution, the influence is supposed to be from the catalytic effect of the NO₂⁻ anions, which comes from the

reduction of NO_3^- anions.²⁸⁹ For the case of NaAc, Kaspar *et al.* confirmed that both COOH and COO^- species can enhance the ORR performance.²⁹⁰ They believe that the reversible adsorption of competitive adsorbates can stabilize the initial and final states of the catalytic cycle, thereby improving the catalytic performance of the electrode. The results presented in **Figure A4B** reveal that Pt_{pc} has better activity towards the ORR in the presence of Ac^- , which is vastly close to the one in the presence of NO_3^- anions when comparing the half-wave potentials ($E_{1/2}$) for the ORR for Pt_{pc} in these two electrolytes.

The PME measurements were further performed for Pt_{pc} in Ar-saturated 0.5 M NaX ($X = \text{NO}_3^-$, ClO_4^- , Cl^- , Ac^- , and SO_4^{2-}) solutions (pH 6). The goal was to elucidate the relationship between the activity performance and the interfacial order of the EDL. As shown in **Figures 4.21B, A5A, and B**, the obtained PME values were ~ 0.18 V, ~ 0.15 V, and ~ 0.07 V vs RHE for the systems containing SO_4^{2-} , ClO_4^- , and NO_3^- , respectively. One can note that there is no clear link between the PME with either the HER or ORR activities. Moreover, Pt_{pc} in both NaAc and NaCl electrolytes portrays three PMEs (**Figure A5C and D**). This is surprising since a system has probably only one PZC²⁹¹ that is related to the PME. The existence of three PMEs is believed to be consistent with the theory about the mass and charge influence from the interfacial water structure.²⁰⁵ However, these findings make it much more difficult to explain the anion effect on the activity. Besides, unlike the case in the cation effect study, the hydration energy of the investigated anions, such as Cl^- (-381 KJ mol^{-1}), NO_3^- (-314 KJ mol^{-1}), and Ac^- (-300 KJ mol^{-1}), is very close to the used cation, Na^+ (-406 KJ mol^{-1}). It is inevitable for the obtained results to be affected by the competition of the cations in the electrolyte.

4.2 The Investigation of the Electrochemical Interface Properties at Cu(111) in Alkaline Solutions

Owing to its unique ability to catalyze the electrochemical conversion of CO₂ and CO into valuable fuels and chemicals, copper (Cu) is widely utilized in different applications.²⁹²⁻²⁹⁶ For instance, the selectivity of CO₂ and CO reduction was studied on polycrystalline Cu in the alkali metal cation containing electrolyte.²⁹⁷ More interestingly, different steps of Cu single crystal yield different products for the same reduction reaction, which can be tuned to achieve improved selectivity.²⁹⁸⁻³⁰⁰ Although many methods are applied in the investigation of the effect of electrochemical conditions on the interfacial structure of Cu/liquid, it is still insufficient to understand the interfacial processes.^{44,301,302} Especially, it has been noticed that the declining performance of Cu can be hugely influenced by electrolyte compositions (pH, cations, anions), which is supposed to be related to the structure of the Cu/liquid interface.³⁰³⁻³⁰⁵ Therefore, understanding the electrochemical Cu/liquid interface is required for the optimization of the studied systems.

In this section, the LICT technique and electrochemical scanning tunneling microscopy (EC-STM) were utilized to investigate the Cu(111)/liquid interface properties and dynamics. Specifically, the PME measurements for Cu(111) in 0.1 M NaClO₄ solutions of different pHs (10, 11, 12, and 13) were conducted. The pH influence on the solid/solution interface was investigated. *In-situ* EC-STM experiments were further performed to correlate the PME with the restructuring of the Cu(111) electrode surface. Our results reveal the true charge distribution and its relationship with the atomic structure of the Cu electrochemical interface, especially the structural dynamics at the PME. Besides, the pH dependence of the PME for Cu(111) in alkaline electrolytes was established.

Initially, CV measurements were conducted to check the electrode surface quality at

various pH values (13, 12, 11, and 10), as is depicted in **Figure 4.28**. All voltammetric profiles show the characteristic peak pair related to the adsorption and desorption of OH-species. Taking pH 13 as an example, the studied potential range is between $-0.9 V_{SHE}$ and $-0.35 V_{SHE}$. The observed peak pair at $\sim -0.65 V_{SHE}$ ($0.12 V_{RHE}$) corresponds to the adsorption and desorption of OH^- ions from the alkaline solutions, which is in accordance with previous studies.^{306,307} It should be mentioned that compared to consistent CVs of single crystal Au and Pt, the voltammetric response of Cu(111) in the alkaline solution can exhibit a small difference to the literature result from the influence of surface pre-treatment, applied potential range³⁰⁸, and used glassware.³⁰⁶ But combining the CV measurement conducted in 0.1 M NaOH solution at the same pH value (see **Figure A6**), the obtained voltammetric profile (**Figure 4.28**) does not display any additional feature for Cu(111) in the alkaline solution containing ClO_4^- , which demonstrates that no specific adsorption of ClO_4^- takes place. Besides, for different pH values, the OH-adsorption peak exhibits ideal Nernstian characteristics with a shift of around 59 mV per pH unit.

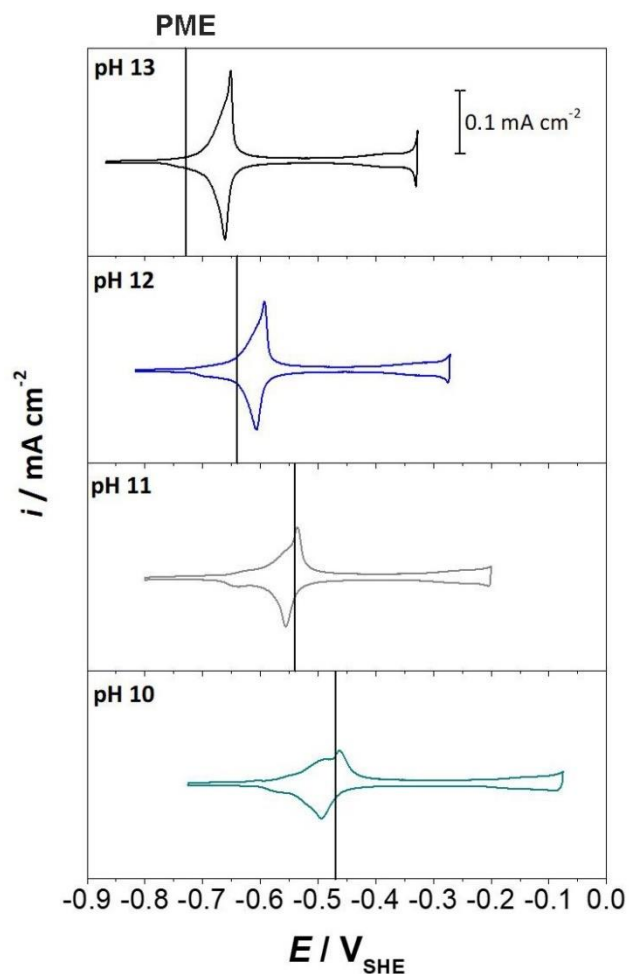


Figure 4.28. Cyclic voltammograms of Cu(111) in 0.1 M NaClO₄ solutions of different pHs (13, 12, 11, and 10). Scan rate: 50 mV s⁻¹. The observed peak pairs correspond to the adsorption and desorption of OH⁻ ions from the alkaline solutions.

As shown in **Figure 4.29**, the LICT measurements were performed for Cu(111) in NaClO₄ solutions of different pHs (13, 12, 11, and 10). All obtained current transients show a rather monotonic decay after the laser heating. This implies that the main contribution to the responses is interfacial water reorganization since bipolar or nonmonotonous current transients would demonstrate that an overlap of different processes with different relaxation rates exist.

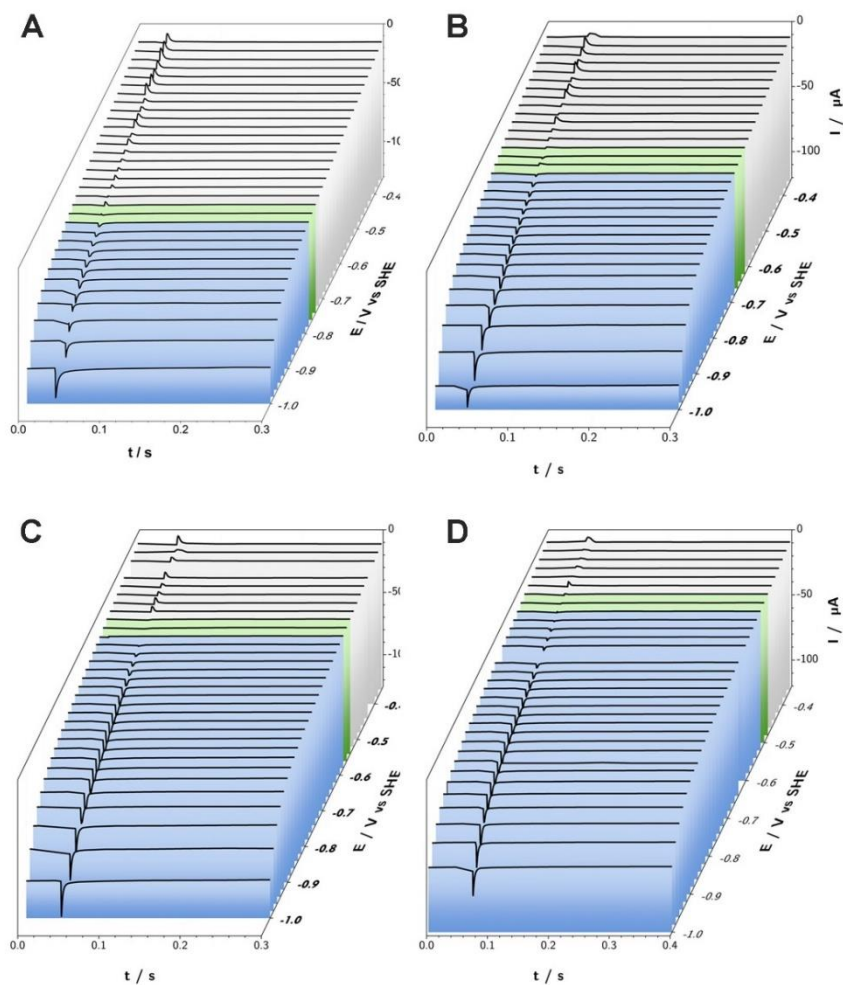


Figure 4.29. 3D plots of the LICT results obtained for Cu(111) in NaClO_4 solution at (A) pH 13, (B) pH 12, (C) pH 11, and (D) pH 10, respectively. The blue color range corresponds to the negative current transients, green to the alteration of current transient sign (i.e., the PME), grey to positive current transients.

To show the PME locations clearly, the corresponding extreme values of the current transients were plotted *versus* the working electrode potential, as shown in **Figure A7**. In addition, one can calculate the charge densities q from the integration of the current transients. Then, the plot of the charge densities against the electrode potential can be used to identify the PME, as shown in **Figure 4.30**.

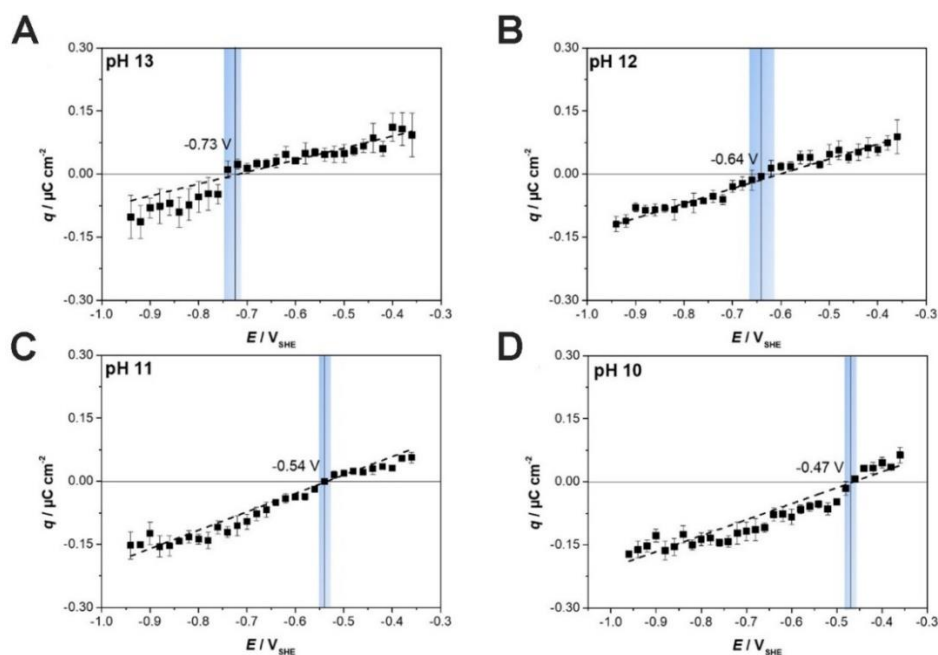


Figure 4.30. Calculated charge densities q (from integration of the current transients) vs E in 0.5 M NaClO_4 at (A) pH 13, (B) pH 12, (C) pH 11, and (D) pH 10, respectively.

As the PME is located at the potential where no excess charge exists on the electrode surface, the PMEs are $-0.73\text{ V}_{\text{SHE}}$, $-0.64\text{ V}_{\text{SHE}}$, $-0.54\text{ V}_{\text{SHE}}$, and $-0.47\text{ V}_{\text{SHE}}$ for pHs 13, 12, 11, and 10, respectively. **Figure 4.31** shows that the PME shifts towards a more negative potential (around 88 mV per pH unit on the SHE scale or $\sim 29\text{ mV}$ per pH unit on the RHE scale) due to the pH increase. At pH 13, the PME is located at the double layer region (see **Figure 4.28**), which is comparable with the literature.³⁰⁹ As discussed in **Section 4.1**, the PME should be independent of the electrolyte pH on the SHE scale in case either the PME is located within the double layer range, or the adsorption process does not involve any change in the free charge. Therefore, the pH dependence of the PME observed for Cu(111) demonstrates that the free charge is dependent on the excess charge of adsorbed OH species. This is similar to what was found on Au(111),^{181,310} Pt(111),²¹², and Ir(111)¹⁷⁹, where the adsorption of anions possesses different adsorption strengths.

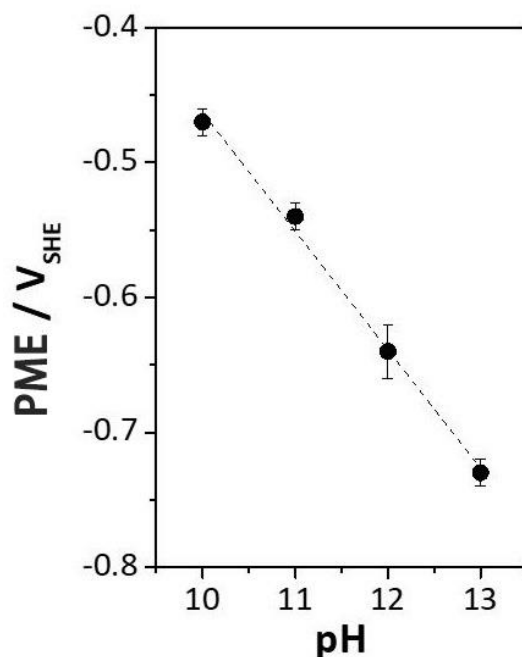


Figure 4.31. The PME for Cu(111) in 0.1 M NaClO₄ solutions at different pH values.

In-situ EC-STM imaging was applied to check the local morphology and structures formed at the Cu(111) electrode surface. The results for Cu(111) in 0.1 M NaClO₄ solutions (pH 13) were taken as an example, as shown in **Figure A8**. The measurements were performed within a potential range of -1.0 V_{SHE} to -0.75 V_{SHE} and a time-dependence at the PME (-0.75 V_{SHE}). **Figure A8A** shows the metallic Cu(111) surface possesses terraces and (vacancy) islands mostly separated by monoatomic steps. However, when altering the applied potential to the PME (-0.75 V_{SHE}), the surface morphology of Cu begins to change slightly within 15 min (marked with arrows and boxes in **Figure A8B** to **F**). After extended time (~23 min) at the PME, substantial (vacancy) island growth and vanishing are visible, as presented in **Figure A8G** and **H**. The changes, able to minimize the surface energy, should be caused by a movement of surface atoms and a beginning reconstruction of the topmost Cu layer. The observed sluggish surface dynamics on Cu(111) at the PME demonstrate that the surface morphology is never completely static. However, the changes proceed rather slowly

when a more positive potential ($> -0.75 V_{\text{SHE}}$) is applied at the Cu surface. This is because anion adsorption processes take place on Cu(111) at higher anodic potentials.³¹¹⁻³¹³

To conclude, we have shown that the potential dependent electrode charge with respect to the PME can immensely influence the atomic structure of the Cu(111) electrode surface, which is essential for understanding the electrochemical reactions taking place at the interface. Moreover, *in-situ* EC-STM imaging revealed that the Cu(111) surface slowly begins to restructure at the potentials close to the PME, where the first subtle morphology and structure changes are observed. The pH effect measurements show that the PME for Cu(111) in 0.1 M NaClO₄ solutions can be shifted by 88 mV per pH unit on the SHE scale, which means that the pH can influence the interfacial structure of Cu in the alkaline solutions. These findings prove that the determination of the PME of Cu in alkaline solutions is now available for interpreting electrocatalysis and electrosorption studies in general.

4.3 The Cation Effect on Metal-Organic Framework Derivatives

Metal-organic frameworks (MOFs) are a class of porous coordination networks that consist of organic linkers and metal ions/clusters.³¹⁴⁻³¹⁸ Owing to their unique properties, such as the diversified framework architectures and high surface areas, MOFs and MOF-derived materials have attracted considerable attention over the years for various applications in medicament delivery^{319,320}, gas storage/separation³²¹⁻³²³, heterogeneous catalysis³²⁴⁻³²⁶, and sensors³²⁷.

Recently, our group has developed a versatile and facile strategy to synthesize mixed metal hydroxide electrocatalysts derived from surface-mounted MOFs (SURMOFs) with excellent OER performance in alkaline media.^{328,329} In this section, the cation effect on SURMOF derivatives was studied by the LICT technique. The experiments

were conducted for the Ni|Fe-[TA]-SURMOF derivatives in 0.1 M AMOH (AM = Li⁺, Na⁺, K⁺, and Cs⁺) solutions. Here, [TA] represents the deprotonated terephthalic acid. As shown in **Figure 4.32**, the OER performance of these derivatives was assessed in the alkaline electrolytes containing different alkali metal cations. It can be observed that the activity towards the OER shows a decrease in the following order: Cs⁺ > K⁺ > Na⁺ > Li⁺, which is in good agreement with the previous reports.³³⁰

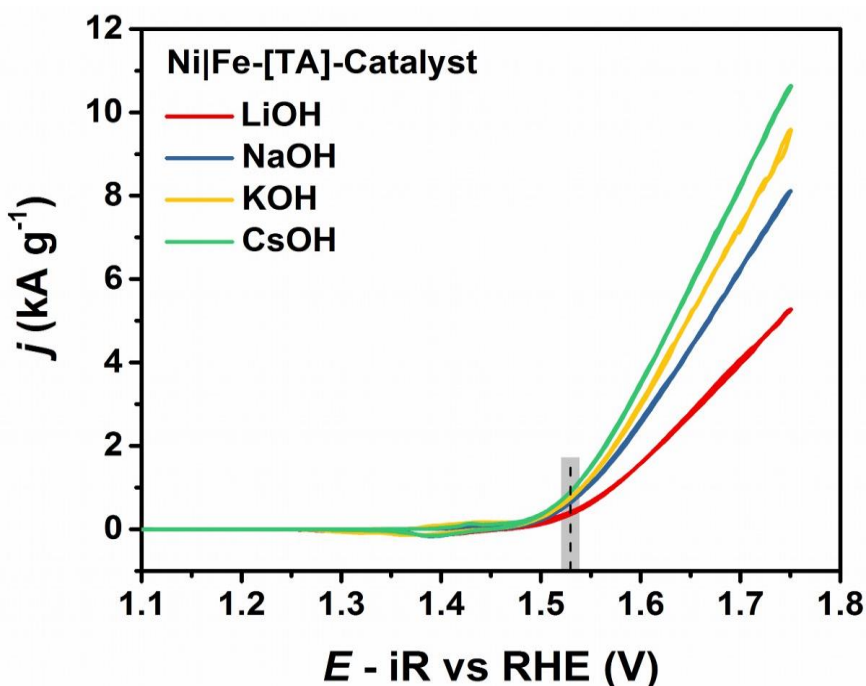


Figure 4.32. OER polarization curves of Ni|Fe-[TA]-Catalysts recorded in O₂-saturated 0.1 M LiOH (pH 13.1), 0.1 M NaOH (pH 13.4), 0.1 M KOH (pH 13.4), and 0.1 M CsOH (pH 13.5) electrolytes. Scan rate, 5 mV s⁻¹. Note, the SURMOFs derivatives are denoted as Catalyst after electrochemical cycling here.

In order to check the interfacial water structure effect on the OER activity of the SURMOF-derived NiFe(OOH) electrocatalysts, the LICT measurements were performed in the corresponding systems containing different alkali metal cations (see **Figure 4.33**). As the PME is located at the potential where no excess charge exists on the electrode surface, the PMEs are around 0.96 V, 0.98 V, 1.00 V, and 1.04 V vs RHE

for 0.1 M LiOH, 0.1 M NaOH, 0.1 M KOH, and 0.1 M CsOH solutions, respectively. It is obvious that the PME increases with the decrease of the alkali metal cation hydration energy.

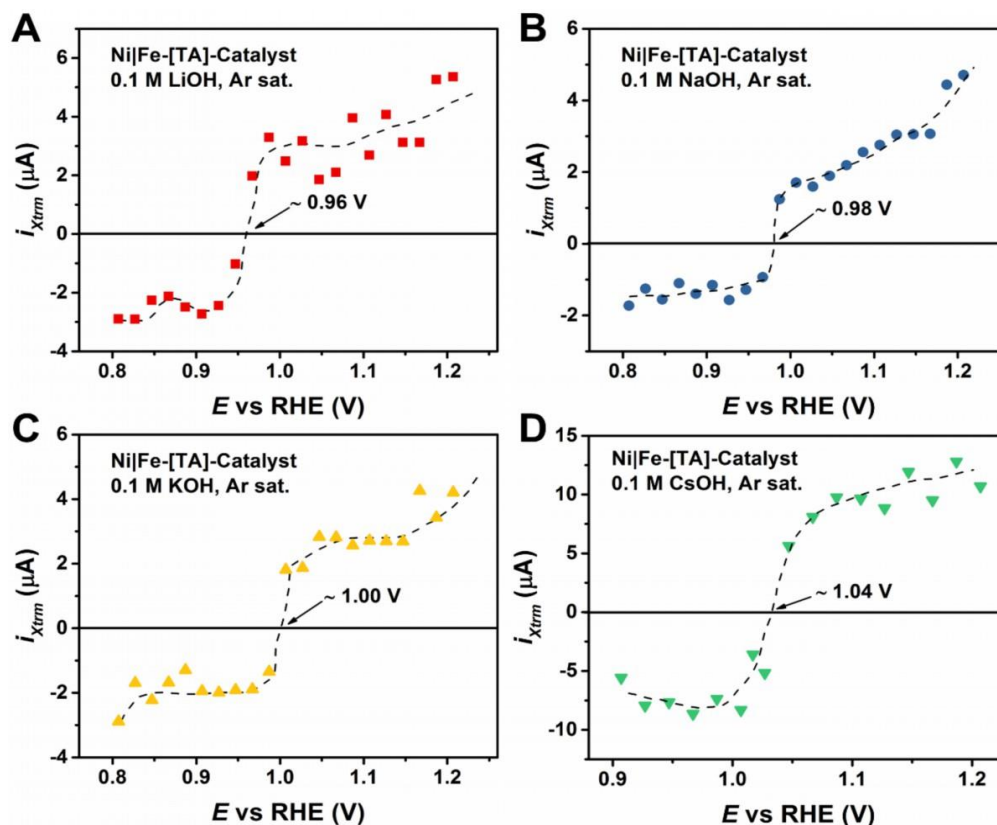


Figure 4.33. (A to D) The maximum current transient values plotted as a function of the applied potential for 0.1 M LiOH (pH 13.1), 0.1 M NaOH (pH 13.4), 0.1 M KOH (pH 13.4), and 0.1 M CsOH (pH 13.5) electrolytes, respectively. One can find the PME values at the point where the current transient changes its sign, i.e., $i_{xtrm} = 0$.

According to the discussion in **Section 4.1.2**, one can assume that the closer the PME is to the thermodynamic equilibrium potential of the OER, the better the OER activity should be. Since the PME for Ni|Fe-[TA]-Catalyst in the presence of Cs^+ is closer to the onset potential of the OER, it has less order of the interface at the onset potential of the OER. Therefore, one can infer that Ni|Fe-[TA]-Catalyst should show better OER performance in the presence of Cs^+ . The observed OER activity results confirm our

expectations. Moreover, the OER activity shows an approximately linear relationship with the PME value (see **Figure 4.34**), which indicates that the OER performance of Ni|Fe-[TA]-Catalyst has a strong correlation with the interface structure influenced by the alkali metal cations in the electrolyte.

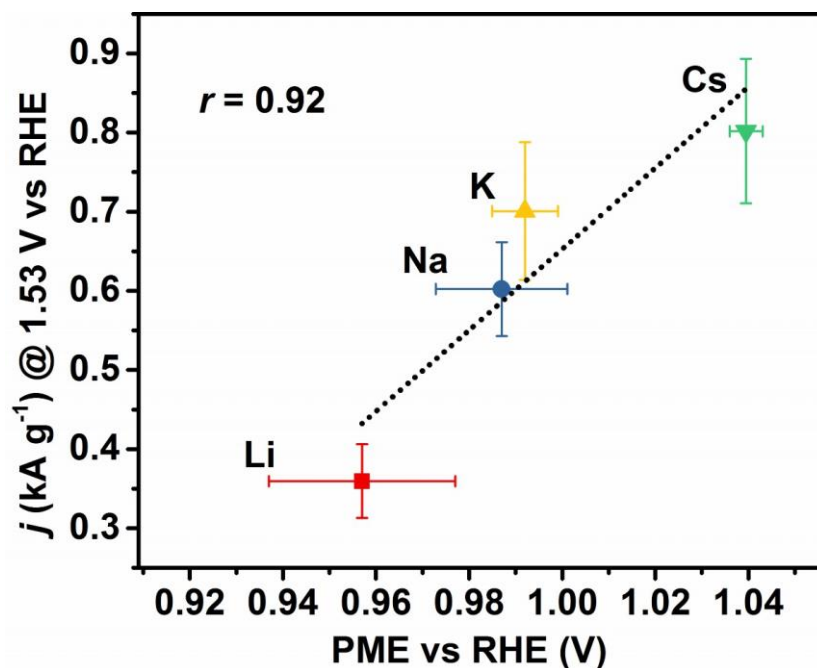


Figure 4.34. The current density at the potential of 1.53 V versus the PMEs of Ni|Fe-[TA]-Catalyst in electrolytes containing alkali metal cations. The Pearson correlation coefficient (r) is 0.92 according to the linear fitting.

In summary, the cation effect on the OER activity of the SURMOF-derived NiFe(OOH) electrocatalysts follows the order of $\text{Cs}^+ > \text{K}^+ > \text{Na}^+ > \text{Li}^+$. Based on the LICT technique, the correlation between the OER performance and the PME was found. The obtained results further confirm our expectation that the closer the PME is to the thermodynamic equilibrium potential of a certain reaction, the faster this reaction should be. Thus, the PME determination with the LICT can be considered a powerful method for the investigation of the electrochemical processes taking place at the electrode/electrolyte interface.

5. Conclusions and Outlook

This work aimed at studying the influence of the electrolyte composition on the properties of the electric double layer (EDL) and the electrode activity. In this respect, the unique laser-induced current transient (LICT) technique was applied in the investigation of various electrochemical systems. The effect of electrolyte pH, alkali metal cation, and anion was systematically investigated. In particular, the hydrogen evolution reaction (HER), the oxygen reduction reaction (ORR), and the oxygen evolution reaction (OER) were selected. Based on the obtained results, it can be inferred that the reaction under study proceeds at a fast rate when the potential of maximum entropy (PME) is closer to the thermodynamic equilibrium potential of that reaction.

In **Section 4.1**, the measurements were conducted for the polycrystalline platinum and gold electrodes in electrolytes of various compositions. The experiments using the LICT technique with cyclic voltammetry (CV) confirmed the influence of electrolyte composition on the properties of the EDL. For both Pt and Au in HClO₄ solutions at different pH values, higher H⁺ concentrations of electrolytes lead to the enhancement of both electrode activities towards the HER, while lower H⁺ concentrations of electrolytes lead to the enhancement of the activities towards the ORR. This is because the PME for lower pH values was closer to the thermodynamic equilibrium potential of the HER, while the PME is closer to the ORR for electrolyte compositions with lower concentrations of H⁺. The introduction of oxygen can also alter the EDL properties because the local protons at the electrode/electrolyte interface can be consumed by reducing O₂ during the LICT measurements; this, in turn, leads to a change of the local pH. Regarding alkali metal cations, the PME showed a higher sensitivity to the pH in the presence of K⁺ than Na⁺. The PME increased with the rise of the electrolyte pH. However, it is worth noting that the PME can be altered sharply at some point (for instance, from pH 4 to 6 for Au in 0.5 M K₂SO₄ solution). Besides, the interfacial structure for Au in the electrolyte containing Na⁺ and K⁺ ions can be hugely different

because of the enormous PME difference for these two cations, for instance, at pH 6. In this case, Na_2SO_4 and K_2SO_4 cannot be considered as equal supporting electrolytes. As for the case in HClO_4 solutions, oxygen can also move the PME to more positive potentials in the electrolyte containing alkali metal cations. When fixing pH at 6, there was a linear relationship between the PME and the HER and ORR activities for Pt electrodes in the presence of alkali metal cations. The PME increased with the decrease of hydration energy in the following order: $\text{Li}^+ < \text{Na}^+ < \text{K}^+ < \text{Cs}^+$. The rate of the HER increased in the Li^+ -containing solutions, while the activity toward the ORR became higher in the presence of Cs^+ . One can deduce that the electrode activity is dependent on the nature of the alkali metal cation since the HER and ORR activities presented a linear trend with the hydration energies of the corresponding alkali metal cations. The results of this part demonstrated that the different H^+ concentrations and the presence of alkali metal cations influence the interfacial structure, which can be further seen in electrocatalytic reactions.

In **Section 4.2**, the LICT technique, together with the *in-situ* EC-STM imaging, was utilized for the investigation of the Cu(111)/liquid interface structure and dynamics. The results illustrated that the atomic structure of the Cu(111) electrode surface could be strongly influenced by the potential dependent electrode charge, which correlates with the PME. Interestingly, *in-situ* EC-STM imaging showed that the Cu(111) surface slowly begins to restructure at the potentials close to the PME. Within a certain period, first subtle morphology and structure alterations can be observed around the PME. Also, the PME for Cu(111) in 0.1 M NaClO_4 solutions can be moved by ~ 88 mV per pH unit on the SHE scale. That means the Cu(111)/electrolyte interface structure is pH-dependent in alkaline media. These findings provide the possibility for investigating the electrochemical interface of other soft coinage metals, such as silver, owing to the importance of the reconstructions under electrochemical reaction conditions in their activity performance.

In **Section 4.3**, the alkali metal cation effect on the OER activity of the surface-mounted metal-organic framework (SURMOF)-derived NiFe(OOH) electrocatalysts in alkaline media was investigated. It was established that the activity of the SURMOF-derivatives towards the OER shows a decreasing order, i.e., $\text{Cs}^+ > \text{K}^+ > \text{Na}^+ > \text{Li}^+$. The LICT measurements revealed that the PME of the SURMOF-derivatives was closer to the thermodynamic equilibrium potential of the OER in the presence of Cs^+ . Furthermore, the obtained PME showed an approximately linear relationship with the OER activity, which evidences a clear correlation between the OER performance of the SURMOF-derivatives and the nature of the alkali metal cation. The observed results in this part further confirm our expectation that the closer the PME is to the thermodynamic equilibrium potential of a certain reaction, the faster that reaction would be.

Overall, the LICT technique shows great potential to be a powerful tool for investigating various electrochemical systems, thanks to its relative simplicity and the ease at which it can be combined with other techniques. The determination of the PME with the LICT method provides information on the EDL structure, which is helpful for better understanding the mechanisms of the electrochemical processes taking place at the electrode/electrolyte interface. The LICT technique has been successfully employed to study noble metal electrodes, non-noble metal electrodes, metal oxides, and polymers. The obtained information about the EDL structure is of significance for the optimization of the studied systems. Particularly interesting is the role of the electrolyte composition in the electrochemical system since its importance in the performance of the electrode activity needs highlighting. The presented results in this thesis demonstrate the ability of the LICT technique to improve the fundamental understanding of electrolyte effects in dissimilar simple or complex electrochemical systems. Therefore, this method can potentially be utilized for other electrochemical systems: for instance, in the presence of organic electrolytes and solid electrolytes. In addition, it can also be applied for the investigation of electrochemical interface reconstruction of other soft coinage metals.

Finally, it is our considered view that this remarkably valuable and unique method can be a powerful tool for studying the mechanism of the interfacial processes and further optimizing the electrochemical system.

Appendix

A. pH Effect in the Presence of Alkali Metal Cations for Pt Electrode

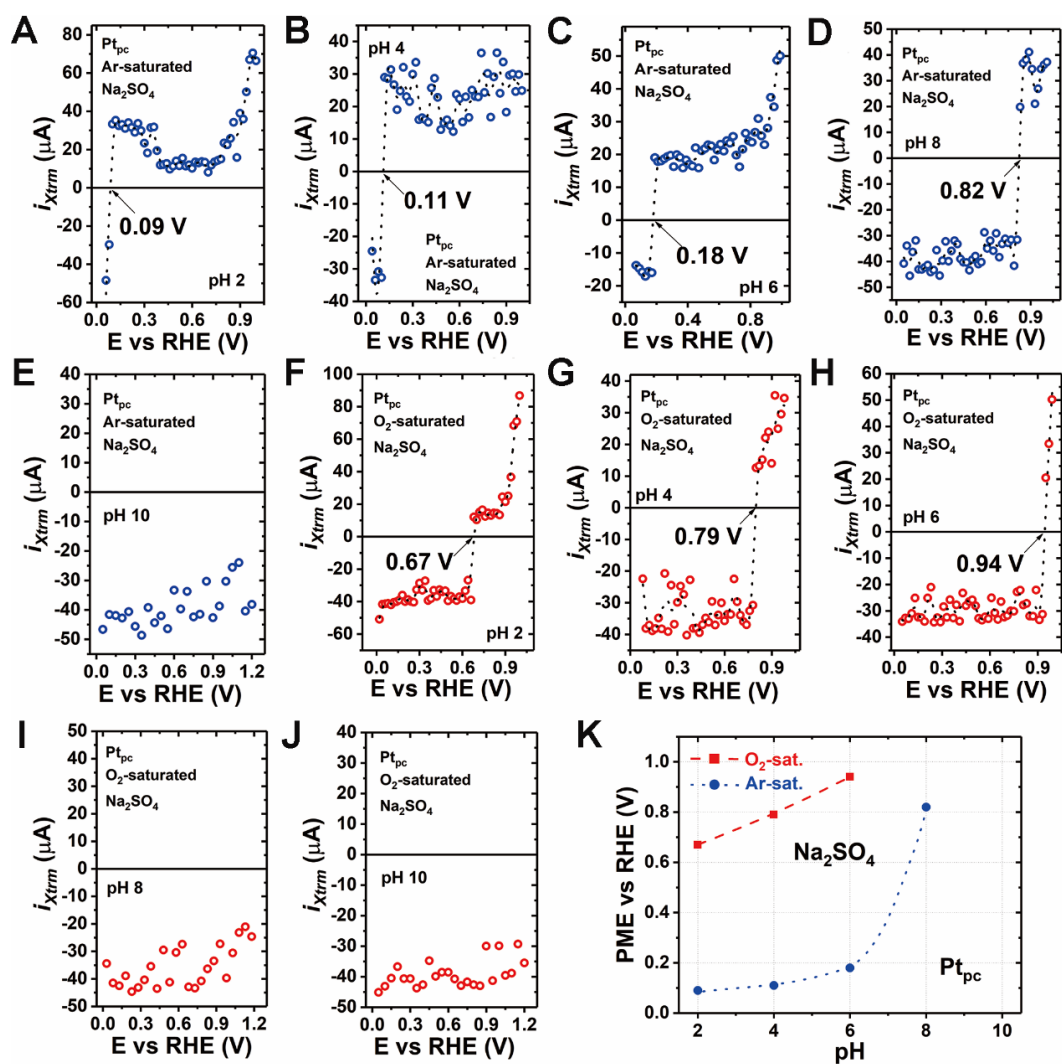


Figure A1. (A to E) Extreme current transients of the LICTs collected for Pt_{pc} immersed into the Ar-saturated 0.5 M Na₂SO₄ solutions of different pHs (2, 4, 6, 8, and 10). (F to J) The similar extreme current values obtained for Pt_{pc} immersed into O₂-saturated 0.5 M Na₂SO₄ solutions of the corresponding pH values. (K) The values of the PME plotted versus pH values for Pt_{pc} in Ar-saturated (blue) and O₂-saturated (red) 0.5 M Na₂SO₄ electrolytes.

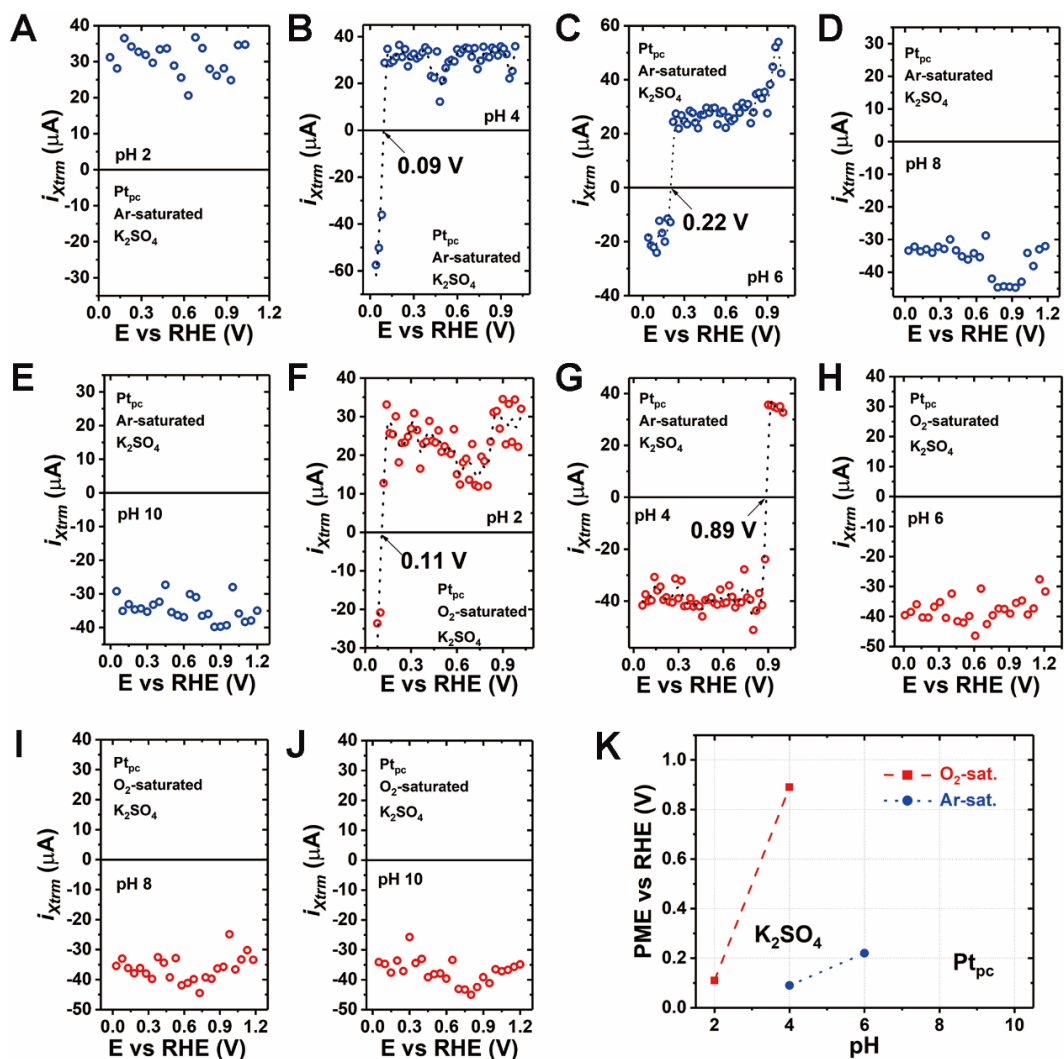


Figure A2. (A to E) Extreme current transients of the LICTs collected for Pt_{pc} immersed into the Ar-saturated 0.5 M K₂SO₄ solutions of different pHs (2, 4, 6, 8, and 10). (F to J) The similar extreme current values obtained for Pt_{pc} immersed into O₂-saturated 0.5 M K₂SO₄ solutions of the corresponding pH values. (K) The values of the PME plotted versus pH values for Pt_{pc} in Ar-saturated (blue) and O₂-saturated (red) 0.5 M K₂SO₄ electrolytes.

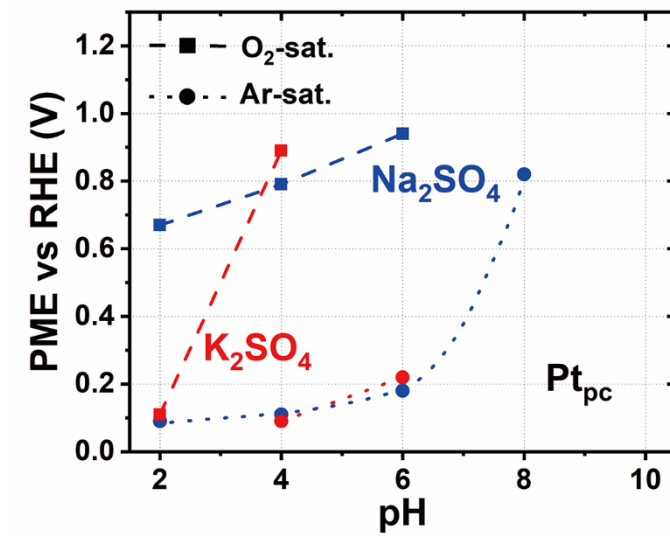


Figure A3. The values of the PME for Pt_{pc} in Ar-saturated (dot) and O₂-saturated (dash) 0.5 M Na₂SO₄ (blue) and K₂SO₄ (red) solutions depicted as a function of the electrolyte pH.

B. Anion Effect for Pt Electrode

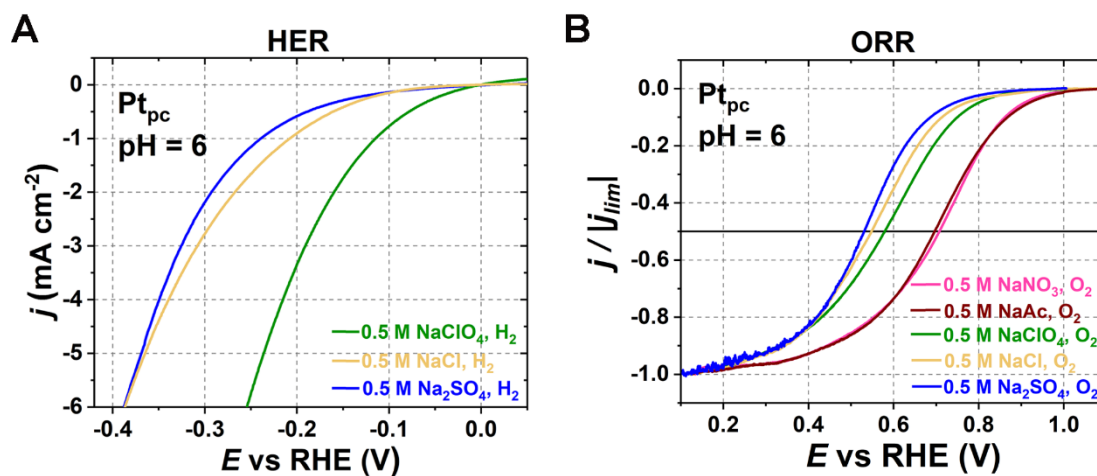


Figure A4. Polarization curves for (A) the HER and (B) the ORR activity for Pt_{pc} immersed into H₂- and O₂-saturated 0.5 M NaX (X = NO₃⁻, ClO₄⁻, Cl⁻, Ac⁻, and SO₄²⁻) solutions of pH 6, respectively.

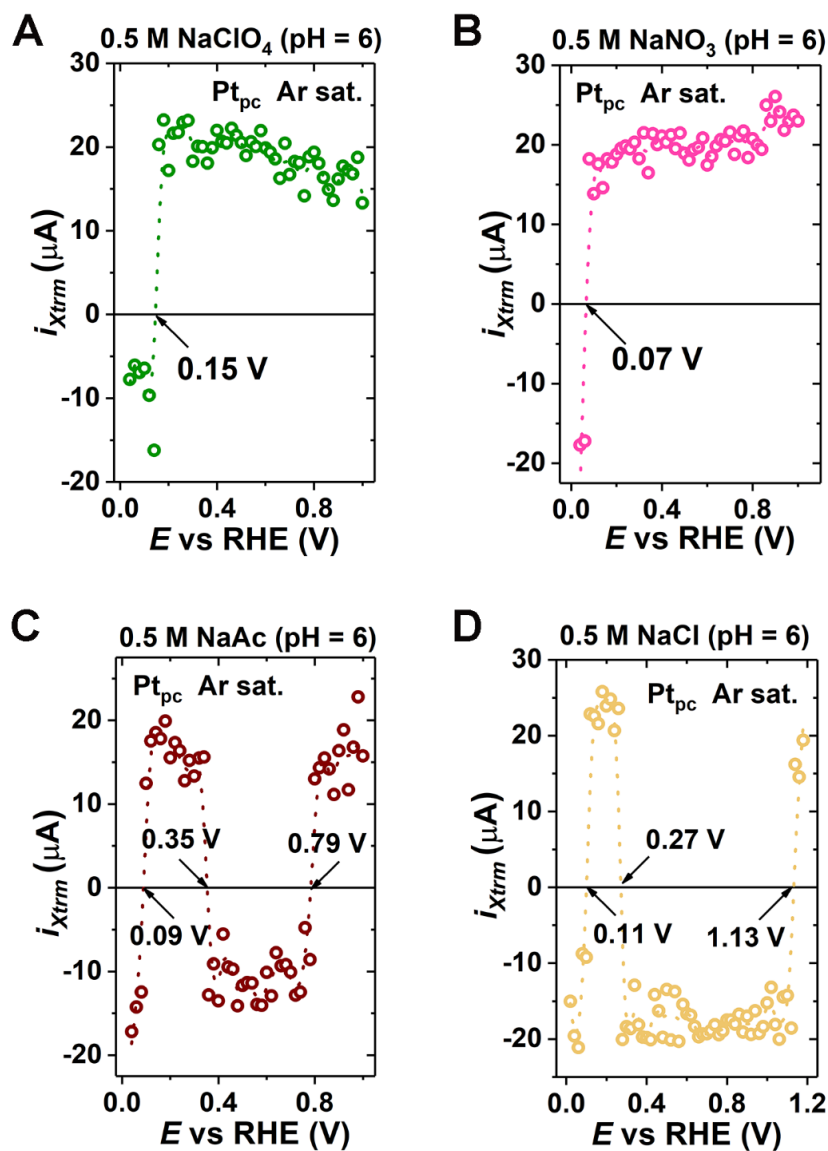


Figure A5. (A to D) The values of i_{xtrm} plotted as a function of the applied potential (going from high to low potentials) in the near-to-neutral pH (pH 6) 0.5 M NaX ($X = ClO_4^-$, NO_3^- , Ac^- , and Cl^-) electrolytes (Ar-saturated). One can find the PME values at the point where the current transient changes its sign, i.e., $i_{xtrm} = 0$.

C. The Electrochemical Interface Structure of Cu(111) in Alkaline Solutions

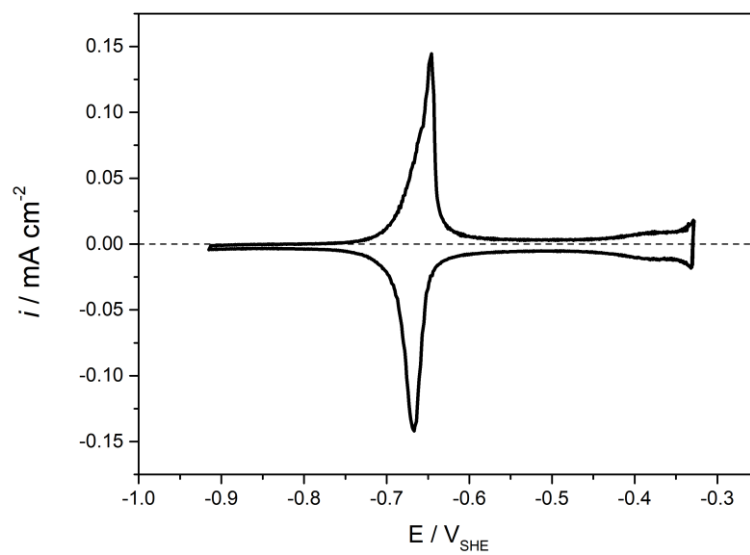


Figure A6. Cyclic voltammetry of Cu(111) in 0.1 M NaOH solution of pH 13. Scan rate: 50 mV s^{-1} .

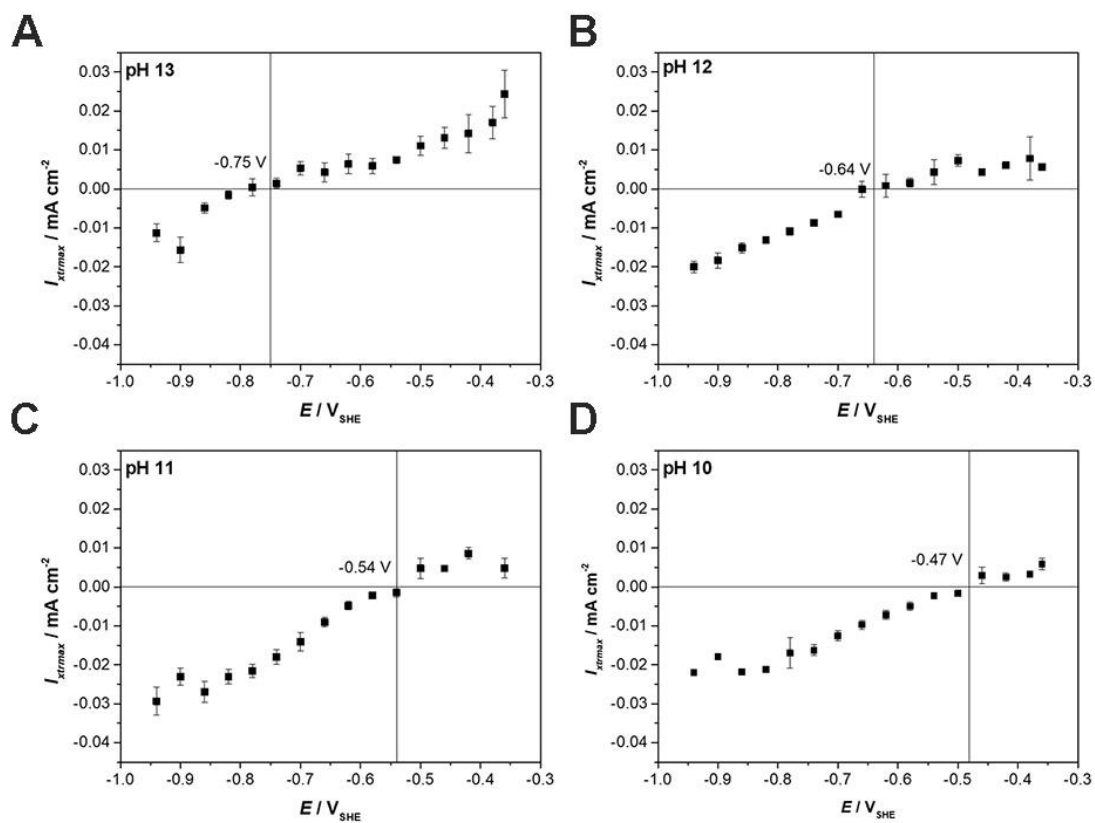


Figure A7. (A to D) The values of maximum current transient values plotted as a function of the applied potential for pHs 13, 12, 11, and 10, respectively. One can find the PME values at the point where the current transient changes its sign, i.e., $i_{xtrm} = 0$.

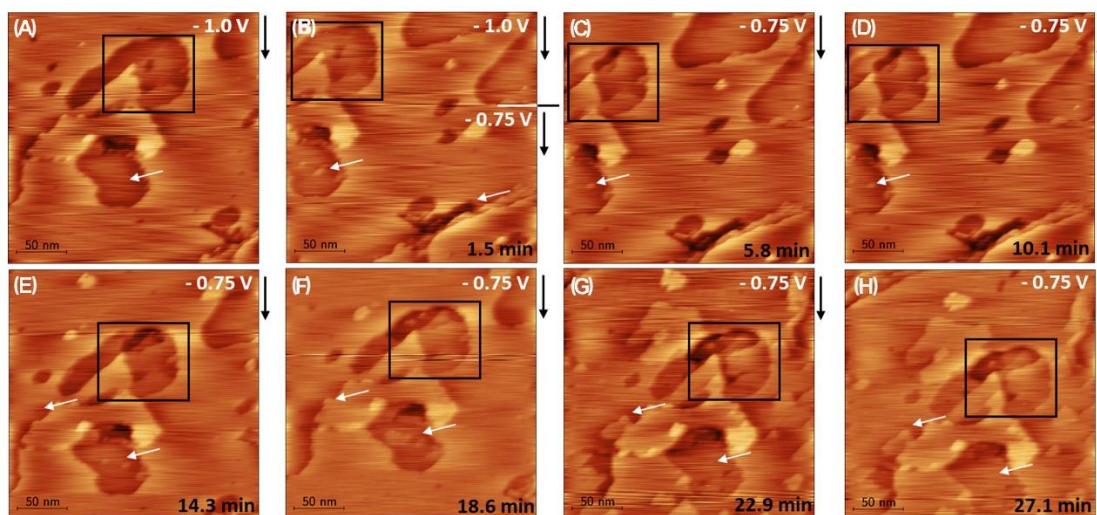


Figure A8. (A) and (B) Time- and potential-dependent sequence of EC-STM images at negative electrode charge ($-1.0 V_{SHE}$) and (B) to (H) at the PME ($-0.75 V_{SHE}$) of Cu(111) in $0.1 M NaClO_4$ solution (pH 13). The morphology of the surface gradually changes, which are highlighted with a square and arrows, marking the location of identical spots on the surface that slightly have moved due to the drift in the images. Size = $250 \times 250 nm^2$, $I_{tip} = 1 nA$, $E_{tip} = -0.40 V_{SHE}$. (Images were recorded by A.Auer, University of Innsbruck)

D. Abbreviations and Symbols

<i>a</i>	ion activity
<i>A</i>	catalytic activity
AFC	alkaline fuel cell
AIMD	<i>ab initio</i> molecular dynamics
AM	alkali metal
<i>c</i>	thermal capacity
<i>C</i>	capacitance/capacitor
<i>C</i>	the concentrations of the reactants
<i>C_d</i>	the differential capacitance of the diffuse layer
<i>C_{dl}</i>	double layer capacitance
<i>C_i</i>	inner double layer capacitance
CA	chronoamperometry
CE	counter electrode
CV	cyclic voltammetry or voltammogram
<i>d</i>	density
DFT	density functional theory
<i>e</i>	elementary charge

E	potential
E^0	standard electrode potential
$E_{1/2}$	half-wave potential
E_{eq}	equilibrium potential
ECSTM	electrochemical scanning tunneling microscopy
EDL	electric double layer
EQCM	electrochemical quartz crystal microbalance
F	Faraday constant
G	Gibbs free energy
H	distance
$H_{ads/des}$	hydrogen adsorption/desorption
HER	hydrogen evolution reaction
HOR	hydrogen oxidation reaction
I	electric current
$i_{X_{trm}}$	the extreme values of the current transients
IHP	inner Helmholtz plane
j	current density
k	reaction rate constant

LBL	layer-by-layer
LICT	laser-induced current transient
<i>M</i>	molar mass
Me	metal
ME	microelectrode
MHDA	16-mercaptohexadecanoic acid
MMO	mercury-mercury oxide electrode
MMS	the mercury-mercurous sulfate reference electrode
MOF	metal-organic framework
n	number of electrons
OH_{ads/des}	hydroxyl adsorption/desorption
OHP	outer Helmholtz plane
OER	oxygen evolution reaction
ORR	oxygen reduction reaction
pc	polycrystalline
PAFC	phosphoric acid fuel cell
PEMFC	polymer electrolyte membrane fuel cell
PME	the potential of maximum entropy

PZC	the potential of zero charge
PZFC	the potential of zero free charge
PZTC	the potential of zero total charge
<i>q</i>	electric charge
<i>q</i>	charge density
R	gas constant
RDE	rotating disk electrode
RE	reference electrode
rpm	rotations per minute
RHE	reversible hydrogen electrode
S	entropy
SCE	saturated calomel electrode
SEIRAS	surface-enhanced infrared absorption spectroscopy
SHE	standard hydrogen electrode
SOFC	solid oxide fuel cell
SSC	silver-silver chloride electrode
SURMOF	surface-mounted metal-organic framework
T	temperature

TA	terephthalic acid
<i>t</i>	time
<i>v</i>	stoichiometric number
<i>v</i>	reaction rate
<i>V</i>	voltage
WE	working electrode
XAS	X-ray absorption spectroscopy
XRS	X-ray scattering
<i>z</i>	valence number
<i>Γ</i>	surface excess charge
<i>Ψ_s</i>	the potential across the EDL
<i>α</i>	transfer coefficient
<i>γ</i>	liquid metal surface tension
<i>ε</i>	dielectric constant
<i>η</i>	overpotential
<i>κ</i>	thermal conductivity
<i>σ</i>	interfacial tension
<i>φ</i>	Galvani potential

φ_0	standard Galvani potential
μ	chemical potential

Spotlight on the Effect of Electrolyte Composition on the Potential of Maximum Entropy: Supporting Electrolytes Are Not Always Inert

Xing Ding,^[a] Batyr Garlyyev,^[a] Sebastian A. Watzele,^[a] Theophilus Kobina Sarpey,^[a] and Aliaksandr S. Bandarenka^{*,[a, b]}

Abstract: The influence of electrolyte pH, the presence of alkali metal cations (Na^+ , K^+), and the presence of O_2 on the interfacial water structure of polycrystalline gold electrodes has been experimentally studied in detail. The potential of maximum entropy (PME) was determined by the laser-induced current transient (LICT) technique. Our results demonstrate that increasing the electrolyte pH and introducing O_2 shift the PME to more positive potentials. Interestingly, the PME exhibits a higher sensitivity to the pH change in the presence of K^+ than Na^+ . Altering the pH of the K_2SO_4 solution from 4 to 6 can cause a drastic shift in the PME. These findings reveal that, for example, K_2SO_4 and Na_2SO_4 cannot be considered as equal supporting electrolytes: it is not a viable assumption. This can likely be extrapolated to other common “inert” supporting electrolytes. Beyond this, knowledge about the near-ideal electrolyte composition can be used to optimize electrochemical devices such as electrolyzers, fuel cells, batteries, and supercapacitors.

Understanding the properties of the electric double layer (EDL) formed between the electrodes and electrolytes is significant for the rational design of energy conversion and storage systems.^[1] One of the critical interfacial properties is the net orientation of solvent (e.g., water) molecules at the electrode/electrolyte interface.^[2] The interfacial water structure, determined by the charge separation at the interface, is influenced by electrode potential, pH of the electrolyte, and its

composition.^[3] A parameter associated with the net orientation of water molecules is the so-called potential of maximum entropy (PME), which is defined as the potential at which the entropy of double-layer formation reaches its maximum.^[4] Knowledge of the PME is critical for assessing the stiffness of the water layer at the interface and, therefore, can be considered as the main reason for energy barriers that hinder mass and charge transfer through the interface.^[2a] At potentials remote from the PME, the water layer at the interface is relatively rigid, which hinders the charge transfer. Inversely, at potentials close to the PME, the interfacial water has the highest disorder and can reorient more freely, enabling easier charge transfer.

The PME can be determined by the laser-induced current transient (LICT) technique.^[5] This methodology is based on the sudden temperature jump effect caused by nanosecond laser pulses. The current relaxation curves are measured at the potentiostatic conditions after laser probing (Scheme 1).^[2b,5] The response from the system after the laser pulse shows the information about the net orientation of water (solvent) molecules at the interface. Therefore, the potential at which the current transient changes its sign corresponds to the state with the maximum disorder, the PME.^[4] This in situ method has been used for studying the interfacial fundamentals of electrodes, such as the investigation of the electric double layer on Au(111) and Pt(111),^[6] the kinetics of the electrochemical process on Pt electrodes,^[7] and the correlation between the interfacial water network and the activity of Pt electrodes.^[2a,8]

Recent studies showed that in many cases, the electrolyte composition affects the rate of catalyzed reactions.^[9] Particularly interesting is the influence of the electrolyte pH and the nature of alkali metal cations present. In all of these cases, the ions interact relatively strongly with the surface affecting the electrochemical processes. For instance, it was shown that the oxygen evolution both in acidic and alkaline media depends on the nature of those “spectator species”.^[10] Likewise, the hydrogen evolution reaction in alkaline media was found to be largely influenced by the electrolyte composition.^[11] However, it is difficult for electrochemists to experimentally establish how the electrolyte compositions affect the electrode/electrolyte interfacial structure and eventually control electrocatalytic activity.

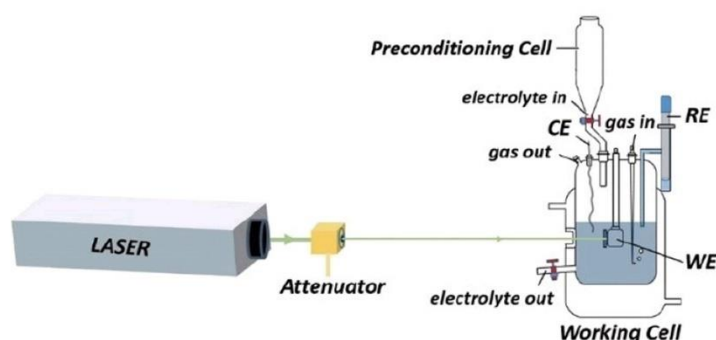
Here, we determine how the PME changes with electrolyte composition for polycrystalline gold (Au_{pc}) electrodes. The investigations were performed in Ar- and O_2 -saturated 0.5 M Na_2SO_4 and K_2SO_4 solutions of different pH with the LICT technique. Na_2SO_4 and K_2SO_4 were chosen because they are

[a] X. Ding, Dr. B. Garlyyev, Dr. S. A. Watzele, T. Kobina Sarpey, Prof. Dr. A. S. Bandarenka
Physics of Energy Conversion and Storage
Technical University of Munich
James-Frank-Strasse 1, 85748 Garching (Germany)
E-mail: bandarenka@ph.tum.de

[b] Prof. Dr. A. S. Bandarenka
Catalysis Research Center TUM
Technical University of Munich
Ernst-Otto-Fischer-Strasse 1, 85748 Garching (Germany)

Supporting information for this article is available on the WWW under <https://doi.org/10.1002/chem.202101537>

© 2021 The Authors. Published by Wiley-VCH GmbH. This is an open access article under the terms of the Creative Commons Attribution License, which permits use, distribution and reproduction in any medium, provided the original work is properly cited.



Scheme 1. Scheme of the experimental setup used to perform the LICT measurements. WE, RE and CE correspond to working, reference, and counter electrode, respectively. More details about the LICT setup can be found in the Supporting Information.

often used as supporting electrolytes in the industry.^[12] Note, the SO_4^{2-} anion with very high hydration energy was selected to minimize the possible disruption of the anion competition. Interestingly, the PME shifts towards more positive potentials with increasing the pH values for Au_{pc} electrodes in either Ar-saturated or O_2 -saturated 0.5 M Na_2SO_4 and K_2SO_4 electrolytes. However, the PME exhibits a higher sensitivity to the pH in the presence of K^+ in comparison to Na^+ . Especially, the PMEs of Au_{pc} in Na_2SO_4 and K_2SO_4 solutions are significantly different at pH 6 or higher, which indicates the drastic variation of the EDL structure in the presence of these two electrolytes. Moreover, the PME values measured in O_2 -saturated solutions are more positive than those measured in Ar-saturated electrolytes.

Initially, the surface quality of the Au electrode was analyzed with cyclic voltammograms (CVs) in Ar-saturated 0.5 M Na_2SO_4 and K_2SO_4 solutions at different pHs. The CVs are shown in Figure 1. For both Na^+ - and K^+ -containing electrolytes at pH 2, CVs of Au_{pc} are comparable with the measurements recorded in 0.1 M H_2SO_4 (see Figure S1 in the Supporting Information). The typical three anodic peaks observed between about 1.3 and 1.6 V versus the reversible hydrogen electrode (RHE) and a sharp reduction peak at about 1.1 V versus RHE can be observed.^[13] However, Figure 1 shows that the change in the pH strongly influences the oxidation and reduction processes on Au_{pc} surface in the Na_2SO_4 and K_2SO_4 solutions. Especially, when increasing the pH of the solution to 6, two broad reduction peaks are observed for Na^+ -containing electrolytes and three peaks in the presence of K^+ within the investigated potential range (Figure S2). This could be because, in a nearly neutral pH solution, the local protons at the interface have a low concentration. Hence, the local pH at the electrode/electrolyte interface can be easily changed during the oxidation and reduction processes on Au_{pc} surface. During the reduction process, the protons at the interface can be quickly consumed, which could result in the reduction of Au oxide at lower potentials.^[14] When the pH is kept constant at pH 6, one can observe the influence of the nature of the alkali metal cation, as shown in Figure S2. It seems that K^+ cations promote the

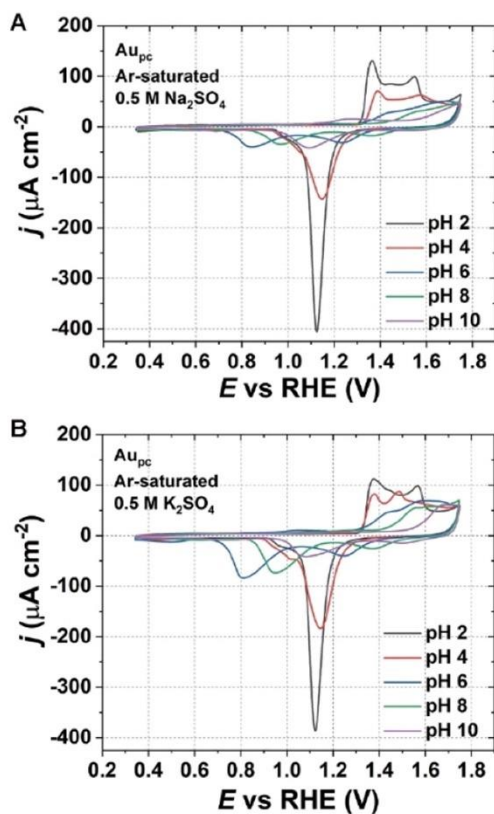


Figure 1. Typical cyclic voltammograms of Au_{pc} in 0.5 M Ar-saturated A) Na_2SO_4 and B) K_2SO_4 electrolytes of different pH values (2, 4, 6, 8, and 10). Scan rate: 50 mV s^{-1} .

oxidation process of Au, which is observed from the increased peak areas compared to Na^+ in Figure S2.

To further investigate the influence of pH and cations on Au_{pc} , the LICt measurements were performed to determine the position of the PME. The analysis was conducted in both Ar- and O_2 -saturated electrolytes. Figure 2 shows the current transients corresponding to Au_{pc} in Ar- and O_2 -saturated 0.5 M Na_2SO_4 solutions (pH 2). Since the sign of the charge of the electrode surface coincides with the current transient, a positive surface charge leads to a positive current transient and vice versa, as illustrated in Figure 2 A and C. Alternatively, the extreme values of the current transients ($i_{x_{trm}}$) can be plotted as a function of the applied potential to find the PME, as indicated in Figure 2 B and D. The potential at which the current transient changes its sign corresponds to the PME. Thus, the PME values for Au_{pc} are 0.19 and 0.35 V in the Ar- and O_2 -saturated 0.5 M Na_2SO_4 solutions (pH 2), respectively.

The PME shifts towards more positive potentials due to the pH increase for both Ar- and O_2 -saturated Na_2SO_4 solutions (Figure 3), which means the PME depends on the pH. However, it should be noted that the pH dependence of the PME also involves the effect of adsorption processes on the free charge distribution at the interface.^[4,15] Because the PME is believed to be independent of the electrolyte pH on the standard hydrogen electrode (SHE) scale when the PME lies within the potential region without adsorption effect.^[16] However, it does not necessarily follow this rule at potentials where adsorption processes influence the free charge.^[15] In the case of Ar-saturated Na_2SO_4 (Figure 3 A–D), the potentials at which the current transient changes its sign are 0.25, 0.34, 0.58, and 0.88 V

for pHs 4, 6, 8, and 10, respectively. While for Au_{pc} in O_2 -saturated Na_2SO_4 solutions (Figure 3 E–H), the locations of the PME are 0.39, 0.46, 0.66, and 0.98 V for pHs 4, 6, 8, and 10, respectively. One can notice that the PME values measured in O_2 -saturated Na_2SO_4 solutions are more positive than the values measured in Ar-saturated solutions for all investigated pH ranges. This is because protons can be consumed at the electrode surface by dissolved O_2 during the laser measurements, which leads to a change of the local pH at the interface between electrode and electrolyte. Consequently, this shifts the location of the PME. Taking this result into consideration, it would also be possible to estimate the local pH at the interface by determining the PME.

Similar trends are observed for Au_{pc} at different pHs of 0.5 M K_2SO_4 solutions, as shown in Figure S3. Namely, increasing pH and introducing O_2 can move the PME to more positive potentials with the exception of the case of Au_{pc} in O_2 -saturated K_2SO_4 from pH 6 to 8. For Au_{pc} in Ar-saturated K_2SO_4 solutions (Figure S3 A–E), the PME values are 0.13, 0.27, 1.26, 1.30, and 1.43 V for pHs 2, 4, 6, 8, and 10, respectively. While the PMEs are shifted to 0.27, 0.37, 1.40, 1.38, and 1.49 V in the case of O_2 -saturated K_2SO_4 solutions for pHs 2, 4, 6, 8, and 10, respectively (Figure S3 F–J). Surprisingly, for Au_{pc} in K_2SO_4 solutions at pH 6, 8, and 10, the PMEs are more positive than the thermodynamic equilibrium potential of the oxygen reduction reaction (1.23 V vs. RHE) but are still moved in the presence of O_2 . This could be because the water structure at the electrode/electrolyte interface can be influenced not only by the dissolved O_2 but also by adsorbed H^+ , OH^- , and SO_4^{2-} on the electrode surface.

When comparing the influence of Na^+ and K^+ on Au_{pc} , the PME exhibits a higher sensitivity to the pH in the presence of K^+ than Na^+ (Figure 4). The pH effect on the PME increases slightly in alkaline solutions in the presence of Na^+ . However, the PME can be drastically changed from pH 4 to 6 for Au_{pc} in K^+ -containing electrolytes, which means that small alterations of pH within this pH range can alter the EDL structure drastically. One possible reason is that the specific adsorption of *OH (* represents the adsorbed species) and sulfate adsorption lead to the phase transition and interfacial water rearrangements in the double layer^[17] and then shifts the location of the PME. When the electrolyte pH is 6 or higher, the difference of the PME value for Au_{pc} in Na_2SO_4 and K_2SO_4 becomes large (ca. 0.92 V at pH 6). In this case, Na_2SO_4 and K_2SO_4 cannot be considered as equal supporting electrolytes. Even at the same conditions, the EDL structure in the presence of these two cations differs drastically. Accordingly, the performance of the electrocatalytic reactions can be significantly changed due to the electrolyte. Combining the CVs in Figure 1, one can deduce that a strong phase transition happens for Au_{pc} in the presence of K^+ . Moreover, the difference in the PME values in the presence of K^+ and Na^+ could also be due to the influence of these two cations on the local pH.

To further check the cation effect, the LICt experiments were performed in a mixed solution (60 mL 0.5 M Na_2SO_4 and 60 mL 0.5 M K_2SO_4) at pH 8. As shown in Figure S4, the PMEs are 0.96 and 1.08 V in the Ar- and O_2 -saturated mixed solutions, respectively. Interestingly, the values of the PME for Au_{pc} in this

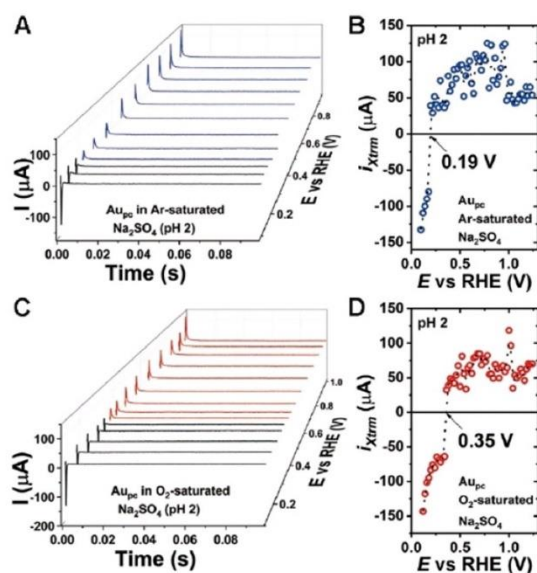


Figure 2. 3D plots of current transients observed after laser pulse with the LICt technique for Au_{pc} in 0.5 M A) Ar- and C) O_2 -saturated Na_2SO_4 solutions (pH 2). The negative current transients in the 3D plots are marked in black. B), D) The corresponding extreme values of the current transients ($i_{x_{trm}}$) as a function of the working electrode potential used to find the PME.

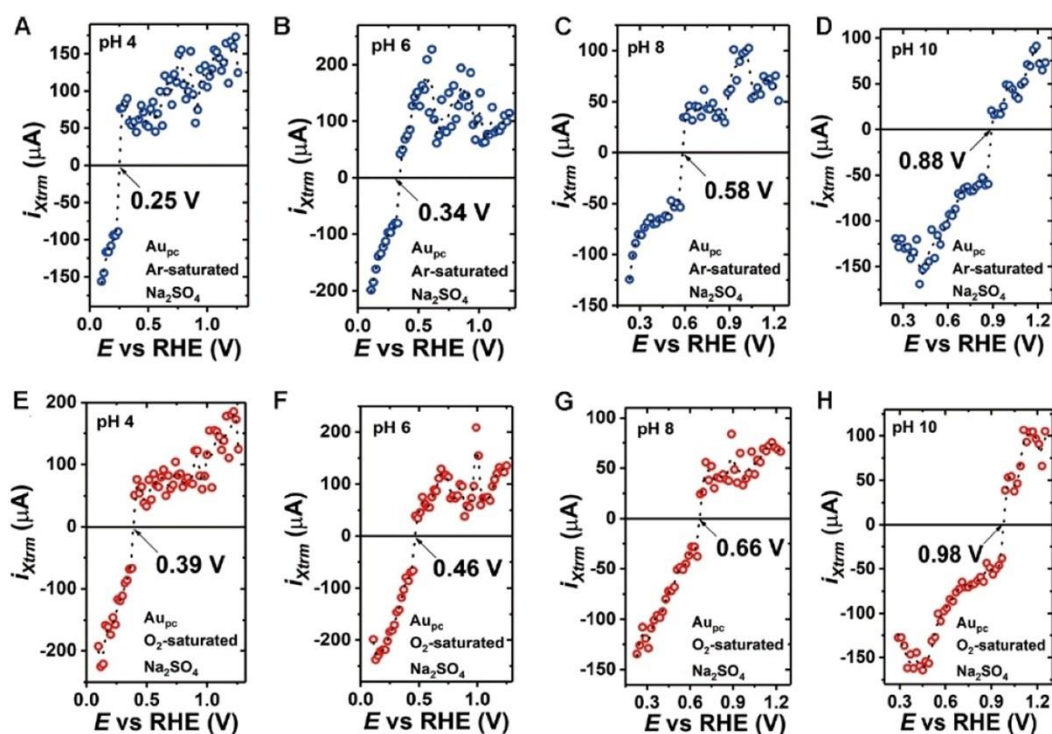


Figure 3. A)–D) Determination of the PME values of the Au_{pc} electrode in 0.5 M Ar-saturated Na_2SO_4 electrolytes at different pH values (4, 6, 8, and 10). E)–H) In O_2 -saturated Na_2SO_4 solutions, the PME increases compared to the case of Ar-saturated electrolytes.

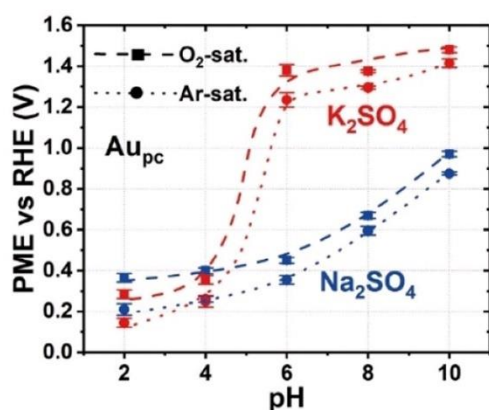


Figure 4. PME values for Au_{pc} in Ar- and O_2 -saturated 0.5 M Na_2SO_4 (blue) and K_2SO_4 (red) solutions depicted as a function of the electrolyte pH. The dashed (O_2 -saturated electrolytes) and dotted lines (Ar-saturated electrolytes) are a guide for the eye.

solution are located between the PMEs of Au_{pc} in Na_2SO_4 and K_2SO_4 solutions at the same pH value. This supports our

hypothesis on the cation effect on the interfacial structure of Au_{pc} .

In conclusion, we have determined the PME by using the LICIT technique to investigate the influence of alkali metal cations, O_2 , and pH on the interfacial structure of Au_{pc} . The presented results demonstrated that an increase in the pH and introduction of O_2 could shift the PME towards more positive potentials in either Na_2SO_4 or K_2SO_4 solution owing to the change in local pH at the interface. When the pH reaches six or higher, the EDL structure for Au_{pc} in Na^+ - and K^+ -containing electrolytes is significantly different because of the large difference in the PME location. Thus, Na_2SO_4 and K_2SO_4 cannot be considered as equal supporting electrolytes in this case. Our findings reveal that the electrolyte composition, even if it is considered as a supporting electrolyte, affects the EDL structure, changes the location of the PME, and influences the electrode processes. Therefore, the determination of the PME by the LICIT method can be a particularly valuable method to evaluate and investigate the influence of the electrolyte composition on the electrochemical processes happening at the electrode/electrolyte interface. We believe this powerful tool can help improve the fundamental understanding of electrolyte effects, which is a prerequisite for rational electrolyte engineering.

Acknowledgments

We are grateful for financial support from the Deutsche Forschungsgemeinschaft under Germany's excellence strategy EXC 2089/1-390776260, Germany's excellence cluster "e-conversion", DFG project BA 5795/4-1 and BA5795/5-1 and DFG research group 2982 under UNusual anODE (UNODE). X. D. acknowledges financial support from the China Scholarship Council (201706170015). Open access funding enabled and organized by Projekt DEAL.

Conflict of Interest

The authors declare no conflict of interest.

Keywords: electrocatalysis · electrolyte influence · gold electrodes · laser-induced current transient · potential of maximum entropy

- [1] a) A. S. Bandarenka, M. T. M. Koper, *J. Catal.* **2013**, *308*, 11–24; b) M. Mavrikakis, *Nat. Mater.* **2006**, *5*, 847–848; c) M. T. M. Koper, *Nanoscale* **2011**, *3*, 2054–2073; d) M. S. Dresselhaus, I. L. Thomas, *Nature* **2001**, *414*, 332–337; e) F. Luo, A. Roy, L. Silvioni, D. A. Cullen, A. Zitolo, M. T. Sougrati, I. C. Oguz, T. Mineva, D. Teschner, S. Wagner, J. Wen, F. Dionigi, U. I. Kramm, J. Rossmeisl, F. Jaouen, P. Strasser, *Nat. Mater.* **2020**, *19*, 1215–1223; f) X. F. Lu, B. Y. Xia, S. Q. Zang, X. W. D. Lou, *Angew. Chem. Int. Ed.* **2020**, *59*, 4634–4650; *Angew. Chem.* **2020**, *132*, 4662–4678; g) A. Kulkarni, S. Siahrostami, A. Patel, J. K. Nørskov, *Chem. Rev.* **2018**, *118*, 2302–2312.
- [2] a) I. Ledezma-Yanez, W. D. Z. Wallace, P. Sebastián-Pascual, V. Climent, J. M. Feliu, M. T. M. Koper, *Nat. Energy* **2017**, *2*, 17031; b) D. Scieszka, C. Sohr, P. Scheibenbogen, P. Marzak, J. Yun, Y. Liang, J. Fichtner, A. S. Bandarenka, *ACS Appl. Mater. Interfaces* **2018**, *10*, 21688–21695; c) F. J. Sarabia, P. Sebastián, V. Climent, J. M. Feliu, *J. Electroanal. Chem.* **2020**, *872*, 114068; d) E. Liu, L. Jiao, J. Li, T. Stracensky, Q. Sun, S. Mukerjee, Q. Jia, *Energy Environ. Sci.* **2020**, *13*, 3064–3074; e) C.-Y. Li, J.-B. Le, Y.-H. Wang, S. Chen, Z.-L. Yang, J.-F. Li, J. Cheng, Z.-Q. Tian, *Nat. Mater.* **2019**, *18*, 697–701.
- [3] a) R. Rizo, E. Sitta, E. Herrero, V. Climent, J. M. Feliu, *Electrochim. Acta* **2015**, *162*, 138–145; b) A. Hamelin, *J. Electroanal. Chem.* **1996**, *407*, 1–11; c) S. Xue, B. Garlyyev, A. Auer, J. Kunze-Liebhäuser, A. S. Bandarenka, *J. Phys. Chem. C* **2020**, *124*, 12442–12447; d) B. Garlyyev, S. Xue, S. Watzele, D. Scieszka, A. S. Bandarenka, *J. Phys. Chem. Lett.* **2018**, *9*, 1927–1930; e) S. Xue, R. W. Haid, R. M. Kluge, X. Ding, B. Garlyyev, J. Fichtner, S. Watzele, S. Hou, A. S. Bandarenka, *Angew. Chem. Int. Ed.* **2020**, *59*, 10934–10938; *Angew. Chem.* **2020**, *132*, 11026–11031.
- [4] A. Ganassin, P. Sebastián, V. Climent, W. Schuhmann, A. S. Bandarenka, J. M. Feliu, *Sci. Rep.* **2017**, *7*, 1–14.
- [5] D. Scieszka, J. Yun, A. S. Bandarenka, *ACS Appl. Mater. Interfaces* **2017**, *9*, 20213–20222.
- [6] a) V. Climent, B. A. Coles, R. G. Compton, *J. Phys. Chem. B* **2001**, *105*, 10669–10673; b) V. Climent, B. A. Coles, R. G. Compton, *J. Phys. Chem. B* **2002**, *106*, 5988–5996.
- [7] V. Climent, N. García-Araez, E. Herrero, J. M. Feliu, *Russ. J. Electrochem.* **2006**, *42*, 1145–1160.
- [8] F. J. Sarabia, P. Sebastián-Pascual, M. T. M. Koper, V. Climent, J. M. Feliu, *ACS Appl. Mater. Interfaces* **2018**, *11*, 613–623.
- [9] a) E. Pérez-Gallent, G. Marcandalli, M. C. Figueiredo, F. Calle-Vallejo, M. T. M. Koper, *J. Am. Chem. Soc.* **2017**, *139*, 16412–16419; b) V. Colic, M. D. Pohl, D. Scieszka, A. S. Bandarenka, *Catal. Today* **2016**, *262*, 24–35; c) S. Ringe, E. L. Clark, J. Resasco, A. Walton, B. Seger, A. T. Bell, K. Chan, *Energy Environ. Sci.* **2019**, *12*, 3001–3014; d) D. Strmcnik, K. Kodama, D. van der Vliet, J. Greeley, V. R. Stamenkovic, N. M. Marković, *Nat. Chem.* **2009**, *1*, 466; e) X. Chen, I. T. McCrum, K. A. Schwarz, M. J. Janik, M. T. M. Koper, *Angew. Chem. Int. Ed.* **2017**, *56*, 15025–15029; *Angew. Chem.* **2017**, *129*, 15221–15225; f) V. Briega-Martos, E. Herrero, J. M. Feliu, *Electrochim. Acta* **2017**, *241*, 497–509.
- [10] B. Garlyyev, S. Xue, M. D. Pohl, D. Reinisch, A. S. Bandarenka, *ACS Omega* **2018**, *3*, 15325–15331.
- [11] S. Xue, B. Garlyyev, S. Watzele, Y. Liang, J. Fichtner, M. D. Pohl, A. S. Bandarenka, *ChemElectroChem* **2018**, *5*, 2326–2329.
- [12] G. Wang, L. Zhang, J. Zhang, *Chem. Soc. Rev.* **2012**, *41*, 797–828.
- [13] a) W. Ma, Y.-L. Ying, L.-X. Qin, Z. Gu, H. Zhou, D.-W. Li, T. C. Sutherland, H.-Y. Chen, Y.-T. Long, *Nat. Protoc.* **2013**, *8*, 439; b) C. Jayabharathi, P. Ahrens, U. Hasse, F. Scholz, *J. Solid State Electrochem.* **2016**, *20*, 3025–3031.
- [14] a) D. Mei, Z. D. He, Y. L. Zheng, D. C. Jiang, Y.-X. Chen, *Phys. Chem. Chem. Phys.* **2014**, *16*, 13762–13773; b) A. Hamelin, *J. Electroanal. Chem.* **1996**, *407*, 1–11; c) P. Rodriguez, N. Garcia-Araez, M. T. M. Koper, *Phys. Chem. Chem. Phys.* **2010**, *12*, 9373–9380.
- [15] A. N. Frumkin, O. A. Petrii, *Electrochim. Acta* **1975**, *20*, 347–359.
- [16] N. Garcia-Araez, V. Climent, J. M. Feliu, *J. Phys. Chem. C* **2009**, *113*, 9290–9304.
- [17] J. Tymoczko, V. Colic, A. S. Bandarenka, W. Schuhmann, *Surf. Sci.* **2015**, *631*, 81–87.

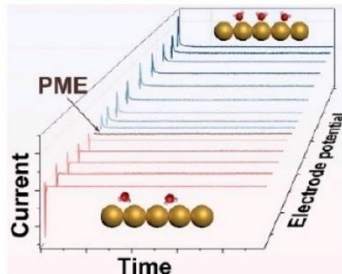
Manuscript received: April 30, 2021

Accepted manuscript online: May 29, 2021

Version of record online: ■■■, ■■■■

COMMUNICATION

Gold standards: By determining the potential of maximum entropy (PME) with the laser-induced current transient technique, the influence of the electrolyte composition on polycrystalline gold has been systematically investigated. Increasing the electrolyte pH and purging O_2 shift the PME to more positive potentials. The electric double-layer structure for Au_{pc} in solutions containing Na^+ and K^+ ions is vastly different when electrolyte pH reaches six or higher. This method enables another approach for the interpretation of interfacial electrocatalytic processes.



X. Ding, Dr. B. Garlyyev, Dr. S. A. Watzel, T. Kobina Sarpey, Prof. Dr. A. S. Bandarenka*

1 – 6

Spotlight on the Effect of Electrolyte Composition on the Potential of Maximum Entropy: Supporting Electrolytes Are Not Always Inert



The Potential of Zero Charge and the Electrochemical Interface Structure of Cu(111) in Alkaline Solutions

Andrea Auer,^{||} Xing Ding,^{||} Aliaksandr S. Bandarenka,^{*} and Julia Kunze-Liebhäuser^{*}

Cite This: <https://dx.doi.org/10.1021/acs.jpcc.0c09289>

Read Online

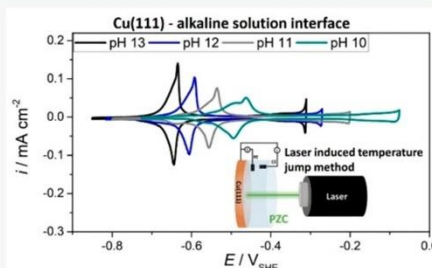
ACCESS |

Metrics & More

Article Recommendations

Supporting Information

ABSTRACT: Copper (Cu) is a unique electrocatalyst, which is able to efficiently oxidize CO at very low overpotentials and reduce CO₂ to valuable fuels with reasonable Faradaic efficiencies. Yet, knowledge of its electrochemical properties at the solid/liquid interface is still scarce. Here, we present the first two-stranded correlation of the potential of zero free charge (pzfc) of Cu(111) in alkaline electrolyte at different pH values through application of nanosecond laser pulses and the corresponding interfacial structure changes by *in situ* electrochemical scanning tunneling microscopy imaging. The pzfc of Cu(111) at pH 13 is identified at $-0.73 V_{SHE}$ in the apparent double layer region, prior to the onset of hydroxide adsorption. It shifts by (88 ± 4) mV to more positive potentials per decreasing pH unit. At the pzfc, Cu(111) shows structural dynamics at both pH 13 and pH 11, which can be understood as the onset of surface restructuring. At higher potentials, full reconstruction and electric field dependent OH adsorption occurs, which causes a remarkable decrease in the atomic density of the first Cu layer. The expansion of the Cu–Cu distance to 0.3 nm generates a hexagonal Moiré pattern, on which the adsorbed OH forms a commensurate (1×2) adlayer structure with a steady state coverage of 0.5 monolayers at pH 13. Our experimental findings shed light on the true charge distribution and its interrelation with the atomic structure of the electrochemical interface of Cu.



1. INTRODUCTION

In recent years, fundamental understanding of the electrochemical interface has been significantly improved, and this can help to further promote the development of alternative systems for clean energy provision. These advances are a prerequisite for the design of efficient electrode materials and interfaces, which allow the transformation of chemical into electric energy or *vice versa* and the synthesis of valuable chemicals.¹ Understanding the electrochemical Cu/liquid interface is of special interest, since Cu has been shown to not only efficiently electro-oxidize CO in alkaline media at low overpotentials through self-activation by the formation of high-energy undercoordinated Cu adatom structures, as we could show recently,² but also reduce CO₂ and CO to valuable hydrocarbons and alcohols with reasonable Faradaic efficiencies.³ This means that Cu is particularly intriguing in terms of its ability to act as a bidirectional electrocatalyst.

One of the most central characteristics of the solid/liquid interface is the potential of zero charge (pzc), where no excess charge prevails at the electrode,⁴ and the disorder of the interfacial water is close to a maximum.^{5,6} The pzc influences all electroadsorption properties and is thus significantly relevant for electrocatalysis in general. In the case of specific adsorption at nonideally polarizable electrodes, which adsorb hydrogen and hydroxide (OH) species, such as Pt⁷ and Cu,^{8,9} it is important to distinguish between total and free charge

density.^{4,6,10,11} The total charge includes both the surface charge, i.e. the true electronic charge on the electrode, and the fraction of charge, which is involved in the adsorption process and which consequently has crossed the interface by being transferred, e.g. from the metal to the solution side.¹² The free charge only reflects the true excess charge on the electrode surface and is therefore mainly responsible for the electric field at the interface. The potential where the total charge density vanishes is called potential of zero total charge (pztc), and the potential where the true surface excess charge density becomes zero is the potential of zero free charge (pzfc).¹¹ The strength of the interfacial electric field, as obtained by the difference between the pzfc and the actual applied electrode potential, heavily affects the electrochemical reactivity. Far away from the pzfc, at high electric fields, a rigid water layer exists very close to the electrode surface, which kinetically hinders charge transfer. Close to the pzfc, the water dipoles have a much higher degree of freedom and can more easily reorient upon

Received: October 13, 2020

Revised: February 16, 2021

charge transfer. Therefore, the activity and rate of any charge transfer reaction critically depends on the position of the pzfc, which dictates the strength of the electric field, because this determines how easily the solvent can accommodate for charge migration.¹³

Determination of the pzfc can be experimentally achieved by applying the so-called laser-induced temperature jump method.^{5,6,14–16} In principle, there are two different measurement procedures: (i) coulometric laser-induced potential transients^{6,15,17} and (ii) potentiostatic laser-induced current transients (LICT).^{14,16,18} Both rely on nanosecond laser pulses inducing a sudden temperature increase at the electrified interface, which causes a distortion of the interface structure. This temperature change as well as the response of the electrode take place at a very short time scale in the submicrosecond range.¹⁴ This allows the separation of purely capacitive processes from Faradaic processes and thus correlation of the pzt with the pzfc, because specific adsorption definitely occurs at a slower rate.^{5,19,20} With method (i), a change is induced at the open circuit potential, which, depending on its sign, is indicative of the orientation of the water dipoles. Method (ii) has been applied in this work: it leads to a certain distortion of the electrified double layer upon heating and is based on subsequent detection of the charge during reorganization of the double layer upon rapid cooling. If the electrode is negatively charged, the nanosecond laser pulse results in negative current transients, and if it is positively charged, positive current transients are measured. The potential of zero transient (pzt) is located at the potentials where the transients change their sign. It is also referred to as potential of maximum entropy (pme) in the case of method (i).

The laser-induced temperature jump method has been successfully employed for the study of interfacial fundamentals of low-index Pt,^{6,19–22} Ir,⁵ and Au^{14,15} single crystals as well as for highly stepped Pt electrocatalysts.²³ More recently, the electric field strength and the order of interfacial water could be correlated with the activity toward the hydrogen evolution reaction (HER) of Ni(OH)₂ modified Pt electrodes.^{13,24} Numerous previous studies also addressed the pH dependence of the interfacial parameters, especially for Pt group metals.^{5,19,20,22,23} Despite the importance of copper in electrocatalysis under alkaline conditions, the actual value of the pzc at the Cu/electrolyte interface under these conditions has only been reported very recently.²⁵ In this study, coulometric laser-induced potential transients have been employed for the examination of the potentials of maximum entropy (pme) of Cu(111) and Cu(100) at pH 13.²⁵ It is known that both pH and adsorption processes strongly influence the interfacial electrochemical properties of metal electrodes,^{5,10,19} i.e. their pzc, and their atomic structures.²⁶ Electrochemical scanning tunneling microscopy (EC-STM) is a powerful tool to visualize the adsorbate- and potential-induced structural changes at the interface *in situ* under perfect electrochemical control. In the case of Cu(*hkl*), electrochemical scanning probe microscopy has significantly contributed to the understanding of important interfacial processes such as SO₄^{2–}^{27,28} and OH[–] electrosorption.^{9,29–31} OH adsorption on Cu(111) is known to proceed together with a surface reconstruction where the density of the first Cu layer decreases and excess Cu is ejected to the top of the terraces in the form of small clusters.^{9,29} Previous studies regarding the OH adsorption on Cu(111) electrodes in 0.1 M NaOH found

an ordered hexagonal OH adsorbate layer with a structural parameter of (0.6 ± 0.2) nm and one adsorbate per unit cell, corresponding to a low coverage of only ~0.2 monolayers (ML) of adsorbed OH species with respect to the unreconstructed Cu(111).^{9,29} Based on the knowledge of the adsorbate lattice parameter, it was assumed that the outermost Cu layer reconstructs to adopt the Cu plane structure in Cu₂O (111) with a Cu–Cu distance of 0.3 nm, on which the OH adsorbate forms a (2 × 2) superstructure.^{9,29} Correlations of copper's activity toward catalytic processes, such as the hydrogen evolution,^{32,33} CO oxidation,² and CO₂ reduction,^{34–36} with interfacial structures has also been shown.

In this work, we provide for the first time a pH-dependent pzfc value for Cu(111) in alkaline solutions using LICT. We combine these studies with *in situ* EC-STM investigations of the electrified Cu(111)/liquid interface structure and dynamics close to the pzfc at two different pH values. This combination allows us to correlate the sign of the true charge at the interface, i.e. the position of the pzfc, with the morphological and structural evolution of the Cu(111) surface. While knowledge of the pzfc in alkaline media is highly relevant on its own, our combined *in situ* study unambiguously provides evidence for a shift of the pzfc with pH. We demonstrate that the pzfc is located at the onset of the Cu(111) reconstruction. This clear correlation emphasizes the role of the free charge on the atomic structure of Cu surfaces. We also provide new structural information on the OH adsorption on Cu(111) at pH 13. Our double-stranded approach helps to generally clarify the role of the electric field on the Cu(111) reconstruction and on the adsorption of electrolyte species. This fundamental understanding is an essential step toward unraveling the complex electrochemical behavior and electrocatalytic activity of Cu(111) electrodes.

2. EXPERIMENTAL SECTION

2.1. Chemicals and Materials. The electrolyte solutions were prepared from NaOH (99.99%, trace metal basis, SigmaAldrich), HClO₄ (99.99%, Suprapur, Merck), and ultrapure water (Milli-Q purification system, >18 MΩ cm, Merck). Ar (Messer, 5.0) was used for deaeration of the electrolytes. Cu(111) crystals (Mateck, Jülich) were mechanically polished with diamond paste (ESCIL) down to 0.25 μm, electropolished in 60% H₃PO₄ (85% EMSURE, Merck) at 1.8 V versus a Cu counter electrode and annealed in a homemade horizontal tube furnace under H₂ flow prior to each experiment. The crystals can be removed while maintaining the H₂ atmosphere, which allows a direct transfer to an Ar-filled (Messer, 5.0) glovebox (Mbraun MB 200 MOD glovebox) to perform the electrochemical scanning tunneling experiments without any traces of oxygen from air.

2.2. Electrochemical and Laser-Induced Current Transient Measurements. All cyclic voltammetry measurements were performed in a standard three-electrode cell configuration, where the electrolyte was filled in a Teflon beaker to avoid any contaminations from glassware. The use of glassware was found to significantly alter the peak shape of the OH adsorption on Cu(111);³⁷ we found however no changes in the measured charge obtained from integration of the current. All cell parts were cleaned in KMnO₄, piranha solution (H₂SO₄ and H₂O₂), and ultrapure water prior to the experiments. A carbon rod counter electrode and either a polytetrafluoroethylene (PTFE) bound activated carbon quasi-reference (AC-QRE) or a Ag/AgCl (saturated KCl) reference

B

<https://dx.doi.org/10.1021/acs.jpcc.0c09289>
J. Phys. Chem. C XXXX, XXX, XXX–XXX

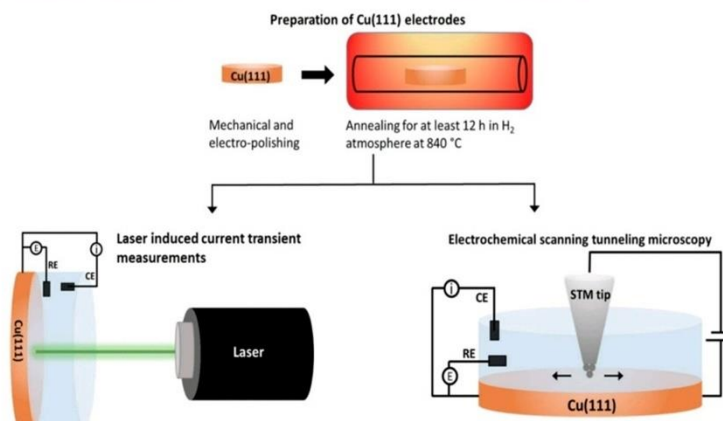


Figure 1. Scheme of preparation and characterization of the electrified Cu(111)/liquid interface. The Cu(111) crystals are reproducibly prepared by mechanical and electro-polishing and subsequent treatment in a H₂ atmosphere at 840 °C for over 12 h. The interdependence of the interface parameters and the structure is investigated *in situ* by laser-induced current transient (LICT) and electrochemical scanning tunneling microscopy (EC-STM) studies.

electrode were used for the electrochemical experiments, and the reference potentials were converted to the standard hydrogen electrode (SHE) scale. All experiments were carried out in completely deaerated, Ar-purged solution using a Biologic VSP 300 (France) potentiostat. Laser-induced current transient (LICT) measurements were carried out in a standard, three-electrode glass cell, which is unavoidable due to the specific setup; unpublished results show no effect of the glassware on the position of the pzfc. A Quanta-Ray INDI pulsed Nd:YAG laser with a wavelength of 532 nm was used for these measurements. Laser pulses with a duration of 5–8 ns (repetition rate of the laser pulse 10 Hz) and an energy of 67 mJ cm⁻² were applied to the Cu(111) crystals with an area of 0.50 cm². The spot size of the laser was adjusted to a diameter of 9 mm. All LICT measurements were performed potentiostatically within the potential range from -1.0 to -0.36 V_{SHE}, which is well below the oxidation onset of Cu(111),^{29,33} with a step size of 20 mV. A detailed description of the LICT setup is given in refs 16 and 18.

2.3. Electrochemical Scanning Tunneling Microscopy.

Electrochemical scanning tunneling microscopy (EC-STM) experiments were performed with a Keysight 5500 scanning probe microscope inside an Ar-filled glovebox to avoid any oxygen contamination. A home-built polychlorotrifluoroethylene (PCTFE) EC-STM cell was employed with polytetrafluoroethylene (PTFE) bound activated carbon quasi-reference and counter electrodes, which is described in detail in ref 38. Electrochemical etching of a tungsten wire was employed to prepare the STM tips, which were subsequently coated with Apiezon wax. The Cu(111) electrode was immersed at open circuit potential, and the formed native copper oxide monolayer was reduced prior to every experiment. The metallic surface was systematically imaged to ensure high quality and large terrace sizes. Representative STM images of the metallic Cu(111) surface are shown in Figure S1 in the Supporting Information (SI). Data representation of the STM images was performed with Gwyddion.³⁹

3. RESULTS AND DISCUSSION

To determine the interdependence of thermodynamic interface parameters and the atomic structure at different pH values in alkaline media, Cu(111) single crystals were investigated via a two-pronged approach, as illustrated in Figure 1. After careful preparation of the Cu electrodes (described in detail in the Experimental Section), they were transferred either to the laser-induced current transient (LICT) setup to determine the position of the potential of zero free charge (pzfc) or to the EC-STM setup to visualize the structures formed at the solid/liquid interface at the potentials of interest.

Cyclic voltammograms (CVs) combined with the corresponding LICT results constitute the fundament of our investigation, because they provide a macroscopic overview of the potential range of interest of Cu(111) in NaClO₄ solution for four pH values in the alkaline regime (Figure 2). The voltammetric profiles (Figure 2a) of the Cu electrode show the characteristic peak pair related to the adsorption and desorption of OH with maxima at around -0.65 V_{SHE} (0.12 V_{RHE}) for pH 13, which is in perfect agreement with the literature.^{2,5,37,40} The OH adsorption peak shows ideal Nernstian behavior with a shift of approximately 59 mV/decade in the investigated alkaline pH range (pH 13–10). It clearly exhibits two regions with different slopes in the current response, which becomes more pronounced at lower pH values. At pH 10, there are clearly two features which can be distinguished. This indicates different adsorption sites, presumably steps at lower potentials and terraces at higher potentials. The current profile of the first feature, attributed to step edge adsorption, appears less steep than the second one. With lower pH, i.e. lower OH⁻ concentration, it flattens further. The sharpness and reversibility of the feature at higher potentials, which might be due to a phase transition of the OH adsorbate, e.g. to an ordered adlayer, is largely conserved for pH 13 and 12 and flattens at pH 11 and 10. The estimated charge from integration of the current density decreases linearly with decreasing pH, exhibiting apparent OH coverages of 0.46 monolayers (ML) at pH 13 and 0.22 ML at pH 10 (see Figure 2b). We must note that, in contrast to consistent CVs of

C

<https://dx.doi.org/10.1021/acs.jpcc.0c09289>
J. Phys. Chem. C XXXX, XXX, XXX–XXX

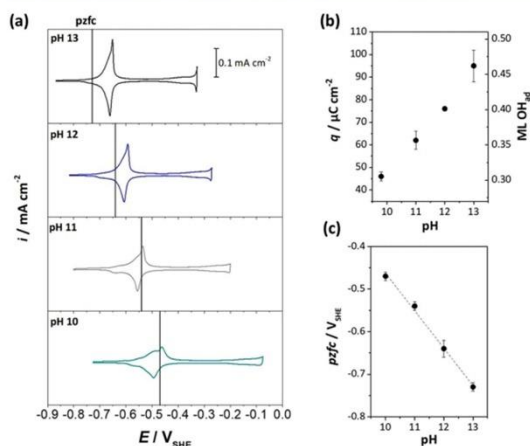


Figure 2. Interdependence of the potential of zero free charge (pzfc) and current versus potential cycles. (a) Cyclic voltammograms (CVs) of Cu(111) in 0.1 M NaClO₄ at different pH values showing the electrochemical behavior in the potential range between $-0.9 V_{SHE}$ and $0.0 V_{SHE}$ (scan rate: 50 mV s^{-1}). The observed peak pairs correspond to the adsorption and desorption of OH⁻ ions from the alkaline solutions. The vertical lines mark the positions of the pzfc. Dependence of (b) the estimated charge, i.e. the coverage with apparent OH monolayers, and (c) the pzfc on the pH. The error bar in (b) is determined through averaging of the charges of at least 3 CVs; the error bars in (c) correspond to the widths of the x -axis intercepts determined from Figure 3a–d.

single crystalline Au and Pt, the voltammetric response of Cu in alkaline solution shows small discrepancies over the literature, which is due to the influence of surface pretreatment, applied potential range,⁴¹ and effect of dissolved glass ware.⁴⁰ Nevertheless, the CV at pH 13 in Figure 2a clearly does not show any additional feature due to the presence of perchlorate ions in the alkaline solution (see the CV of Cu(111) measured in 0.1 M NaOH shown in Figure S2 for comparison), which means that no visible specific adsorption of ClO₄⁻, i.e. a charge transfer reaction, occurs. The pzfc values for Cu(111), i.e. the pzfc, where no excess free charge resides on the metal, are measured at $-0.73 V_{SHE}$, $-0.64 V_{SHE}$, $-0.54 V_{SHE}$, and $-0.47 V_{SHE}$ for pH 13, 12, 11, and 10, respectively (see vertical lines in Figure 2a and Figure 3), which corresponds to a shift of $(88 \pm 4) \text{ mV}$ per pH unit on the SHE scale or approximately 29 mV/dec on the RHE scale (see Figure 2c). At pH 13, the pzfc is located within the apparent double layer region, before the onset of the OH adsorption in good agreement with the pme of $-0.71 V_{SHE}$ for Cu(111), that was very recently reported in ref 25. It continuously shifts toward higher potentials for lower pH values and is therefore located within the OH adsorption region for both pH 11 and 10.

Figure 3 depicts the calculated charge densities q from integration of the current transients of Cu(111) at the four different pH values as functions of the electrode potential E . The corresponding maximum current values are shown in Figure S3. Mean values and standard deviations of the charges result from averaging six (pH 13 and 12) or three (pH 11 and 10) transient data sets (see Figure 3a–d). The x -intercepts are determined through linear fits of the q versus E plots. This linear behavior is expected for an equivalent circuit consisting of the solution resistance and the double layer capacitance in

series and is, therefore, representative for the double layer region of the given Cu(111)/liquid interface. However, it has to be noted that the double layer charge is only partially measured with LICT.⁴² Remarkably, the slopes of the q versus E plots are all in the same capacitance range between 0.3 and $0.4 \mu F \text{ cm}^{-2}$, independent of the pH value, and a linear charge increase is also observed at potentials more positive than the OH adsorption regions in all cases. This strongly indicates that the specific OH adsorption charge does not contribute to the laser-induced current transients.

The original LICT data are shown as 3D plots in Figure S4. All recorded current transients in the whole pseudocapacitive potential range show a rather monotonic decay after the sharp increase due to the laser pulse (Figure 3e,f). Semilogarithmic plots of two representative current transients are depicted in Figure S5. The mostly linear decay of the transients implies that the dominating contribution to the responses is solvent reorganization,^{5,25} i.e. that no specific adsorption process is measured. Bipolar or nonmonotonous responses would clearly indicate an overlap of different processes with unequal rates, such as double-layer restructuring and specific adsorption of ions. Such nonmonotonous profiles have been previously reported for highly acidic or alkaline conditions and are due to fast adsorption processes.^{19,20} In the present case, the recorded decay is influenced by the large cell constant of $160\text{--}250 \Omega$, as it is usually found in LICT measurements, which makes kinetic studies of the relaxation process in the microsecond time-scale difficult, and which limits the accuracy for the detection of different time constants. However, laser-induced current transients are well deployable for the determination of the pzfc if specific adsorption contributions can be excluded. Here, the absence of the contribution of specific adsorption can be based on the linear q versus E trends in Figure 3 that show the same slopes for all four pH values.

A similar pH dependence of the pzfc, determined with the temperature jump method, has been reported for the case of Pt(111) in alkaline solution, where a positive pzt shift with decreasing pH is found resulting in pzfc values lying within the OH adsorption regime.²⁰ This is in contrast to acidic or neutral media, where the pzfc of Pt electrodes was found to be constant with pH on the SHE scale.²² A comparable shift of the pzt by 30 mV/dec on the RHE scale has been reported for Ir(111) electrodes in solutions ranging from pH 5 to 1.⁵ The pH dependence of the pzfc of metals that adsorb hydrogen and OH species, e.g. Pt group metals, has been described through theoretical thermodynamic analysis with the following equation:¹⁰

$$\left(\frac{\partial E}{\partial \mu_{H^+}} \right)_{\sigma=0} = \frac{1}{1 - \left(\frac{\partial \sigma}{\partial F \Gamma_H} \right)_{E_{RHE}, \mu_{CA}}} \quad (1)$$

where E is the electrode potential measured versus a constant reference electrode,¹⁰ μ_{H^+} and μ_{CA} are the chemical potentials of the H⁺ and the salt (CA: cation, anion) ions, σ is the free charge density, $F \Gamma_H$ is the thermodynamic excess charge of adsorbed hydrogen, and F the Faraday constant. According to this equation, the pzfc is independent of the pH, when it lies within the double layer region and $\left(\frac{\partial \sigma}{\partial F \Gamma_H} \right) \rightarrow -\infty$. If the pzfc lies within the hydrogen region, there are several cases: (i) The adsorption does not involve any change in the free charge,

D

<https://dx.doi.org/10.1021/acs.jpcc.0c09289>
J. Phys. Chem. C XXXX, XXX, XXX–XXX

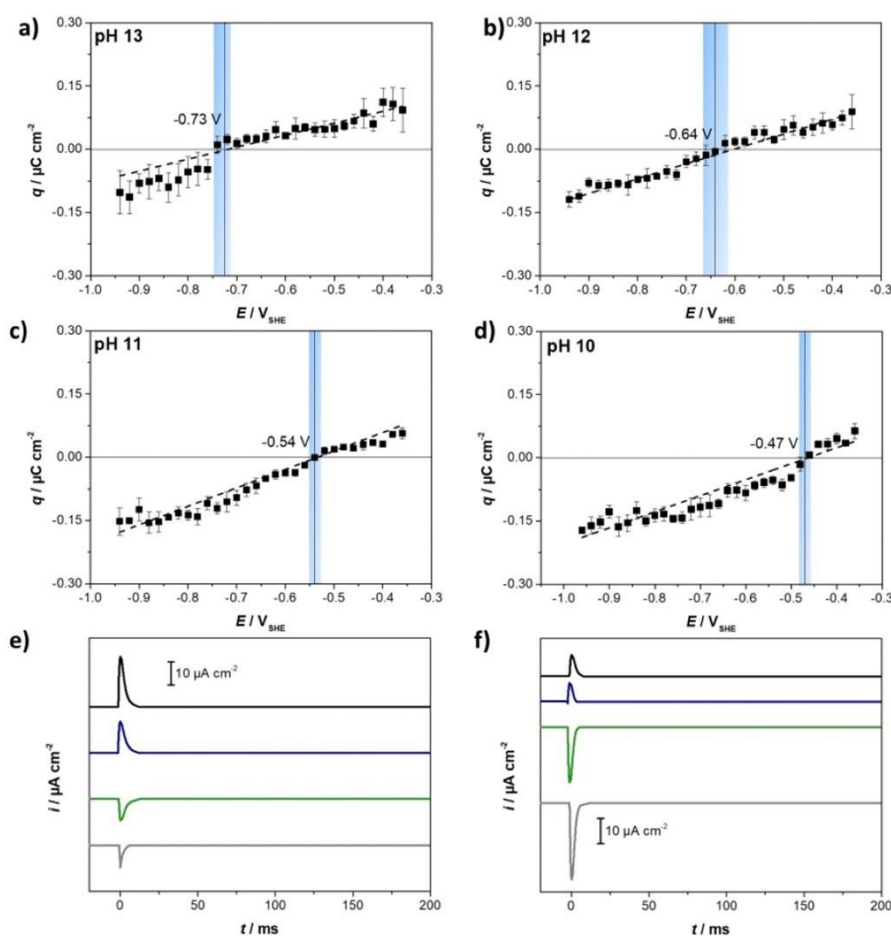


Figure 3. pH dependence of the pzc at Cu(111). Calculated charge densities q from integration of the current transients vs E in 0.5 M NaClO₄ at (a) pH 13, (b) pH 12, (c) pH 11, and (d) pH 10. Examples of the recorded transients at selected potentials after background subtraction are shown for pH 13 (e) and pH 11 (f); selected semilogarithmic plots are shown in Figure S5 in the Supporting Information.

which leads to $\left(\frac{\partial \sigma}{\partial F_{\text{H}}}\right)_{E_{\text{RHE}}, \mu_{\text{Ca}}} = 0$ and a shift of -59 mV/dec with increasing pH. (ii) The hydrogen adsorption has an effect of $1 > \left(\frac{\partial \sigma}{\partial F_{\text{H}}}\right) > 0$ on the free charge, and the potential shift toward negative potentials is even greater than that for the potential of the RHE.¹⁰ It therefore seems reasonable that an analogous expression exists for the dependence of the free charge on the excess charge of adsorbed OH, F_{OH} , which explains the observed shift of the pzc with pH for Cu(111) in highly alkaline solution. This influence of adsorbates on the free charge is expected to be very similar to an adsorbate induced change in the work function of a metal.⁴³

In order to clarify the interdependence of the reconstruction, the OH adsorption process and the free excess charge at the metal, as determined by the position of the pzc, *in situ* ECSTM imaging was employed. Due to the observed pzc shift toward higher potentials with lower pH, and its apparent overlap with the OH adsorption regime (see Figure 2),

possible charge and/or adsorption induced interface changes at both pH 13 and pH 11 are investigated. Figure 4 shows ECSTM image sequences during potential steps from the apparent double layer region to the pzc at pH 13 (Figure 4a) and pH 11 (Figure 4b). At both pH 13 and 11, the metallic Cu(111) surface is first imaged at sufficiently negative potentials $E < \text{pzc}$. Both surfaces are characterized by terraces and (vacancy) islands mostly separated by monatomic steps. After the potential step to the pzc at pH 13 (-0.75 V_{SHE}), small changes of the surface morphology are observed within 15 min (Figure 4a). After prolonged time at the pzc (~ 23 min), substantial (vacancy) island growth and vanishing is visible. Black and yellow boxes and arrows in Figure 4a mark identical positions in the images where vacancy islands or islands form. The observed changes must result from a movement of surface atoms and a starting reconstruction of the topmost Cu layer, which is likely due to an adaption of the surface structure to the change of charge. At a slightly more positively charged electrode (at -0.70 V), gradual surface changes are still observed for over 100 min, but they occur

E

<https://dx.doi.org/10.1021/acs.jpcc.0c09289>
J. Phys. Chem. C XXXX, XXX, XXX–XXX

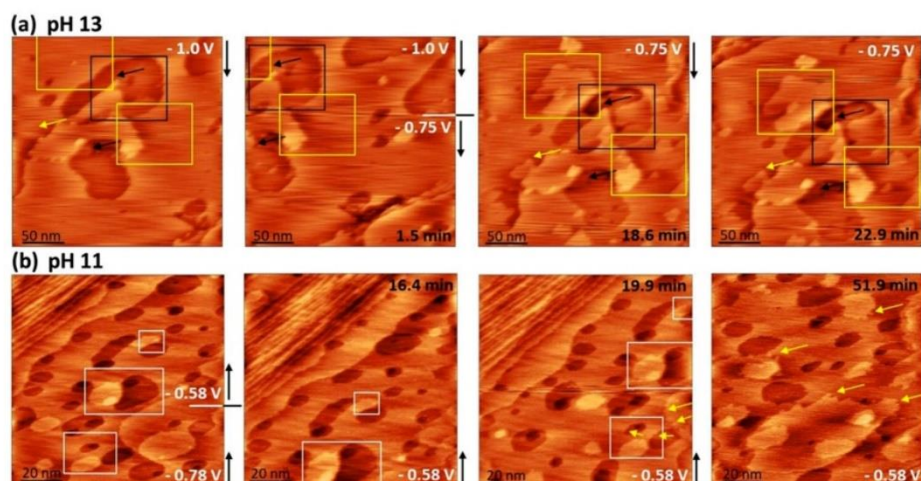


Figure 4. EC-STM imaging to visualize structural and morphological changes at the pzc. Time- and potential-dependent sequences of EC-STM images at pH 13 (a) and pH 11 (b). The morphology of the surface undergoes gradual changes, which are highlighted with black (vacancy island formation) and yellow (island formation) squares and arrows in (a), marking the position of identical spots on the surface that slightly move due to a drift in the images. The white boxes in (b) mark identical spots, while yellow arrows point to morphologically changed step edges. (a) Size = (250×250) nm². (b) Size = (100×100) nm², $I_{ip} = 1$ nA, $E_{ip} = -0.40$ V_{SHE}.

more drastically than at the pzc (Figure S6 in the Supporting Information). At pH 11, the potential step to the pzc (-0.58 V_{SHE}) does also not lead to abrupt morphology or structure changes (Figure 4b). Only step edge roughening, an indication of OH specifically adsorbing at the step edges, is observed after prolonged imaging of >20 min (see Figure 4b, yellow arrows). The drift in Figure 4b does not allow comparison of identical spots (marked with white boxes in Figure 4b) after prolonged cycling, but careful analysis of the step edge appearance clearly shows that roughening occurs. For additional clarity, low resolution images demonstrating the homogeneity of the Cu(111) surface before and after the step edge roughening are depicted in Figure S7. The appearance and disappearance of islands and the roughening of steps observed at both pH 13 and pH 11 within a comparable time period is a clear indication of surface mass transport.

At pH 11, the pzc is positioned where clear Faradaic currents are observed in the CV. Nonetheless, no distinct structural changes are visible on the terraces at this potential. This and the very pronounced step edge roughening supports our hypothesis that the shoulder at more negative potentials, which becomes more pronounced at lower pH values, might be attributed to OH adsorption at step edges. One plausible explanation for our findings is that the pzc triggers the reconstruction and that the Cu–Cu distance widening is a structural adjustment to the induced positive charge. The role of the sharp feature at more positive potentials in the CVs is elucidated through a potential step beyond this peak and subsequent imaging with EC-STM at pH 13 and 11 (Figure 5). A much higher degree of mass transport and a complete reconstruction of the Cu(111) surface, as manifested by the nucleation and growth of numerous Cu islands,⁹ is observed. After full reconstruction and OH adsorption, the surface morphology and structure are found to be completely static in the time frame of the experiment, which clearly differs from the observations at the pzc. At both pH 13 and pH 11, small

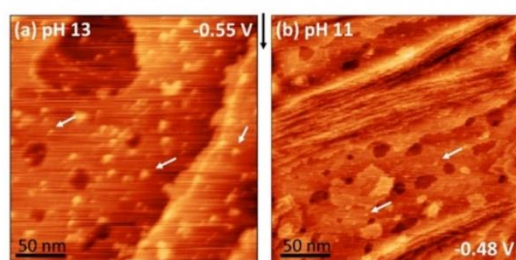


Figure 5. Steady-state surface morphology and structure of Cu(111) after OH adsorption at (a) pH 13 and (b) pH 11. Size = (250×250) nm², $I_{ip} = 1$ nA, $E_{ip} = -0.40$ V_{SHE}.

adsorbed Cu clusters are formed due to the ejection of excess Cu, which seem to form both round and linear structures that especially reside at the step edges (see Figure 5, marked with arrows). On Cu in alkaline media, this is known to result from the formation of a less dense first Cu layer, where the Cu–Cu distance is increased, and the excess Cu is ejected to the top of the terraces in the form of small, adsorbed clusters.^{9,28}

Previous structure studies of the Cu(111) reconstruction were performed in O₂ containing alkaline solutions,^{9,29} and it is very likely that due to the high oxygen affinity of Cu, the molecular O₂ influences the OH adsorption process, e.g. by coadsorption or dissociation at the electrode surface. In the following, we present new structural information on the OH adsorbate layer imaged in completely deaerated alkaline solution at pH 13 (see Figure 6) in an Ar-filled glovebox (see Experimental Section). It is important to note that we could only image this structure at potentials after the sharp feature of the OH adsorption peak. This and the sharp and reversible occurrence of the peak indicates that it originates from a transition from a random to an ordered OH adsorbate layer. High resolution STM images at -0.55 V_{SHE} exhibit both

F

<https://dx.doi.org/10.1021/acs.jpcc.0c09289>
J. Phys. Chem. C XXXX, XXX, XXX–XXX

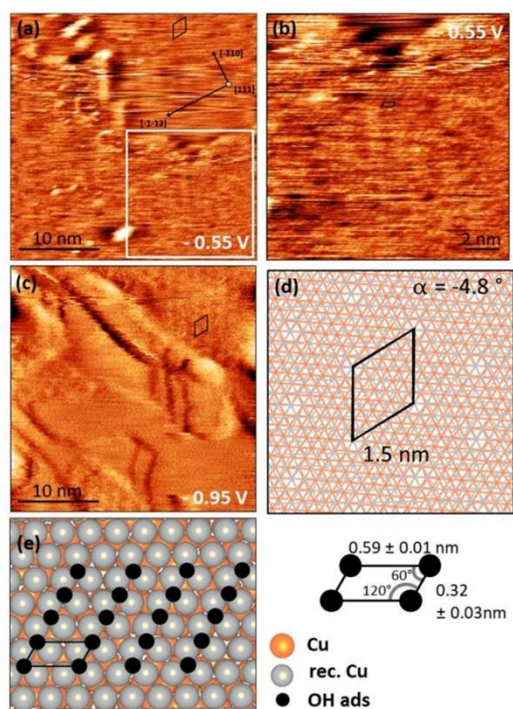


Figure 6. OH-adsorbate structure and its Moiré pattern are visible under exclusion of ambient air at pH 13. ((a) and (b)) High resolution images of Cu(111) at the OH adsorption potential ($-0.55 V_{\text{SHE}}$). The zoom marked in (a) is shown in (b). (c) Image of the Moiré structure, which is still partially present even after OH desorption at $-0.95 V$. Structural models: (d) hexagonal long-range modulation (Moiré pattern), (e) commensurate (1×2) superstructure of adsorbed OH on the reconstructed Cu surface.

a short-range ordered structure as well as a long-range modulation, which is attributed to a Moiré pattern (Figure 6a and b). A similar coincidence cell was observed upon SO_4^{2-} adsorption on Cu(111) at positive potentials in dilute acidic electrolyte.²⁷ The OH adsorbate induced Moiré pattern is locally persistent after OH desorption, as shown in Figure 6c. The observed hexagonal modulation can be best rationalized by an expansion of the first Cu layer to a Cu–Cu distance of 0.3 nm and a rotation of -4.8° (see Figure 6d). In this model, the Moiré periodicity of 1.5 nm is caused by the lattice mismatch between the first expanded and the second nonexpanded Cu layer. Despite the rather limited quality of the images, due to tunneling in alkaline electrolyte in a glovebox, it can be furthermore assumed, based on the intermolecular distances and angles measured in Figure 6, that the adsorbed OH forms a commensurate (1×2) structure on the reconstructed Cu layer. This corresponds to 0.5 ML of adsorbed hydroxyl species with respect to the reconstructed Cu. A possible model including the unit cell is depicted in Figure 6e. It has to be noted that a (2×2) OH adsorbate structure formation cannot be excluded if the STM data alone are considered. In the literature, the coverage determined by integration of the current density of the CV usually corresponds to 0.33 ML, which is always related to the

unreconstructed Cu(111) layer and thus to a charge of $\sim 280 \mu\text{C cm}^{-2}$, which is calculated by assuming the presence of one OH molecule per Cu atom of the unreconstructed surface.^{37,44} The new structural insights provided by the EC-STM images in this work make it possible to correlate the OH adsorbate layer with the reconstructed Cu surface, which corresponds to $\sim 205 \mu\text{C cm}^{-2}$, i.e. 1.28×10^{15} atoms/ cm^2 . These considerations yield ~ 0.5 ML OH coverage with respect to the reconstructed surface, both estimated from the CV measurements ($(95 \pm 7) \mu\text{C cm}^{-2}$ or (0.46 ± 0.04) ML) and determined from the STM images (see Figure 6). This correlation adds evidence to the proposed OH adlayer structure. A first indication of two different OH adsorption domains is presented in Figure S8 in the Supporting Information. It is noteworthy that, in all the OH adsorption experiments that we conducted under exclusion of air inside the glovebox, the adsorbate structure with its dark appearance initiating to form at the terrace borders, well-known from previous studies,^{9,29,45} could never be observed, while we were able to image it in an EC-STM outside the glovebox under air exposure with the same single crystals (see Figure S9). This clearly indicates that oxygen plays a crucial role for this type of reconstruction. It is very likely that the Moiré pattern has not been visible earlier, due to coadsorption phenomena of oxygen.

The general trend of Cu electrodes to reconstruct dynamically not only upon anion adsorption but also under reaction conditions, e.g., during hydrogen evolution,^{32,33} $\text{CO}_{(2)}$ reduction,^{34–36} or CO oxidation,² can be rationalized by its low cohesive energy of 3.5 eV compared to other, more stable metals like Pt (5.84 eV).⁴⁶ Therefore, the restructuring of Cu electrodes, here due to adjustment of the first Cu layer to the induced positive surface charge after the pzfc and subsequent anion adsorption, is an important factor that influences its electrochemical reactivity.

4. CONCLUSION

We have shown that interfacial conditions, such as the potential dependent electrode charge with respect to the pzfc, largely influence the atomic structure of the Cu(111) electrode surface, and *vice versa*, which has essential consequences for electrochemical reactions in which surface adsorbates are involved. This plays a central role in electrocatalysis due to the importance of the catalyst surface properties for intermediate adsorption and activation. For the first time, the pzfc of Cu(111) has been measured as a function of pH in alkaline media and is found to move to more positive potentials by (88 ± 4) mV per decreasing pH unit. While at pH 13 the pzfc lies in the apparent double layer region, prior to the onset of OH adsorption, it continuously shifts toward more positive potentials reaching a position within the OH adsorption regime at lower pH values. *In situ* EC-STM imaging at pH 13 and pH 11 reveal that the Cu(111) surface slowly starts to restructure at the pzfc, where first subtle morphology and structure changes are observed, while no OH adsorbate layer is yet visible on the terraces. This slow change assigned to the onset of the Cu(111) reconstruction is understood as a direct consequence of the change in free excess metal charge that is determined by the position of its pzfc in alkaline solutions. The driving force for the OH adsorption process is then triggered by the increasing positive free charge on the metal with further increasing potential. The adsorption charge directly relates to the strength of the electric field at the interphase. Consequently, the strongest electric

G

<https://dx.doi.org/10.1021/acs.jpcc.0c09289>
J. Phys. Chem. C XXXX, XXX, XXX–XXX

field leads to the highest OH adsorption charge at pH 13. The sharp feature in the CV possibly marks the transition to an ordered OH adsorbate layer that can be visualized at sufficiently positive potentials under the conditions applied in this work. At pH 13, high-resolution STM images recorded under oxygen exclusion reveal a (1 × 2) adsorbate layer of OH species on the reconstructed first Cu layer, which expands to a Cu–Cu distance of 0.3 nm upon reconstruction. Due to the mismatch between the lattice parameters of the reconstructed first and the nonreconstructed second Cu layer, a hexagonal Moiré pattern appears. These findings give a realistic picture of the electrochemical Cu(111)/electrolyte interface in an alkaline environment and emphasize the possibility of soft coinage metals, such as Cu, Ag, or Au, which are important in electrocatalysis, to undergo similar reconstructions under electrochemical reaction conditions, which strongly influences their activity.

■ ASSOCIATED CONTENT

Supporting Information

The Supporting Information is available free of charge at <https://pubs.acs.org/doi/10.1021/acs.jpcc.0c09289>.

Additional EC-STM images for pH 13 and pH 11; CV of Cu(111) in pure NaOH; maximum current values of the transient versus E plot, 3D plots of laser-induced current transients of Cu(111); semilogarithmic plots of current transients; structural model of two rotational adsorption domains (PDF)

■ AUTHOR INFORMATION

Corresponding Authors

Julia Kunze-Liebhäuser – Institute of Physical Chemistry, University Innsbruck, Innsbruck 6020, Austria; orcid.org/0000-0002-8225-3110; Email: julia.kunze@uibk.ac.at
Aliaksandr S. Bandarenka – Physics of Energy Conversion and Storage (ECS), Physics Department, Technical University of Munich, 85748 Garching, Germany; Catalysis Research Center TUM, 85748 Garching, Germany; orcid.org/0000-0002-5970-4315; Email: bandarenka@ph.tum.de

Authors

Andrea Auer – Institute of Physical Chemistry, University Innsbruck, Innsbruck 6020, Austria; orcid.org/0000-0002-8004-1587
Xing Ding – Physics of Energy Conversion and Storage (ECS), Physics Department, Technical University of Munich, 85748 Garching, Germany

Complete contact information is available at: <https://pubs.acs.org/doi/10.1021/acs.jpcc.0c09289>

Author Contributions

[†]A.A. and X.D. contributed equally.

Notes

The authors declare no competing financial interest.

■ ACKNOWLEDGMENTS

A.A. is a recipient of a doctorate (DOC) Fellowship of the Austrian Academy of Sciences at the Institute of Physical Chemistry. X.D. acknowledges financial support from the China Scholarship Council. A.B. acknowledges financial support from German Research Foundation (DFG) under

Germany's Excellence Strategy–EXC 2089/1–390776260, cluster of excellence “e-conversion” which is gratefully acknowledged. J.K.-L. acknowledges funding by the Austrian Science Fund (FWF) via Grant I-4114-N37. We acknowledge V. Climent and J. Feliu from the University of Alicante, who made us aware of the importance of avoiding glassware in the Cu(111) electrochemistry.

■ REFERENCES

- (1) Markovic, N. M. Electrocatalysis: Interfacing Electrochemistry. *Nat. Mater.* **2013**, *12*, 101–102.
- (2) Auer, A.; Andersen, M.; Wemig, E. M.; Hörmann, N. G.; Buller, N.; Reuter, K.; Kunze-Liebhäuser, J. Self-Activation of Copper Electrodes during CO Electro-Oxidation in Alkaline Electrolyte. *Nat. Catal.* **2020**, *3*, 797–803.
- (3) Nitopi, S.; Bertheussen, E.; Scott, S. B.; Liu, X.; Engstfeld, A. K.; Horch, S.; Seger, B.; Stephens, I. E. L.; Chan, K.; Hahn, C.; et al. Progress and Perspectives of Electrochemical CO₂ Reduction on Copper in Aqueous Electrolyte. *Chem. Rev.* **2019**, *119*, 7610–7672.
- (4) Frumkin, A. N.; Petrii, O. A.; Damaskin, B. B. Potentials of Zero Charge. In *Comprehensive Treatise of Electrochemistry*; Bockris, J. O., Conway, B. E., Yeager, E., Eds.; Springer: 1980; pp 221–285.
- (5) Ganassin, A.; Sebastián, P.; Climent, V.; Schuhmann, W.; Bandarenka, A. S.; Feliu, J. M. On the pH Dependence of the Potential of Maximum Entropy of Ir(111) Electrodes. *Sci. Rep.* **2017**, *7*, 1–14.
- (6) Martínez-Hincapié, R.; Sebastián-Pascual, P.; Climent, V.; Feliu, J. M. Investigating Interfacial Parameters with Platinum Single Crystal Electrodes. *Russ. J. Electrochem.* **2017**, *53*, 227–236.
- (7) Berná, A.; Climent, V.; Feliu, J. M. New Understanding of the Nature of OH Adsorption on Pt(111) Electrodes. *Electrochem. Commun.* **2007**, *9* (12), 2789–2794.
- (8) Jović, V. D.; Jović, B. M. Surface Reconstruction during the Adsorption/Desorption of OH-Species onto Cu(111) and Cu(100) in 0.1 M NaOH Solution. *J. Serb. Chem. Soc.* **2002**, *67*, 531–546.
- (9) Maurice, V.; Strehblow, H.-H.; Marcus, P. In Situ STM Study of the Initial Stages of Anodic Oxidation of Cu(111) in Aqueous Solution. *Surf. Sci.* **2000**, *458*, 185–194.
- (10) Frumkin, A. N.; Petrii, O. A. Potentials of Zero Total and Zero Free Charge of Platinum Group Metals. *Electrochim. Acta* **1975**, *20*, 347–359.
- (11) Trasatti, S.; Lust, E. The Potential of Zero Charge. In *Modern Aspects of Electrochemistry*; White, R. E., Ed.; Springer: New York, 1999; pp 1–215.
- (12) Bockris, J. O.; Khan, S. U. M. *Surface Electrochemistry - A Molecular Level Approach*; Springer Science+Business: New York, 1993.
- (13) Ledezma-Yanez, I.; Wallace, W. D. Z.; Sebastián-Pascual, P.; Climent, V.; Feliu, J. M.; Koper, M. T. M. Interfacial Water Reorganization as a pH-Dependent Descriptor of the Hydrogen Evolution Rate on Platinum Electrodes. *Nat. Energy* **2017**, *2*, 17031.
- (14) Climent, V.; Coles, B. A.; Compton, R. G. Laser Induced Current Transients Applied to a Au(111) Single Crystal Electrode. A General Method for the Measurement of Potentials of Zero Charge of Solid Electrodes. *J. Phys. Chem. B* **2001**, *105*, 10669–10673.
- (15) Climent, V.; Coles, B. A.; Compton, R. G. Laser-Induced Potential Transients on a Au(111) Single-Crystal Electrode. Determination of the Potential of Maximum Entropy of Double-Layer Formation. *J. Phys. Chem. B* **2002**, *106*, 5258–5265.
- (16) Scieszka, D.; Yun, J.; Bandarenka, A. S. What Do Laser-Induced Transient Techniques Reveal for Batteries? Na- and K-Intercalation from Aqueous Electrolytes as an Example. *ACS Appl. Mater. Interfaces* **2017**, *9*, 20213–20222.
- (17) Benderskii, V. A.; Velichko, G. I. Temperature Jump in Electric Double-Layer Study. Part I. Method of Measurements. *J. Electroanal. Chem. Interfacial Electrochem.* **1982**, *140*, 1–22.
- (18) Scieszka, D.; Sohr, C.; Scheibenbogen, P.; Marzak, P.; Yun, J.; Liang, Y.; Fichtner, J.; Bandarenka, A. S. Multiple Potentials of

H

<https://dx.doi.org/10.1021/acs.jpcc.0c09289>
J. Phys. Chem. C XXXX, XXX, XXX–XXX

- Maximum Entropy for a $\text{Na}_2\text{Co}[\text{Fe}(\text{CN})_6]$ Battery Electrode Material: Does the Electrolyte Composition Control the Interface? *ACS Appl. Mater. Interfaces* **2018**, *10*, 21688–21695.
- (19) García-Araez, N.; Climent, V.; Feliu, J. Potential-Dependent Water Orientation on Pt(111), Pt(100), and Pt(110), as Inferred from Laser-Pulsed Experiments. Electrostatic and Chemical Effects. *J. Phys. Chem. C* **2009**, *113*, 9290–9304.
- (20) Sarabia, F. J.; Sebastián, P.; Climent, V.; Feliu, J. M. New Insights into the Pt (hkl)-Alkaline Solution Interphases from the Laser Induced Temperature Jump Method. *J. Electroanal. Chem.* **2020**, *872*, 114068.
- (21) Climent, V.; Coles, B. A.; Compton, R. G. Coulostatic Potential Transients Induced by Laser Heating of a Pt(111) Single-Crystal Electrode in Aqueous Acid Solutions. Rate of Hydrogen Adsorption and Potential of Maximum Entropy. *J. Phys. Chem. B* **2002**, *106*, 5988–5996.
- (22) Sebastián, P.; Martínez-Hincapié, R.; Climent, V.; Feliu, J. M. Study of the Pt (111) | Electrolyte Interface in the Region Close to Neutral pH Solutions by the Laser Induced Temperature Jump Technique. *Electrochim. Acta* **2017**, *228*, 667–676.
- (23) García-Araez, N.; Climent, V.; Feliu, J. M. Potential-Dependent Water Orientation on Pt(1 1 1) Stepped Surfaces from Laser-Pulsed Experiments. *Electrochim. Acta* **2009**, *54*, 966–977.
- (24) Sarabia, F. J.; Sebastián-Pascual, P.; Koper, M. T. M.; Climent, V.; Feliu, J. M. Effect of the Interfacial Water Structure on the Hydrogen Evolution Reaction on Pt(111) Modified with Different Nickel Hydroxide Coverages in Alkaline Media. *ACS Appl. Mater. Interfaces* **2019**, *11* (1), 613–623.
- (25) Sebastián-Pascual, P.; Sarabia, F. J.; Climent, V.; Feliu, J. M.; Escudero-Escribano, M. Elucidating the Structure of the Cu-Alkaline Electrochemical Interface with the Laser-Induced Temperature Jump Method. *J. Phys. Chem. C* **2020**, *124* (42), 23253–23259.
- (26) Magnussen, O. M. Ordered Anion Adlayers on Metal Electrode Surfaces. *Chem. Rev.* **2002**, *102*, 679–726.
- (27) Broekmann, P.; Wilms, M.; Arenz, M.; Sp, A.; Wandelt, K. Atomic Structure of Cu (111) Surfaces in Dilute Sulfuric Acid Solution. In *Topics in Applied Physics, Solid-liquid Interfaces; Macroscopic Phenomena – Microscopic Understanding*; Wandelt, K., Thurgate, S., Eds.; Springer: Heidelberg, 2003; Vol. 85, pp 141–199.
- (28) Arenz, M.; Broekmann, P.; Lennartz, M.; Vogler, E.; Wandelt, K. In-Situ Characterization of Metal/Electrolyte Interfaces: Sulfate Adsorption on Cu(111). *Phys. Status Solidi Appl. Res.* **2001**, *187*, 63–74.
- (29) Kunze, J.; Maurice, V.; Klein, L. H.; Strehblow, H. H.; Marcus, P. In Situ STM Study of the Effect of Chlorides on the Initial Stages of Anodic Oxidation of Cu(111) in Alkaline Solutions. *Electrochim. Acta* **2003**, *48*, 1157–1167.
- (30) Matsuoka, O.; Ono, S. S.; Nozoye, H.; Yamamoto, S. Structure and Dynamics of Oxy Overlayer on Cu(111) Electrode Surfaces in Alkaline Aqueous Solution Revealed by Electrochemical STM and Quartz Crystal Microbalance Measurement. *Surf. Sci.* **2003**, *545*, 8–18.
- (31) Cruickshank, B. J.; Sneddon, D. D.; Gewirth, A. A. In Situ Observations of Oxygen Adsorption on a Cu(100) Substrate Using Atomic Force Microscopy. *Surf. Sci.* **1993**, *281*, 308–314.
- (32) Huynh, T. M. T.; Broekmann, P. From In Situ towards In Operando Conditions: Scanning Tunneling Microscopy Study of Hydrogen Intercalation in Cu(111) during Hydrogen Evolution. *ChemElectroChem* **2014**, *1*, 1271–1274.
- (33) Matsushima, H.; Taranovskyy, A.; Haak, C.; Gründer, Y.; Magnussen, O. M.; Gründer, Y.; Magnussen, O. M.; Gründer, Y.; Magnussen, O. M. Reconstruction of Cu(100) Electrode Surfaces during Hydrogen Evolution. *J. Am. Chem. Soc.* **2009**, *131*, 10362–10363.
- (34) Huang, J.; Hörmann, N.; Oveisi, E.; Loiudice, A.; De Gregorio, G. L.; Andreussi, O.; Marzari, N.; Buonsanti, R. Potential-Induced Nanoclustering of Metallic Catalysts during Electrochemical CO_2 Reduction. *Nat. Commun.* **2018**, *9*, 1–9.
- (35) Grosse, P.; Gao, D.; Scholten, F.; Sinev, I.; Mistry, H.; Roldan Cuenya, B. Dynamic Changes in the Structure, Chemical State and Catalytic Selectivity of Cu Nanocubes during CO_2 Electroreduction: Size and Support Effects. *Angew. Chem., Int. Ed.* **2018**, *57*, 6192–6197.
- (36) Kim, Y. G.; Javier, A.; Baricuatro, J. H.; Torelli, D.; Cummins, K. D.; Tsang, C. F.; Hemminger, J. C.; Soriaga, M. P. Surface Reconstruction of Pure-Cu Single-Crystal Electrodes under CO_2 Reduction Potentials in Alkaline Solutions: A Study by Seriatim ECSTM-DEMS. *J. Electroanal. Chem.* **2016**, *780*, 290–295.
- (37) Tiwari, A.; Heenen, H. H.; Bjørnlund, A. S.; Maagaard, T.; Cho, E.; Chorkendorff, I.; Kristoffersen, H. H.; Chan, K.; Horch, S. Fingerprint Voltammograms of Copper Single Crystals under Alkaline Conditions: A Fundamental Mechanistic Analysis. *J. Phys. Chem. Lett.* **2020**, *11*, 1450–1455.
- (38) Auer, A.; Kunze-Liebhäuser, J. A Universal Quasi-Reference Electrode for In Situ EC-STM. *Electrochem. Commun.* **2019**, *98*, 15–18.
- (39) Necas, D.; Klapetek, P. Gwyddion: An Open-Source Software for SPM Data Analysis. *Centr. Eur. J. Phys.* **2012**, *181*–188.
- (40) Tiwari, A.; Maagaard, T.; Chorkendorff, I.; Horch, S. Effect of Dissolved Glassware on the Structure-Sensitive Part of the Cu(111) Voltammogram in KOH. *ACS Energy Lett.* **2019**, *4*, 1645–1649.
- (41) Engstfeld, A. K.; Maagaard, T.; Horch, S.; Chorkendorff, I.; Stephens, I. E. L. Polycrystalline and Single-Crystal Cu Electrodes: Influence of Experimental Conditions on the Electrochemical Properties in Alkaline Media. *Chem. - Eur. J.* **2018**, *24*, 17743–17755.
- (42) Jaworski, R. K.; McCreery, R. L. Laser-Induced Transient Currents on Glassy Carbon Electrodes. *J. Electrochem. Soc.* **1993**, *140*, 1360–1365.
- (43) Schmickler, W.; Santos, E. *Interfacial Electrochemistry*, 2nd ed.; Springer Science+Business: Heidelberg, Dordrecht, London, New York, 2010.
- (44) Bagger, A.; Arán-Ais, R. M.; Halldin Stenlid, J.; Campos dos Santos, E.; Arnarson, L.; Degn Jensen, K.; Escudero-Escribano, M.; Roldan Cuenya, B.; Rossmeisl, J. Ab Initio Cyclic Voltammetry on Cu(111), Cu(100) and Cu(110) in Acidic, Neutral and Alkaline Solutions. *ChemPhysChem* **2019**, *20*, 3096–3105.
- (45) Kunze-Liebhäuser, J. Electrochemical Scanning Tunneling Microscopy Studies of Copper Oxide Formation—A Review. In *Encyclopedia of Interfacial Chemistry*; Wandelt, K., Ed.; Elsevier: 2018; Vol. 5, pp 107–120.
- (46) Eren, B.; Zherebetsky, D.; Patera, L. L.; Wu, C. H.; Bluhm, H.; Africh, C.; Wang, L.-W.; Somorjai, G. A.; Salmeron, M. Activation of Cu(111) Surface by Decomposition into Nanoclusters Driven by CO Adsorption. *Science* **2016**, *351*, 475–478.

References

1. D. Gielen, F. Boshell, D. Saygin, M. D. Bazilian, N. Wagner and R. Gorini, *Energy Strategy Rev.*, 2019, **24**, 38-50.
2. D. Parra, L. Valverde, F. J. Pino and M. K. Patel, *Renewable Sustainable Energy Rev.*, 2019, **101**, 279-294.
3. S. Sharma, S. Basu, N. P. Shetti and T. M. Aminabhavi, *Sci. Total Environ.*, 2020, **713**, 136633.
4. H. B. Wu and X. W. D. Lou, *Sci. Adv.*, 2017, **3**, eaap9252.
5. B. Dunn, H. Kamath and J.-M. Tarascon, *Science*, 2011, **334**, 928-935.
6. Z. W. Seh, J. Kibsgaard, C. F. Dickens, I. Chorkendorff, J. K. Nørskov and T. F. Jaramillo, *Science*, 2017, **355**.
7. X. Ren, L. Dong, D. Xu and B. Hu, *Int. J. Hydrogen Energy*, 2020, **45**, 34326-34345.
8. S. A. Sherif, F. Barbir and T. N. Veziroglu, *Electr. J.*, 2005, **18**, 62-76.
9. A. X. Y. Mah, W. S. Ho, C. P. C. Bong, M. H. Hassim, P. Y. Liew, U. A. Asli, M. J. Kamaruddin and N. G. Chemmangattuvalappil, *Int. J. Hydrogen Energy*, 2019, **44**, 5661-5675.
10. F. Dawood, M. Anda and G. Shafiullah, *Int. J. Hydrogen Energy*, 2020, **45**, 3847-3869.
11. L. B. Weger, J. Leitão and M. G. Lawrence, *Int. J. Hydrogen Energy*, 2021, **46**, 5875-5890.
12. B. Tanç, H. T. Arat, Ç. Conker, E. Baltacioğlu and K. Aydin, *Int. J. Hydrogen Energy*, 2020, **45**, 26344-26356.
13. A. Olabi, T. Wilberforce and M. A. Abdelkareem, *Energy*, 2020, **214**, 118955.
14. M. A. Abdelkareem, E. T. Sayed, H. O. Mohamed, M. Obaid, H. Rezk and K.-J. Chae, *Prog. Energy Combust. Sci.*, 2020, **77**, 100805.
15. E. T. Sayed, T. Eisa, H. O. Mohamed, M. A. Abdelkareem, A. Allagui, H. Alawadhi and K.-J. Chae, *J. Power Sources*, 2019, **417**, 159-175.
16. P. Ahmadi, S. H. Torabi, H. Afsaneh, Y. Sadegheih, H. Ganjehsarabi and M. Ashjaee, *Int. J. Hydrogen Energy*, 2020, **45**, 3595-3608.
17. P. N. Sheth and B. Babu, *Int. J. Hydrogen Energy*, 2010, **35**, 10803-10810.
18. D. Milani, A. Kiani and R. McNaughton, *Int. J. Hydrogen Energy*, 2020, **45**, 24125-24145.

19. A. Ajanovic and R. Haas, *Int. J. Hydrogen Energy*, 2020, **46**, 10049-10058.
20. I. E. Agency, *The Future of Hydrogen: Seizing Today's Opportunities*. 2019.
21. S. Y. Tee, K. Y. Win, W. S. Teo, L. D. Koh, S. Liu, C. P. Teng and M. Y. Han, *Adv. Sci.*, 2017, **4**, 1600337.
22. B. You and Y. Sun, *Acc. Chem. Res.*, 2018, **51**, 1571-1580.
23. W. Wang, M. Xu, X. Xu, W. Zhou and Z. Shao, *Angew. Chem., Int. Ed.*, 2020, **59**, 136-152.
24. F. Yu, H. Zhou, Y. Huang, J. Sun, F. Qin, J. Bao, W. A. Goddard, S. Chen and Z. Ren, *Nat. Commun.*, 2018, **9**, 1-9.
25. Y. Li, J. Chen, P. Cai and Z. Wen, *J. Mater. Chem. A*, 2018, **6**, 4948-4954.
26. X. Li, J. Yu, J. Jia, A. Wang, L. Zhao, T. Xiong, H. Liu and W. Zhou, *Nano Energy*, 2019, **62**, 127-135.
27. A. S. Bandarenka, H. A. Hansen, J. Rossmeisl and I. E. Stephens, *Phys. Chem. Chem. Phys.*, 2014, **16**, 13625-13629.
28. T. Jiang, D. Mowbray, S. Dobrin, H. Falsig, B. Hvolbæk, T. Bligaard and J. K. Nørskov, *J. Phys. Chem. C*, 2009, **113**, 10548-10553.
29. C. V. Rao, C. R. Cabrera and Y. Ishikawa, *J. Phys. Chem. Lett.*, 2010, **1**, 2622-2627.
30. C. Wang, M. Chi, D. Li, D. Strmcnik, D. Van der Vliet, G. Wang, V. Komanicky, K.-C. Chang, A. P. Paulikas and D. Tripkovic, *J. Am. Chem. Soc.*, 2011, **133**, 14396-14403.
31. M. D. Pohl, V. Colic, D. Scieszka and A. S. Bandarenka, *Phys. Chem. Chem. Phys.*, 2016, **18**, 10792-10799.
32. V. Colic and A. S. Bandarenka, *ACS Catal.*, 2016, **6**, 5378-5385.
33. I. M. Sadiek, A. M. Mohammad, M. E. El-Shakre and M. S. El-Deab, *Int. J. Hydrogen Energy*, 2012, **37**, 68-77.
34. S. M. El-Refaei, M. Awad, B. El-Anadouli and M. M. Saleh, *Electrochim. Acta*, 2013, **92**, 460-467.
35. S.-Y. Ma, H.-H. Li, B.-C. Hu, X. Cheng, Q.-Q. Fu and S.-H. Yu, *J. Am. Chem. Soc.*, 2017, **139**, 5890-5895.
36. V. Murugadoss, J. Lin, H. Liu, X. Mai, T. Ding, Z. Guo and S. Angaiah, *Nanoscale*, 2019, **11**, 17579-17589.
37. X. Hu, Q. Zhou, P. Cheng, S. Su, X. Wang, X. Gao, G. Zhou, Z. Zhang and J. Liu, *Appl. Surf. Sci.*, 2019, **488**, 326-334.
38. L. R. Aveiro, A. G. da Silva, V. S. Antonin, E. G. Candido, L. S. Parreira, R. S.

- Geonmonond, I. C. de Freitas, M. R. Lanza, P. H. Camargo and M. C. Santos, *Electrochim. Acta*, 2018, **268**, 101-110.
39. Y. Yan, J. Lin, J. Cao, S. Guo, X. Zheng, J. Feng and J. Qi, *J. Mater. Chem. A*, 2019, **7**, 24486-24492.
40. G. O. Larrazábal, A. J. Martín and J. Pérez-Ramírez, *J. Phys. Chem. Lett.*, 2017, **8**, 3933-3944.
41. M. Tavakkoli, E. Flahaut, P. Peljo, J. Sainio, F. Davodi, E. V. Lobiak, K. Mustonen and E. I. Kauppinen, *ACS Catal.*, 2020, **10**, 4647-4658.
42. S. Xue, R. W. Haid, R. M. Kluge, X. Ding, B. Garlyyev, J. Fichtner, S. Watzele, S. Hou and A. S. Bandarenka, *Angew. Chem., Int. Ed.*, 2020, **59**, 10934-10938.
43. V. Colic, M. D. Pohl, D. Scieszka and A. S. Bandarenka, *Catal. Today*, 2016, **262**, 24-35.
44. M. R. Singh, E. L. Clark and A. T. Bell, *Phys. Chem. Chem. Phys.*, 2015, **17**, 18924-18936.
45. T. J. Hersbach, I. T. McCrum, D. Anastasiadou, R. Wever, F. Calle-Vallejo and M. T. Koper, *ACS Appl. Mater. Interfaces*, 2018, **10**, 39363-39379.
46. E. Pérez-Gallent, G. Marcandalli, M. C. Figueiredo, F. Calle-Vallejo and M. T. Koper, *J. Am. Chem. Soc.*, 2017, **139**, 16412-16419.
47. X. Chen, I. T. McCrum, K. A. Schwarz, M. J. Janik and M. T. Koper, *Angew. Chem., Int. Ed.*, 2017, **56**, 15025-15029.
48. L. E. Botello, J. M. Feliu and V. Climent, *ACS Appl. Mater. Interfaces*, 2020, **12**, 42911-42917.
49. M. J. Farias, C. Busó-Rogero, A. A. Tanaka, E. Herrero and J. M. Feliu, *Langmuir*, 2019, **36**, 704-714.
50. E. Garnier, F. J. Vidal-Iglesias, J. M. Feliu and J. Solla-Gullón, *Front. Chem.*, 2019, **7**, 527.
51. R. M. Arán-Ais, Y. Yu, R. Hovden, J. Solla-Gullón, E. Herrero, J. M. Feliu and H. D. Abruña, *J. Am. Chem. Soc.*, 2015, **137**, 14992-14998.
52. A. Auer, X. Ding, A. S. Bandarenka and J. Kunze-Liebhäuser, *J. Phys. Chem. C*, 2021, **125**, 5020-5028.
53. O. Bičáková and P. Straka, *Int. J. Hydrogen Energy*, 2012, **37**, 11563-11578.
54. A. C. Garcia, T. Touzalin, C. Nieuwland, N. Perini and M. T. Koper, *Angew. Chem., Int. Ed.*, 2019, **58**, 12999-13003.
55. I. Katsounaros and K. J. Mayrhofer, *Chem. Commun.*, 2012, **48**, 6660-6662.
56. D. Strmcnik, K. Kodama, D. van der Vliet, J. Greeley, V. R. Stamenkovic and

- N. Marković, *Nat. Chem.*, 2009, **1**, 466-472.
57. J. Suntivich, E. E. Perry, H. A. Gasteiger and Y. Shao-Horn, *Electrocatalysis*, 2013, **4**, 49-55.
 58. J. Tymoczko, V. Colic, A. Ganassin, W. Schuhmann and A. S. Bandarenka, *Catal. Today*, 2015, **244**, 96-102.
 59. M. A. Omole, V. A. Okello, V. Lee, L. Zhou, O. A. Sadik, C. Umbach and B. Sammakia, *ACS Catal.*, 2011, **1**, 139-146.
 60. J. D. Froehlich and C. P. Kubiak, *J. Am. Chem. Soc.*, 2015, **137**, 3565-3573.
 61. O. Diaz-Morales, T. J. Hersbach, D. G. Hettterscheid, J. N. Reek and M. T. Koper, *J. Am. Chem. Soc.*, 2014, **136**, 10432-10439.
 62. J. Rodríguez-López and A. J. Bard, *J. Am. Chem. Soc.*, 2010, **132**, 5121-5129.
 63. E. Lamy-Pitara, S. El Mouahid and J. Barbier, *Electrochim. Acta*, 2000, **45**, 4299-4308.
 64. S. Zhu, X. Hu and M. Shao, *Phys. Chem. Chem. Phys.*, 2017, **19**, 7631-7641.
 65. J. Y. Shin, Y. S. Kim, Y. Lee, J. H. Shim, C. Lee and S.-G. Lee, *Asian J. Chem.*, 2011, **6**, 2016-2021.
 66. J. Durst, C. Simon, F. Hasché and H. A. Gasteiger, *J. Electrochem. Soc.*, 2014, **162**, F190.
 67. R. Subbaraman, D. Tripkovic, D. Strmcnik, K.-C. Chang, M. Uchimura, A. P. Paulikas, V. Stamenkovic and N. M. Markovic, *Science*, 2011, **334**, 1256-1260.
 68. D. Strmcnik, M. Uchimura, C. Wang, R. Subbaraman, N. Danilovic, D. Van Der Vliet, A. P. Paulikas, V. R. Stamenkovic and N. M. Markovic, *Nat. Chem.*, 2013, **5**, 300-306.
 69. Y. Zhong, K. Ueno, Y. Mori, T. Oshikiri and H. Misawa, *J. Phys. Chem. C*, 2015, **119**, 8889-8897.
 70. T. Takashima, K. Hashimoto and R. Nakamura, *J. Am. Chem. Soc.*, 2012, **134**, 1519-1527.
 71. F. Prieto, I. Navarro and M. Rueda, *J. Phys. Chem.*, 1996, **100**, 16346-16355.
 72. B. Conway and G. Jerkiewicz, *Electrochim. Acta*, 2000, **45**, 4075-4083.
 73. S. Trasatti, *J. Electroanal. Chem. Interfacial Electrochem.*, 1972, **39**, 163-184.
 74. D. Strmcnik, P. P. Lopes, B. Genorio, V. R. Stamenkovic and N. M. Markovic, *Nano Energy*, 2016, **29**, 29-36.
 75. B. B. Blizanac, C. A. Lucas, M. E. Gallagher, M. Arenz, P. N. Ross and N. Marković, *J. Phys. Chem. B*, 2004, **108**, 625-634.

76. P. Sabatier and J. Senderens, *C. R. Acad. Sci. Paris*, 1902, **134**, 689-691.
77. J. Kari, J. P. Olsen, K. Jensen, S. F. Badino, K. B. Krogh, K. Borch and P. Westh, *ACS Catal.*, 2018, **8**, 11966-11972.
78. A. Balandin, in *Adv. Catal.*, Elsevier, 1969, vol. 19, pp. 1-210.
79. G. Ertl, H. Knözinger and J. Weitkamp, *Handbook of heterogeneous catalysis*. 1997.
80. M. Āuroviĉ, J. Hnát and K. Bouzek, *J. Power Sources*, 2021, **493**, 229708.
81. J. K. Nørskov, T. Bligaard, J. Rossmeisl and C. H. Christensen, *Nat. Chem.*, 2009, **1**, 37-46.
82. A. J. Medford, A. Vojvodic, J. S. Hummelshøj, J. Voss, F. Abild-Pedersen, F. Studt, T. Bligaard, A. Nilsson and J. K. Nørskov, *J. Catal.*, 2015, **328**, 36-42.
83. Y. Zhang, J. Zhang and J. Huang, *J. Phys. Chem. Lett.*, 2019, **10**, 7037-7043.
84. R. Jinnouchi, K. Kodama, A. Nagoya and Y. Morimoto, *Electrochim. Acta*, 2017, **230**, 470-478.
85. R. B. Rankin and C. T. Waldt, *J. Phys. Chem. C*, 2019, **123**, 13236-13245.
86. Y. Zheng, Y. Jiao, M. Jaroniec and S. Z. Qiao, *Angew. Chem., Int. Ed.*, 2015, **54**, 52-65.
87. G. Zhu, F. Liu, Y. Wang, Z. Wei and W. Wang, *Phys. Chem. Chem. Phys.*, 2019, **21**, 12826-12836.
88. J. Wang, R. Xu, Y. Sun, Q. Liu, M. Xia, Y. Li, F. Gao, Y. Zhao and S. T. John, *J. Energy Chem.*, 2021, **55**, 162-168.
89. T. Zambelli, J. Wintterlin, J. Trost and G. Ertl, *Science*, 1996, **273**, 1688-1690.
90. D. Guo, R. Shibuya, C. Akiba, S. Saji, T. Kondo and J. Nakamura, *Science*, 2016, **351**, 361-365.
91. Y. Sun, S. Gao, F. Lei and Y. Xie, *Chem. Soc. Rev.*, 2015, **44**, 623-636.
92. V. R. Stamenkovic, D. Strmcnik, P. P. Lopes and N. M. Markovic, *Nat. Mater.*, 2017, **16**, 57-69.
93. I. Langmuir, *Trans. Faraday Soc.*, 1922, **17**, 621-654.
94. H. S. Taylor, *Proc. R. Soc. Lond.. Series A, Containing Papers of a Mathematical and Physical Character*, 1925, **108**, 105-111.
95. G. Somorjai, *Annu. Rev. Phys. Chem.*, 1994, **45**, 721-751.
96. J. H. Pfisterer, Y. Liang, O. Schneider and A. S. Bandarenka, *Nature*, 2017, **549**, 74-77.
97. R. W. Haid, R. M. Kluge, Y. Liang and A. S. Bandarenka, *Small Methods*, 2020,

- 5, 2000710.
98. Y. Liang, D. McLaughlin, C. Csoklich, O. Schneider and A. S. Bandarenka, *Energy Environ. Sci.*, 2019, **12**, 351-357.
 99. H. Reiss and A. Heller, *J. Phys. Chem.*, 1985, **89**, 4207-4213.
 100. E. Guggenheim, *J. Phys. Chem.*, 2002, **33**, 842-849.
 101. E. Guggenheim, *J. Phys. Chem.*, 2002, **34**, 1540-1543.
 102. S. Trasatti, *J. Electroanal. Chem.*, 1999, **476**, 90-91.
 103. X. Li, X. Hao, A. Abudula and G. Guan, *J. Mater. Chem. A*, 2016, **4**, 11973-12000.
 104. L. Li, P. Wang, Q. Shao and X. Huang, *Chem. Soc. Rev.*, 2020, **49**, 3072-3106.
 105. J. Joy, J. Mathew and S. C. George, *Int. J. Hydrogen Energy*, 2018, **43**, 4804-4817.
 106. S. J. Moniz, S. A. Shevlin, D. J. Martin, Z.-X. Guo and J. Tang, *Energy Environ. Sci.*, 2015, **8**, 731-759.
 107. Y. Yan, B. Y. Xia, B. Zhao and X. Wang, *J. Mater. Chem. A*, 2016, **4**, 17587-17603.
 108. S. Anantharaj, S. R. Ede, K. Sakthikumar, K. Karthick, S. Mishra and S. Kundu, *ACS Catal.*, 2016, **6**, 8069-8097.
 109. S. Gupta, M. K. Patel, A. Miotello and N. Patel, *Adv. Funct. Mater.*, 2020, **30**, 1906481.
 110. M. Q. Yang, J. Wang, H. Wu and G. W. Ho, *Small*, 2018, **14**, 1703323.
 111. M. Zeng and Y. Li, *J. Mater. Chem. A*, 2015, **3**, 14942-14962.
 112. S. Watzele, J. Fichtner, B. Garlyyev, J. N. Schwämmlein and A. S. Bandarenka, *ACS Catal.*, 2018, **8**, 9456-9462.
 113. J. M. Bockris and E. Potter, *J. Electrochem. Soc.*, 1952, **99**, 169.
 114. B. Conway and B. Tilak, *Electrochim. Acta*, 2002, **47**, 3571-3594.
 115. T. Shinagawa, A. T. Garcia-Esparza and K. Takanabe, *Sci. Rep.*, 2015, **5**, 1-21.
 116. M. G. Walter, E. L. Warren, J. R. McKone, S. W. Boettcher, Q. Mi, E. A. Santori and N. S. Lewis, *Chem. Rev.*, 2010, **110**, 6446-6473.
 117. I. Ledezma-Yanez, W. D. Z. Wallace, P. Sebastián-Pascual, V. Climent, J. M. Feliu and M. T. Koper, *Nat. Energy*, 2017, **2**, 17031.
 118. M. Bajdich, M. García-Mota, A. Vojvodic, J. K. Nørskov and A. T. Bell, *J. Am. Chem. Soc.*, 2013, **135**, 13521-13530.

119. Y. Yao, S. Hu, W. Chen, Z.-Q. Huang, W. Wei, T. Yao, R. Liu, K. Zang, X. Wang and G. Wu, *Nat. Catal.*, 2019, **2**, 304-313.
120. Y. Wang, X. Li, M. Zhang, Y. Zhou, D. Rao, C. Zhong, J. Zhang, X. Han, W. Hu and Y. Zhang, *Adv. Mater.*, 2020, **32**, 2000231.
121. S. Zhao, M. Li, M. Han, D. Xu, J. Yang, Y. Lin, N. E. Shi, Y. Lu, R. Yang and B. Liu, *Adv. Funct. Mater.*, 2018, **28**, 1706018.
122. S. Divanis, T. Kutlusoy, I. M. I. Boye, I. C. Man and J. Rossmeisl, *Chem. Sci.*, 2020, **11**, 2943-2950.
123. T. Wu, S. Sun, J. Song, S. Xi, Y. Du, B. Chen, W. A. Sasangka, H. Liao, C. L. Gan and G. G. Scherer, *Nat. Catal.*, 2019, **2**, 763-772.
124. P. Liu, B. Chen, C. Liang, W. Yao, Y. Cui, S. Hu, P. Zou, H. Zhang, H. J. Fan and C. Yang, *Adv. Mater.*, 2021, **33**, 2007377.
125. J. D. Michael, E. L. Demeter, S. M. Illes, Q. Fan, J. R. Boes and J. R. Kitchin, *J. Phys. Chem. C*, 2015, **119**, 11475-11481.
126. W. R. Grove, *London, Edinburgh Dublin Philos. Mag. J. Sci.*, 1839, **14**, 127-130.
127. K. Prater, *J. Power Sources*, 1990, **29**, 239-250.
128. Y. Wang, K. S. Chen, J. Mishler, S. C. Cho and X. C. Adroher, *Appl. Energy*, 2011, **88**, 981-1007.
129. H. Mohammed, A. Al-Othman, P. Nancarrow, M. Tawalbeh and M. E. H. Assad, *Energy*, 2019, **172**, 207-219.
130. D. E. Curtin, R. D. Lousenberg, T. J. Henry, P. C. Tangeman and M. E. Tisack, *J. Power Sources*, 2004, **131**, 41-48.
131. K. Dannenberg, P. Ekdunge and G. Lindbergh, *J. Appl. Electrochem.*, 2000, **30**, 1377-1387.
132. S. Sharma and B. G. Pollet, *J. Power Sources*, 2012, **208**, 96-119.
133. A. Chandan, M. Hattenberger, A. El-Kharouf, S. Du, A. Dhir, V. Self, B. G. Pollet, A. Ingram and W. Bujalski, *J. Power Sources*, 2013, **231**, 264-278.
134. B. Lim, E. Majlan, W. Daud, T. Husaini and M. I. Rosli, *Ionics*, 2016, **22**, 301-316.
135. F. T. Wagner, B. Lakshmanan and M. F. Mathias, *J. Phys. Chem. Lett.*, 2010, **1**, 2204-2219.
136. W. Ni, A. Krammer, C. S. Hsu, H. M. Chen, A. Schüler and X. Hu, *Angew. Chem., Int. Ed.*, 2019, **58**, 7445-7449.
137. W. Sheng, A. P. Bivens, M. Myint, Z. Zhuang, R. V. Forest, Q. Fang, J. G. Chen

- and Y. Yan, *Energy Environ. Sci.*, 2014, **7**, 1719-1724.
138. Z. Zhuang, S. A. Giles, J. Zheng, G. R. Jenness, S. Caratzoulas, D. G. Vlachos and Y. Yan, *Nat. Commun.*, 2016, **7**, 1-8.
 139. V. Hasannaemi and S. Mukherjee, *Sci. Rep.*, 2019, **9**, 1-8.
 140. D.-W. Wang and D. Su, *Energy Environ. Sci.*, 2014, **7**, 576-591.
 141. C. Song and J. Zhang, in *PEM fuel cell electrocatalysts and catalyst layers*, Springer, 2008, pp. 89-134.
 142. A. Kulkarni, S. Siahrostami, A. Patel and J. K. Nørskov, *Chem. Rev.*, 2018, **118**, 2302-2312.
 143. J. K. Nørskov, J. Rossmeisl, A. Logadottir, L. Lindqvist, J. R. Kitchin, T. Bligaard and H. Jonsson, *J. Phys. Chem. B*, 2004, **108**, 17886-17892.
 144. G. S. Harzer, J. N. Schwämmlein, A. M. Damjanović, S. Ghosh and H. A. Gasteiger, *J. Electrochem. Soc.*, 2018, **165**, F3118.
 145. W. Jin, H. Du, S. Zheng, H. Xu and Y. Zhang, *J. Phys. Chem. B*, 2010, **114**, 6542-6548.
 146. M. F. Li, L. W. Liao, D. F. Yuan, D. Mei and Y.-X. Chen, *Electrochim. Acta*, 2013, **110**, 780-789.
 147. K. Wan, Z. Yu, X. Li, M. Liu, G. Yang, J. Piao and Z. Liang, *ACS Catal.*, 2015, **5**, 4325-4332.
 148. H. Wang and L. Pilon, *J. Phys. Chem. C*, 2011, **115**, 16711-16719.
 149. R. Burt, G. Birkett and X. Zhao, *Phys. Chem. Chem. Phys.*, 2014, **16**, 6519-6538.
 150. M. Gouy, *J. Phys. Theor. Appl.*, 1910, **9**, 457-468.
 151. D. L. Chapman, *London, Edinburgh Dublin Philos. Mag. J. Sci.*, 1913, **25**, 475-481.
 152. H.-J. Butt and M. Kappl, *Surface and interfacial forces*, Wiley Online Library, 2010.
 153. O. Stern, *Z. Elektrochem. Angew. Phys. Chem.*, 1924, **30**, 508-516.
 154. D. C. Grahame, *Chem. Rev.*, 1947, **41**, 441-501.
 155. W. Xing, S. Qiao, R. Ding, F. Li, G. Lu, Z. Yan and H. Cheng, *Carbon*, 2006, **44**, 216-224.
 156. N. S. Choi, Z. Chen, S. A. Freunberger, X. Ji, Y. K. Sun, K. Amine, G. Yushin, L. F. Nazar, J. Cho and P. G. Bruce, *Angew. Chem., Int. Ed.*, 2012, **51**, 9994-10024.

157. F. da Costa Lopes and E. H. Watanabe, *Proceedings of IEEE Brazilian power electronics conference*, 2009. p. 775-782.
158. A. Gross, F. Gossenberger, X. Lin, M. Naderian, S. Sakong and T. Roman, *J. Electrochem. Soc.*, 2014, **161**, E3015.
159. M. Tahir, L. Pan, F. Idrees, X. Zhang, L. Wang, J.-J. Zou and Z. L. Wang, *Nano Energy*, 2017, **37**, 136-157.
160. Y. Yang, M. Luo, W. Zhang, Y. Sun, X. Chen and S. Guo, *Chem*, 2018, **4**, 2054-2083.
161. C. Hu, L. Zhang and J. Gong, *Energy Environ. Sci.*, 2019, **12**, 2620-2645.
162. K. J. Schweighofer, X. Xia and M. L. Berkowitz, *Langmuir*, 1996, **12**, 3747-3752.
163. R. Rizo, E. Sitta, E. Herrero, V. Climent and J. M. Feliu, *Electrochim. Acta*, 2015, **162**, 138-145.
164. A. Hamelin, *J. Electroanal. Chem.*, 1996, **407**, 1-11.
165. Y. Tong, F. Lapointe, M. Thämer, M. Wolf and R. K. Campen, *Angew. Chem., Int. Ed.*, 2017, **56**, 4211-4214.
166. C.-Y. Li, J.-B. Le, Y.-H. Wang, S. Chen, Z.-L. Yang, J.-F. Li, J. Cheng and Z.-Q. Tian, *Nat. Mater.*, 2019, **18**, 697-701.
167. M. F. Toney, J. N. Howard, J. Richer, G. L. Borges, J. G. Gordon, O. R. Melroy, D. G. Wiesler, D. Yee and L. B. Sorensen, *Nature*, 1994, **368**, 444-446.
168. A. Frumkin and A. Gorodetskaja, *Z. Phys. Chem.*, 1928, **136**, 215-227.
169. Q.-S. Chen, J. Solla-Gullón, S.-G. Sun and J. M. Feliu, *Electrochim. Acta*, 2010, **55**, 7982-7994.
170. S. D. Argade and E. Gileadi, in *Electrosorption*, Springer, 1967, pp. 87-115.
171. N. M. Vargas-Barbosa and B. Roling, *J. Chem. Phys.*, 2018, **148**, 193820.
172. R. Martínez-Hincapié, P. Sebastián-Pascual, V. Climent and J. M. Feliu, *Electrochem. Commun.*, 2015, **58**, 62-64.
173. A. El-Aziz, R. Hoyer, L. Kibler and D. Kolb, *Electrochim. Acta*, 2006, **51**, 2518-2522.
174. G. A. Attard, O. Hazzazi, P. B. Wells, V. Climent, E. Herrero and J. M. Feliu, *J. Electroanal. Chem.*, 2004, **568**, 329-342.
175. T. Pajkossy, L. Kibler and D. Kolb, *J. Electroanal. Chem.*, 2005, **582**, 69-75.
176. A. S. Bondarenko, I. E. Stephens, H. A. Hansen, F. J. Pérez-Alonso, V. Tripkovic, T. P. Johansson, J. Rossmeisl, J. K. Nørskov and I. Chorkendorff, *Langmuir*, 2011, **27**, 2058-2066.

177. V. Climent, G. Attard and J. M. Feliu, *J. Electroanal. Chem.*, 2002, **532**, 67-74.
178. T. Pajkossy and D. Kolb, *Electrochem. Commun.*, 2003, **5**, 283-285.
179. A. Ganassin, P. Sebastián, V. Climent, W. Schuhmann, A. S. Bandarenka and J. M. Feliu, *Sci. Rep.*, 2017, **7**, 1-14.
180. S. Trasatti, *J. Electroanal. Chem. Interfacial Electrochem.*, 1974, **54**, 437-441.
181. V. Climent, B. A. Coles and R. G. Compton, *J. Phys. Chem. B*, 2001, **105**, 10669-10673.
182. G. Lippmann, Relations entre les phénomènes électriques et capillaires. Gauthier-Villars Paris, France, 1875.
183. G. Beni and S. Hackwood, *Appl. Phys. Lett.*, 1981, **38**, 207-209.
184. P. Horsman, B. E. Conway and E. Yeager, *Comprehensive Treatise of Electrochemistry: The Double Layer*, Springer Science & Business Media, 2013.
185. L.-H. Shao, J. Biener, D. Kramer, R. N. Viswanath, T. F. Baumann, A. V. Hamza and J. Weissmüller, *Phys. Chem. Chem. Phys.*, 2010, **12**, 7580-7587.
186. B. B. Damaskin and O. A. Petrii, *J. Solid State Electrochem.*, 2011, **15**, 1317-1334.
187. R. Parsons, *Chem. Rev.*, 1990, **90**, 813-826.
188. M. Vorsina and A. Frumkin, *Doklady Akad. Nauk. S.S.S.R.*, 1939, **24**, 918-921.
189. D. Leikis, K. Rybalka, E. Sevastyanov and A. Frumkin, *J. Electroanal. Chem. Interfacial Electrochem.*, 1973, **46**, 161-169.
190. K. Ojha, N. Arulmozhi, D. Aranzales and M. T. Koper, *Angew. Chem., Int. Ed.*, 2020, **59**, 711-715.
191. J. Clavilier, R. Albalat, R. Gomez, J. Orts, J. M. Feliu and A. Aldaz, *J. Electroanal. Chem.*, 1992, **330**, 489-497.
192. C. D. Silva, G. Cabello, W. A. Christinelli, E. C. Pereira and A. Cuesta, *J. Electroanal. Chem.*, 2017, **800**, 25-31.
193. M. J. Weaver, *Langmuir*, 1998, **14**, 3932-3936.
194. V. Climent, R. Gómez and J. M. Feliu, *Electrochim. Acta*, 1999, **45**, 629-637.
195. B. Alvarez, V. Climent, A. Rodes and J. M. Feliu, *Phys. Chem. Chem. Phys.*, 2001, **3**, 3269-3276.
196. B. Alvarez, V. Climent, J. M. Feliu and A. Aldaz, *Electrochem. Commun.*, 2000, **2**, 427-430.
197. R. Gómez, V. Climent, J. M. Feliu and M. J. Weaver, *J. Phys. Chem. B*, 2000, **104**, 597-605.

198. V. Climent, E. Herrero and J. M. Feliu, *Electrochem. Commun.*, 2001, **3**, 590-594.
199. H. Ebert, R. Parsons, G. Ritzoulis and T. VanderNoot, *J. Electroanal. Chem. Interfacial Electrochem.*, 1989, **264**, 181-193.
200. G. Attard and A. Ahmadi, *J. Electroanal. Chem.*, 1995, **389**, 175-190.
201. A. Ahmadi, E. Bracey, R. W. Evans and G. Attard, *J. Electroanal. Chem.*, 1993, **350**, 297-316.
202. A. Frumkin, O. Petrii and B. Damaskin, in *Comprehensive Treatise of Electrochemistry*, Springer, 1980, pp. 221-289.
203. F. J. Sarabia, P. Sebastián, V. Climent and J. M. Feliu, *J. Electroanal. Chem.*, 2020, **872**, 114068.
204. E. Liu, L. Jiao, J. Li, T. Stracensky, Q. Sun, S. Mukerjee and Q. Jia, *Energy Environ. Sci.*, 2020, **13**, 3064-3074.
205. D. Scieszka, C. Sohr, P. Scheibenbogen, P. Marzak, J. Yun, Y. Liang, J. Fichtner and A. S. Bandarenka, *ACS Appl. Mater. Interfaces*, 2018, **10**, 21688-21695.
206. V. Climent, B. A. Coles, R. G. Compton and J. M. Feliu, *J. Electroanal. Chem.*, 2004, **561**, 157-165.
207. V. Climent, N. García-Araez, R. Compton and J. M. Feliu, *J. Phys. Chem. B*, 2006, **110**, 21092-21100.
208. V. Benderskii and G. Velichko, *J. Electroanal. Chem. Interfacial Electrochem.*, 1982, **140**, 1-22.
209. V. Benderskii, G. Velichko and I. Kreitus, *J. Electroanal. Chem. Interfacial Electrochem.*, 1984, **181**, 1-20.
210. J. F. Smalley, C. Krishnan, M. Goldman, S. W. Feldberg and I. Ruzic, *J. Electroanal. Chem. Interfacial Electrochem.*, 1988, **248**, 255-282.
211. V. Climent, B. A. Coles and R. G. Compton, *J. Phys. Chem. B*, 2002, **106**, 5258-5265.
212. V. Climent, B. A. Coles and R. G. Compton, *J. Phys. Chem. B*, 2002, **106**, 5988-5996.
213. N. García-Araez, V. Climent and J. M. Feliu, *J. Am. Chem. Soc.*, 2008, **130**, 3824-3833.
214. J. Harrison, J. Randles and D. Schiffrin, *J. Electroanal. Chem. Interfacial Electrochem.*, 1973, **48**, 359-381.
215. A. Yamakata and M. Osawa, *J. Phys. Chem. C*, 2008, **112**, 11427-11432.
216. V. Briega-Martos, E. Herrero and J. M. Feliu, *Curr. Opin. Electrochem.*, 2019,

- 17, 97-105.
217. P. Sebastián, A. P. Sandoval, V. Climent and J. M. Feliu, *Electrochem. Commun.*, 2015, **55**, 39-42.
218. G. A. Mabbott, *J. Chem. Educ.*, 1983, **60**, 697.
219. P. T. Kissinger and W. R. Heineman, *J. Chem. Educ.*, 1983, **60**, 702.
220. J. J. Van Benschoten, J. Y. Lewis, W. R. Heineman, D. A. Roston and P. T. Kissinger, *J. Chem. Educ.*, **60**, 772.
221. P. Daubinger, J. Kieninger, T. Unmüssig and G. A. Urban, *Phys. Chem. Chem. Phys.*, 2014, **16**, 8392-8399.
222. R. Kohen, E. Beit-Yannai, E. M. Berry and O. Tirosh, *Methods Enzymol.*, 1999, **300**, 285-296.
223. S. Chevion and M. Chevion, *Ann. N. Y. Acad. Sci.*, 2000, **899**, 308-325.
224. G. Denuault, M. V. Mirkin and A. J. Bard, *J. Electroanal. Chem. Interfacial Electrochem.*, 1991, **308**, 27-38.
225. L. Marcoux and T. O'Brien, *J. Phys. Chem.*, 1972, **76**, 1666-1668.
226. C. Amatore, S. p. Arbault and A. C. Koh, *Anal. Chem.*, 2010, **82**, 1411-1419.
227. Y. Wang, E. I. Rogers and R. G. Compton, *J. Electroanal. Chem.*, 2010, **648**, 15-19.
228. K. Nisancioglu and J. Newman, *J. Electrochem. Soc.*, 1974, **121**, 523.
229. W. Kang, R. Li, D. Wei, S. Xu, S. Wei and H. Li, *RSC Adv.*, 2015, **5**, 94210-94215.
230. B. Lim, M. Jiang, P. H. Camargo, E. C. Cho, J. Tao, X. Lu, Y. Zhu and Y. Xia, *Science*, 2009, **324**, 1302-1305.
231. A. R. Silva Olaya, B. Zandersons and G. Wittstock, *ChemElectroChem*, 2020, **7**, 3670-3678.
232. W. Ma, Y.-L. Ying, L.-X. Qin, Z. Gu, H. Zhou, D.-W. Li, T. C. Sutherland, H.-Y. Chen and Y.-T. Long, *Nat. Protoc.*, 2013, **8**, 439.
233. F. Scheijen, G. Beltramo, S. Hoeppeener, T. Housmans and M. T. Koper, *J. Solid State Electrochem.*, 2008, **12**, 483-495.
234. J. Kunze, V. Maurice, L. H. Klein, H.-H. Strehblow and P. Marcus, *J. Phys. Chem. B*, 2001, **105**, 4263-4269.
235. A. Auer and J. Kunze-Liebhäuser, *Electrochem. Commun.*, 2019, **98**, 15-18.
236. A. S. Bandarenka and M. T. Koper, *J. Catal.*, 2013, **308**, 11-24.
237. B. C. Steele and A. Heinzl, in *Materials For Sustainable Energy: A Collection*

of Peer-Reviewed Research and Review Articles from Nature Publishing Group, World Scientific, 2010, pp. 224-231.

238. N. Marković and P. Ross Jr, *Surf. Sci. Rep.*, 2002, **45**, 117-229.
239. M. T. Koper, *Nanoscale*, 2011, **3**, 2054-2073.
240. H. A. Gasteiger, S. S. Kocha, B. Sompalli and F. T. Wagner, *Appl. Catal., B*, 2005, **56**, 9-35.
241. M. Dresselhaus and I. Thomas, *Nature*, 2001, **414**, 332-337.
242. M. Mavrikakis, *Nat. Mater.*, 2006, **5**, 847-848.
243. S. Mukerjee, S. Srinivasan, M. P. Soriaga and J. McBreen, *J. Phys. Chem.*, 1995, **99**, 4577-4589.
244. W. Li, F. Li, H. Yang, X. Wu, P. Zhang, Y. Shan and L. Sun, *Nat. Commun.*, 2019, **10**, 5074.
245. C.-F. Li, J.-W. Zhao, L.-J. Xie, J.-Q. Wu, Q. Ren, Y. Wang and G.-R. Li, *Angew. Chem., Int. Ed.*, 2021, doi: 10.1002/anie.202104148.
246. T. Ueno, H. Tanaka, S. Sugawara, K. Shinohara, A. Ohma, N. Hoshi and M. Nakamura, *J. Electroanal. Chem.*, 2017, **800**, 162-166.
247. K. Kodama, R. Jinnouchi, N. Takahashi, H. Murata and Y. Morimoto, *J. Am. Chem. Soc.*, 2016, **138**, 4194-4200.
248. J. Greeley, I. Stephens, A. Bondarenko, T. P. Johansson, H. A. Hansen, T. Jaramillo, J. Rossmeisl, I. Chorkendorff and J. K. Nørskov, *Nat. Chem.*, 2009, **1**, 552-556.
249. D. J. Weber, M. Janssen and M. Oezaslan, *J. Electrochem. Soc.*, 2019, **166**, F66-F73.
250. G. C. Ferreira, B. C. Batista and H. Varela, *PLoS One*, 2012, **7**, e50145.
251. S. Zhu and M. Shao, *ECS Trans.*, 2018, **85**, 15.
252. D. Scieszka, J. Yun and A. S. Bandarenka, *ACS Appl. Mater. Interfaces*, 2017, **9**, 20213-20222.
253. N. Garcia-Araez, V. Climent and J. M. Feliu, *J. Phys. Chem. C*, 2009, **113**, 9290-9304.
254. A. Frumkin and O. Petrii, *Electrochim. Acta*, 1975, **20**, 347-359.
255. A. Auer, X. Ding, A. S. Bandarenka and J. Kunze-Liebhäuser, *J. Phys. Chem. C*, 2021, **125**, 5020-5028.
256. W. Sheng, Z. Zhuang, M. Gao, J. Zheng, J. G. Chen and Y. Yan, *Nat. Commun.*, 2015, **6**, 1-6.

257. V. Briega-Martos, E. Herrero and J. M. Feliu, *Electrochim. Acta*, 2017, **241**, 497-509.
258. R. J. Forster, *Chem. Soc. Rev.*, 1994, **23**, 289-297.
259. W.-H. Hu, G.-Q. Han, F.-N. Dai, Y.-R. Liu, X. Shang, B. Dong, Y.-M. Chai, Y.-Q. Liu and C.-G. Liu, *Int. J. Hydrogen Energy*, 2016, **41**, 294-299.
260. D. Gao, J. Wang, H. Wu, X. Jiang, S. Miao, G. Wang and X. Bao, *Electrochem. Commun.*, 2015, **55**, 1-5.
261. B. Blizanac, P. Ross and N. Markovic, *Electrochim. Acta*, 2007, **52**, 2264-2271.
262. P. S. Lamoureux, A. R. Singh and K. Chan, *ACS Catal.*, 2019, **9**, 6194-6201.
263. J. Zheng, W. Sheng, Z. Zhuang, B. Xu and Y. Yan, *Sci. Adv.*, 2016, **2**, e1501602.
264. S. Štrbac, R. Adžić and A. Hamelin, *J. Electroanal. Chem. Interfacial Electrochem.*, 1988, **249**, 291-310.
265. B. E. Conway, *Prog. Surf. Sci.*, 1995, **49**, 331-452.
266. J. Chen, L. Nie and S. Yao, *J. Electroanal. Chem.*, 1996, **414**, 53-59.
267. A. C. Garcia and M. T. Koper, *ACS Catal.* 2018, **8**, 9359-9363.
268. M. Matsumoto, T. Miyazaki and H. Imai, *J. Phys. Chem. C*, 2011, **115**, 11163-11169.
269. A. Kongkanand and J. M. Ziegelbauer, *J. Phys. Chem. C*, 2012, **116**, 3684-3693.
270. M. Nakamura, N. Sato, N. Hoshi and O. Sakata, *ChemPhysChem*, 2011, **12**, 1430-1434.
271. C. Stoffelsma, P. Rodriguez, G. Garcia, N. Garcia-Araez, D. Strmcnik, N. M. Markovic and M. T. Koper, *J. Am. Chem. Soc.*, 2010, **132**, 16127-16133.
272. B. Garlyyev, S. Xue, S. Watzele, D. Scieszka and A. S. Bandarenka, *J. Phys. Chem. Lett.*, 2018, **9**, 1927-1930.
273. S. Xue, B. Garlyyev, A. Auer, J. Kunze-Liebhäuser and A. S. Bandarenka, *J. Phys. Chem. C*, 2020, **124**, 12442-12447.
274. D. Mei, Z. Da He, Y. L. Zheng, D. C. Jiang and Y.-X. Chen, *Phys. Chem. Chem. Phys.*, 2014, **16**, 13762-13773.
275. P. Rodriguez, N. Garcia-Araez and M. T. Koper, *Phys. Chem. Chem. Phys.*, 2010, **12**, 9373-9380.
276. J. Tymoczko, V. Colic, A. S. Bandarenka and W. Schuhmann, *Surf. Sci.*, 2015, **631**, 81-87.
277. D. D. Bode Jr, T. N. Andersen and H. Eyring, *J. Phys. Chem.*, 1967, **71**, 792-797.

278. M. Auinger, I. Katsounaros, J. C. Meier, S. O. Klemm, P. U. Biedermann, A. A. Topalov, M. Rohwerder and K. J. Mayrhofer, *Phys. Chem. Chem. Phys.*, 2011, **13**, 16384-16394.
279. S. Xue, B. Garlyyev, S. Watzele, Y. Liang, J. Fichtner, M. D. Pohl and A. S. Bandarenka, *ChemElectroChem*, 2018, **5**, 2326-2329.
280. J. Hasted, D. Ritson and C. Collie, *J. Phys. Chem.*, 1948, **16**, 1-21.
281. A. Manzo-Robledo, C. Lévy-Clément and N. Alonso-Vante, *Electrochim. Acta*, 2014, **117**, 420-425.
282. G. Mohanakrishna, K. Vanbroekhoven and D. Pant, *J. CO₂ Util.*, 2016, **15**, 57-64.
283. M. E. Gamboa-Aldeco, E. Herrero, P. S. Zelenay and A. Wieckowski, *J. Electroanal. Chem.*, 1993, **348**, 451-457.
284. A. Kolics and A. Wieckowski, *J. Phys. Chem. B*, 2001, **105**, 2588-2595.
285. K. Kunimatsu, M. Samant and H. Seki, *J. Electroanal. Chem. Interfacial Electrochem.*, 1989, **258**, 163-177.
286. T. Schmidt, U. Paulus, H. A. Gasteiger and R. Behm, *J. Electroanal. Chem.*, 2001, **508**, 41-47.
287. J. Wang, N. M. Markovic and R. Adzic, *J. Phys. Chem. B*, 2004, **108**, 4127-4133.
288. Y.-F. Huang, P. J. Kooyman and M. T. Koper, *Nat. Commun.*, 2016, **7**, 1-7.
289. D. Sharon, D. Hirsberg, M. Afri, F. Chesneau, R. Lavi, A. A. Frimer, Y.-K. Sun and D. Aurbach, *ACS Appl. Mater. Interfaces*, 2015, **7**, 16590-16600.
290. K. Holst-Olesen, L. Silvioli, J. Rossmeisl and M. Arenz, *ACS Catal.*, 2019, **9**, 3082-3089.
291. V. Emets and B. Damaskin, *Russ. J. Electrochem.*, 2009, **45**, 45-57.
292. M. K. Birhanu, M. C. Tsai, A. W. Kahsay, C. T. Chen, T. S. Zeleke, K. B. Ibrahim, C. J. Huang, W. N. Su and B. J. Hwang, *Adv. Mater. Interfaces*, 2018, **5**, 1800919.
293. H. Xie, T. Wang, J. Liang, Q. Li and S. Sun, *Nano Today*, 2018, **21**, 41-54.
294. A. Rendon-Calle, S. Builes and F. Calle-Vallejo, *Curr. Opin. Electrochem.*, 2018, **9**, 158-165.
295. C. W. Lee, K. D. Yang, D. H. Nam, J. H. Jang, N. H. Cho, S. W. Im and K. T. Nam, *Adv. Mater.*, 2018, **30**, 1704717.
296. S. Nitopi, E. Bertheussen, S. B. Scott, X. Liu, A. K. Engstfeld, S. Horch, B. Seger, I. E. Stephens, K. Chan and C. Hahn, *Chem. Rev.*, 2019, **119**, 7610-7672.
297. A. Murata and Y. Hori, *Bull. Chem. Soc. Jpn.*, 1991, **64**, 123-127.

298. Y. Hori, H. Wakebe, T. Tsukamoto and O. Koga, *Surf. Sci.*, 1995, **335**, 258-263.
299. I. Takahashi, O. Koga, N. Hoshi and Y. Hori, *J. Electroanal. Chem.*, 2002, **533**, 135-143.
300. J. Frese, *Electrochemical reduction of CO₂ at solid electrodes*, Elsevier: Amsterdam, 1993.
301. E. L. Clark, J. Resasco, A. Landers, J. Lin, L.-T. Chung, A. Walton, C. Hahn, T. F. Jaramillo and A. T. Bell, *ACS Catal.*, 2018, **8**, 6560-6570.
302. P. Lobaccaro, M. R. Singh, E. L. Clark, Y. Kwon, A. T. Bell and J. W. Ager, *Phys. Chem. Chem. Phys.*, 2016, **18**, 26777-26785.
303. Y. Hori, A. Murata and R. Takahashi, *J. Chem. Soc., Faraday Trans. 1: Physical Chemistry in Condensed Phases*, 1989, **85**, 2309-2326.
304. Y. Hori, A. Murata, R. Takahashi and S. Suzuki, *J. Am. Chem. Soc.*, 1987, **109**, 5022-5023.
305. G. Kyriacou and A. Anagnostopoulos, *J. Appl. Electrochem.*, 1993, **23**, 483-486.
306. A. Tiwari, T. Maagaard, I. Chorkendorff and S. Horch, *ACS Energy Lett.*, 2019, **4**, 1645-1649.
307. A. Tiwari, H. H. Heenen, A. S. Bjørnlund, T. Maagaard, E. Cho, I. Chorkendorff, H. H. Kristoffersen, K. Chan and S. Horch, *J. Phys. Chem. Lett.*, 2020, **11**, 1450-1455.
308. A. K. Engstfeld, T. Maagaard, S. Horch, I. Chorkendorff and I. E. Stephens, *Chem. Eur. J.*, 2018, **24**, 17743-17755.
309. P. Sebastian-Pascual, F. J. Sarabia, V. Climent, J. M. Feliu and M. Escudero-Escribano, *J. Phys. Chem. C*, 2020, **124**, 23253-23259.
310. Z. Su, J. Leitch and J. Lipkowski, *Z. Phys. Chem*, 2012, **226**, 995-1009.
311. V. Maurice, H.-H. Strehblow and P. Marcus, *Surf. Sci.*, 2000, **458**, 185-194.
312. W.-H. Li and R. J. Nichols, *J. Electroanal. Chem.*, 1998, **456**, 153-160.
313. M. Arenz, P. Broekmann, M. Lennartz, E. Vogler and K. Wandelt, *Phys. Status Solidi (a)*, 2001, **187**, 63-74.
314. H. Furukawa, K. E. Cordova, M. O'Keeffe and O. M. Yaghi, *Science*, 2013, **341**.
315. S. Kitagawa, *Acc. Chem. Res.*, 2017, **50**, 514-516.
316. Z. Fan, J. Wang, W. Wang, S. Burger, Z. Wang, Y. Wang, C. Wöll, M. Cokoja and R. A. Fischer, *ACS Appl. Mater. Interfaces*, 2020, **12**, 37993-38002.
317. R. Banerjee, A. Phan, B. Wang, C. Knobler, H. Furukawa, M. O'Keeffe and O. M. Yaghi, *Science*, 2008, **319**, 939-943.

318. J. H. Carter, X. Han, F. Y. Moreau, I. da Silva, A. Nevin, H. G. Godfrey, C. C. Tang, S. Yang and M. Schröder, *J. Am. Chem. Soc.*, 2018, **140**, 15564-15567.
319. P. Horcajada, C. Serre, M. Vallet-Regí, M. Sebban, F. Taulelle and G. Férey, *Angew. Chem.*, 2006, **118**, 6120-6124.
320. P. Horcajada, T. Chalati, C. Serre, B. Gillet, C. Sebrie, T. Baati, J. F. Eubank, D. Heurtaux, P. Clayette and C. Kreuz, *Nat. Mater.*, 2010, **9**, 172-178.
321. Y. Belmabkhout, P. M. Bhatt, K. Adil, R. S. Pillai, A. Cadiou, A. Shkurenko, G. Maurin, G. Liu, W. J. Koros and M. Eddaoudi, *Nat. Energy*, 2018, **3**, 1059-1066.
322. X. Han, S. Yang and M. Schröder, *Nat. Rev. Chem.*, 2019, **3**, 108-118.
323. O. K. Farha, A. Ö. Yazaydn, I. Eryazici, C. D. Malliakas, B. G. Hauser, M. G. Kanatzidis, S. T. Nguyen, R. Q. Snurr and J. T. Hupp, *Nat. Chem.*, 2010, **2**, 944-948.
324. D. Farrusseng, S. Aguado and C. Pinel, *Angew. Chem., Int. Ed.*, 2009, **48**, 7502-7513.
325. A. Corma, H. García and F. Llabrés i Xamena, *Chem. Rev.*, 2010, **110**, 4606-4655.
326. L. Jiao, Y. Wang, H. L. Jiang and Q. Xu, *Adv. Mater.*, 2018, **30**, 1703663.
327. I. Stassen, N. Burtch, A. Talin, P. Falcaro, M. Allendorf and R. Ameloot, *Chem. Soc. Rev.*, 2017, **46**, 3185-3241.
328. W. Li, S. Watzele, H. A. El-Sayed, Y. Liang, G. Kieslich, A. S. Bandarenka, K. Rodewald, B. Rieger and R. A. Fischer, *J. Am. Chem. Soc.*, 2019, **141**, 5926-5933.
329. W. Li, S. Xue, S. Watzele, S. Hou, J. Fichtner, A. L. Semrau, L. Zhou, A. Welle, A. S. Bandarenka and R. A. Fischer, *Angew. Chem., Int. Ed.*, 2020, **59**, 5837-5843.
330. Q. Gao, C. Ranjan, Z. Pavlovic, R. Blume and R. Schlögl, *ACS Catal.*, 2015, **5**, 7265-7275.